Bulk and interfacial thermal transport in microstructural porous materials with application to fuel cells

by

Hamidreza Sadeghifar

M.Sc., Sharif University of Technology, 2007

B.Sc., Amirkabir University of Technology (Tehran Polytechnic), 2004

Dissertation Submitted in Partial Fulfillment of the
Requirements for the Degree of
Doctor of Philosophy

in the
School of Mechatronic Systems Engineering
Faculty of Applied Sciences

SIMON FRASER UNIVERSITY

Spring 2015

Approval

Name: **Hamidreza Sadeghifar**

Degree: **Doctor of Philosophy**

Title: ***Bulk and interfacial thermal transport in microstructural porous materials with application to fuel cells***

Examining Committee: **Chair:** Ahmad Rad
Professor

Majid Bahrami
Co-Supervisor
Associate Professor
School of Mechatronic Systems Engineering

Ned Djilali
Co-Supervisor
Professor
Department of Mechanical Engineering
University of Victoria

Michael Eikerling
Supervisor
Professor
Department of Chemistry

Erik Kjeang
Internal Examiner
Assistant Professor
School of Mechatronic Systems Engineering

Elod Gyenge
External Examiner
Professor
Department of Chemical & Biological Engineering
University of British Columbia

Date Defended/Approved: April 13, 2015

Partial Copyright Licence

Abstract

The performance, reliability and durability of fuel cells are strongly influenced by the operating conditions, especially temperature and compression. Adequate thermal and water management of fuel cells requires knowledge of the thermal bulk and interfacial resistances of all involved components. The porous, brittle and anisotropic nature of most fuel cell components, together with the micro/nano-sized structures, has made it challenging to study their transport properties and thermal behavior.

The main purpose of this research was to explore, and guide the improvement of, the thermal behavior of fuel cell materials under compression. Thickness-based methods, having the capability of deconvoluting bulk from the contact resistance, were employed to accurately measure the thermal conductivity of several gas diffusion layers (GDLs) with different PTFE loading. The interfacial thermal resistances of these GDLs with adjacent micro porous layer (MPL) and graphite bipolar plate (BPP) were also determined, through both systematic experiments and comprehensive models developed in this work. The thermal conductivity of a *coated* MPL as a function of compression and that of a Ballard graphite BPP with respect to temperature were also measured and reported in this thesis. Higher values of contact resistance compared to the bulk resistance at low compression and the reduction of GDL thermal conductivity with PTFE loading are among the main findings of this study.

The present work also revealed the following novel counter-intuitive facts: (i) contact resistance may decrease with increasing the porosity of the mating porous materials; (ii) the conventional notion that the thermal conductivity of fibrous materials decreases with increasing porosity does not necessarily hold; and (iii) fiber spacing can be as crucial as porosity to the transport properties of fibrous media. The main conclusion is that the equations that are based solely on porosity should be either discarded or used, with caution, over the limited range of conditions under which they have been formulated.

Through a series of experiments combined with theoretical analyses, this thesis presents some key data that helps unravel some unexplained trends reported in the literature. It also provides novel insights into the unexplored thermal behavior of fuel cell components and guides the modification of their micro-structures for better heat management of fuel cells.

Keywords: Contact resistance; thermal conductivity; gas diffusion layer; micro porous layer; graphite bipolar plate, fuel cell

To my beloved family

and in memory of my father

Acknowledgements

I sincerely thank my supervisors, Dr. Majid Bahrami and Prof. Ned Djilali, for the four years of support and guidance. It was a privilege for me to work with Prof. Djilali, a true scholar, and I really enjoyed working with him.

Chris Miller, the former LAEC's lab engineer, and also James Thompson, Richard Douglas and Gus Lauv, the LAEC's undergraduate students (co-ops), helped me with the calibration and improvement of the TCR machine. Their sincere efforts are appreciated.

My special thanks go to Marius Haiducu, the LAEC's lab manager, and Dr. Wendell Huttema for always being available for discussion.

Undergraduate co-ops, Boyang Fan, Charlie Bennett, Yue Dong and Tilku Khangura, helped me with permeability and electrical tests (not reported in this thesis) as well as with testbeds designs. I appreciate their work and wish them success in life.

I would also like to thank the former and present students of LAEC at SFU and my colleagues at The Institute for Integrated Energy Systems at UVic (IESVic). The group meeting times were exciting and informative to me, especially with the broad range of the topics discussed.

Ballard Power Systems, especially research scientist Katie Green, is appreciated for providing several graphite blank samples with different thicknesses. I enjoyed discussing the different aspects of the graphite samples project with Katie Green due to her rational and proper feedback.

The collaboration with Mercedes Benz Fuel Cell (MBFC) during this research is highly appreciated (EGP/441778-2012 Mercedes Engage, 31-619297). I especially thank Dr. Taryn Biggs for her collaboration with me during projects with MBFC.

Monthly meetings with AFCC experts, research engineer Mickey Tam, Dr. Juergen Stumper, Dr. Andreas Putz and Dr. Ehsan Sadeghi, have been fruitful and productive. I thank them all for the technical discussion and the collaboration (NSERC CRD AFCC, 31-614105).

I wish to heartily thank SGL Carbon Group for providing me with tons of gas diffusion and micro porous layers samples and for technical guidance. I deeply appreciate their collaboration and generosity.

Words cannot express the gratitude I feel for my beloved mother, sisters, brothers and my dearest friend, Farnaz, for their endless affection, love, encouragement and support.

Table of Contents

List of Tables

List of Figures

List of Acronyms

AFCC	Automotive Fuel Cell Cooperation
ASTM	American Society for Testing and Materials
BPP	Bipolar plate
CB	Carbon black
CF	Carbon fiber
CL	Catalyst layer
DAQ	Data acquisition
DOE	US Department of Energy
ECR	Electrical contact resistance
FEM	Finite element method
FIB	Focused ion beam
FM	Fluxmeter
GDL	Gas diffusion layer
GP	Graphene
HOR	Hydrogen Oxidation Reaction
IESVic	The Institute for Integrated Energy Systems
IUPAC	International Union of Pure and Applied Chemistry
LFM	Lower fluxmeter
LAEC	Laboratory for Alternative Energy Conversion
MBFC	Mercedes Benz Fuel Cell
MEA	Membrane electrode assembly
MIP	Mercury intrusion porosimetry
MPL	Micro porous layer
NG	Natural graphite
NPFR	Novolac phenol formaldehyde resins
NSERC	Natural Sciences and Engineering Research Council of Canada
ORR	Oxygen reduction reaction
PDF	Probability density function

PEM	Polymer electrolyte membrane
PEMFC	Polymer electrolyte membrane fuel cell
PTFE	Polytetrafluoroethylene
SEM	Scanning electron microscopy
SFU	Simon Fraser University
SGL	Sigracet
SS	Stainless steel
TCR	Thermal contact resistance
TEM	Transmission electron microscopy
TGP	Toray
UFM	Upper fluxmeter
UVic	University of Victoria

Nomenclature

Symbol	Description	Unit
A, A	GDL cross-sectional area	m^2
a	Half of contact strip length	m
a	Major radius of contact area between one fiber and one carbon particle	m
a,b	Major and minor semi axes of elliptical contact	
a,b	Upper and lower integral bonds (variable p)	
AA,BA, DA,BC	Different types of Sigracet GDLs (0,5,20, 5 (&MPL on one side) %PTFE, respectively)	
AR	Aspect ratio (=l/w)	
A_{fP}	The area on each fiber surface that MPL carbon particles can come in contact with	m^2
b	Length of non-contacting area, b=λ/2-a	m
b	Minor radius of contact area between one fiber and one carbon particle	m
BPP	Bipolar plate	
c	Constant	
Calc.	Based on calculation or derivation	
CB	Carbon black	
d	Fiber diameter	m or µm
Derv.	Derived parameter or equation	
dev.	deviation	
d_f	Fiber diameter	m or µm
d_{fsc}	Diameter of fiber surface curvature at the contact interface	m or µm
d_p	MPL carbon particle diameter	m or µm
$d_{p,ave}$	Average pore diameter	m or µm
E	Young (elastic) modulus	Pa
ECR	Electrical contact resistance	Ω or mΩ cm^2

E^*	$= (\frac{1-v_C^2}{E_C} + \frac{1-v_F^2}{E_F})$ Effective Young (elastic) modulus	Pa
Exp.	Experimental value	
E'	Effective elastic modulus	Pa
F	Force applied on the entire GDL	N
F	Force	N
F(p)	Statistical distribution function of variable p	N
F_1	Integral function of ($\rho'\rho''^{-1}$)	N
F_{max}	Maximum force on each contact point	N
GDL	Gas Diffusion Layer	
k	Thermal conductivity	W m^{-1} K^{-1}
k_{eff}	Effective thermal conductivity	W m^{-1} K^{-1}
I	Current density	A cm^{-2}
l	Distance between two fibers in the x direction	m or μm
l_{f}	Fiber length	m or μm
l_{fap}	Apparent fiber length	m or μm
l_{fap}	Apparent fiber length	m or μm
$l_{\text{f real}}$	Real fiber length	m or μm
M	Arbitrary quantity or quantity of interest	
Meas.	Based on measurement	
Meas.	Measured value or parameter	
MIP	Mercury Intrusion Porosimetry	
MPL	Micro Porous Layer	
M_g	Gas molecular weight	kg $kgmol^{-1}$
M_s	Solid molecular weight	kg $kgmol^{-1}$
N	Number of data measured	
N_{f}	Number of fibers contacting the surface at the pressure of P	
N_{ft}	Total number of fibers contacting the surface	
N_{s}	Number of troughs (strips) each fiber has (forms on the flat surface)	
N_A	Number of the measured areas between fibers	

N_f	Number of fibers contacting the MPL surface at a pressure of P	
N_{ft}	Total number of fibers	
N_p	Number of carbon particles in contact with all the fibers at a compression of P	
N_p^{1f}	Number of carbon particles in contact with all the fibers at a compression of P per one fiber	
N_{p-1f}	Number of carbon particles that may contact one fiber at a compression of P	
N_s	Number of troughs each fiber has	
n_s	Number of asperities contacting the surface of another body in contact	
n_{st}	Total number of asperities contacting the surface	
P	Compression; compressive pressure; pressure	bar or Pa
P	Pressure on the entire GDL	bar or Pa
P	Probability	
p	Random variable (deviation from the average value)	
PDF	Probability density function	
PEMFC	Polymer electrolyte membrane fuel cell	
P_{st}	Pressure at which all the fibers contact the surface	bar or Pa
PTFE	Polytetrafluoroethylene	
P_{GDL}	GDL pressure (Pressure on the entire GDL)	bar or Pa
$p_{d_{pj}}$	Probability of having carbon particles with a diameter of d_{pj}	bar or Pa
$\bar{p}$	Mean pressure	bar or Pa
R	Thermal resistance	KW^{-1}
R_{c}	Spreading/constriction resistance on cylinder side resistance	KW^{-1}
R_{c}	Spreading/constriction resistance on cylinder side resistance	KW^{-1}
R_{co}	Constriction resistance	KW^{-1}
R_{sp}	Spreading resistance	KW^{-1}
R_F	Spreading/constriction resistance on flat surface side	KW^{-1}
R_F	Spreading/constriction resistance on flat surface side	KW^{-1}

SGL	Sigracet	
SS	Stainless steel	
T	Temperature	^{o}C or K
t	Half of strip width	m
t	Thickness	m or μm
t_0	Nominal thickness reported by the manufacturer	m or μm
Temp.	Temperature	
TCR, TCR	Thermal contact resistance	KW^{-1}
TCR_A	Specific-area TCR: Thermal contact resistance per unit area (=TCR×A)	KW^{-1} m^2
u	Half of the width of the rectangular channel area	m
w	Distance between two fibers in the y direction	m or μm
wt%	Weight percent	
x	A space variable defined along the cylinder axis	m
Pr	Prandtl number	

Greek letter

Δ	Amplitude of fiber waviness	m or μm
γ	Non-dimentional separation	
ε	Porosity	
λ	Wavelength of fiber waviness	m or μm
σ	Root mean square (RMS) roughness of GDL (=d_f for the parametric study)	m or μm
υ	Poisson's ratio	
α	Thermal accommodation parameter	
μ	Mean (Gaussian distribution)	
β	Fluid property parameter	
γ	Heat capacity ratio	
η	Modulus of elliptic integral	
θ	Angle between two fibers	Rad

$\bar{\theta}$	Average value of the measured angles	Rad
λ	Ratio of relative radius of curvature ($\rho'\rho''^{-1}$)	
ρ', ρ''	Major and minor relative radii of curvature	m
σ	Standard deviation (Gaussian distribution)	
Λ	Mean free path of gas molecules	m
σ	GDL roughness	m or μm
ψ	Active area percentage of GDL (MPL) surface that can come to contact with MPL (GDL)	

Subscript

1	Bottom block of the unit cell
2	Top block of the unit cell
∞	Standard condition state
ave	Average value
BPP	Bipolar plate
C	Cylinder
cont	Continuous phase
cor	Corrected value
cr	Critical value
dis	Dispersed phase
eff	Effective (overall) value
el	Elastic
f	Fiber
F	Flat surface
FM	Fluxmeter
g	Gas
gc	Gas filled gap
GDL	Gas Diffusion Layer or related to GDL
i	*i*-th component of a set of variables or summation index
i	Carbon particle *i*

j	Carbon particle with diameter of d_{pj}
m	Measured
mac	Macro
max	Maximum value
mic	Micro
min	Minimum value
MPL	Micro porous layer or related to MPL
n	Summation index
p	Carbon particles of MPL
ref	Reference value
s	Solid (carbon fiber)
s	Based on series model
p	Based on parallel model
SGL	Sigracet
SGL_BA	Sigracet GDLs of type BA
SGL_BC	Sigracet GDLs of type BC
Sub	Substrate of GDLs containing MPL
t	Total value
tot	Total
ψ	Related to probability of active areas of GDL and/or MPL that may come to contact

Superscript

$f-MPL$	Contact between one fiber and MPL carbon particles
$f-p$	Contact between one fiber and one carbon particle
*	Correction factor

Executive Summary

The performance and durability of a proton exchange membrane fuel cell (PEMFC) are strictly connected to the transport properties of its components with regard to the heat and water management. A PEMFC produces a considerable amount of waste heat and tolerates only a small deviation in temperature from its design point. The heat distribution through a PEMFC stack needs precise temperature control in order for the PEMFC to run efficiently. Such stringent thermal requirements, coupled with the complex and delicate micro-structures of the components, necessitate an accurate thermal management. A proper thermal management provides the balance between the generated heat and its removal, which determines the operating temperature of the fuel cell. An inadequate heat management leads to a either high or low operating temperature, which leads to the typical consequences as listed in the table below.

The consequences of improper heat management of PEMFCs

Temp.	Issue	Main consequence	Negative effect on
High	Local hot spots	Intensified degradation	Durability/performance
	Membrane dehydration	Ionic conductivity drop	Performance
Low	Decreased reaction kinetics	Increased kinetic losses	Performance
	Heating up catalyst layer	Slow start-up	Durability/performance
	Vapor over-condensation	Flooding	Performance
	Low species diffusivities	Increased transfer losses	Performance

Heat transfer through a PEMFC is highly dependent on the thermal properties of its porous micro and nano-sized materials, especially gas diffusion layers (GDLs) and micro porous layers (MPLs). A proper heat balance inside a stack is connected particularly to the thermal conductivity of the components and specifically to the interfacial heat transfer occurring at their interfaces. This thesis is aimed to provide fundamental understanding of the thermal behavior of PEMFC materials, namely: bipolar plates (BPPs), GDLs and MPLs, as well as their thermal contact resistances (TCRs). Key guidance on improving GDLs and MPLs thermal properties are also presented, which can be useful to fuel cell manufacturers to improve PEMFCs performance and durability.

1) Gas diffusion layers (GDLs)

GDLs are fibrous porous materials composed of a dense array of carbon fibers. They play an important role in the thermal and electrical connection between the BPP and the electrode. The main functions of GDLs are to provide conductivity and help gases to come in contact with the catalyst. The thermal and interfacial resistances of GDLs, together with the porosities and microstructural features, determine their functionality.

Many of the characterization of GDLs transport properties have to date been performed as a function of porosity with little attention devoted to other geometrical properties. A statistical unit cell model is developed in this thesis for predicting the GDLs thermal conductivity by introducing new approaches for determining geometrical properties such as:

- Intersecting fibers angles.
- Characteristic distances between fibers/aspect ratios.

The dependency of the thermal conductivity on these geometrical parameters is analyzed, and the GDL structure is identified for optimal heat conduction. The contributions/ findings include:

- Fibers aspect ratio is as important as porosity in determining thermal conductivity.
- The traditional notion that a porous medium with higher porosity has a lower thermal conductivity does not necessarily hold.
- Two fibrous media with the same porosity may have completely different conductivities.
- The highest thermal conductivity of a GDL occurs at an aspect ratio of unity.
- The highest possible value of the thermal conductivity for fibrous media is independent of aspect ratio and fiber diameter but depends upon porosity and fiber angles.

The geometrical concepts and the measured data presented in this thesis help unravel some unexplained trends reported in the literature and provide novel insights into optimization of GDLs structure. The methodology can be extended to estimate other transport properties such as electrical conductivity, permeability and diffusivity.

1.1) PTFE treatment

In PEMFCs, GDLs are treated with Teflon (PTFE) in order to make the material hydrophobic. Although PTFE improves water transport inside GDLs, it has some side effects on heat management due to its low thermal conductivity. PTFE also increases mass transfer losses as it reduces the GDL porosity. For these reasons, an optimum value of PTFE loading is desirable, which makes it necessary to investigate its effect on PEMFC heat and water management.

Through both modeling and experiments, the effect of PTFE on GDL thermal conductivity is thoroughly explored. In particular, this study reveals:

- The unimportant role of PTFE distribution inside a GDL.
- The important effect of PTFE scattered on the GDL surface on its thermal conductivity.

It is also observed that:

- PTFE reduces thermal conductivity, even though porosity decreases.
- PTFE increases the contact resistance of GDLs with clamping surfaces.

It is worth noting the reductive effect of PTFE on GDLs thermal conductivity in spite of decreasing their porosity. In general, PTFE negatively impacts heat removal from PEMFCs despite its well-proved effect on water management.

2) Micro porous layer (MPL)

Many of the standard GDLs that are produced today come with an MPL composed of carbon particles and PTFE. Although the positive impact of MPLs on PEMFC performance was well proved through experiments, its role in thermal and electrical management of PEMFCs has not yet been well understood. Many studies reported the following incorrect, uncorroborated point: MPLs fill in the gaps between CLs and GDLs and hence minimize the contact resistance.

This point was erroneously asserted to be one reason for the PEMFC performance improvement as a result of using MPLs. However, the findings of this PhD program shows that, contrary to widely-accepted beliefs, MPLs cannot only decrease the GDL thermal conductivity, but also dramatically increase the contact resistance. Any improvement in PEMFC performance as a result of adding MPLs to MEAs should have other reasons, mostly attributed to the positive impact of MPLs on water management and on gas reactant distribution inside the electrodes.

2.1) Thermal conductivity of an MPL coated on a GDL

A precise and systematic approach is adopted to measure the thermal conductivity of a coated MPL. Applying the 'two thickness method' to two different thicknesses of GDL substrates with and without MPL yields the thermal conductivity of the *coated* MPL. This thesis reports the only data available in the literature for the thermal conductivity of a coated MPL. This MPL resistance has been accurately deconvoluted from the other present resistances including the TCR between the MPL and the clamping surfaces.

2.2) Effect of MPL on the GDL thermal resistance

The key findings of this thesis regarding the MPL influence on GDL resistance are as follows:

- MPL reduces thermal conductivity, even though porosity decreases.
- MPL increases the contact resistance of GDLs at the interface with the clamping surfaces.
- MPL increases the contact resistance significantly compared to GDLs with zero or low PTFE content.

The findings of this study show that MPLs have a negative impact on the heat transfer inside the stack despite their positive effect on the water management as asserted in the literature.

3) GDL-MPL Thermal Contact Resistance (TCR)

GDLs coated with an MPL on one side, such as SGL BC types, improve the PEMFC water management. However, due to the very low thermal conductivities of carbon black and PTFE mixed with it, MPL adversely influences the heat transfer inside the stack. As

a result, knowing the thermal contact resistance of MPLs with the GDL substrates will be useful to both heat and water managements of PEMFCs.

A novel analytic model for GDL-MPL TCR is developed and validated experimentally which reveals the following findings:

- TCR between two porous materials may decrease with their porosities.
- The conventional notion that TCR decreases with porosity is not necessarily true.

With increasing the porosity of GDLs and MPLs:

- Diffusivity of reactants to the CL surface increases and mass transfer losses decrease.
- Contact resistance typically increases and so do ohmic losses.

The novel finding here can be considered as a criterion for using GDLs and MPLs with higher porosities in PEMFCs, which enables one to enhance diffusivity while reducing TCR (and also electrical contact resistance). The porosity range of PEMFC porous materials is restricted to specific values considering both ohmic and mass transfer losses. Since there is a trade-off between these two types of losses in terms of GDLs and MPLs porosities, an optimum value of the porosities can lead to an improvement to the performance. Ultimately, considering other GDL parameters such as fiber diameters and aspect ratios, an optimized structure of fibrous GDLs with the maximum possible porosity can result in a noticeable improvement in PEMFCs efficiency and performance. Particularly, this point can be important at high current densities where mass transfer losses dramatically increase, which leads to a noticeable reduction in the PEMFC efficiency. This can be an intriguing topic for future research.

4) Graphite bipolar plate (BPP)

Bipolar plate is a multi-functional component within a PEMFC stack, which conducts heat and electrons through the cells, as one of its main functions. An inadequate contact

between a BPP and a GDL deteriorates the PEMFC performance by disturbing its electrical and heat management.

In this thesis, thermal conductivity of a graphite BPP is measured under different temperatures and pressures using the two thickness method. The bulk resistance of the BBP samples is deconvoluted from their contact resistances with the clamping surfaces. This allows not only accurately measuring the thermal conductivity of the BBP but also addressing the effect of compression, PTFE, MPL, out-of-flatness and cyclic loads on its TCR with different GDLs. The key results are summarized below:

- Thermal conductivity of the graphite BPP decreases with increasing temperature.
- The TCR of the BPP with the clamping surfaces reduces with temperature.
- The BPP-GDL TCR increases with both MPL and PTFE, regardless of the PTFE loading.
- High PTFE loading, MPL and BPP out-of-flatness increase the GDL-BPP TCR dramatically.
- The BPP-GDL TCR can be the dominant resistance in GDL-BPP assembly.
- Load cycling reduces the total thermal resistance of the BPP-GDL assembly considerably.
- The reduction effect of load cycling on the thermal resistance of the BPP-GDL assembly is more pronounced for GDLs with lower PTFE loading.

An analytic model is also developed for fibrous-plate contact resistance that, contrary to all the TCR models, considers the waviness of the fibers. This model reveals that fiber waviness, diameter and surface curvature, as well as GDL porosity, have a strong influence on TCR whereas fiber length does not affect the TCR when the porosity is kept constant. The insights gained through this work can open alternative avenues for tailoring and optimizing the microstructure of fibrous porous media such as GDLs from the viewpoint of manufacturing process and transport properties.

5) Effect of clamping pressure

In general, there is a trade-off between ohmic losses and mass transfer losses as a result of compression. For porous materials of MEA, with increasing stack clamping pressure:

- Ohmic resistances reduce as bulk and contact resistances decrease.
- Mass transfer increases as porosity decreases.

This point demonstrates that increasing stack clamping pressure is useful as long as the porosities of fuel cell components do not decrease dramatically. The variations of thermal conductivities of GDLs, MPLs and BPPs and their interfacial resistances with compression are thoroughly addressed in this work. The following can be used as a framework and database for fuel cell manufactures and development:

- Data of deconvoluted contact from bulk resistances of GDLs, MPLs and BPPs over compression.
- Guidance given on improving the thermal (and possibly electrical) properties of GDLs and MPLs with regard to their microstructures, porosity and the clamping pressure.

The following figure shows the road map and the deliverables for the present research.

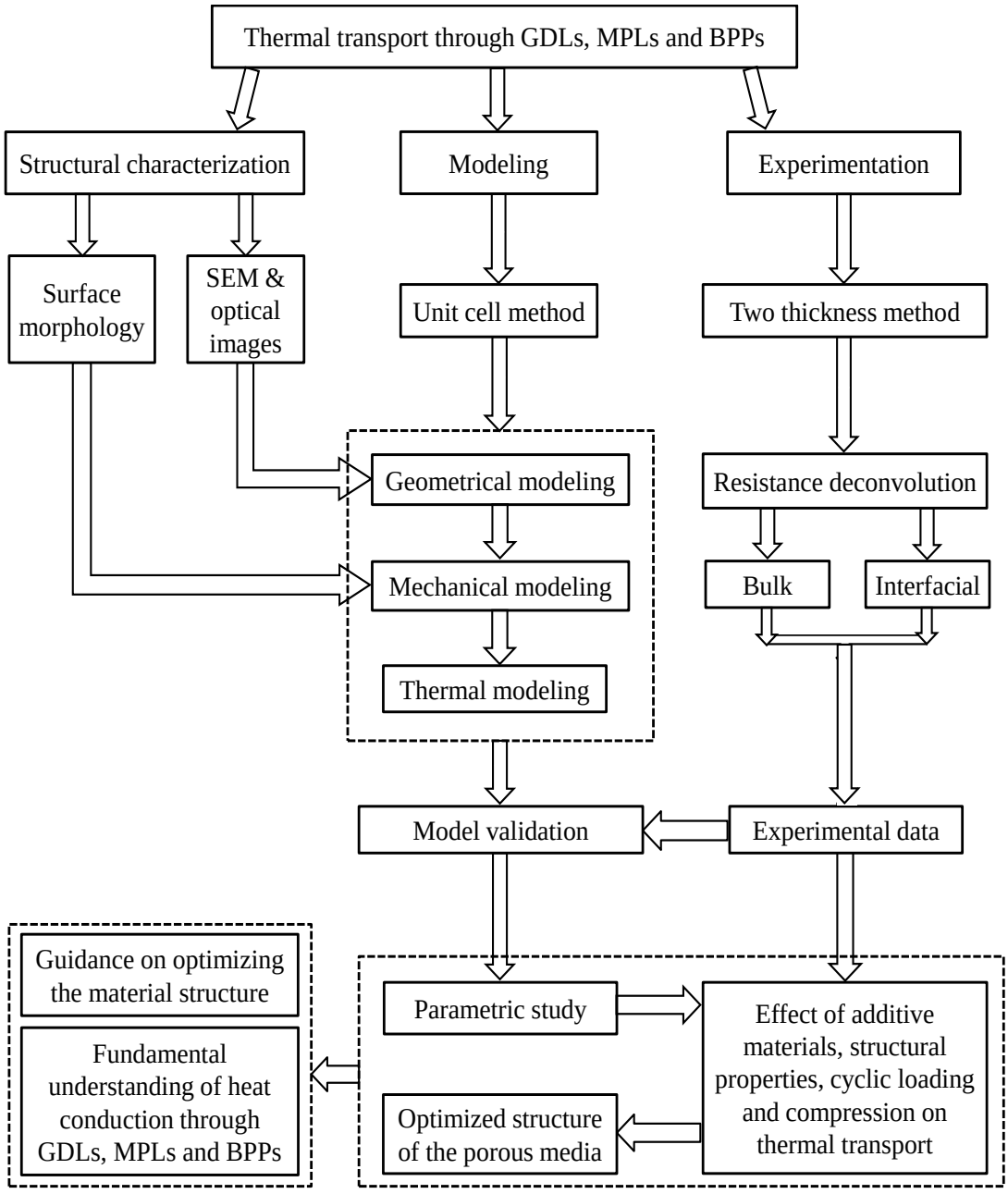

Road map and deliverables for the present dissertation

Chapter 1.

Introduction

1.1. Setting the scene

The supply of clean and sustainable energy is one of the most important challenges facing humanity in the 21st century. Fuel cell technology has the potential to contribute to a more efficient and secure energy supply and to address the climate change by reducing emissions [1][2].

A polymer electrolyte membrane fuel cell (PEMFC) is an electrochemical device that converts the chemical energy of hydrogen into electricity, water and heat. Fuel cells are unique in terms of the variety of their applications and sizes; they can provide energy for systems as large as a power station and as small as a cell phone. They are currently being investigated as an alternative to the internal combustion engines in transportation applications and, in general, as a secure and clean supply of energy in the future.

Although fuel cells are one of the best candidates to replace gasoline-based engine, the technology is still immature for large-scale commercialization [2] [3] [4]. Critical prerequisites for the commercialization of fuel cells are improvements in their performance, reliability and durability as well as reductions in their production costs [5] [6] [3]. Figure 1.1 shows the target cost for fuel cells as defined by the US Department of Energy (DOE). The DOE has reduced the target cost of automotive PEMFCs from $106/kW in 2006 to $55/kW in 2014 and is targeting a cost of $30/kW [7]. Other target

values set by the DOE are: (i) Demonstrated 2,500-hour (75,000 miles) durability for PEMFC systems in vehicles operating under real-world conditions, with less than 10% degradation [8], (ii) improved performance of stationary fuel cells [9], and (iii) advanced manufacturing methods and materials that enable a 50% decrease in the cost of porous (gas diffusion) layers compared to 2008 costs [10]. These targets indicate the importance of durability and performance of fuel cells and that substantial research and development is still required to reach these ultimate targets.

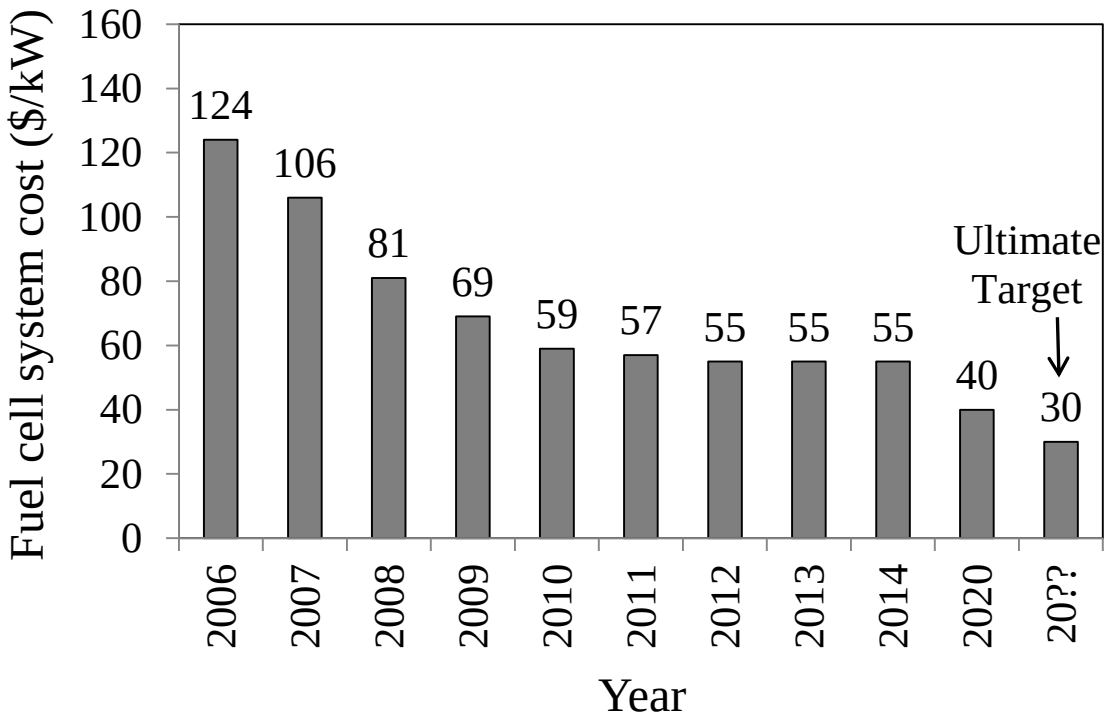

Figure 1.1. Projected transportation PEMFC system cost defined by the DOE based on projection to high-volume manufacturing (500,000 units/year) [7]

1.1.1. Fibrous porous materials

A porous medium is a solid with voids distributed throughout the bulk of its body. The basic characteristic of such medium is porosity, which plays a major role in defining its transport properties (fluid, mass, heat and electrical charge transfer). The properties can be improved by determining and manipulating the key parameters through modeling and experiments. This approach can help modify and improve the structure of the manufactured porous medium to enhance the transport property of interest, with minor side effects on its other properties. The key findings can be employed for manufacturing new materials with improved properties.

The last decade has witnessed a dramatic growth in the application of fibrous porous materials in existing and emerging technologies such as bioengineering, energy, electronics, and water filtration, to name a few. Examples of these fibrous materials are gas diffusion layers for fuel cells, textile composites for tissue engineering, zeolite membranes for water treatment, porous hydrogels for neural tissue, graphene coated textiles as capacitor, and fiber reinforced concrete. Figure 1.2 shows several fibrous porous materials with different applications.

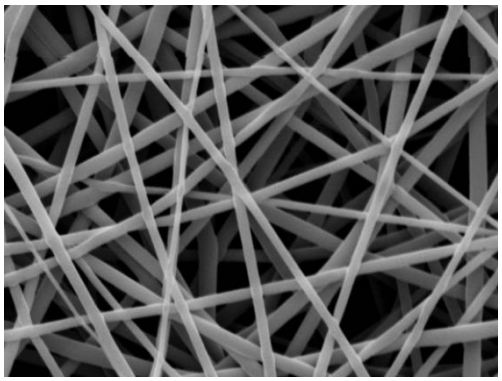

a): A fibrous material [11]

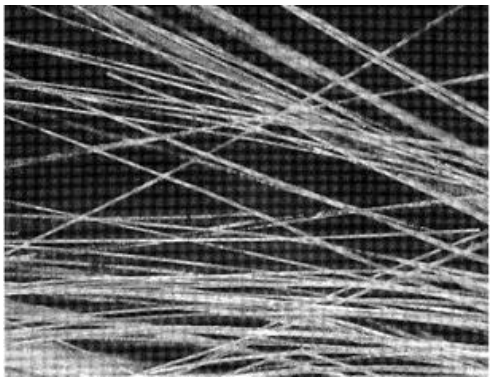

b): A fibrous catalyst [11]

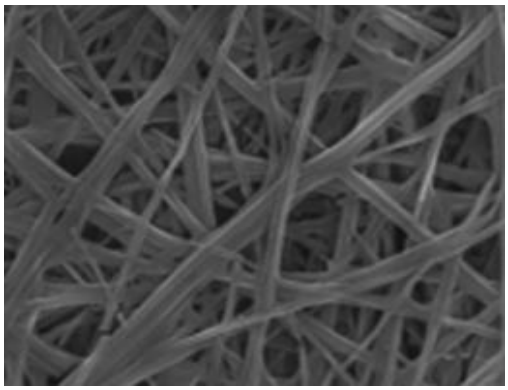

c) A hydrogel nanocomposite catalyst [12]

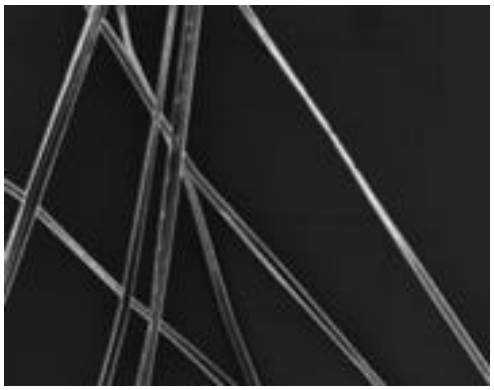

d) A porous carbon paper [13]

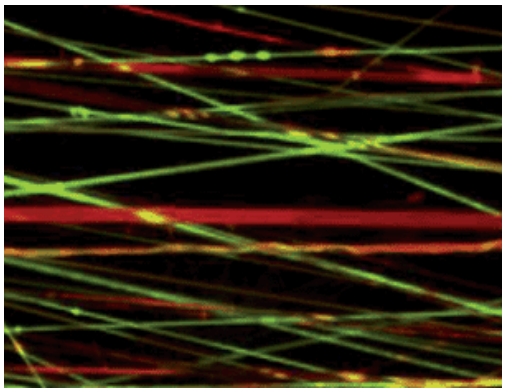

e) A highly porous composite scaffold [14]

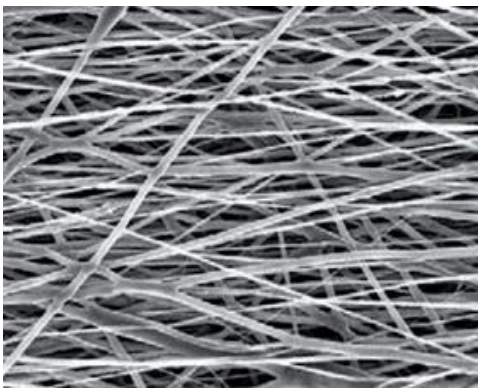

f) A compact composite scaffold [14]

Figure 1.2. Different fibrous materials widely used in existing & emerging technologies (adapted with permission from the original references)

According to the orientation of the fibers, fibrous structures can be categorized into three different groups as shown in Figure 1.3 [15]:

- One-directional (1D) media, where the fibers' axes are parallel to each other, e.g. tube banks;
- Bi-directional (2D) media, where the fibers' axes extend along parallel planes, with an arbitrary orientation within these planes, e.g., gas diffusion layers (GDLs) of fuel cells.
- Three-directional (3D) media, where the fibers' axes are randomly positioned and oriented in any given volume.

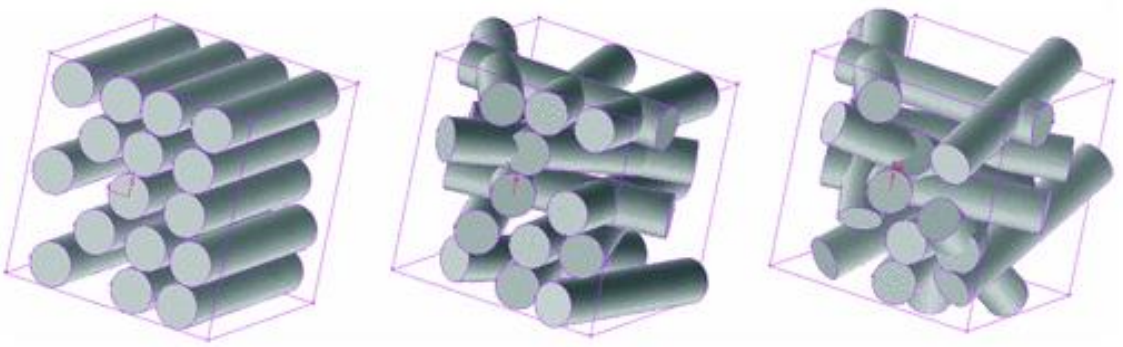

(a) 1D (b) 2D (c) 3D

Figure 1.3. Fibrous porous media categorized in three groups in terms of structure and fiber orientation (adapted with permission from Ref. [15])

Fibrous materials are generally anisotropic, and more specifically orthotropic i.e., the transport properties in one direction differ from those on the other two directions. The materials studied in this thesis are generally 2D fibrous media. The terms "fibrous

material" or "fibrous medium" will denote a 2D fibrous medium unless otherwise specified.

1.1.2. Porous materials composed of spherical particles

Porous materials made of spherical particles are widely used in a number of applications, such as porous carbons, aerogels, catalysts, adsorbents, ion exchange materials. These materials provide high surface area and an open framework structure, which enables production of materials with multiscale porosity.

According to the International Union of Pure and Applied Chemistry (IUPAC) [16], porous materials can be classified into three categories based on the effective width of the pores: macro porous (>50 nm), meso porous (2 ~50 nm), and micro porous materials (<2 nm). The fibrous and porous materials studied in this thesis lie within the macro and meso porous groups.

1.2. PEMFC components

PEMFCs are made of stacked individual cells, called membrane electrode assemblies (MEAs). As shown in Figure 1.4, the main components of a PEMFC are a porous catalyst layer (CL) that are coated on the polymer electrolyte membrane (PEM) and the fibrous porous gas diffusion layers (GDLs) that are usually accompanied by another porous material called the micro porous layer (MPL). The MEA is under compression in between two bipolar plates (BPPs). As mentioned earlier, PEMFCs generate electricity, heat and water. Figure 1.4 also shows all the thermal and electrical resistances available

in a PEMFC, which include the bulk resistances of all the components and the interfacial (contact) resistances between the contacting components.

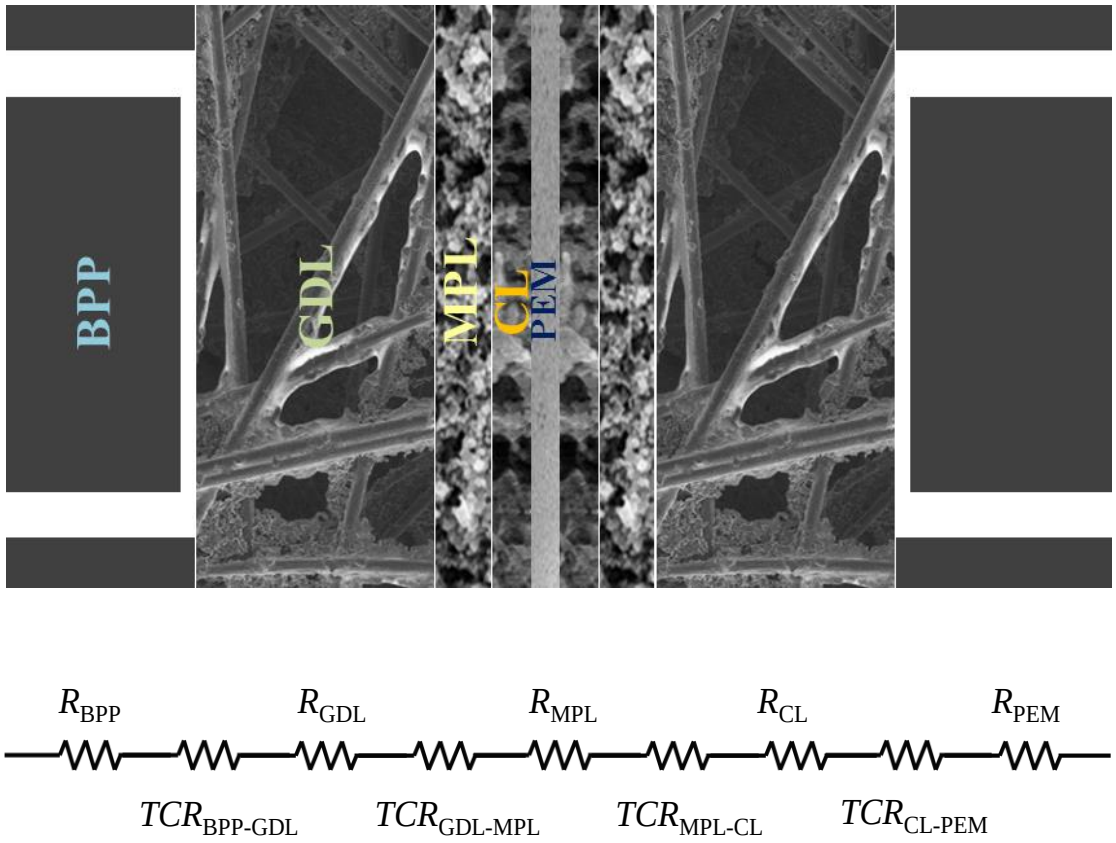

Figure 1.4. Main components of a fuel cell and their bulk and interfacial resistances

1.3. How do PEMFCs work?

A PEMFC converts the chemical energy released during the electrochemical reaction of hydrogen and oxygen into electrical energy, as shown schematically in Figure 1.5. A stream of hydrogen is fed through the anode side of the MEA. At the anode side, the

hydrogen is catalytically split into protons and electrons. This oxidation half-cell reaction or Hydrogen Oxidation Reaction (HOR) is represented by:

$$H_2 \rightarrow 2H^+ + 2e^- \qquad (1\text{-}1)$$

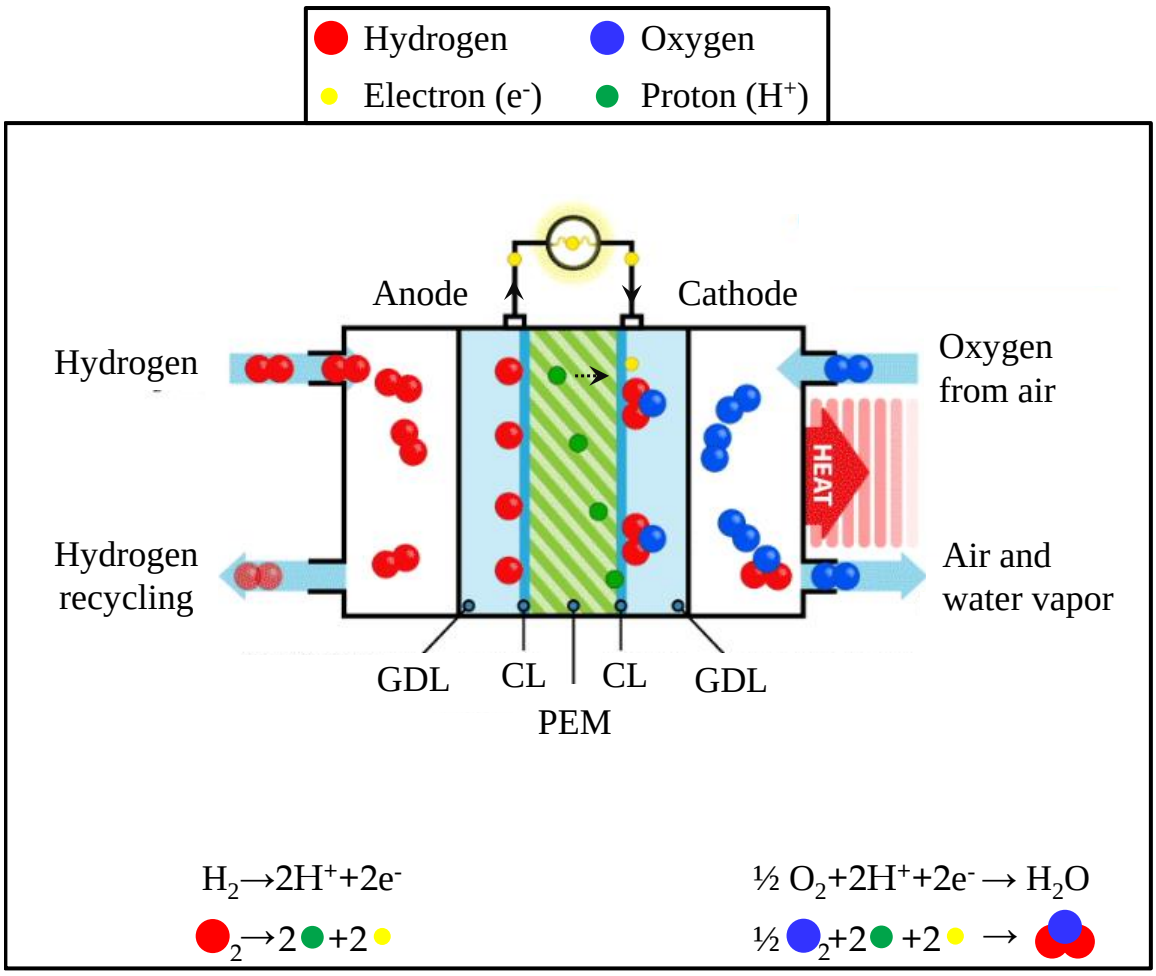

Figure 1.5. A schematic showing how a PEMFC works

The newly formed protons migrate through the membrane to the cathode. The electrons go through an external circuit to the cathode side of the MEA, thus generating the current output of the fuel cell. A stream of oxygen is fed into the MEA cathode where oxygen molecules react with the protons passing through the membrane and with the electrons arriving through the external circuit to form water molecules. This oxygen reduction reaction (ORR) is represented by:

$$\tfrac{1}{2}\, O_2 + 2H^+ + 2e^- \rightarrow H_2O \qquad (2\text{-}1)$$

These reactions produce water and heat, which have to be removed from the cell through proper thermal and water management.

1.4. Thermal management of PEMFCs

Thermal management is one of the key challenges on the path to full commercialization [17] [18] [19] [20] [21]. There are different heat transfer modes and issues in PEMFC components and different practical cooling systems are used. Kandlikar and Lu [17] provided a succinct summary of the PEMFC heat management, the different heat transfer modes inside PEMFCs components and the link between heat and water management of PEMFCs.

1.4.1. Heat generation

Heat generation in a PEMFC includes entropic reactions heat, irreversibilities of the electrochemical reactions and ohmic losses, as well as the heat released by water condensation [22]. The entropic heat is related to the entropy change of the electrochemical reaction and must be balanced inside an operating cell to maintain a

constant temperature. The irreversibility of the electrochemical reactions [17] generate significant amount of heat on both anode and cathode sides of a PEMFC. However, more heat is generated at the cathode side due to the higher entropy change and overpotentials [23] [24] [25] [26]. For this reason, the temperature at the cathode side is higher than that at the anode side, which makes it more challenging to keep a uniform temperature distribution across the MEA. The electrical resistances arose from the electron and proton transfer lead to the ohmic heat inside a cell. This ohmic loss can be reduced by using higher conductive materials. The heat generated by the entropy change, reaction irreversibility and ohmic losses account for 55%, 35% and 10% of the total heat release, respectively [27], which reduce the power output of a PEMFC considerably [17].

1.4.2. Heat transfer in PEMFCs

The heat generated in a PEMFC is primarily removed by conduction through the components, convection by the feed streams and convection over the external surfaces of the stack. The thermal properties of individual components in a PEMFC, along with other transport properties such as permeability, significantly affect the rate of heat removal. The thermal conductivities of PEMFC materials are usually obtained from either *ex-situ* measurements or *in-situ* determinations inside a PEMFC [17]. In some cases where experimentation is not feasible, robust models are the only tools available to determine the thermal conductivity. In general, experimental data supported by theoretical analyses provide a better platform for analyzing the thermal properties of porous and anisotropic micro/nanoscale components of PEMFCs.

The mechanisms of heat transfer differ between the various components. In porous components, i.e., CLs, GDLs and MPLs, both conduction and convection contribute in various degrees to the heat transfer while heat is transferred through the PEM via conduction. Heat transfer also occurs as a result of coupling with mass transfer

phenomena inside the cell. One of the most important couplings is between the heat and water transport in a PEMFC: (i) evaporation and condensation of water inside the pores absorbs or releases the latent heat; (ii) water and heat transports are coupled through the heat pipe effect (temperature variations lead to phase change, which affects water transport, and vice versa) [28]; and (iii) the vapor pressure is a strong function of temperature [17].

1.4.3. Fuel cell stack cooling

There are several factors that play major roles in removing heat from, and in designing an effective cooling system for, PEMFCs. The first is operating temperature, which has to be kept at about 80 °C. This temperature is much lower than the typical 500-700 °C [29] operating temperature of internal combustion engines. This makes the thermal management of PEMFC more challenging than that of the internal combustion engines, as there is a lower temperature difference for cooling PEMFCs. Second, the heat generated in a PEMFC has to be removed by an effective cooling system since the exhaust streams cannot meet the heat removal requirements. The third issue is related to water condensation and vaporization inside the cell, which has to be taken into account in the heat balance. These requirements for proper heat removal from a stack, but still can be met by using oversized radiators, represent major challenges in the design of PEMFC cooling system especially in automotive applications [17] [30].

1.4.4. Non-uniform temperature distribution in a PEMFC

In a PEMFC, there should be a balance between the heat generation and the heat removal rates in order to keep the operating temperature at a required steady-state level. The temperature inside a PEMFC peaks at the cathode CL due to the large amount of heat

generated by the electrochemical reaction [31] [32] [33]. This has been observed from experimental measurements [34] and predicted by various thermal models [22] [27] [35]. A temperature drop of ~5 °C is expected across the MEA at the current density of 1 A cm^{-2} [34] [36]. This temperature difference, which significantly influences the water and heat transport in a PEMFC, is mostly dictated by the thermal conductivities of the MEA components and their interfacial resistances. The brittle, anisotropic and microstructural nature of the MEA components complicates the thermal measurements and heat transfer modeling [17] [37].

1.4.5. Coupled heat and water transport in a PEMFC

The heat transfer in a PEMFC is inherently linked to water transport and is influenced by water phase change [21] [38] [39]. According to Eikerling [40], water vapor is desirable in the cathode CL, and this can be achieved through adequate and simultaneous thermal and water management of PEMFCs. The thermal gradients across the MEA play significant roles in the water transport toward the gas channels and its phase change within the MEA. These gradients are highly dependent on the transport properties, specifically thermal resistances, of the PEMFC components. A detailed review of the transport mechanisms of water in conjunction with the temperature distribution inside the stack is given by Kandlikar and Lu [21].

1.4.6. Thermal management issues in a PEMFC

Figure 1.4 also illustrates schematically the various bulk and interfacial resistances. The transport and physical properties of MEA components, coupled with the interactions at their interfaces, are crucial for determining the performance of PEMFCs and enhancing their efficiencies [1] [39] [41]. Specifically, knowledge of the thermal bulk and contact

resistances of all involved components is essential for proper thermal and water management of PEMFCs [11] [12] [43] [44] [45]. An inadequate temperature distribution may cause local hot spots in the cell, which can intensify degradation of the cell components, especially MEAs, and reduce their lifetime. In addition to this, higher temperatures in the cell reduce the membrane humidity and, therefore, its ionic conductivity, as well as the maximum theoretical voltage the cell can produce [46]. Any excessive drop in operating temperature, on the other hand, can cause reductions in reaction kinetics and species diffusivities, leading to malfunction [45] [47]. In addition to the above phenomena, heating of the catalysts during the start-up of PEMFCs, especially in sub-zero conditions [24] [25], is also highly dependent on the thermal conductivity of the cell components, especially GDLs [50]. Table 1.1 summarizes the main factors and phenomena affected directly by heat management of a PEMFC.

Table 1.1. Main factors affected by the heat management of a PEMFC and the consequences of improper heat management

Main phenomenon/issue in/for a PEMFC	Main consequence	Negative effect on PEMFC's
Local hot spots	Intensified degradation	Lifetime
Membrane dehydration	Ionic conductivity drop	Performance & Lifetime
Temperature drop	Decreased reaction kinetics	Performance
Temperature drop	Low species diffusivities	Performance
Inability to heat CL	Slow start-up	Reliability & Lifetime
Water management	Flooding or cell humidity drop	Performance

As shown in Table 1.1, there are a number of issues in PEMFCs related to the transport properties of the cell components, especially thermal conductivity and interfacial resistances of the components, specifically those of treated and untreated GDLs. Investigating the dependency of these properties on salient variables such as compression, humidity, additive materials of PTFE and MPL, cyclic load and hysteresis behavior are vital for understanding and improving the performance and longevity of PEMFCs. However, due to difficulties in experiments and complexity in modeling, relatively few experimental work and modeling studies have been reported to date on the thermal bulk and contact resistance of fuel cell materials [51] [52]–[54] [55] [56]–[58]. The brittle, porous and anisotropic nature of most fuel cell components, together with their low thicknesses, has made it challenging to measure and analytically model their thermal resistances.

The lack of experimental and analytical work is one of the key motivations for this study. This research intends to develop a framework in which the microstructure and properties of the porous media required to enhance PEMFC's performance can be studied. The focus will be mainly on gas diffusion layers, micro porous layers and the graphite bipolar plates, and interactions at their interfaces. The in-plane electrical conductivity and through-plane thermal resistance of catalyst-coated membrane will also be studied as part of this program but is not reported due to the confidentiality issues.

It is worth emphasizing that in order to achieve the optimum fuel cell performance, it is essential to improve understanding of the characteristics of GDLs and MPLs, i.e. their structure, pore size, porosity, thermal and electrical conductivities, gas permeability, wettability, surface morphology and water management. This is because GDLs and MPLs are the functional components that provide a support structure for gas and water transport in PEMFCs. They play a crucial role when the oxidant is air, especially when the fuel cell operates in the higher current density region. For these reasons, analysis and characterization of GDLs and MPLs are crucial to improving the performance and durability of PEMFCs. There has been a noticeable growth in the research and

development of GDLs' and MPLs' characteristics and behavior to improve their properties [59]. The present thesis attempts to provide some key data on GDLs' and MPLs' characteristics and their bulk and interfacial thermal behavior. The optimized structure of GDLs and MPLs for having higher thermal conductivities and lower contact resistances will also be discussed in detail.

1.5. Polarization curves: Impact of contact resistances

The main impact of GDL and MPL conductivities and contact resistances are on ohmic loss, which is one of the main losses in normal fuel cell operation. The contribution from the contact resistance to the ohmic loss has been reported to be approximately equal to that from the proton conduction resistance in the membrane [60] [61] [62]. Chang et al. [60] reported that in the practical range of stacking pressure, e.g. 10 bar, the magnitude of electrical resistance becomes less than 50 $m\Omega\ cm^2$, whereas a fully hydrated Nafion 112 membrane has an electrical resistance of 70 $m\Omega\ cm^2$ [63].

A plot of cell potential against current density under a set of constant operating conditions, known as a polarization curve, is the standard tool for characterizing the performance of fuel cells. A polarization curve shows information on the performance losses in the cell. The curve has three major regions: kinetics or activation loss; ohmic loss; and mass transfer loss. Polarization curves shown in Figure 1.6 [64] show how the ohmic loss decreases with compression. It should be noted that the optimum compression at which the overall performance of a fuel cell is highest is not necessarily the highest or lowest clamping pressure applied. Since the variation of bulk resistance with compression is small for fuel cell thin components, the decrease of ohmic loss with compression is largely attributed to the reduction in the contact resistance between the fuel cell components (ionic conductivity is also important). This underscores the importance of contact resistance and its direct impact on fuel cell performance. Yin et al. [65] and

Salaberri and Vera [66] have shown that at low assembly pressures, the inadequate electrical contact between the GDL and the BPP greatly deteriorates the cell performance. Therefore, the role of the contact resistance on the fuel cell performance is critical [60] [67] [68] [69] and need to be thoroughly investigated.

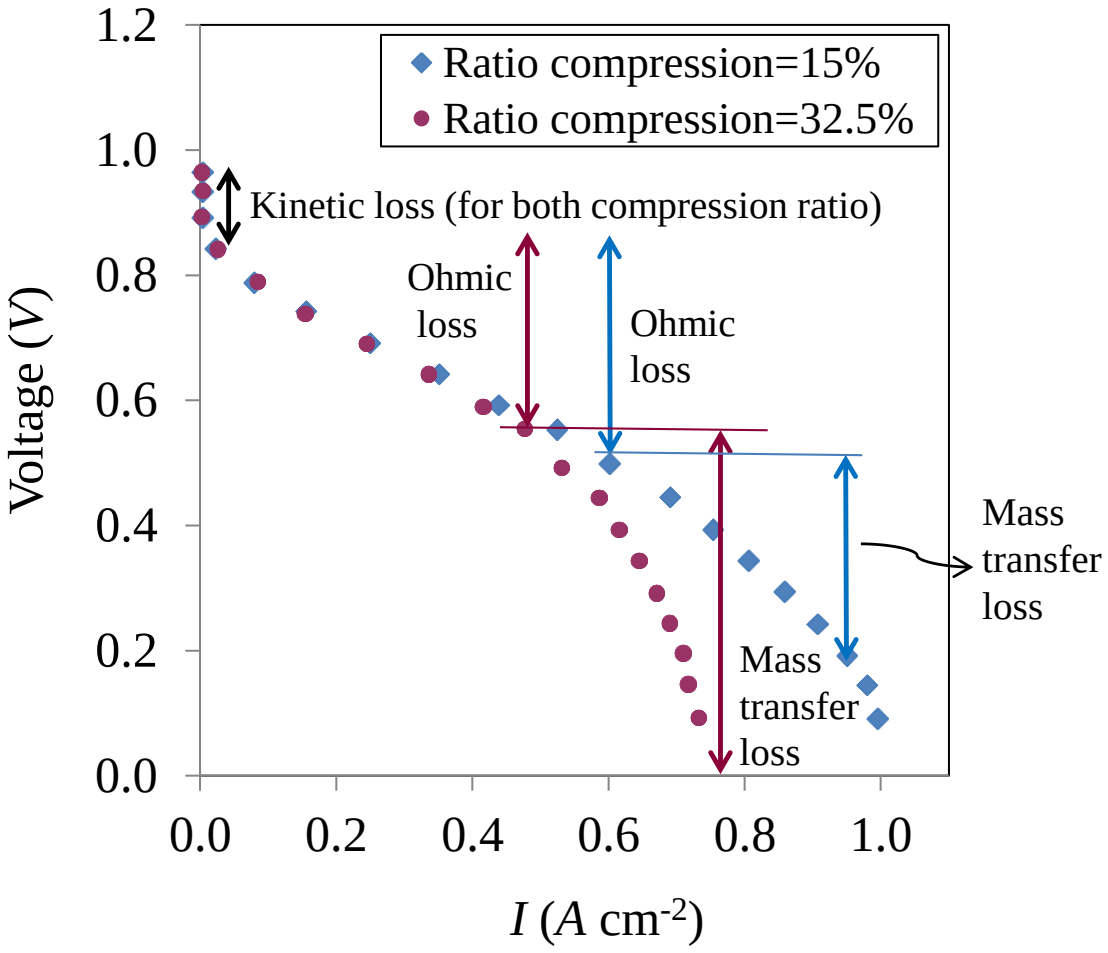

Figure 1.6. **Effect of GDL compression ratio on the performance of a PEMFC. The compression ratio of the GDL is defined as the ratio of the change in operating thickness to the GDL original thickness (reprinted with permission from Ref. [64])**

1.6. Polarization curves: Ohmic versus mass transfer losses

The effect of GDL compression on fuel cell performance was experimentally studied in several works. Yim et al. [70] observed that the decrease of contact resistance by high GDL compression affects more dominantly on the stack performance than the increase of mass transport resistance in the present stack configurations. The polarization curves of Ref. [64] shown in Figure 1.6 also clearly illustrate the effect of compression on the cell performance. In general, there is a trade-off between ohmic and mass transfer losses as a result of compression [71] [72] [73] [74] [75] [76] [77]. The more the compression, the lower the contact resistance but the higher the mass-transfer overpotential would be since the porosities of the components decrease with compression. This point indicates that increasing stack clamping pressure is useful as long as the porosities of the fuel cell components do not decrease dramatically (also see [67] [70] [75] [78]). An interesting question is whether *it is possible to reduce contact resistance while increasing porosity?*

If it were possible, both ohmic and mass transfer losses would be reduced, which could eventually result in an improvement in the PEMFC performance. This challenging question is addressed in Chapter 6 of this thesis.

One of the main side effects to PEMFCs performance due to increasing the porosity of GDLs is related to the reduction in thermal and electrical conductivity. As a result, it would be preferable to increase porosity without decreasing thermal and electrical conductivity. This raises another question: how can the fuel cell manufacturers increase GDL porosity without decreasing its conductivity? This question is addressed and answered in Chapter 4 of this study by referring to the GDL structure and its manipulation. The impact of porosity and compression on bulk and contact resistances, which can directly affect the cell ohmic losses, are central issues discussed in detail in this thesis.

1.7. Objectives

One of the key parameters that directly affects both heat and water management of a PEMFC, as well as durability and longevity of its components, is the temperature distribution inside the MEA [2] [79] [80] [81] [82] [83] [84] [85]. This temperature distribution is highly dependent on the thermal conductivity of the components, especially GDL [48] [86] [87]. It is also affected by contact resistance at the interfaces of adjacent MEA component [81]. As a result, the accurate prediction of GDL thermal conductivity and quantifying its dependency on salient parameters such as compression, microstructural characteristics and additive materials such as PTFE and MPL are essential for understanding and improving the performance and longevity of PEMFCs. A similar study on contact resistance is also required to understand the unexplored phenomena occurring at the interfaces of fuel cell components. For instance, the effect of PTFE [88] and MPL on GDL thermal conductivity and on its contact resistance with adjacent layers has not yet been well understood and needs to be addressed thoroughly and accurately. The thermal conductivity of coated MPLs is still unknown and has to be measured with sufficient accuracy. A comprehensive study is required to reveal the effect of GDL and fiber specifications on its contact resistance with flat surfaces such as bipolar plates.

These studies provide a data-base and framework for the fundamental understanding of heat conduction through GDLs, MPLs and BPPs and their interfaces. They can also guide the development of new materials that improve the heat (and possibly electrical) management of PEMFCs by shedding light on the thermal behavior of these components. Analytic models developed in this research can be useful for the design, simulation and optimization of PEMFCs since conventional trial-and-error or computational approaches are time-consuming and not economically viable.

1.8. Contributions

The present work contributes to the science and technology of fuel cells by characterizing the bulk/interfacial thermal properties and key parameters effective for thermal (and possibly electrical) management of PEMFCs; specifically the thesis clarifies and quantifies:

(1) Impact of fiber spacing or aspect ratio and how to determine it for a fibrous medium.

- The traditional notion that porosity always decreases the thermal conductivity of a porous material is not necessarily true. This is a novel finding that can help improve the transport properties of fibrous materials considerably.

(2) Thermal conductivity of a graphite BPP as a function of temperature (Ballard project).

(3) Thermal conductivity of 14 untreated and PTFE-treated Sigracet GDLs.

(4) Thermal conductivity of coated MPLs.

(5) Effect of compression and PTFE on GDL thermal conductivity and contact resistance.

(6) Impact of MPL on GDL thermal conductivity and contact resistance.

(7) Effect of cyclic loading and hysteresis behavior on thermal resistances of GDLs.

(8) Key parameters that affect the thermal/electrical conductivity and TCR/ECR, with the hope of optimizing the GDL and MPL and of manufacturing new materials with improved transport properties.

Table 1.2 summarizes the main parameters that affect the heat management of PEMFCs and have been studied in this work. The knowledge of the thermal behavior of fuel cell components sheds light on their realistic impact on PEMFC heat management. This can ultimately lead to a better heat and water management and a more sophisticated design and manufacturing of PEMFCs.

Table 1.2. Factors and issues affecting the heat management of PEMFCs and discussed in this thesis

Factor/parameter/treatment	What they affect
Microstructure of GDLs: Porosity, fiber spacing, diameter, waviness and angles	Thermal conductivity
	GDL-BPP TCR
	GDL-MPL TCR
Treating a GDL with PTFE	Thermal conductivity
	TCR
Coating a GDL with an MPL	Thermal conductivity
	TCR
Microstructure of MPLs: Porosity and carbon particles diameter	GDL-MPL TCR
BPP out-of-flatness (machining)	GDL-BPP TCR

The literature review in the next chapter identifies a number of controversial issues and typical questions regarding heat management of PEMFCs, about which there is still a debate in the literature. These include, e.g., the question of whether thermal conductivity increases or drops with porosity, fiber spacing and additive materials, and the question of what the impacts of temperature and surface treatment are on the thermal behavior of PEMFC components. These issues are resolved through a series of experiments combined with theoretical analysis, see Table 1.3. Studying the items listed in Table 1.2 enables us to analyze the controversial aspects of the thermal behavior of PEMFC components as listed in Table 1.3. Answers to these key questions can reveal unexplored behavior of fuel cell components, which leads to determining some counter-intuitive phenomena that affect both thermal and electrical management of PEMFCs. It is hoped that the findings

of this work will be useful for enhancing PEMFC performance and longevity by characterizing and optimizing the structure, transport properties, design and manufacturing aspects of their micro/nano-scaled components. Based on these criteria, the work plan shown in Figure 1.7 has been taken for the present PhD program.

Table 1.3. Controversial issues and common questions addressed in this thesis

Items to be studied
Reduction of GDL thermal conductivity with porosity & fiber spacing?
Reduction of GDL thermal conductivity with PTFE-treatment?
Reduction of TCR with porosity?
Thermal conductivity of a *coated* MPL
Variation of thermal conductivity of a graphite BPP with temperature
Variation of TCR and thermal conductivity with compression
Role of MPL in the heat management of PEMFCs

1.9. Thesis outline

This thesis is organized into 8 chapters and 3 appendices. The present chapter (Chapter 1) includes an introduction on background and motivation, as well as the importance and all deliverables of the work covered in the present program. A critical and comprehensive review of the pertinent literature is presented in the next Chapter to motivate the research directions. In particular, the main drawbacks of the available work in the literature and the gaps in knowledge of the transport properties of porous materials are discussed in detail. All the experimental data measured through this work, along with a detailed

description of the experimental apparatus, are included in Chapter 3. Chapter 4 incorporates the modeling of thermal conductivity of both untreated and PTFE-treated GDLs, and introduces new techniques for determining fibers angles and fiber spacing in GDLs. The remarkable impact of fiber spacing on GDL thermal conductivity is presented in this chapter. Chapter 5 shows through lateral optical images of GDLs that fibers are wavy and not straight. With this information, the contact resistance between wavy GDLs fibers and a flat plate is modeled analytically. The thermal contact resistance between fibrous media such as GDLs and porous media made of spherical particles including MPLs is modeled in Chapter 6. This chapter also presents the counter-intuitive reduction of TCR with porosity, which occurs under specific conditions. The challenges encountered during this PhD program, the solutions, the sources used for conducting this project are all presented in Chapter 7. The industrial collaborators that provided some samples and technical information are also included in Chapter 7. Finally, Chapter 8 concludes the dissertation with a summary of the main achievements and a perspective on possible future work. Appendix A provides the thermal conductivity of Pyrex 7740 as a function of temperature. Two 1-in circular samples of Pyrex 7740 with different thicknesses were used to calibrate the thermal resistance measurement machine in this work. The experimental uncertainties reported in the thesis are estimated using the procedure described in Appendix B. The tabulated experimental data of this research are presented in Appendix C. Appendix D presents the article usage dashboard, which is available only for the articles published after May 2013.

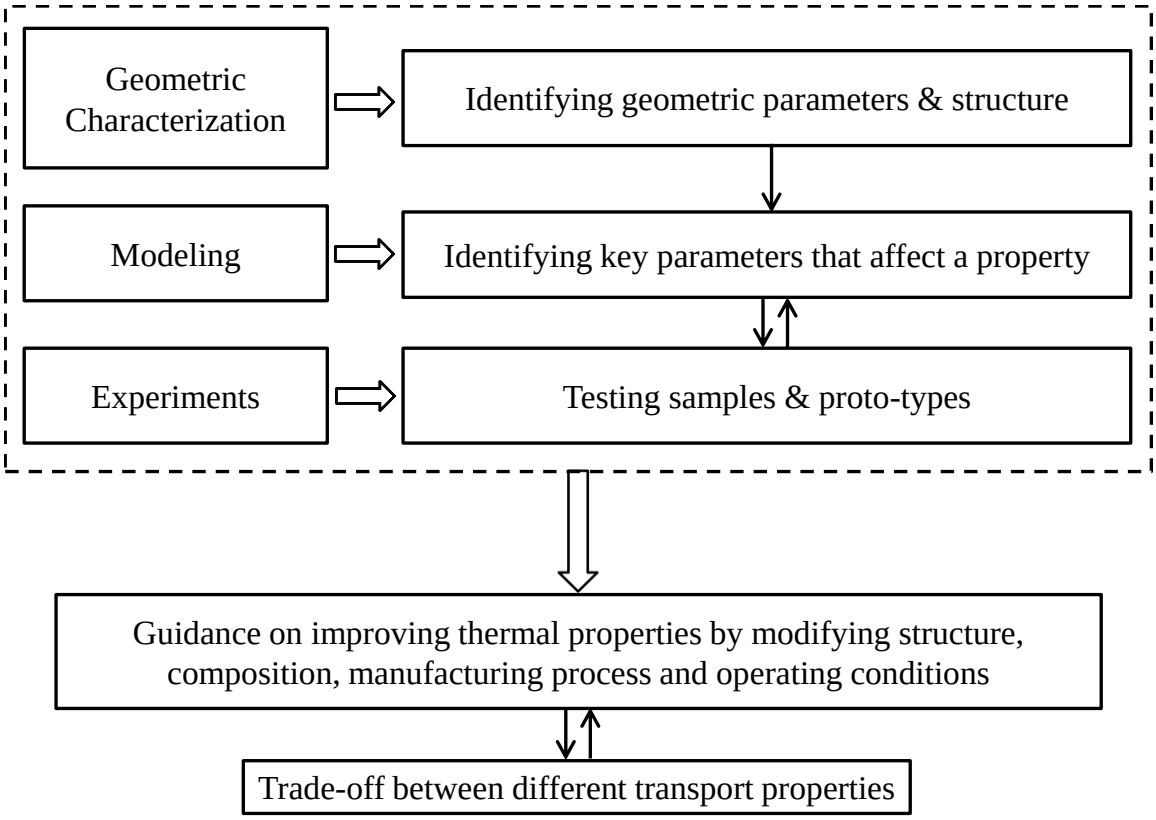

Figure 1.7. Research directions and general road map for the present four-year PhD project

Chapter 2.

Literature review

2.1. Thermal conductivity of GDLs

2.1.1. Experimental studies

Limited, and often contradictory, information is available in the literature on the bulk and interfacial thermal resistances of GDLs (see, e.g., Refs. [51] [54] [89]) and, hence, more sophisticated measurements are required. In principle, there are two classes of methods for measuring thermal conductivity [90]: (1) transient and (2) steady state methods, usually referred to as guarded heat flowmeter methods. Although transient tests are much faster, they usually need the sample heat capacity [49] [86] [90], which is difficult to measure accurately for porous materials [86] [90]. *In-situ* measurements of thermal properties are also challenging due to the porous nature and the micro scale of the components and the complexity of the numerous phenomena occurring simultaneously within an operating PEMFCs. The guarded heat flowmeter method is known as the most accurate one for measuring the thermal conductivity of porous materials, where an effective value for thermal conductivity is required [90].

To date, there have been few thermal conductivity studies of GDLs using the steady state method. Khandelwal and Mench [91] and Sadeghi et al. [56] [58] [92] measured the through-plane thermal conductivity of different GDLs with two thicknesses of one material to deconvolute the contact resistance. No sample thickness measuring device and

no vacuum chamber (to best minimize heat loss from the sample) were used in thermal conductivity measurements of Ref. [91], which may have decreased the accuracy of its measurements. Ramouse et al. [43], Karimi et al. [90], and Burheim et al. [93] used the same guarded method, but with a different approach, for the measurement of GDL thermal conductivity. They assumed a negligible contact resistance between two (or more) stacked samples, which cannot be accurate for two porous samples with noticeable roughness. On the other hand, Alhazmi et al. [94] considered the contact resistance between the stacked samples by considering the slope of the total resistance-thickness line. However, the determinant of the systems of the resultant equations sounds to be zero and it is not clear how they could solve the equations mathematically. In turn, they combined the number of samples with the GDL thickness in one term but not in another term of the same equation. *In-situ* measurement of the thermal conductivity of GDLs were reported by Burford & Mench [95], Vie et al. [96] and Kawase et al. [97]. They provided total resistances including contact resistance based on local measurements inside the stacks. Table 2.1 summarizes the details of the experimental work conducted for measuring the GDL thermal conductivity. It should be noted that the work employing the transient methods were also included in this table. Xu et al. [42] measured thermal conductivity of dry and saturated GDL samples by using a Hot Disk TPS2500S Thermal Constants Analyzer, which is based on a transient method. They asserted that the device can deconvolute the contact resistance from the bulk resistance by referring to Refs. [98] [99]. It is worth mentioning that some transient methods, such as the one used in Ref. [86] for the measurements of the in-plane thermal conductivity of GDLs, requires the heat capacity values of the tested GDLs, which was estimated as a function of the heat capacities of pure solid and fluid phases by using mixing rules. Such estimations may introduce considerable uncertainties and reduce the level of confidence for the thermal conductivity determinations.

Table 2.1. Measurement of GDLs through-plane thermal conductivities

Authors	Types of GDLs & thermal conductivity ($W\ m^{-1}\ K^{-1}$)	Remarks *
Burford & Mench (2004) [95]	E-Tek ELAT: 0.13-0.19	❖ *In-situ* measurement. ❖ Estimated from temperature difference inside a fuel cell. ❖ Total resistance (bulk + contact) was measured.
Ihonen et al. (2004) [100]	SGL 10BC: Thermal impedance of 10-24 $K\ cm^2\ W^{-1}$ for P=0.5-12 bar	❖ Thermal impedance. ❖ Total resistance (bulk + contact) was measured. ❖ Large heat loss. ❖ Neglected radial heat conduction.
Vie et al. (2004) [96]	ETEK ELAT: 0.2	❖ *In-situ* measurement. ❖ Large thermocouples inserted into the fuel cell. ❖ Large uncertainty for some of the tests. ❖ Single local measurements.
Khandelwal and Mench (2006) [91]	Toray-H-60 & 90: 1.80 and 1.24 (at 26 and 73 °C, respectively) SGL 24AA,BA, DA: 0.48, 0.31, 0.22 (58 °C) E-Tek ELAT: 0.22 (33 °C)	❖ Measuring heat flux through the sample using insulation (10% overestimation [91]). ❖ No thickness measurement. ❖ Only one compression (22 bar). ❖ Neglected TCR between a double layer E-Tek ELAT. ❖ Contact resistance deconvolution using two thickness method.
Ramouse et al. (2008) [43]	Quintech: 0.36-1.36 (20 °C) SGL: 0.26-0.34 (20 °C)	❖ Neglected TCR between stacked samples. ❖ Upper and lower bonds for thermal conductivity could be provided.
Radhakrishnan (2009) [41]	SGL 25BC & 35BC: 0.6-0.9 Toray-H-060 and -120: 1.6-1.9 (P=0.4-13 bar)	❖ Heat guarded plate. ❖ No vacuum to minimize heat loss. ❖ Considering either of MPL-coated GDLs 25BC and 35BC as one GDL.

Kawase et al. (2009) [97]	Toray-H-060: 2.8 (*P*=19 bar)	❖*In-situ* measurement. ❖ Estimated from temperature difference in a working fuel cell. ❖ Total resistance (bulk + contact) was measured.
Karimi et al. (2010) [90]	SpectraCarb: 0.25-0.7 (0.7-13.8 bar & 70 °C) SolviCore: 0.24-0.51 (0.7-13.8 bar & 70 °C)	❖ Measuring heat flux through the sample using insulation (no vacuum to best minimize the heat loss). ❖ Neglected TCR between the stacked samples.
Burheim et al. (2010) [93]	SolviCore: 0.27, 0.36, 0.40 (25 °C) Toray-H-60: 0.41, 0.53, 0.66 (25 °C) (*P*=4.6, 9.3, 13.9 bar)	❖ Measuring heat flux through the sample using insulation (no vacuum to best minimize the heat loss). ❖ Neglected TCR between stacked samples. ❖ All thermal conductivities were measured at three pressures.
Sadeghi et al. (2011) [56]	Toray-H-60 & 90: 1.5-2 (3.5-15bar & 70 °C)	❖ Using a vacuum chamber to best minimize the radial heat loss from the sample and fluxmeters. ❖ Contact resistance deconvolution using two thickness method.
Zamel et al. (2011) [49]	Toray-H-120: 1.1-1.8 (low deformation) 0.1-0.5 (high deformation) (-50-120 °C)	❖ Transient method. ❖ Thermal capacitance (Slug) calorimeter was used. ❖ Assuming constant thermal diffusivity for GDL. ❖ Neglected contact resistance.
Burheim et al. (2011) [101]	Toray-H-60: 0.5-0.73 (5% PTFE) 1.4-1.5 (5% PTFE, wet) 0.48-0.69 (10% PTFE) 0.28-0.32 (60% PTFE) (*P*=4.6-13.9)	❖ Measuring heat flux through the sample using insulation (no vacuum to best minimize the heat loss). ❖ Neglected TCR between stacked samples. ❖ All thermal conductivities measured at three compression.
Teertstra et al. (2011) [102]	SolviCore: 0.25-0.52 SpectraCarb: 0.28-0.6 (*P*=0.7-13.8 bar)	❖ Parallel thermal conductance (PTC) technique in vacuum. ❖ Neglected TCR. ❖ In-plane thermal conductivity.

Burheim et al. (2013) [103]	SGL 24DA: 0.247, 0.332, 0.403 (*P*=4.6, 9.3, 13.9 bar) SGL 24BC: 0.369 (9.3 bar) SGL 25BC: 0.270 (9.3 bar)	❖ Measuring heat flux through the sample using insulation (no vacuum to best minimize the heat loss). ❖ Neglected TCR between stacked samples. ❖Aged & wet samples.
Alhazmi et al. (2014) [94]	SGL GDLs: 0.25-0.55 (*T*=35–80 °C)	❖ A home-made apparatus similar to the guarded heat flowmeter. ❖ It is not clear how the equations (with a seemingly zero determinant) have been solved.
Xu et al. (2014) [42]	U-105 (MRC 105), SGL Sigracet® 25 BC, and General Motors (GM): 0.2-0.9, 0.15-0.7, 0.12-0.13 (Dry) (*P*=1-20 bar)	❖ Transient method. ❖ A Hot Disk TPS2500S Thermal Constants Analyzer was used to measure the thermal conductivity. ❖ Two samples of each GDL were layered for each stress–strain measurement. ❖ Dry & wet samples.
Toray [104]	Toray-H-60: 1.7 (25 °C)	❖ No published information.

* In the work that used the steady-state guarded methods, some insulation was employed around the sample and the fluxmeters to minimize the radial heat loss except Refs. [56] [102] where a vacuum chamber was employed.

2.1.2. Models in the literature

A few models have been presented in the literature for estimating the through-plane thermal conductivity of GDLs. Most of these models are based on porosity only and do not consider other important geometrical parameters such as fiber angles and aspect ratio, that is, the ratio of the distance between fibers in the in-plane (x-y) directions. The main idea in such models is to reconstruct a porous structure having the same porosity as the actual GDL, and then use a theoretical model to calculate the thermal conductivity on the basis of the solid and pore fractions, i.e., porosity. The results show similar values for thermal conductivity of different GDLs having the same porosity and sometimes overestimate [44] or underestimate [43] [45] the measured thermal conductivity. Considering the complexity of the structure of fibrous porous media, improvements in model accuracy are likely to require consideration of all salient geometric parameters. In the present work, an attempt is made to incorporate the intersecting angle and characteristic distance between fibres into a new analytical model. Table 2.2 summarizes the effective medium theory based models and Table 2.3 lists the computational work available in the literature for the estimation of GDL thermal conductivity. It is worth noting that the effective-medium theory based models are based on one parameter, i.e., porosity. This is the main drawback of such models as they do not consider fiber spacing.

Table 2.2. Effective medium theory-based models for thermal conductivity of GDLs

Author(s)	Model/equation	Remarks
Ref. [105]	$k_{\text{eff,p}} = \varepsilon k_{\text{air}} + (1-\varepsilon)k_{\text{s}}$ $k_{\text{eff,s}} = \dfrac{1}{\varepsilon/k_{\text{air}} + (1-\varepsilon)/k_{\text{s}}}$	❖ Series & parallel models. ❖ No fiber orientation was considered.
Carson et al. (2005) [106]	$k_{\text{eff}} = \frac{1}{4}((3(1-\varepsilon)-1)k_{\text{s}} + \big(2-3(1-\varepsilon)\big)k_{\text{air}} + \Big(\big[(3(1-\varepsilon)-1)k_{\text{s}} + \big(2-3(1-\varepsilon)\big)k_{\text{air}}\big]^2 + 8k_{\text{air}}k_{\text{s}}\Big)^{0.5})$	❖ Effective medium theory: A random, mutual dispersion of two components. ❖ No fiber orientation was considered.
Wang et al. (2008) [107]	$k_{\text{eff}} = \dfrac{k_{\text{eff,s}}}{2}\left(\sqrt{1+\dfrac{8k_{\text{eff,p}}}{k_{\text{eff,s}}}}-1\right)$	❖ Co-continuous model: Both phases are assumed to be continuous. ❖ No fiber orientation was considered.
Eucken (1940) [108]	$k_{\text{eff}} = k_{\text{cont}}(1-\varepsilon_{\text{cont}}) + k_{\text{dis}}(1-\varepsilon_{\text{dis}})\frac{3k_{\text{cont}}}{2k_{\text{cont}}+k_{\text{dis}}}/(1-\varepsilon_{\text{cont}}) + (1-\varepsilon_{\text{dis}})\frac{3k_{\text{cont}}}{2k_{\text{cont}}+k_{\text{dis}}}$	❖ Maxwell-Euken model: One phase is assumed to be dispersed in a second, continuous phase.
Das et al. (2010) [109]	$\dfrac{k_{\text{eff}}}{k_s} = 1 - \dfrac{3\varepsilon f(\varepsilon)}{3} - (1-\varepsilon)$	❖ Series model for the lower limit. ❖ Parallel model for the upper limit. ❖ No fiber orientation was considered.
Zamel et al. (2010) [110]	$f(\varepsilon) = A(1-\varepsilon)^B \exp\big(C(1-\varepsilon)\big)$ *A*, *B* and *C* are constant.	❖ Numerical carbon-paper GDLs. ❖ Describes the effective thermal conductivity as a function of porosity and thermal conductivity of the solid and gas species.
Zhang and Zhang (2014) [111]	$\dfrac{k_{\text{eff}}}{k_{\text{s}}} = 1 - 0.975(1-\varepsilon)^{-0.002} \exp\big(0.77(1-\varepsilon)\big)\left(\dfrac{3\varepsilon}{3-(1-\varepsilon)}\right)$	❖ Fitted to simulated results.

Table 2.3. Computational and analytical models for GDL thermal conductivity

Author(s)	Remarks
Wang et al. (2007) [44]	❖ Lattice Boltzmann modeling. ❖ Numerical study. ❖ TCR was not considered.
Becker et al. (2009) [112]	✓ Phase Contrast Tomographic Microscopy (structural model). ❖ TCR was not considered.
Nitta et al. (2008) [113]	❖ Numerical method. ❖ TCR was not considered.
Ramousse et al. (2008) [43]	❖ Upper and lower bounds based on effective medium theory.
Sadeghi et al. (2008) [57]	✓ Analytic model. ✓ TCR was considered. ❖ Fiber spacing was assumed to be unity.
Pfrang et al. (2010) [45]	✓ Based on x -ray CT data. ❖ TCR was not considered.
Veyret & Tsotridis (2010) [114]	✓ 3D structural model. ❖ Numerical computation of the energy transport equation. ❖ TCR was not considered.
Pfrang et al. (2011) [105]	✓ Based on structural model. ❖ TCR was not considered.
Yablecki et al. (2012) [115]	✓ Based on Sadeghi et al.'s model with some changes. ❖ Compression reduces thermal conductivity.
Jiang et al. (2012) [116]	❖ An exact closed form formula of the local effective thermal conductivity is obtained by solving Laplace's equation. ❖ Series model is used for thermal conductivity and for the heat flux inside the fibrous medium.
Huang & Zhang (2014) [117] [118]	❖ Finite volume method combined with experimental data. ❖ TCR was not considered for the fibrous insulation sample. ❖ Fitting experimental parameters to one-dimensional energy equation to back-calculate the thermal conductivity of the fibrous insulation.

✓: shows the advantage of the work. ❖: shows more information on the work.

2.2. Thermal conductivity of MPL

Few experimental studies have been to date performed to measure the thermal conductivity of MPL. Burheim et al. [93] obtained the through-plane thermal conductivity of an MPL equal to 0.6 W m^{-1} K^{-1} from measurements performed on an MPL-membrane assembly. Karimi et al. [90] measured the thermal conductivity of the MPL of SolviCore GDLs in the range of 0.25–0.52 W m^{-1} K^{-1} at 70 °C for a compression pressure of 0.7–13.8 bar. In the same lab and for the same type of GDL, i.e., SolviCore, the thermal conductivity of the MPL was also measured by Unsworth et al. [119] [120] by subtracting the measured thermal conductivity of a SolviCore carbon paper coated with the MPL from that of a bare one. The reported MPL thermal conductivity was 0.30 W m^{-1} K^{-1} and independent of the compression pressures. Unsworth et al. [119], contrary to Ref. [90], found a negligible thermal contact resistance of the MPL with the iron clamping surfaces and attributed this result to the high surface contact area of the MPL. It is worth mentioning that none of the other work performed for measuring the MPL thermal conductivity [90] [93] [119] have to date taken into account the TCR between MPL and substrate. In addition, as mentioned in Table 2.1, the tests of Refs. [90] [93] and Ref. [119] have not been performed in a vacuum chamber and the thermal contact resistance between the stacked GDLs has also been simply omitted.

Using a transient laser flash method for a stand-alone MPL, Burlatsky et al. [121] reported the thermal conductivity of MPL from 0.035 and 0.057 W m^{-1} K^{-1}, with low and high PTFE content, to 0.097 W m^{-1} K^{-1} (MTM187 modified substrate hot plate method) by referring to an unpublished reference. However, the thermal conductivities of the MPL reported in Ref. [121] are close to the thermal conductivity of air (0.026 W m^{-1} K^{-1}) and therefore are unlikely to be accurate, considering the typical porosity of MPLs [87] [122] [123].

Table 2.4. Experimental studies reporting the thermal conductivity of MPLs

Author	Materials	Thermal conductivity ($W\ m^{-1}\ K^{-1}$)	Remarks
Burlatsky et al. (2009) [121]	Stand-alone MPL	0.035-0.097	❖ Transient laser flash method (details were not reported.)
Karimi et al. (2010) [90]	SolviCore	0.25–0.52	❖ P=0.7-13.8 bar & T=70 °C ❖ Neglected $TCR_{GDL-GDL}$
Unsworth et al. (2012) [119]	SolviCore	0.3	❖ Neglected TCR_{MPL-FM} ❖ Independent of compression
Burheim et al. (2013) [124]	Stand-alone MPL	0.05-0.12	❖ Neglected $TCR_{MPL-MPL}$

2.3. Thermal conductivity of graphite and metallic BPPs

Design constraints, low cost, mechanical strength, high chemical stability and high conductivity are among the main factors of selecting and manufacturing efficient bipolar plates. To meet the above requirements, bipolar plates with different composition and types have been used. Carbon-carbon, carbon-polymer and metallic bipolar plates are the most common ones being tested to date to reach an optimal material. Due to this diverse composition, a broad range of thermal conductivity from 5 to 200 $W\ m^{-1}\ K^{-1}$, have been reported for bipolar plates. Table 2.5 summarizes the thermal conductivities reported for different bipolar plates. There is no information on the device or method used for measuring the thermal conductivity of the biplolar plates for the some of the work as listed in this Table 2.5.

Table 2.5. Thermal conductivity of bipolar plates reported in the literature

Author	Material	Value ($W\ m^{-1}\ K^{-1}$)	Remarks
Frano Barbir (2005) [125]	Graphite	98	❖ No details of measurement were reported.
	Graphite/polymer mix	20	
	Graphite POCO	95	
	BBP 4 SGL	20.5	
	PPG 86 SGL	14	
	BMC940	19.2	
Chen et al. (2007) [126]	Composite BPP (75wt% Graphite and different Carbon Nano Tube contents)	54-63	❖ No details of measurement were reported.
	Composite BPP (different graphite contents)	59-63	
	Composite BPP (75wt% Graphite and different Ni-graphite contents)	51-59	
Spiegel (2007) [127]	BPP	16, 19, 22	❖ No details of measurement were reported.
Shimpalee et al. (2009) [128]	A Graphite BPP	20	❖ A numerical modeling considering a value of 20 for the thermal conductivity of BPP.
Hsiao et al. (2010) [129]	A nanocomposite (low graphene)	27.2	❖ The thermal conductivity was measured using a Hot Disk thermal analyzer (TPS2500, Sweden), based on the TPS method [130].
Zheng et al. (2010) [131]	A BPP	20-50	❖ A numerical analysis considering a value of 20-50 for the thermal conductivity of BPP.
Wang and Chen (2011) [132]	A graphite BPP	100	❖ A numerical modeling considering a value of 100 for the thermal conductivity of BPP.

Taherian (2012) [133] [134]	Triple-filler composites	9.6	❖ No details of measurement were reported.
Gao et al. (2012) [135]	A BPP	52	❖ No details of measurement were reported.
Shahsavari et al. (2012) [136]	A graphite BPP	30-60	❖ A numerical parametric study.
Ghosh et al. (2014) [137]	CF/CB/NG/NPFR 5/5/60/30 % *	50	❖ Thermal conductivity measuring instrument (Gunt: WL376, Germany) was used. ❖ Temperature at different points along the sample was measured. ❖ No contact resistance was considered. [a]: Effect of fiber length [b]: Effect of Graphene
	GP/CF/CB/NG/NPFR 1.5/5/5/58.5/30 %	77	
	CF/CB/NG/NPFR 5/5/60/30 %	20-40[a]	
	CF (1mm)/CB/ (NG+GP)/NPFR 5/5/60/30 %	50-73[b]	

* CF: Carbon fiber; CB: Carbon black; NG: Natural graphite; GP: Graphene; and NPFR: Novolac phenol formaldehyde resins.

2.4. Thermal contact resistance between GDL-BPP

Due to experimental difficulties, *no measurement* has been reported to date on the *thermal* contact resistance (TCR) between GDLs and graphite BPP [123] [138]. Consequently, this contact resistance has either been neglected or roughly estimated in modeling studies [90] [67]. The only attempt to estimate the *thermal* contact resistance between BPP and GDLs ($TCR_{\text{GDL-BPP}}$) to date is due to Nitta et al. [113], which was based on simulations using Fluent, with an unverified assumption of 128 W m^{-1} K^{-1} for the thermal conductivity of the graphite BPP. The reported thermal conductivity of the GDL was several times higher than typical values found in the literature and was also independent of compression. These results are inconsistent with physical observations and with several experimental studies showing the significant dependency of GDL thermal conductivity on compression [49] [51] [52] [57] [89] [92] [139].

Since there is no data for $TCR_{GDL\text{-}BPP}$ except for that of Nitta et al. [113] and also due to similarity between thermal and electrical resistances, it can be useful to know the models and experimental procedures on how to deconvolute the electrical contact resistance between BPP and GDL from their bulk resistances. Table 2.6 summarizes all modeling and experimental studies conducted on electrical contact resistances between GDLs and graphite or metallic BPPs ($ECR_{GDL\text{-}BPP}$).

Table 2.6. Modeling and experimental studies on *electrical* contact resistance (ECR) between BPP and GDLs

Author(s)	Sample & compression	Remarks
Miachon and Aldebert (1995) [61]	- Electrode - Copper current collector R=20-28 mΩ cm^2	❖ *In-situ* measurement of ECR. ❖ Numerical computation of the energy transport equation. ❖ Total resistance between the electrode and graphite plate was reported (no deconvolution).
Makkus et al. (2000) [140]	- Stainless steel BPP - E-tek electrode - P=2-12 bar - R=25-50 mΩ cm^2	❖ A thin gold wire was placed between the E-tek backing plus electrode and the membrane. ❖ Total resistance between BPP and membrane was measured (no deconvolution).
Ihonen et al. (2001) [141]	- ELAT® gas backing - Stainless steel BPP - P=0-80 bar - R=0-260 mΩ cm^2	❖ *In-situ* ECR measurements. ❖ Unplated and plated stainless steel. ❖ *Ex-situ* measurements were used to validate the in-situ contact resistance measurements. ❖ ECR was measured *ex-situ* on small samples similarly to the measurements by Barbir et al. (1999) [142]. ❖ The associated error can, in the worst case, make the quantitative measurements invalid.
Wang et al. (2003) [143]	- Carbon paper - Stainless steel BPP	❖ Stainless steel (SS) bipolar plate. ❖ Modified Davies' method [144]. ❖ All bulk resistances were neglected. ❖ $R=ECR_{GDL\text{-}BPP}$ + all bulk resistances.

	- P=1.5-18 bar - R=100-1500 mΩ cm^2	
Cho et al. (2004) [145]	- Graphite BPP - Composite - P=0-33 bar - R=30-95 mΩ cm^2	❖ Copper plates were used (corrosion issue). ❖ Using the four-point probe technique, bulk resistivity of samples was measured. ❖ Total resistance of each assembly was named as contact resistance.
Mishra et al. (2004) [76]	- Carbon paper - Graphite BPP - P=5-30 bar - R=1-6 mΩ cm^2	➢ $ECR_{GDL\text{-}BPP}$ modeling: ❖ A fractal asperity based model based on data obtained using surface profilometric measurement systems. ❖ A volume fraction weighted harmonic mean was used for the bulk resistivity of the gas diffusion layer. ➢ $ECR_{GDL\text{-}BPP}$ experimental data: ❖ A BPP/GDL assembly was used. ❖ Gold plates were used. ❖ Electrical resistivity of graphite, carbon paper and gold plate were set as known values (no reference provided).
Matsuura et al. (2006) [146]	- TGP-H-090 - A metallic BPP - R=30-95 mΩ cm^2	❖ Total resistance of BPP, copper plates and the GDL sandwiched in between them was measured. ❖ The electric contact between a metallic bipolar plate and another cell part was evaluated by a structural analysis with a finite element method and a compression test. ❖ Copper plate were used (corrosion issue).
Zhou et al. (2006) [147]	- SGL GDLs - BPP - P=10 bar - R=0.1-1.2 mΩ m	❖ A power relationship between interfacial resistance and contact pressure was considered based on Ref. [76]: $ECR=a(b/P)^c$ where a, b and c are constants obtained from experiment, P compression and ECR is electrical contact resistance. ❖ Finite element method (FEM). ❖ Fitted formula based on Refs. [76] and [143].
Zhang et al. (2006)	- GDL TGP-H-120 - Graphite BPP	➢ $ECR_{GDL\text{-}BPP}$ modeling: ❖ Contact resistance–pressure constitutive

[68]	- P=5-50 bar - R=3-10 mΩ cm^2	relation. ❖ FEM model. ❖ Smooth interface between BPP and GDLs is assumed. Both models are based on experimental data. ➢ $ECR_{GDL\text{-}BPP}$ experimental data: ❖ Electrical conductivity of the GDL and BPP were set as known values (no reference provided). ❖ An experimental setup similar to Ref. [76]. ❖ The sandwiched graphite plates/GDL assembly was placed between two gold plates. ❖ BPP/GDL assembly was sued. ❖ Flat and smooth BPP.
X. Yan et al. (2006) [148]	P=1-14 bar R_{tot}=15-170 mΩ cm^2	❖ Total resistance of BPP/GDL assembly was measured. ❖ I–V curves for the single cells are used.
Zhou et al. (2007) [149] [150]	- SGL GDLs - BPP - P=5-30 bar - R=1-6 mΩ cm^2	➢ $ECR_{GDL\text{-}BPP}$ modeling: ❖ A micro-scale numerical model for $ECR_{BPP\text{-}GDL}$. ❖ Spherical asperity on BPP surface - cylindrical fibers of GDLs. ❖ An elastic finite element method was used to solve the sphere–beam contact problem numerically (numerical study). ❖ Holm equation [151] was used for the ECR estimation. ➢ $ECR_{GDL\text{-}BPP}$ experimental data: ❖ Experimental data of GDL-BPP ECR. ❖ Electrical resistivity of carbon fiber and BPP were set as known values. ❖ Copper plate was used for electrical tests. ❖ The change of the bulk resistance of BPP and GDL during compression was neglected.
Chang et al. (2007) [60]	- Carbon paper GDL - Graphite BPP - P=0-35 bar	❖ Experimental measurement of $ECR_{GDL\text{-}BPP}$. ❖ GDL/BPP assembly was used. ❖ Copper plate was used (corrosion issue). ❖ No information about the GDL and BPP bulk resistance was provided.

	- R=30-1000 mΩ cm^2	
Kraytsberg et al. (2007) [152]	- GDL Toray paper - Stainless steel BPP R= 350 mΩ	➢ $ECR_{BPP\text{-}GDL}$ modeling: ❖ GDL/BPP assembly was used for ex situ measurement. ❖ Holm equation [151] was used for bulk resistivity estimations. ➢ $ECR_{BPP\text{-}GDL}$ experimental data: ❖ Toray, copper and BPP resistivity were sat to known value. ❖ Copper probes were used (corrosion issue). ❖ No details of the testbed were provided. ❖ Some of the resistances were estimated and found to be negligible. ❖ Effect of compression was not considered.
Wu et al. (2008) [150] (2009) [153]	- GDL Toray TGP-H-30 - A grade FU 4369 graphite plate. - P=0-35 bar - R=30-1000 mΩ cm^2	❖ An analytical modeling based on Holm's equation [151]. ❖ The micro-contact between a BPP asperity and a carbon fiber was modeled as a hemisphere in contact with an external cylinder using the Greenwood–Williamson (GW) model for rough surfaces [154]. ❖ Unknown GDL carbon fiber length density. ❖ Electrical resistivity of carbon fiber and BPP are taken from Refs. [149] and [153], respectively.
Lai et al. (2008) [155]	- Toray TGP-H-060 - A flat graphite plate	❖ *Ex-situ* experimental measurement of contact resistance. ❖ FE modeling. ❖ Corrosion of copper plate was not considered. ❖ GDL and BPP bulk resistances were taken from Ref. [149]. ❖ A mechanical–electrical FEM model was developed to predict the contact resistance between the BPP and GDL based on the experimental interfacial contact resistivity.

Andre et al. (2009) [156]	- SS specimen - H2315 T10A Freudenberg carbon felt *P*=2-30 bar *ECR*=0-600 mΩ cm^2	❖ Bulk resistance of SS alloys was deduced from 4-probe measurements using Van Der Pauw method. ❖ Contact resistance was measured by a 2-probe device. ❖ SS specimen was sandwiched between two carbon felt. ❖ The assembly was compressed between two coppers. ❖ Unknown copper and GDL electrical bulk resistances.
Avasarala and Haldar (2009) [77]	- GDL TGP-H-060 - A molded graphite BPP - *P*=5-65 bar *ECR*=24-32 mΩ cm^2	❖ Untreated Toray® TGP-H-060 carbon papers were used. ❖ GDL-BPP assembly. ❖ The BPP-GDL assembly was sandwiched between gold coated copper plates. ❖ BPP bulk resistance was adapted from the manufacturer's datasheet. ❖ GDL electrical bulk resistance was assumed to be known. ❖ $ECR_{GDL\text{-}BPP}$ was obtained from the total resistance of the GDL-BPP assembly.
Zhou et al. (2011) [157]	- GDLs - BPPs - No numerical results reported.	❖ A power function model for determining the relationship between contact resistivity and contact pressure: $ECR=aP^b$ where *a* and *b* are the fitting parameters based on the experimental data.
Mason et al. (2012) [158]	- GDL Toray H120 - Graphite BPP - *P*=2-25 bar - *R*=14-28 mΩ cm^2	❖ Resistance measurements were achieved using Electrochemical Impedance Spectroscopy (EIS). ❖ The resistance is a summation of the BPP-GDL interface, fiber bulk resistance and GDL internal fiber connections and bulk system resistance.
El-harouf (2012) [159]	Woven GDLs HCB and TCC - *P*=0-38 bar: - *R*=5-45 mΩ cm^2	❖ ECR was measured. ❖ Gold plated stainless steel (SS) current collectors. ❖ Resistance was measured by the 4-wire Kelvin method. ❖ GDL and BPP resistivity were assumed to be negligible.

Ismail et al. (2013) [160]	- SGL GDLs - A graphite BPP *P*=5-27 bar *R*=0-130 Ωm cm^{-2} *P*=0-27 bar *R*=3.5-10 Ωm cm^{-2}	❖ The resistivity of the graphite plate was provided by the supplier. ❖ The volume-weighted harmonic mean of the resistivity. of air and the carbon fiber was used in order to estimate the resistivity of the GDL: $k_{\mathrm{GDL}} = \frac{1}{\frac{\varepsilon}{k_{\mathrm{air}}}+\frac{1-\varepsilon}{k_{\mathrm{fiber}}}}$ ❖ The change in the GDL resistance while compressing the GDL was ignored. ❖ Interfacial contact resistance between stacked GDLs was assumed to be negligible.
Netwall (2013) [161]	- SGL GDL 25BC - Graphite plate *P*=0-22 bar *R*=50-150 Ωm cm^{-2}	❖ *In-situ* measurement using impedance. ❖ Gold electrode was used. ❖ *Ex-situ* measurements similar to Ref. [149]. ❖ $ECR_{\text{Gold-MPL}}$ is assumed to be the same as $ECR_{\text{Gold-GDL}}$.
Singdeo et al. (2014) [162]	- GDL SGL 25-series - Graphite BPP - *P*=0-80 bar: *ECR*=4-30 and *ECR*=5-28 mΩ cm^2 for carbon paper and carbon cloth GDLs, respectively.	➢ $ECR_{\text{GDL-BPP}}$ modeling: ❖ An analytic models based on asperity on a graphite BPP. ❖ Gaussian distribution of asperities on the BPP surface. ❖ Surface spectral moments as outlined by Nayak et al. (1971) [163] was used to estimate unknown parameters. ❖ Straight fibers and rough BPP are assumed. ➢ $ECR_{\text{GDL-BPP}}$ experimental data: ❖ Bulk resistances of the GDL and BPP were taken from Refs. [153] and [164], respectively. ❖ BPP/GDL assembly resistance was measured using four probe method. ❖ Brass plates were used as clamping surfaces.
Li et al. (2014) [165]	- HCP GDLs - A BPP *P*=15-50 bar *ECR*=1-7 mΩ cm^2	❖ Measurement of BPP-GDL ECR. ❖ Electrical conductivity of BPP and GDL were taken from Ref. [68]. ❖ A relationship of pressure and contact resistivity was established by the least square method. ❖ Based on the commercial code ABAQUS, a

		FEA was performed to predict the contact resistivity.
Sow et al. (2015) [166]	- SGL GDLs - SS BPP $ECR_{BPP-GDL}$ = 0-180 P=0-45 bar	❖ AS impedance spectroscopy. ❖ Deconvolution of bulk from contact resistance. ❖ Two or multiple thickness method was not used. ❖ Contact resistance between sensing electrode and the sample was omitted. ❖ Results are sensitive to the size of electrode. ❖ Resistivity of BPP was set to a known value.

2.5. Thermal contact resistance between GDL-MPL

No experimental or theoretical data has been reported to date for the thermal contact resistance at the complex interface of GDLs and MPLs. The data of thermal conductivities of both GDLs and MPLs and their contact resistances with clamping surface are required for measuring GDL-MPL TCR, which have been overlooked by all the studies in the literature. In this thesis, the GDL-MPL TCR are estimated for two different types of SGL GDLs and reported as the first and the only data of this type of TCR available in the literature.

2.6. Summary: Gaps in the literature

Though much effort has been devoted to the study and characterization of fuel cell porous media, the preceding review reveals a number of fundamental gaps and unresolved questions. Most of the studies and work conducted to date did not deconvolute the bulk resistance from the contact resistance and only reported a combination of these two resistances. Table 2.7 summarizes the unresolved questions and the gaps in the literature regarding the thermal bulk and interfacial resistances of GDLs, MPLs and BPPs and their thermal behavior. The work conducted in this research is designed to resolve these questions and fill the gaps by providing an experimental database supported by theoretical analyses, which can be beneficial for the heat management of PEMFCs.

Table 2.7. Gaps in the literature regarding the thermal behavior of GDLs, MPLs and BPPs with respect to the heat management of PEMFCs

Property/parameter	Gaps in the literature & controversial issues
Thermal conductivity of untreated GDLs (modeling)	❖ Impact of fiber spacing on GDL thermal conductivity? ❖ How to determine fiber spacing in GDLs?
Thermal conductivity of PTFE-treated GDLs (modeling)	❖ Lack of an analytic model considering the TCR between fibers, all GDL geometrical parameters, and the PTFE scattered on the GDL surface. ❖ Why and how the filling PTFE decreases thermal conductivity while it increases the solid fraction of GDLs?
Thermal conductivity of GDLs (experiments)	❖ A little accurate information is available (limited data). ❖ Contact resistance was often combined with bulk resistance. ❖ Effect of PTFE and MPL on GDL thermal conductivity?
Thermal conductivity of MPLs (experiments)	❖ No *ex-situ* data of the thermal conductivity of coated MPLs. ❖ Deconvolution of contact from bulk resistance was often overlooked.
GDL-MPL TCR (modeling)	❖ No (analytic) models. ❖ Completely overlooked in the literature.
GDL-MPL TCR (experiments)	❖ No data.
Thermal conductivity of a graphite BPP	❖ No experimental data on the thermal conductivity of a graphite BPP as a function of temperature.
GDL-BPP TCR (modeling)	❖ No models considering the waviness of GDL fibers. ❖ Only one data (Ref. [113]) based on an unverified value for the thermal conductivity of the graphite BPP.
GDL-BPP TCR (experiments)	❖ No experimental data of the TCR between *graphite* BPP and GDLs. ❖ Effect of out-of-flatness on the TCR? ❖ Effect of PTFE and MPL on the TCR?

Chapter 3.

Experimental apparatus, methodology and results

3.1. Experimental apparatus: Thermal contact resistance machine

In this thesis, the thermal contact resistance (TCR) apparatus shown in Figure 3.1 was used for all thermal conductivity and thermal resistance measurements. The design of this apparatus, also called TCR machine for short, is based on the guarded heat flux meter device as recommended by the ASTM E1225 [167]. The TCR machine, shown in Figure 3.2, is comprised of two disk plates and also two cylindrical Armco-iron heat fluxmeters, in between which the sample is located. A temperature gradient is induced across the sample using an electric heater, imbedded in the upper plate as a heat source (the hot plate), and a cold refrigerant liquid (Ethylene Glycol), circulated inside the lower plate as a heat sink (the cold plate). The temperatures along each fluxmeter are measured using 6 T-type thermocouples placed at 5 mm distances, i.e., 12 thermocouples in total. From the temperature profiles, recorded by a data acquisition system using LabView, the contact surface temperatures, T_n and T_m, can be extrapolated using a linear regression, see Figure 3.3. The difference between the two extrapolated temperatures of T_n and T_m and their average can be taken as the temperature drop across the sample and the sample temperature, respectively. The heat transfer is limited to one-dimensional conduction, from the upper (hot) plate to the lower (cold) plate, by creating a high vacuum condition inside the test chamber. This vacuum provides a more accurate measurement over other available TCR machines that employ insulation around their fluxmeters and sample

instead of using a vacuum chamber. The control of the compression pressure applied on the sample is performed using a hydraulic pressure device (ENERPAC P392) and the pressure is measured using a load cell located beneath the cold plate. The measurement and monitoring of the changes in the thickness of the compressed sample is carried out with a laser displacement sensor (Acuity AR700-1). Knowing the thermal conductivity of the Armco-iron fluxmeters and the measured temperature profile along them, the heat transferred through the sample and the temperature drop across it can be obtained, which yields the total thermal resistance.

Figure 3.1. Thermal conductivity and contact resistance apparatus (TCR machine)

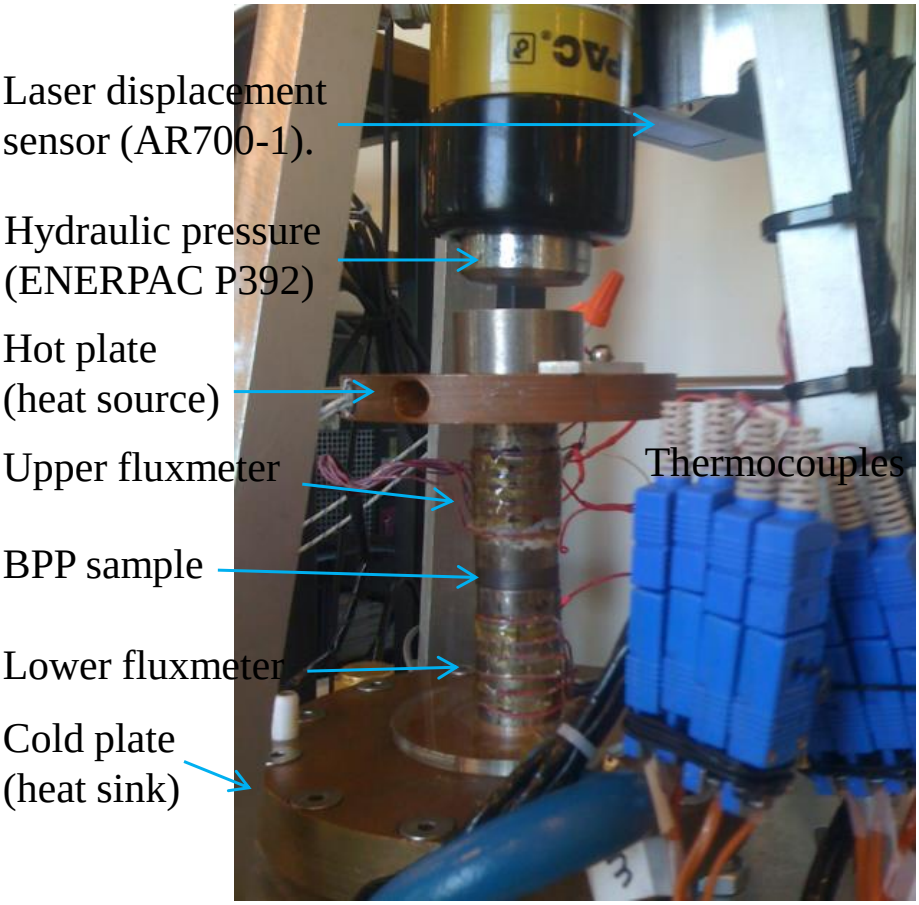
Laser displacement sensor (AR700-1).
Hydraulic pressure (ENERPAC P392)
Hot plate (heat source)
Upper fluxmeter
BPP sample
Lower fluxmeter
Cold plate (heat sink)
Thermocouples

(a)

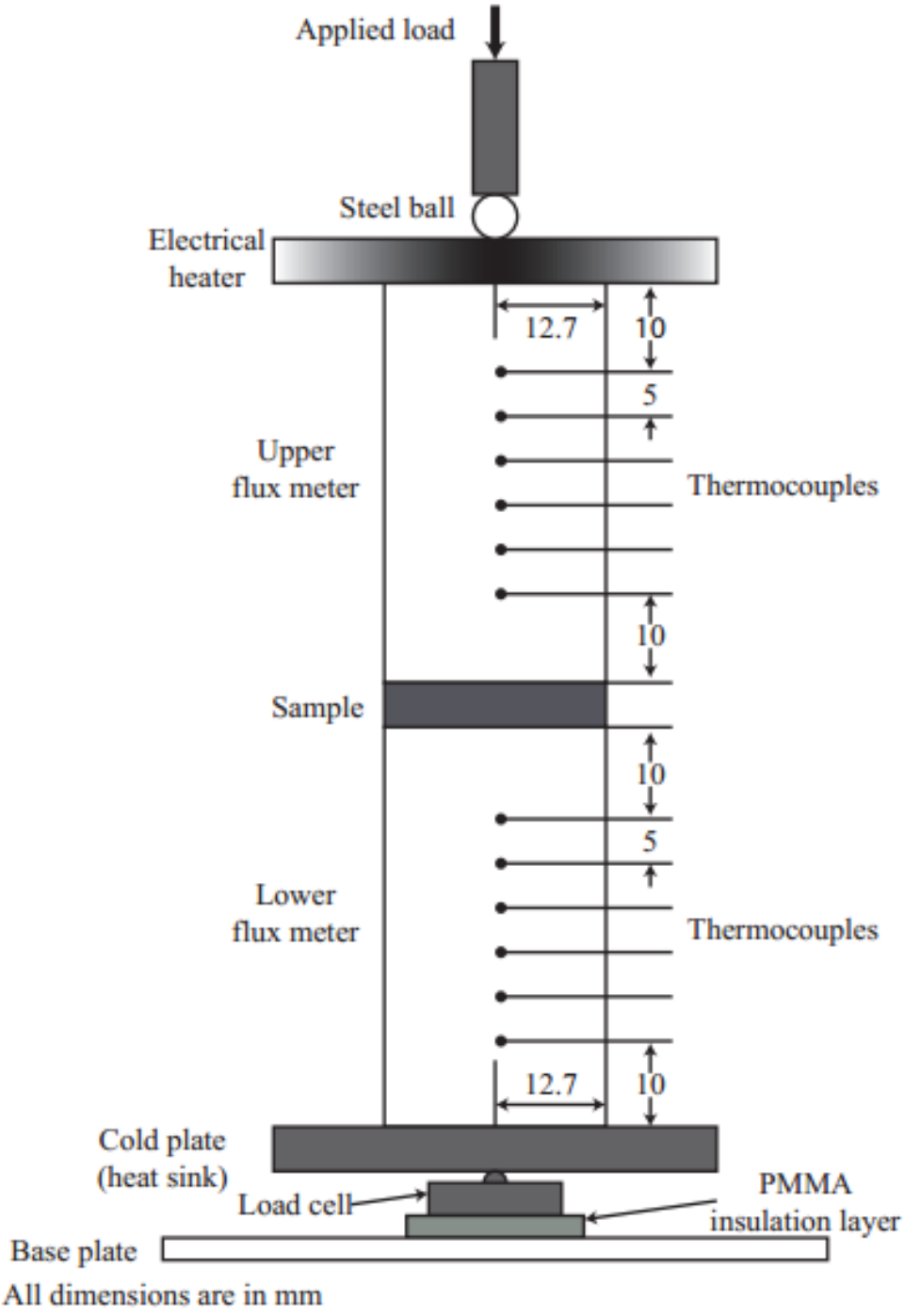
Applied load
Steel ball
Electrical heater
12.7
10
5
Upper flux meter
Thermocouples
10
Sample
10
5
Lower flux meter
Thermocouples
12.7
10
Cold plate (heat sink)
Load cell
PMMA insulation layer
Base plate
All dimensions are in mm

(b)

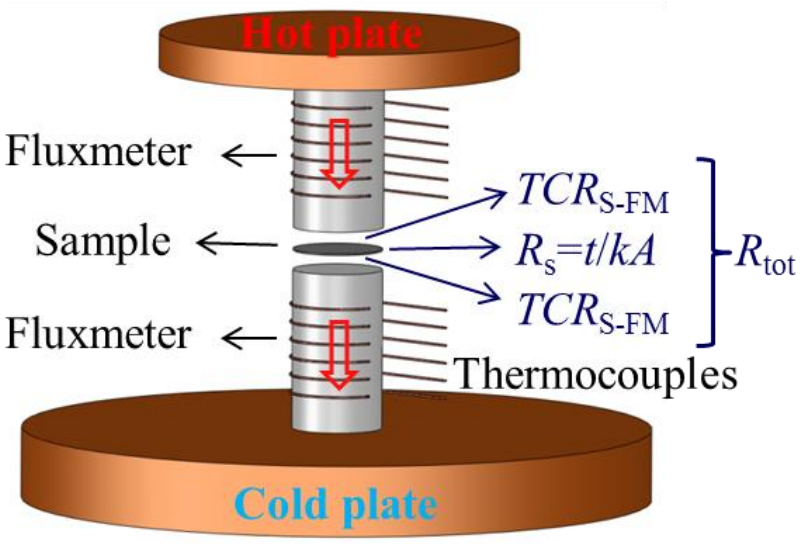

(c)

Figure 3.2. **(a) Components of the TCR testbed used for thermal resistance measurement in this study, (b) TCR testbed with the position of thermocouples, and (c) Schematic of the fluxmeters and thermocouples with the heat transferred from the hot plate to the cold plate through the sample shown as red arrows. All components are operated within a vacuum chamber (not shown).**

The total thermal resistance of a sample sandwiched between the two fluxmeters can be written as:

$$R_{\mathrm{tot}} = \frac{t}{kA} + 2TCR \tag{3-1}$$

where t [m] and k [W m^{-1} K^{-1}] represent the thickness and the thermal conductivity of the sample, respectively. A [m^2] stands for the cross-sectional area of the fluxmeters and of the sample, TCR [K W^{-1}] denotes the thermal contact resistance at the interface between the sample and the fluxmeters, and R_{tot} [K W^{-1}] represents total thermal resistance, which can be measured as:

$$R_{\mathrm{tot}} = \frac{(T_{\mathrm{n}} - T_{\mathrm{m}})}{Q} \tag{3-2}$$

where Q [W], the heat rate passing through the sample, can be obtained by averaging the heat transfer rates measured through the two fluxmeters. The heat transfer rate Q can be calculated from the temperature gradients inside either fluxmeters based on the Fourier's law of heat conduction:

$$Q = k_{\mathrm{FM}}(T) A \frac{dT}{dx} \tag{3-3}$$

In Eq. (3-3), k_{FM} [W m^{-1} K^{-1}] is the thermal conductivity of Armco-iron fluxmeter ($k_{\mathrm{FM}} = 10^{-4}T(^{\circ}\mathrm{C})^2 - 0.046T(^{\circ}\mathrm{C}) + 75.233$) and $\frac{dT}{dx}$ is the slope of the T-x lines showing the linear variation of the temperature along either fluxmeter, as illustrated in Figure 3.3. The focus in this study will be on the experimental procedure utilized in conducting the tests to de-convolute the contact resistance between the sample and the fluxmeters from the other present resistances.

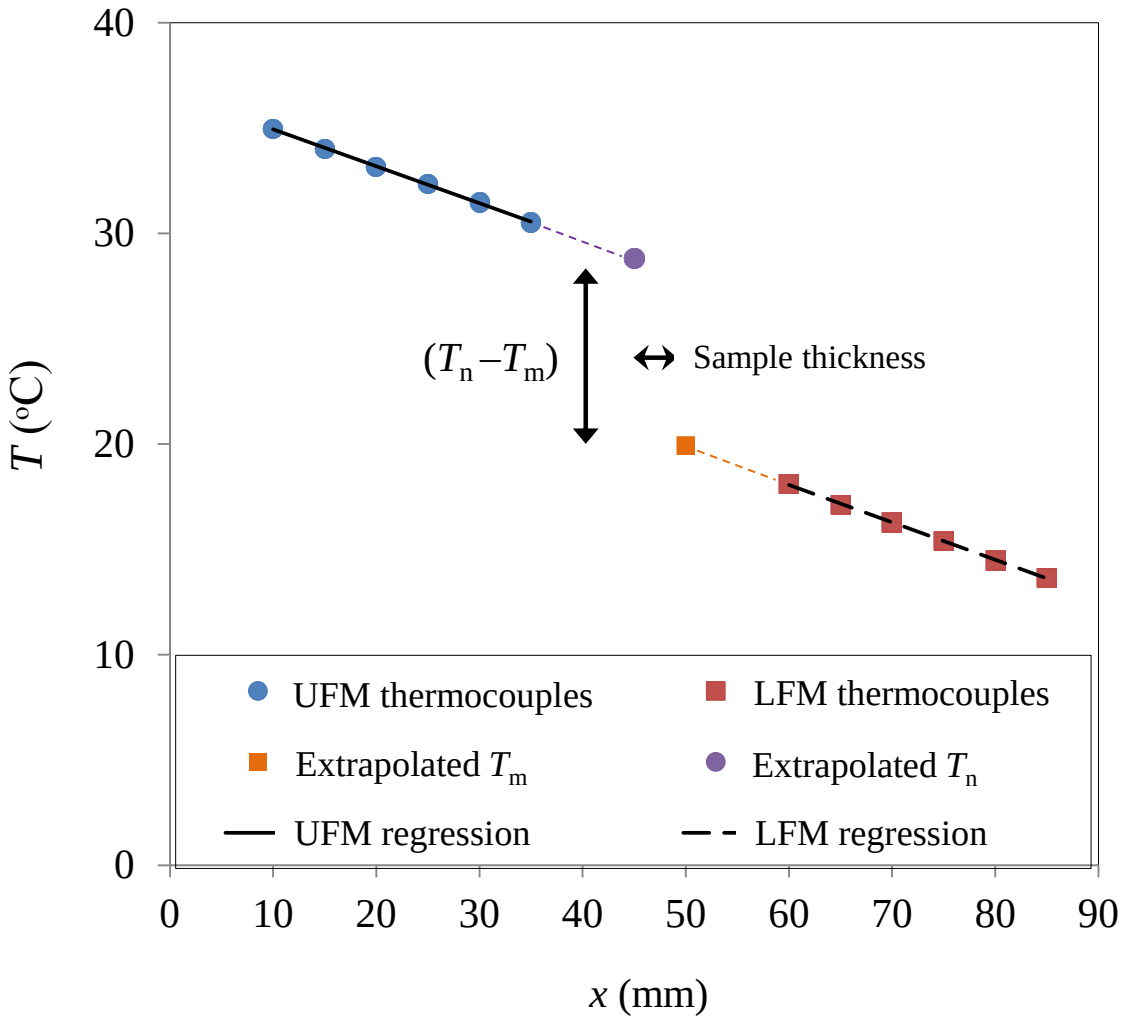

Figure 3.3. Temperature gradients inside the lower and upper fluxmeters (LFM and UFM) and the extrapolated temperature drop across the sample

3.2. Two thickness method

Using two samples of the same material with different thicknesses t_1 and t_2 (Figure 3.4), the bulk resistance (thermal conductivity) can be deconvoluted from the contact resistance of the sample. The total value of the thermal resistance for each sample can be written as:

$$R_{\mathrm{tot}_1} = \frac{t_1}{kA} + 2TCR \tag{3-4}$$

$$R_{\mathrm{tot}_2} = \frac{t_2}{kA} + 2TCR \tag{3-5}$$

TCR, the thermal contact resistance between the sample and the fluxmeters, is, unlike the bulk resistance $t_i/kA = R_i$ (i=1,2), independent of the sample thickness (t_i). R_{tot}, the total resistance, is the only *measurable* resistance here.

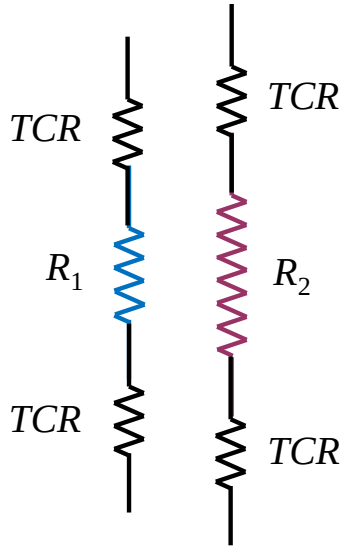

Figure 3.4. Thermal resistance network for samples with different thicknesses (R_1=t_1/kA and R_2=t_2/kA) (also see Figure 3.2)

The sample thermal conductivity *k* and the *TCR* are the two unknowns that can be obtained from two Eqs. (3-4) and (3-5) as follows:

$$k = \frac{(t_2 - t_1)}{(R_{\mathrm{tot}_2} - R_{\mathrm{tot}_1})A} \tag{3-6}$$

$$TCR = \frac{(t_2 R_{\mathrm{tot}_1} - t_1 R_{\mathrm{tot}_2})}{2(t_2 - t_1)} \tag{3-7}$$

This accurate and effective way of de-convoluting thermal contact resistance (*TCR*) from bulk, and in fact from measurable total resistance, is called two-thickness method.

3.2.1. Testbed accuracy

The accuracy of the TCR machine was verified using two Pyrex 7740 [168] calibration samples with different thicknesses of 3.3 and 9.0 mm, which have thermal resistances on the same order of magnitude of typical GDLs (see Appendix A). The tests were conducted at two pressures of 7 and 11 bar at the temperature of approximately 50 °C. The test results shown in Figure 3.5 were satisfactory, as the maximum difference between the measured and manufacturer's data was 8% and the measurements well agreed within uncertainty to the manufacturer's data.

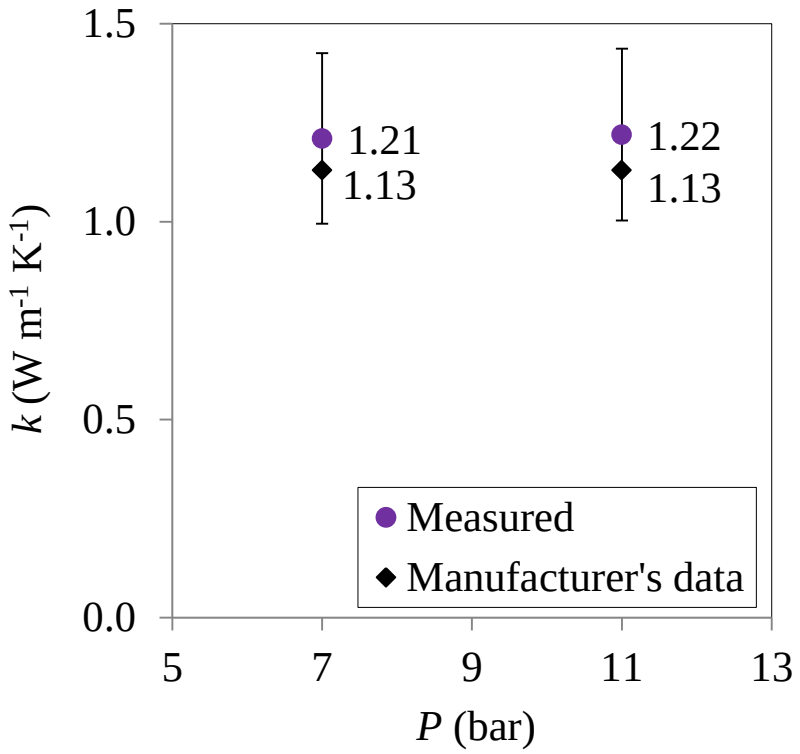

Figure 3.5. Calibration sample data showing the accuracy of the TCR machine

3.2.2. Uncertainty analysis

The uncertainty in the total resistance and thermal conductivity measurements of similar test apparatuses have been calculated using the procedure in Appendix B in conjunction with different relations in Refs. [47] [58] [90] [91] [92] [119] [169]. The analysis accounts for error propagation from measured to calculated quantities

The resistance and thermal conductivity measured by the TCR machine is a function of the following parameters:

$$R_{\text{tot}} = \frac{\Delta T}{Q} = \text{f}(Q, \Delta T(A, k_{\text{FM}}, T, x)) \qquad (3\text{-}8)$$

$$k = \mathrm{f}(R_{\mathrm{tot}}, t, A) \tag{3-9}$$

where ΔT is the temperature difference across the sample and all the other parameters have already been defined. The uncertainty for the thermal resistance can be calculated from the root-sum-square or quadrature method [170] [171] [172]:

$$\frac{\delta R_{\mathrm{tot}}}{R_{\mathrm{tot}}} = \sqrt{(\frac{1}{2}\frac{\delta Q}{Q})^2 + (\frac{\delta T}{T})^2 + (\frac{\delta A}{A})^2 + (\frac{\delta k_{\mathrm{FM}}}{k_{\mathrm{FM}}})^2 + (\frac{\delta x}{x})^2} \tag{3-10}$$

The following equations should be used for the uncertainty calculations of the thermal conductivity k and TCR considering Eqs. (3-6) and (3-7) (see Refs. [171] [172]):

$$\frac{\delta k}{k} = \sqrt{\left(\frac{\sqrt{\delta R_{tot_2}{}^2 + \delta R_{tot_1}{}^2}}{R_{tot_2} - R_{tot_1}}\right)^2 + \left(\frac{\sqrt{\delta t_2{}^2 + \delta t_1{}^2}}{t_2 - t_1}\right)^2 + (\frac{\delta A}{A})^2} \tag{3-11}$$

$$\frac{\delta TCR}{TCR} = \sqrt{\left(\frac{\sqrt{\delta t_2{}^2 + \delta R_{tot_1}{}^2 + \delta t_1{}^2 + \delta R_{tot_2}{}^2}}{t_2 R_{\mathrm{tot1}} - t_1 R_{\mathrm{tot2}}}\right)^2 + \left(\frac{\sqrt{\delta t_2{}^2 + \delta t_1{}^2}}{t_2 - t_1}\right)^2} \tag{3-12}$$

All the parameters and the associated uncertainties resulting from this analysis are summarized in Table 3.1 and Table 3.2. Note that the main uncertainty stems from the heat flow rate passing through the fluxmeters, *Q*.

Table 3.1. Uncertainty of involving parameters in the thermal resistance measurements in the present study

Material	$\frac{\delta Q}{Q}$	$\frac{\delta T}{T}$	$\frac{\delta A}{A}$	$\frac{\delta k_{\mathrm{FM}}}{k_{\mathrm{FM}}}$	$\frac{\delta x}{x}$	$\frac{\delta R_{tot}}{R_{tot}}$ (%)
Calibration sample	0.148	0.003	0.002	0.003	0.010	7.5
GDLs	0.095	0.003	0.002	0.003	0.010	4.8
BPPs	0.113	0.003	0.002	0.003	0.010	5.7

Table 3.2. Uncertainty in the measurement of thermal conductivity and thermal contact resistance for different samples

Material	δt (µm)	$\frac{\delta t}{t}$	$\frac{\delta k}{k}$ (%)	$\frac{\delta TCR}{TCR}$ (%)
Calibration sample	±100	0.022	17.3	13.8
GDLs	±10	0.050	18.6	10.0
BPPs	±100	0.050	20.2	18.1

3.3. Samples used in this work

3.3.1. Sigracet GDL samples

Different treated and untreated SIGRACET [173] gas diffusion layers, series SGL 24 and 34, as well as 25 and 35 (Figure 3.6) were tested to obtain their thermal conductivity. The advantage of working with this type of GDLs is that the effect of PTFE and MPL on their thermal resistances can be separately investigated. Substrates of SGL BA and DA are fabricated by adding 5 and 20 wt% PTFE to the *plain* (untreated) substrate AA, respectively, and the BC type is the BA substrate with MPL on one side, see Figure 3.7 [173]. The numbers 24 and 34, as well as 25 and 35, included in the GDL names, refer to their thicknesses, as reported in Table 3.3. Hence, the only difference between the substrates of SGLs 24 and 34 and those of SGLs 25 and 35 is their thicknesses, which makes the two thickness method an appropriate approach for measuring thermal conductivity and contact resistance.

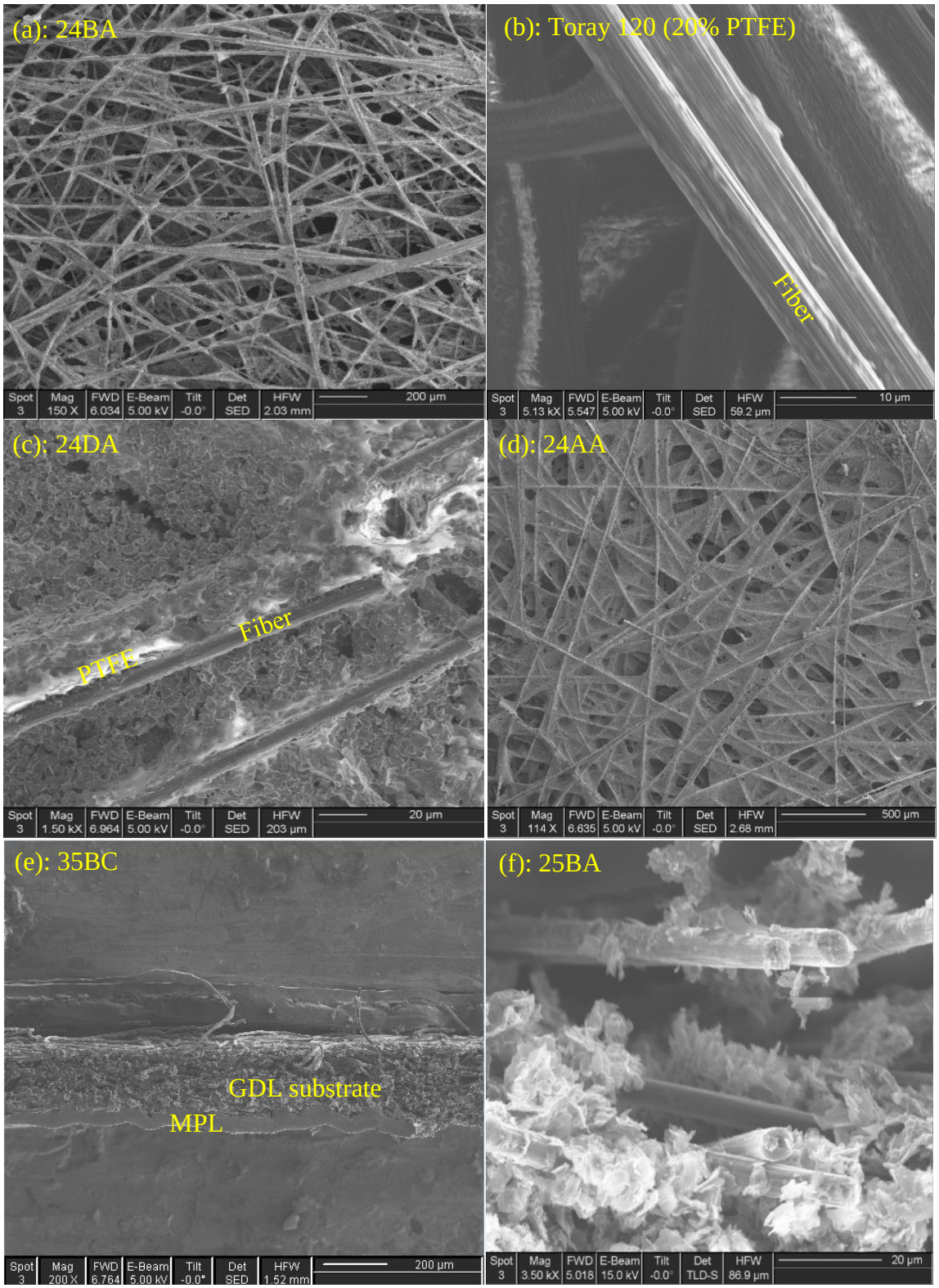
(a): 24BA
Spot 3 | Mag 150 X | FWD 6.034 | E-Beam 5.00 kV | Tilt -0.0° | Det SED | HFW 2.03 mm | 200 µm
(b): Toray 120 (20% PTFE)
Fiber
Spot 3 | Mag 5.13 kX | FWD 5.547 | E-Beam 5.00 kV | Tilt -0.0° | Det SED | HFW 59.2 µm | 10 µm
(c); 24DA
PTFE
Fiber
Spot 3 | Mag 1.50 kX | FWD 6.964 | E-Beam 5.00 kV | Tilt -0.0° | Det SED | HFW 203 µm | 20 µm
(d): 24AA
Spot 3 | Mag 114 X | FWD 6.635 | E-Beam 5.00 kV | Tilt -0.0° | Det SED | HFW 2.68 mm | 500 µm
(e): 35BC
GDL substrate
MPL
Spot 3 | Mag 200 X | FWD 6.764 | E-Beam 5.00 kV | Tilt -0.0° | Det SED | HFW 1.52 mm | 200 µm
(f): 25BA
Spot 3 | Mag 3.50 kX | FWD 5.018 | E-Beam 15.0 kV | Tilt -0.0° | Det TLD-S | HFW 86.9 µm | 20 µm

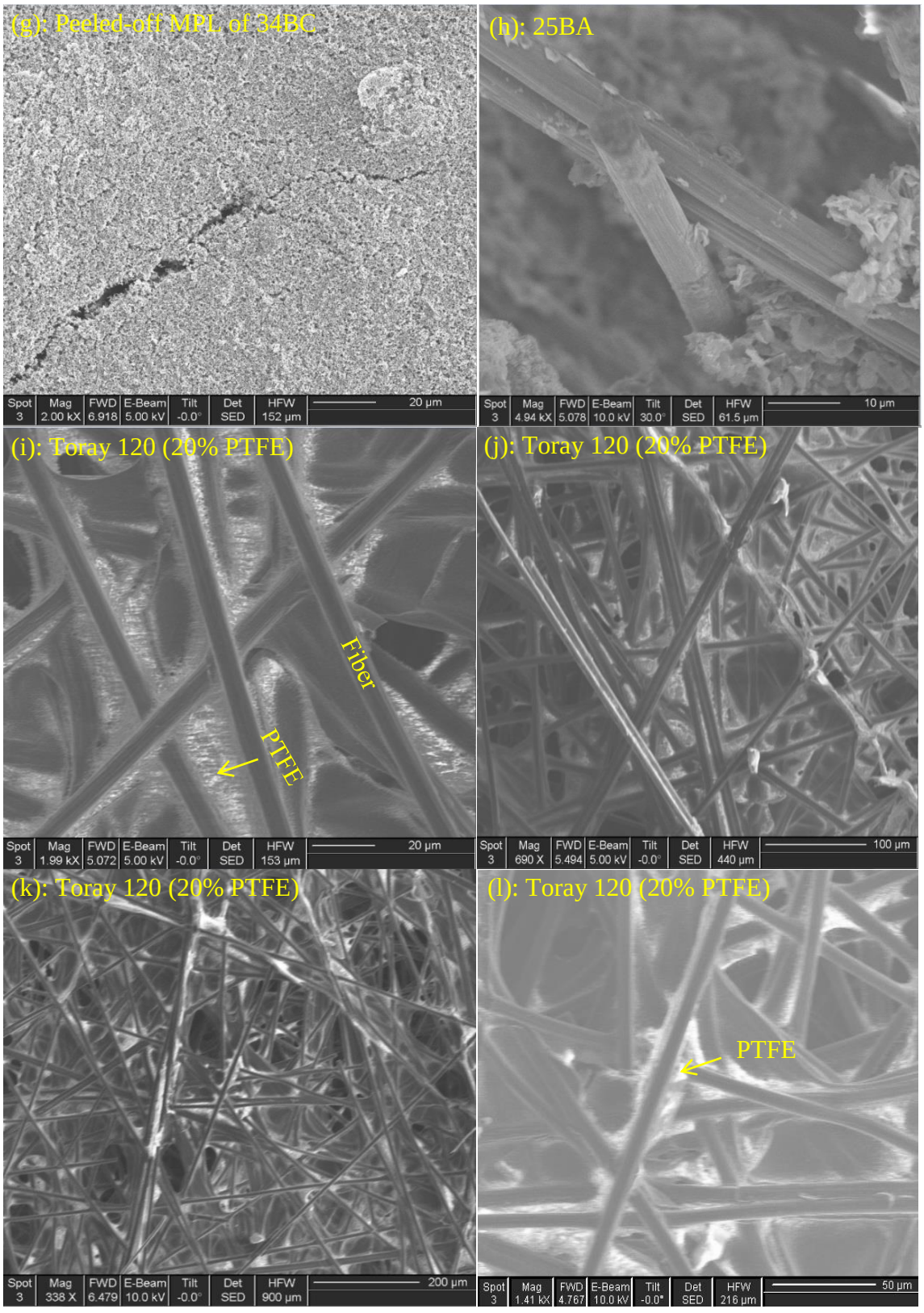
(g): Peeled-off MPL of 34BC
Spot 3 | Mag 2.00 kX | FWD 6.918 | E-Beam 5.00 kV | Tilt -0.0° | Det SED | HFW 152 µm | 20 µm
(h): 25BA
Spot 3 | Mag 4.94 kX | FWD 5.078 | E-Beam 10.0 kV | Tilt 30.0° | Det SED | HFW 61.5 µm | 10 µm
(i): Toray 120 (20% PTFE)
Fiber
PTFE
Spot 3 | Mag 1.99 kX | FWD 5.072 | E-Beam 5.00 kV | Tilt -0.0° | Det SED | HFW 153 µm | 20 µm
(j): Toray 120 (20% PTFE)
Spot 3 | Mag 690 X | FWD 5.494 | E-Beam 5.00 kV | Tilt -0.0° | Det SED | HFW 440 µm | 100 µm
(k): Toray 120 (20% PTFE)
Spot 3 | Mag 338 X | FWD 6.479 | E-Beam 10.0 kV | Tilt -0.0° | Det SED | HFW 900 µm | 200 µm
(l): Toray 120 (20% PTFE)
PTFE
Spot 3 | Mag 1.41 kX | FWD 4.767 | E-Beam 10.0 kV | Tilt -0.0° | Det SED | HFW 216 µm | 50 µm

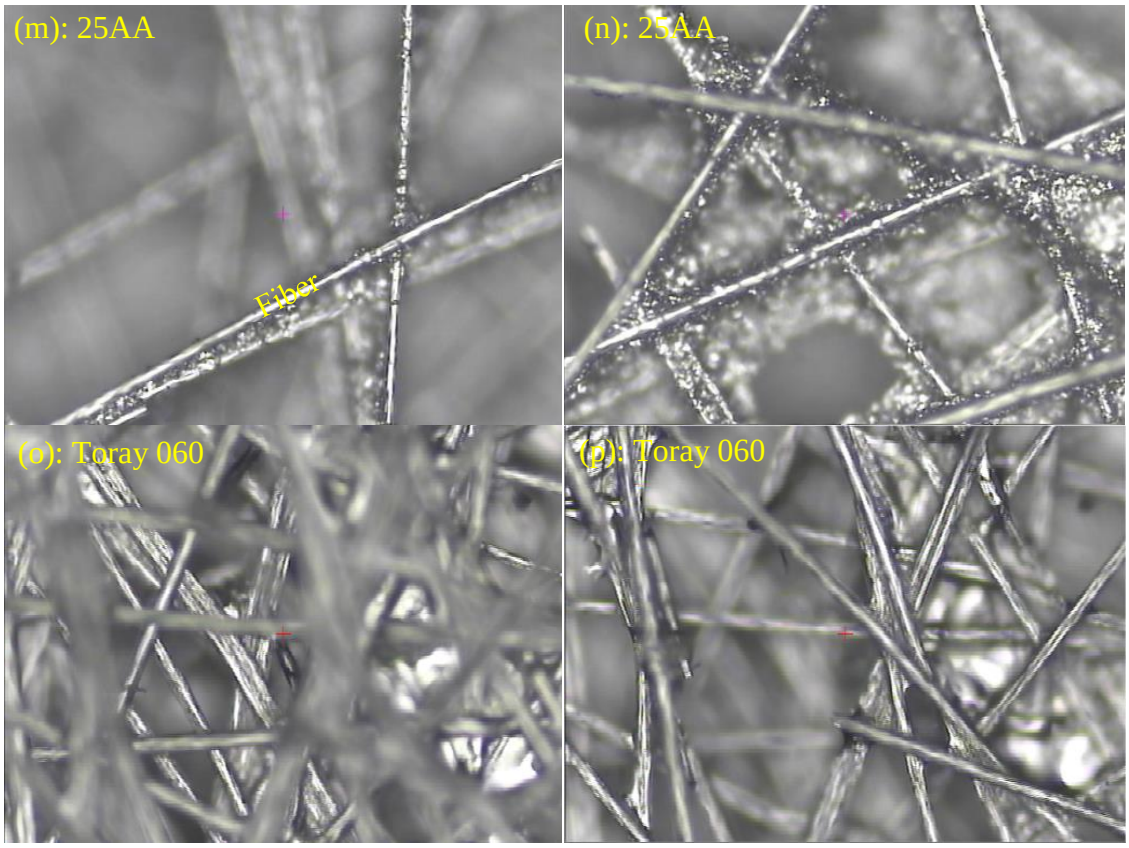

Figure 3.6. **SEM and optical images of some Sigracet GDLs: (a)-(l) SEM image of a different Sigracet GDLs; (m)-(p) Optical images of SGL and Toray GDLs**

AA	YA	YC

Y	A	B	D
Wt.% PTFE	0	5	20

Figure 3.7. GDLs of SGL AA, BA, DA, and BC (the black layer represents MPL and the gray one represents GDL substrate with 0% PTFE) [173]

Table 3.3. Specifications of SIGRACET GDLs studied in the present work

SGL	24				25			34				35		
	AA	BA	DA	BC	AA	BA	BC	AA	BA	DA	BC	AA	BA	BC
Porosity (%)	88	84	72	76	92	88	80	88	84	72	76	92	88	80
Thickness (µm) ±10	190	190	190	235	190	190	235	280	280	280	315	300	300	325
PTFE Thickness on each surface (µm)	0	1.5	3	-	0	1	-	0	1.5	3	-	0	1	0

3.3.2. Ballard BPP samples

Three graphite bipolar plate blank samples of the same material (machined from one blank plate) with different thicknesses of 2.95, 4.94, and 5.84 mm (Figure 3.8), herein referred to in terms of their thicknesses, were employed for thermal conductivity measurements. Before performing any measurements, some surface analysis tests were carried out on all three samples to ensure the acceptable flatness of the sample surfaces. The deviations in the flatness of the sample surfaces, obtained by a surface dial indicator Mitutoyo MTT513-412 (Figure 3.9), are summarized in Table 3.4.

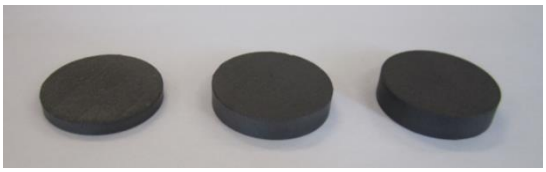

Figure 3.8. Ballard's graphite BPP samples with different nominal thicknesses of 2.95, 4.94 and 5.84 mm

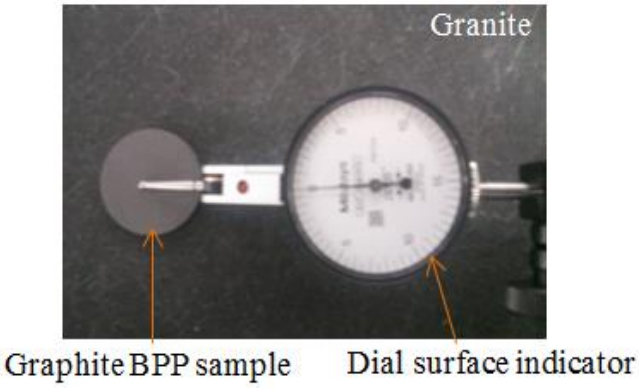

Figure 3.9. Measuring deviations in the flatness of the BPP sample surfaces using a dial test indicator

Table 3.4. Maximum deviations in the flatness of the studied samples' surfaces

Sample thickness (mm)	**2.95**	**4.94**	**5.84**
	Max. dev. in flatness (mm) /0.0127		
One surface	0.5	<1.5	0.5
The other surface	<0.5	<0.75	<0.5

In order to measure the most accurate thermal conductivity values using the two thickness method, the 2.95 and 5.84 samples that showed proper surface flatness are selected. Sample 4.94 is only used later for investigating the effect of BPP out-of-flatness on its thermal contact resistance with GDLs.

3.4. Thermal resistance (conductivity) of the graphite BPP (R_{BPP})

Applying the two-thickness method to the BPP samples with different thicknesses yields the thermal conductivity of the BPP and its contact resistance with the fluxmeters. In this study, the thermal conductivity or resistance of the BPP (R_{BBP}) is required for determining its TCR with the GDLs. The tests are performed at five different temperatures to gain the thermal conductivity of the BPP as a function of temperature (Figure 3.10).

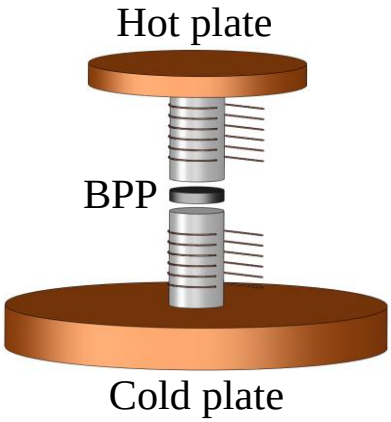

Figure 3.10. A BPP sample sandwiched between the two fluxmeters of the TCR machine for thermal conductivity measurements

The thermal conductivity of the graphite BPP is plotted as a function of temperature and compression in Figure 3.11. The thermal conductivity does not change with compression, as expected; however, it increases with decreasing temperature. The temperature dependency of the BPP thermal conductivity, shown in Figure 3.12, can be approximated by a third-order polynomial equation as:

$$k = (5.713 \times 10^{-5})T^3 - (4.653 \times 10^{-3})T^2 - 0.188T + 24.718 \quad (3\text{-}13)$$

where k and T represent thermal conductivity (W m^{-1} K^{-1}) and temperature (°C), respectively. The slope of the k-T curve decreases with increasing temperature from 10 to 70 ^{o}C.

It should be noted that the typical range of compression in PEMFC is between 8 and 15 bar. In this study, in order to prevent any damage to the microstructure of the graphite BPPs, the tests have been conducted at lower compression (<7 bar).

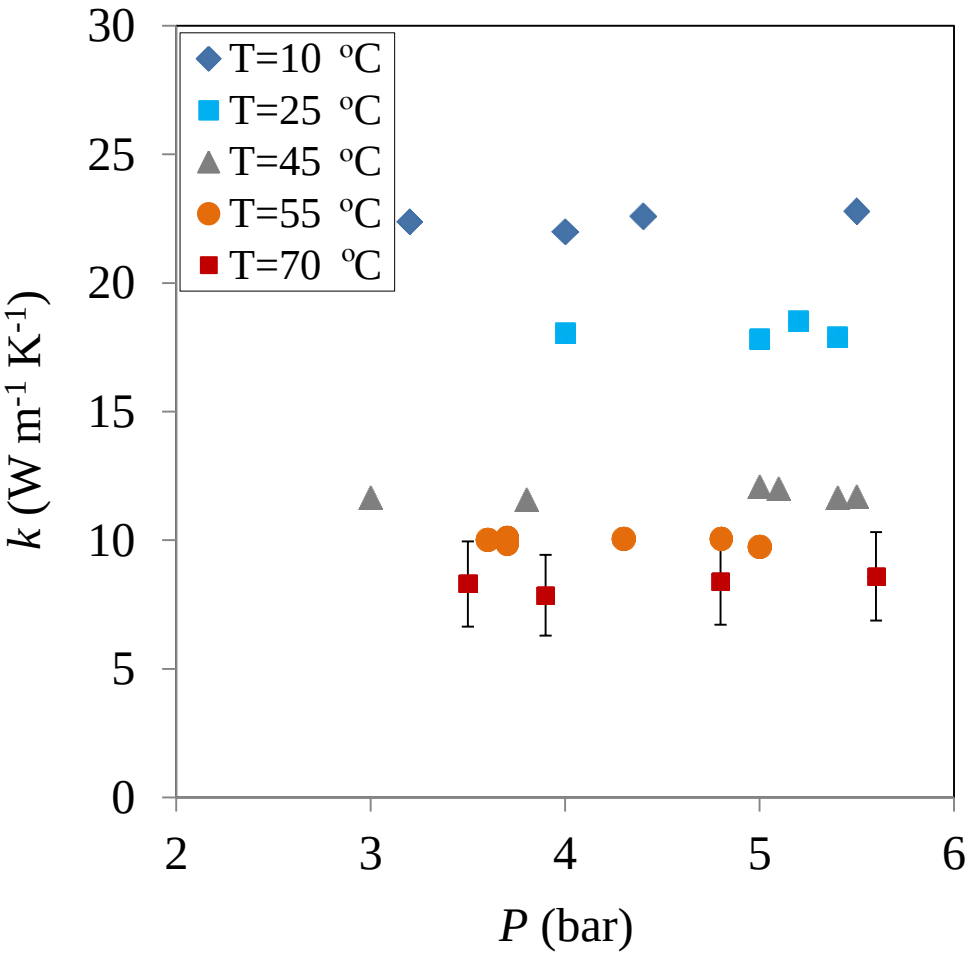

Figure 3.11. **Thermal conductivity of the graphite BPP (k_{BPP}) at different temperatures and compression (obtained from repeated tests): $R_{BPP}=t_{BPP}/(k_{BPP}A)$**

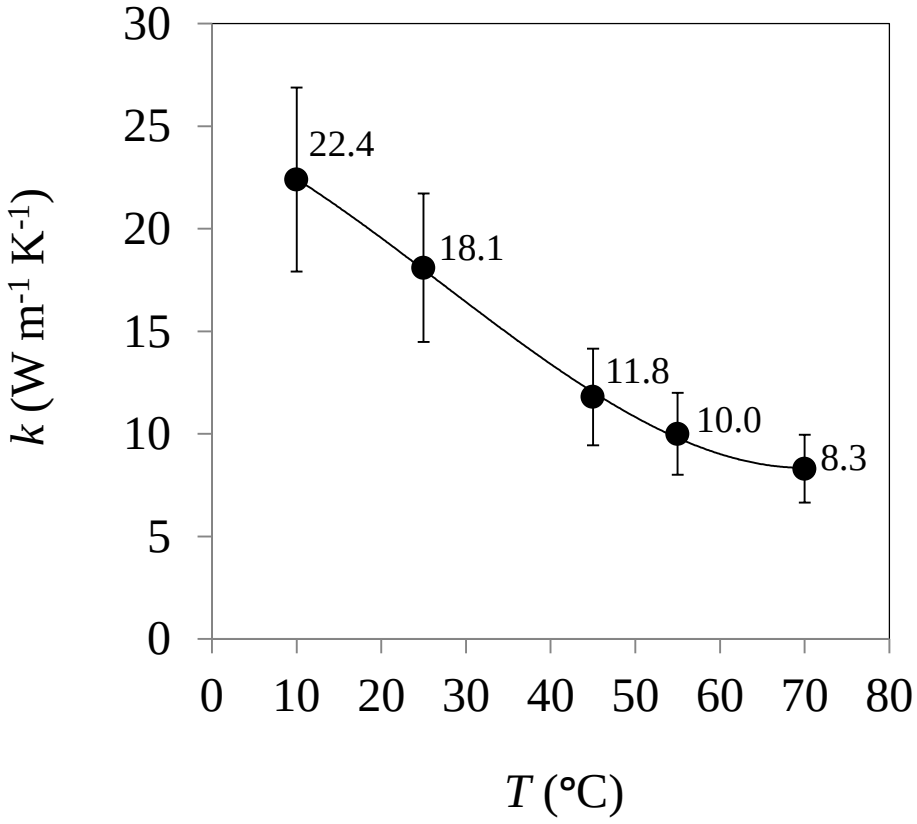

Figure 3.12. Thermal conductivity of the graphite BPP (k_{BPP}) as a function of temperature

3.4.1. Thermal contact resistance of the graphite BPP with fluxmeters

The TCR between the BPP and the Armco-iron fluxmeters decreases with both pressure and temperature, as shown in Figure 3.13. The results show that the effect of temperature on this TCR is, however, much stronger than that of compression. The descending trend of the TCR with temperature is similar to the trends observed for the data of other solid-solid contact resistance available in the literature; see e.g. Ref. [174].

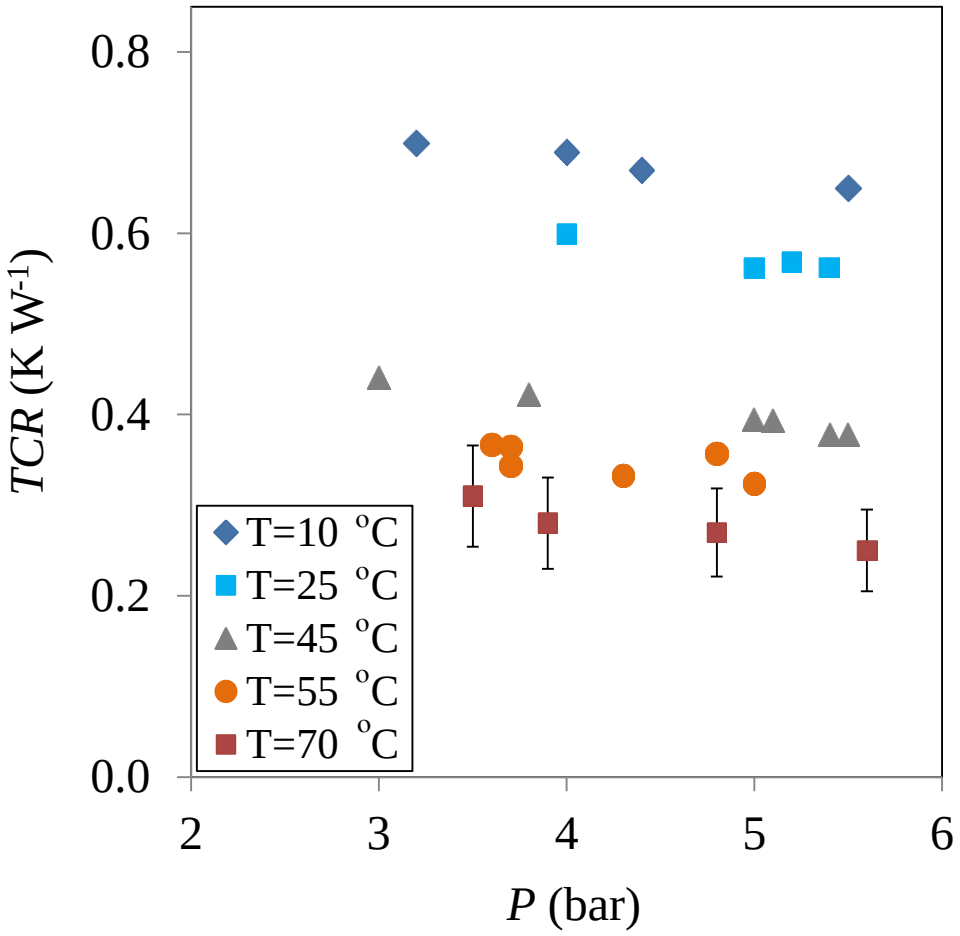

Figure 3.13. **TCR between the graphite BPP and the Armco-iron fluxmeters at different temperatures and compression (obtained from repeated tests).**

3.5. Thermal resistance (conductivity) of GDLs (R_{GDL}) and their contact resistance with the fluxmeters ($TCR_{GDL\text{-}FM}$)

Sigracet (SGL) GDLs are available in two thicknesses [173], which allow determining their thermal conductivity (bulk resistance: R_{GDL}) and their contact resistances with the fluxmeters (TCR_{GDL-FM}) in terms of compression using the two-thickness method (Figure 3.14). The GDL bulk and contact resistances (R_{GDL} and TCR_{GDL-FM}) are both required for determining its TCR with the graphite BPP.

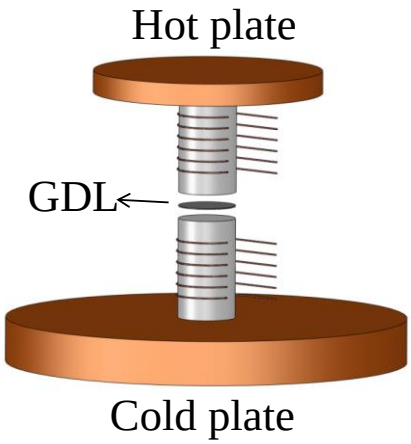

Figure 3.14. A GDL sandwiched between the two fluxmeters of the TCR machine for thermal conductivity measurements.

The thermal conductivities of SGL 24 & 34 AA, BA, DA, and BC and those of series 25 & 35 AA, BA, and BC are shown in Figure 3.15. The effect of PTFE loading (content) and compression is discussed in the following subsection.

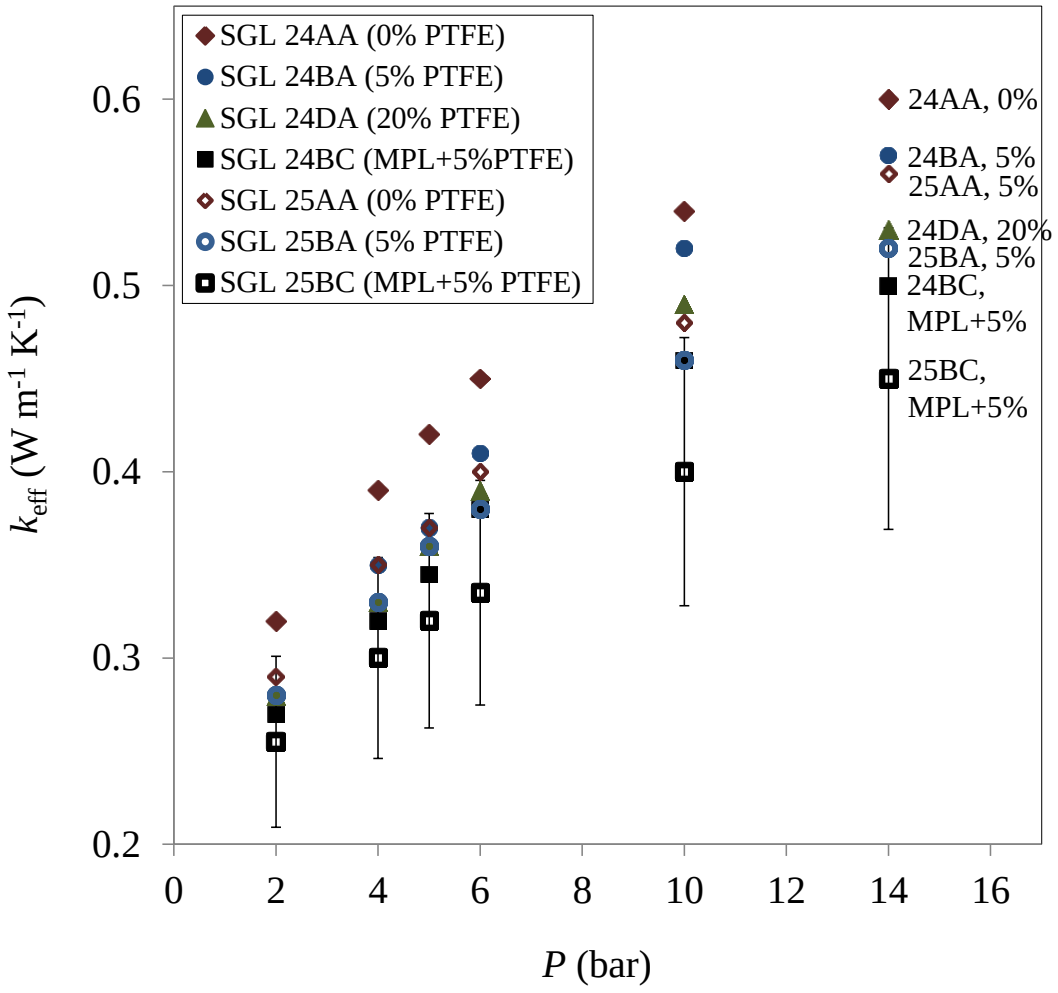

Figure 3.15. Thermal conductivity of Sigracet untreated and treated GDLs (k_{GDL}) as a function of compression: $R_{GDL}=t_{GDL}/(k_{GDL}A)$

3.5.1. Effect of PTFE on GDL thermal conductivity

Figure 3.16 also depicts the effect of different PTFE loading on the through-plane thermal conductivity. The reduction in thermal conductivity with PTFE is clearly shown in Figure 3.16 and can be attributed to the low thermal conductivity of PTFE, which increases the overall thermal resistance of the entire GDL. The trend observed here is in

qualitative agreement with the results of Khandelwal and Mench [91] and Burheim *et al.* [93] [101] [103], but not with the negligible changes reported in Ref. [49] even for 60 wt% PTFE.

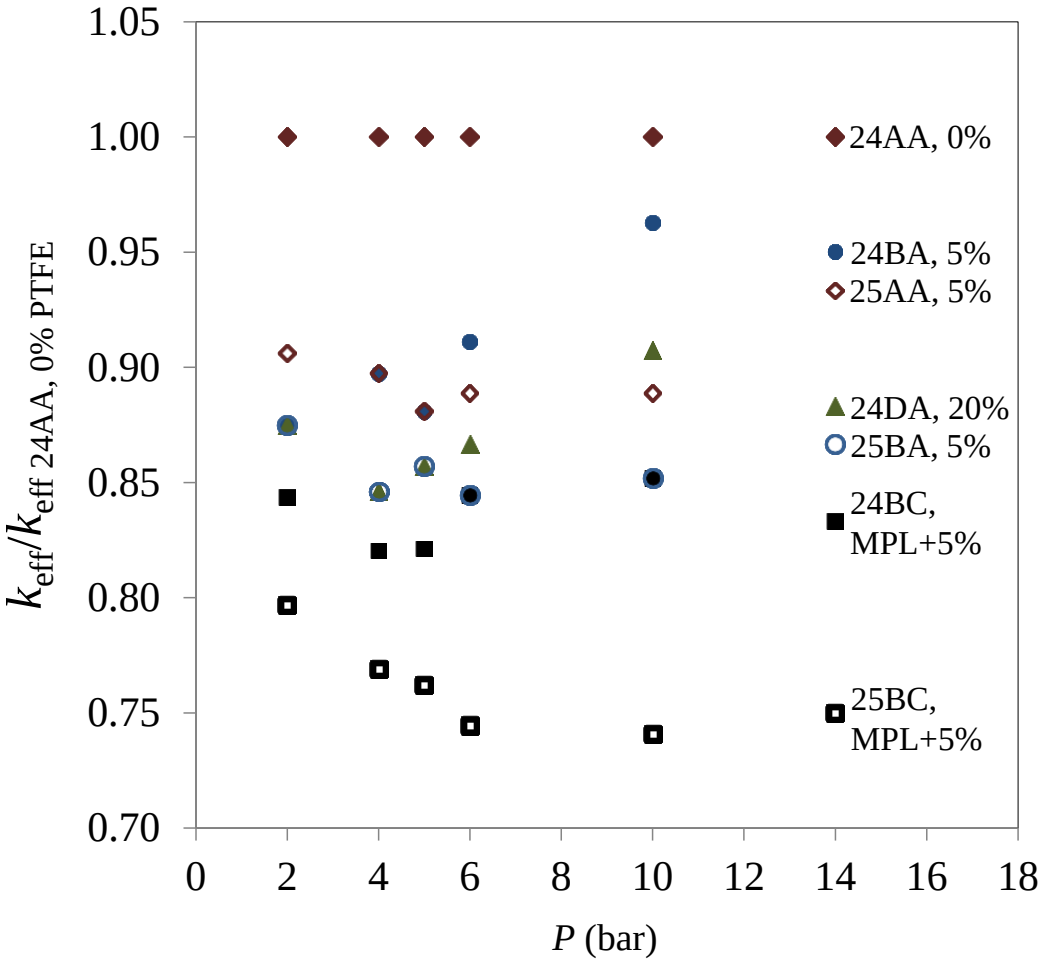

Figure 3.16. Variation of thermal conductivity with pressure and effect of PTFE and MPL on the thermal conductivity of a GDL substrate: Comparison between thermal conductivities of the studied GDLs with reference to the thermal conductivity of SGL 24AA (0% PTFE)

It is interesting to note that the highest decrease observed in thermal conductivity on Figure 3.16 pertains to an increase in PTFE from 5 to 20 wt%. The effect of 5% PTFE loading is negligible, as the data of substrates AA (0% PTFE) and BA (5% PTFE) almost overlap or are very close to each other. It is worth mentioning that the general trend of PTFE loading in thermal conductivity reduction is the same for the two series SGL GDLs investigated.

It is also important to note that, contrary to the through-plane thermal conductivity, the in-plane conductivity does not decrease with PTFE; rather, a slight increase was observed in Ref. [58]. This is attributed to the very thin layer of PTFE covering the fiber layers on both surfaces of GDL which only influences the GDL thermal resistance in the through-plane direction and has no impact on the in-plane conduction. However, since the low thermal conductivity material of air is replaced by PTFE, it is reasonable to expect a slight increase in the in-plane thermal conductivity, as observed experimentally and predicted analytically in Ref. [58] (see Figure 3.17). However, Zamel et al. [86] reported an opposite trend. This might be due to their use of a "mixing rule" instead of direct measurement to estimate the bulk values of the heat capacity and, eventually, of the thermal conductivity of the GDLs studied in Ref. [86]. In addition, the transient method employed in Ref. [86] for the thermal conductivity measurements is not appropriate for GDLs commercially coming in very thin thicknesses [87] [90].

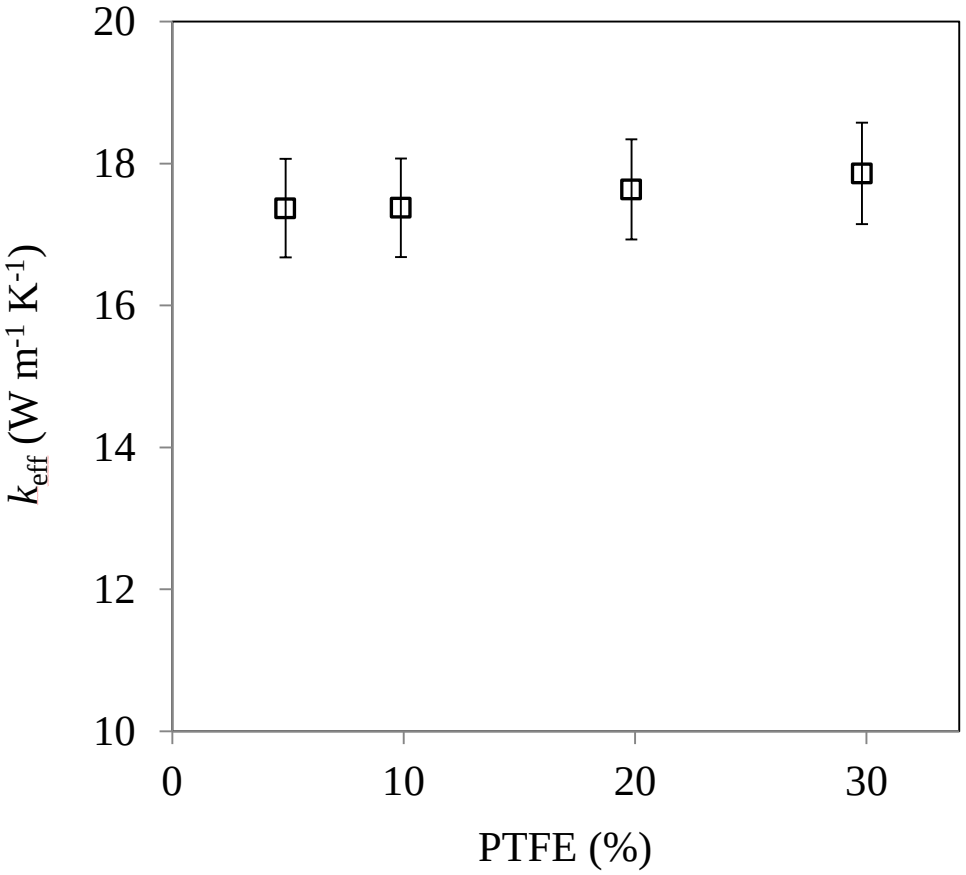

Figure 3.17. In-plane thermal conductivity of Toray carbon paper TGP-H-120 over a range of PTFE contents [58]

3.5.2. Thermal contact resistance of GDLs with the fluxmeters

Figure 3.18, showing the thermal contact resistances of the tested GDLs with the Armco-iron fluxmeters of the TCR machine, indicates that the TCR always decreases with compression, regardless of the PTFE content or MPL coating. This contact resistance is, in turn, a by-product of the two-thickness tests performed on the GDLs. However, it still reveals the behaviour of GDL-plate TCRs and can be deemed as a reference data for the TCR between GDLs and metallic BPPs.

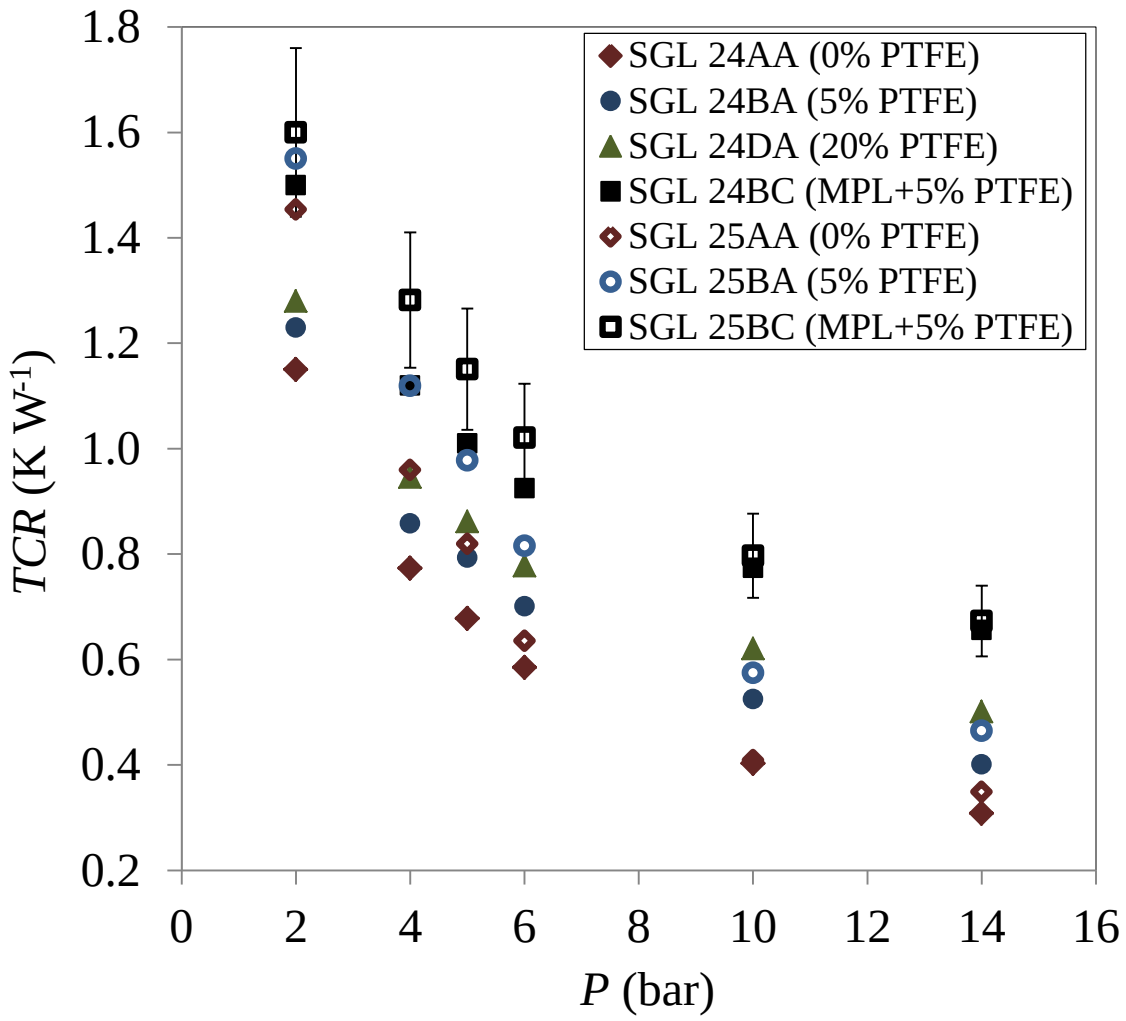

Figure 3.18. Thermal contact resistances of Sigracet untreated and treated GDLs with the Armco-iron fluxmeters (FM) as a function of compression: $TCR_{GDL\text{-}FM}$ & $TCR_{MPL\text{-}FM}$

3.5.3. Effect of PTFE on GDL-FM thermal contact resistance

Our data (Figure 3.18) shows that the thermal contact resistance between each of GDLs and the Armco-iron fluxmeters (FM) increases with PTFE. Remarkably, at lower compressive pressures, the thermal contact resistance becomes much more sensitive to PTFE treatment. In other words, with increasing compression, the effect of PTFE on thermal contact resistance decreases. These results provide qualitative insights into the thermal contact resistance between a metallic bipolar plate and GDL, as function of PTFE loading, compression and porosity.

3.6. Thermal conductivity of MPL and its effect on contact resistance

GDLs coated with an MPL on one side, such as SGL BC types, or on both sides [47] [175], provide better electrical contacts between the GDL and catalyst or BPP and reduce ohmic losses, as the main component of MPL is the high electrical conductive material of carbon black. However, due to the low thermal conductivity of carbon black and the hydrophobic agent of PTFE mixed with it, MPL may adversely influence the heat transfer in the fuel cell stack. As a result, knowing the thermal conductivity of MPL, as well as its thermal contact resistance with the GDL substrate, can be beneficial to the heat management of fuel cells. However, due to the complication associated with maintaining the integrity of this layer after separation from the substrate, experimental measurements of its thermal conductivity can be troublesome [87]. This problem is circumvented in the present study using the procedures described below.

The total thermal resistance inside a GDL treated with MPL (Figure 3.19) can be written as:

$$R_{\mathrm{GDL}} = R_{\mathrm{Sub}} + R_{\mathrm{MPL}} + TCR_{\mathrm{Sub-MPL}} \tag{3-14}$$

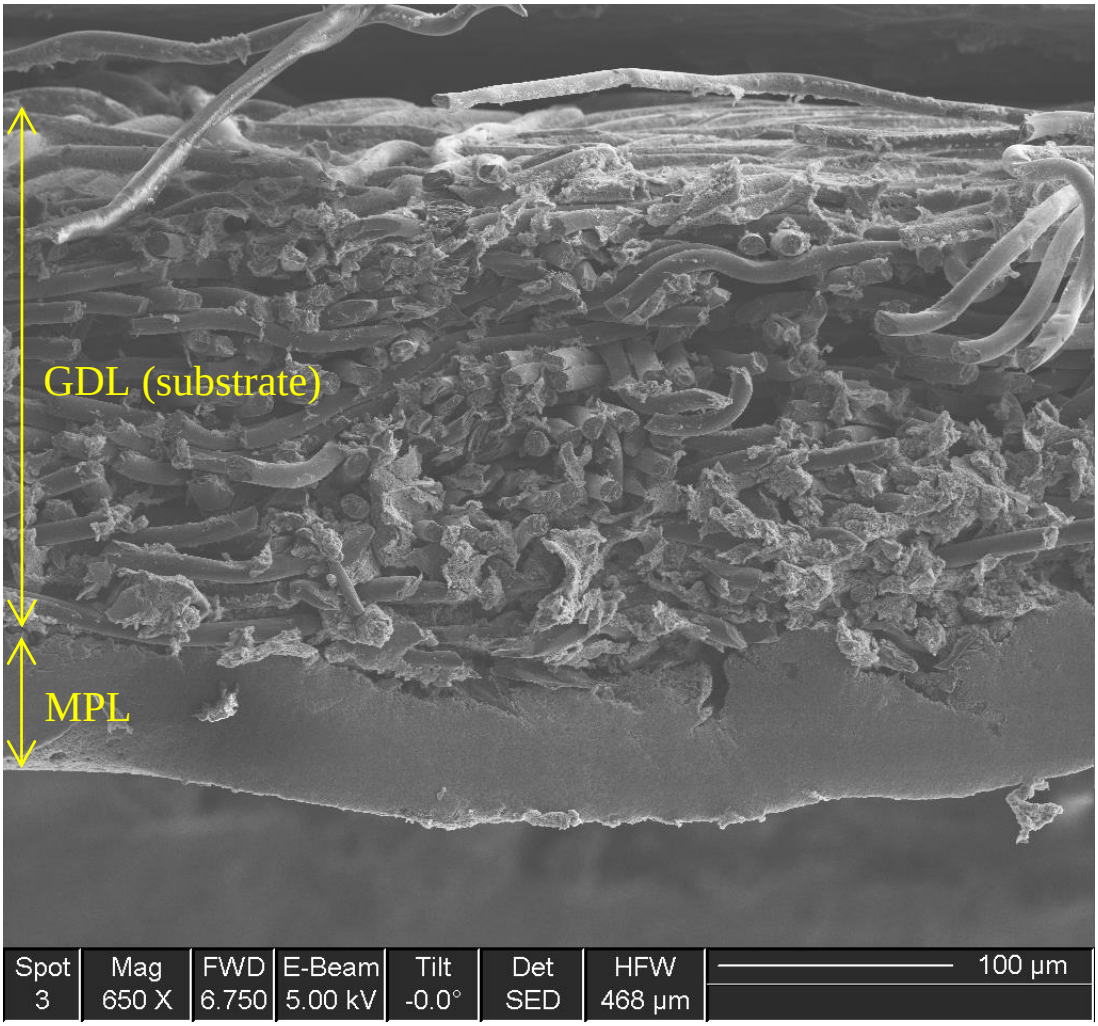

Figure 3.19. SEM image of the cross-section of a GDL with an MPL (GDL substrate-MPL assembly of SGL 35BC)

It is important to note that although the MPL and GDL substrate interpenetrate rather than form a distinct and well-defined interface, there is nonetheless a contact resistance between the two media, $TCR_{\text{Sub-MPL}}$, which has been overlooked in all the previous studies aimed at determining the GDL thermal conductivity, see e.g. [121] [102] [176]. This resistance should be deconvoluted from the bulk resistance of the GDL. Having measured the thermal resistance of a GDL coated with MPL, the thermal bulk resistance of the MPL and its thermal contact resistance with the GDL substrate can be obtained using the two-thickness method. The determination of the MPL conductivity is independent of the contact resistance between the substrate and MPL.

Measuring the thermal resistance of two different thicknesses of a GDL coated with MPL and subtracting it from the thermal bulk and interfacial resistance of the GDL substrate yields the thermal conductivity of the MPL. Sigracet GDL pairs SGL 24 & 34BC and also SGL 25 & 35BC include MPLs and GDL substrate with different thicknesses, which enables one to measure the thermal conductivity of the MPL.

Figure 3.20 shows the thermal conductivity of MPLs of SGL 24BC and SGL 25BC, measured in the present study, as a function of compression. The thermal conductivity of both MPL increases with compression up to around 10 bar and then decreases. The thermal conductivity of SGL 24BC MPL lies in the range of 0.37-0.55 W m^{-1} K^{-1}, showing a little lower values of thermal conductivity compared to the ones of MPL SGL 25BC ranging from 0.41 to 0.71 W m^{-1} K^{-1} within a pressure range of 2-14 bar. Note that the penetration depths and the interfacial contact resistances of the two MPLs coated on SGL 24BC and SGL 25BC are different as their substrates, i.e., SGL 24BA and SGL 25BA, differ from each other in terms of porosity and fiber spacing [52].

It should be noted that the SGL GDLs of type BC are fabricated with an MPL coating on one side of SGL BA with 5 wt% PTFE. In order to accurately determine the effect of MPL on the thermal conductivity of GDLs and their contact resistances with other materials, the results of BC type materials are compared with BA types. Figure 3.15 and

Figure 3.18 show that MPL reduces thermal conductivity to some extent and increases contact resistance dramatically. This finding is in qualitative agreement with Ref. [90] but not with the result of another study conducted by the same group on the same type of GDL (SolviCore) [119] reporting a negligible contact resistance of MPL with iron clamping surfaces. These uncorroborated findings of Ref. [119] were attributed to the high surface contact area of the MPL. It should be noted that none of the previously reported measurements of MPL thermal conductivity [90] [93] [119] [120] accounts for the TCR between MPL and substrate. In addition, the tests reported in Refs. [90] [119] [120] were not performed in a vacuum chamber to minimize heat loss from the sample and the thermal contact resistance between stacked GDLs was simply omitted.

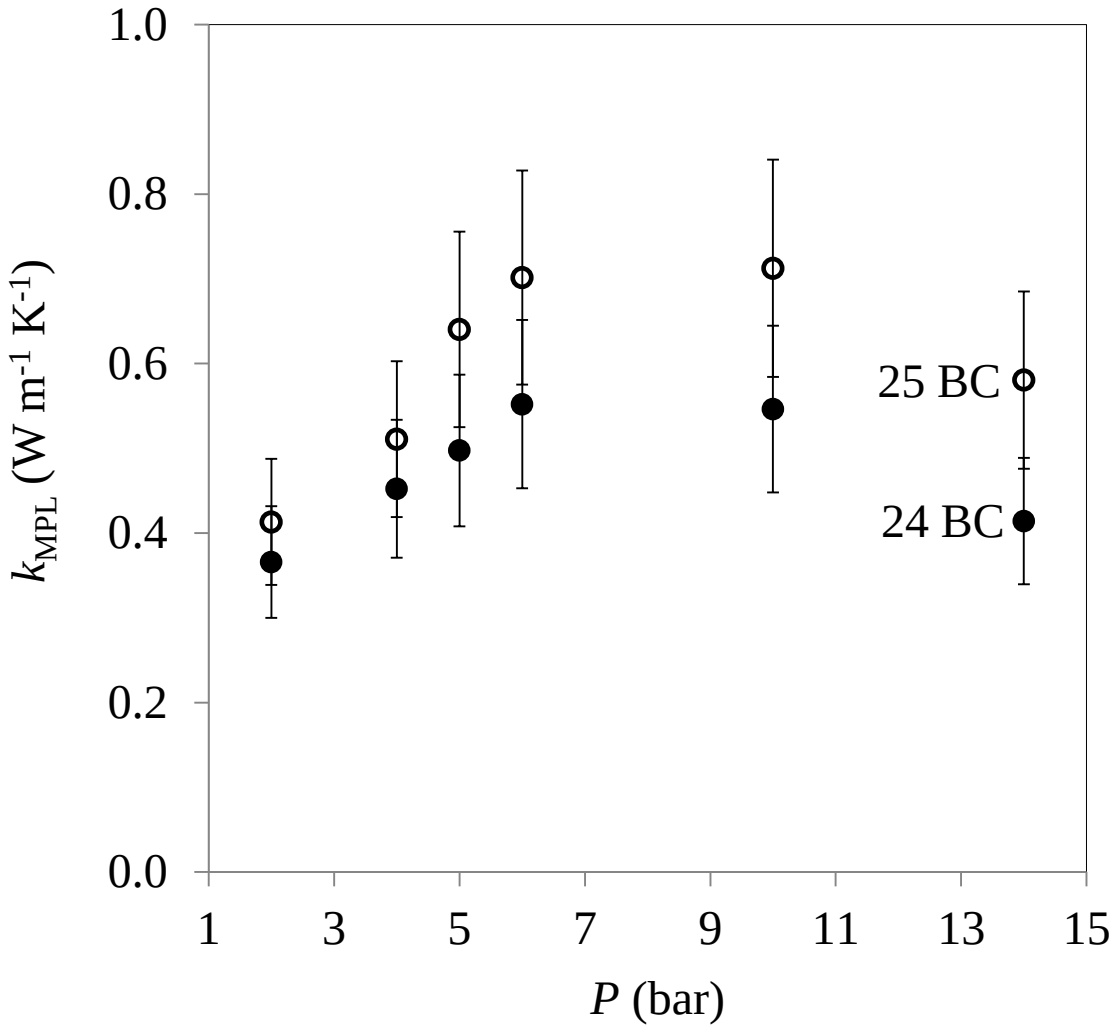

Figure 3.20. Thermal conductivity of SGL MPLs as a function of compression

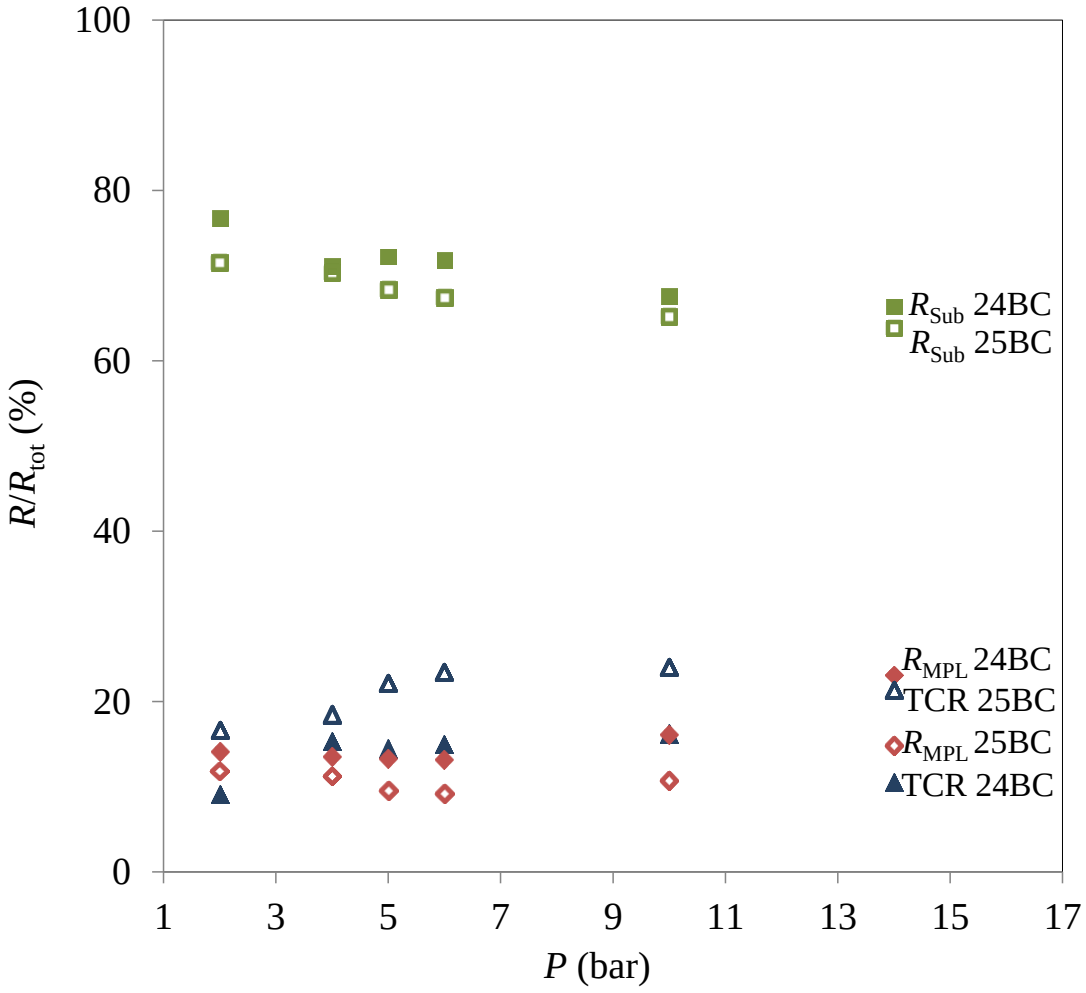

Figure 3.21. Interfacial resistances inside a GDL-MPL assembly (Eq. (3-14)): TCR here represents the contribution of the thermal contact resistance between MPL and the GDL substrate to the total resistance

3.7. Thermal resistances inside GDLs containing an MPL

Figure 3.21 presents the contribution of each resistance in Eq. (3-14) to the total resistance of the GDLs SGL 24BC and 25BC, and reveals that the thermal contact resistance between substrate and MPL is in fact comparable with the resistance of the

MPL itself. It should be noted that the thickness of substrate in SGL BC is several times (~7 times) higher than that of the MPL. Assuming the same thickness of the MPL and substrate, it could be argued that the thermal contact resistance between substrate and MPL, which is independent of the thickness of either component, can exceed either of the substrate and MPL resistances.

Figure 3.21 also shows that with increasing compression (up to 10 bar), the impact of MPL on contact resistance and on the GDL thermal conductivity becomes more pronounced, and in general, the contribution of MPL to the increased total resistance increases. Note that the contribution of MPL resistance to the GDL resistance is proportional to the ratio of the MPL thickness to that of the substrate. For GDL substrates with thermal conductivities sufficiently higher than that of the MPL, this ratio should be kept as low as possible in order to reduce the adverse influence of MPL on the bulk thermal conductivity of the GDL.

3.8. Effect of compression on the thermal resistances of GDLs

The thermal conductivity of all the GDLs increases with compression as shown in Figure 3.15, whereas their thermal contact resistance with the clamping surface decreases (Figure 3.18). These reductions in the bulk and contact resistances can be attributed to a better contact between fibers of two adjacent layers and between the GDL and the iron clamping surface (fluxmeters) under higher compression, respectively.

3.8.1. Variation of GDL thicknesses with compression

Carbon-based gas diffusion layers, typically made of 30-50 layers of carbon fibers attached to each other, are of thicknesses ranging from 150 to 500 µm. Because of the porous nature of the GDL and the elastic nature of the carbon fibers, the thickness of GDLs can change notably with compression. Figure 3.22 shows the variations in thickness with pressure increasing up to 15 bar.

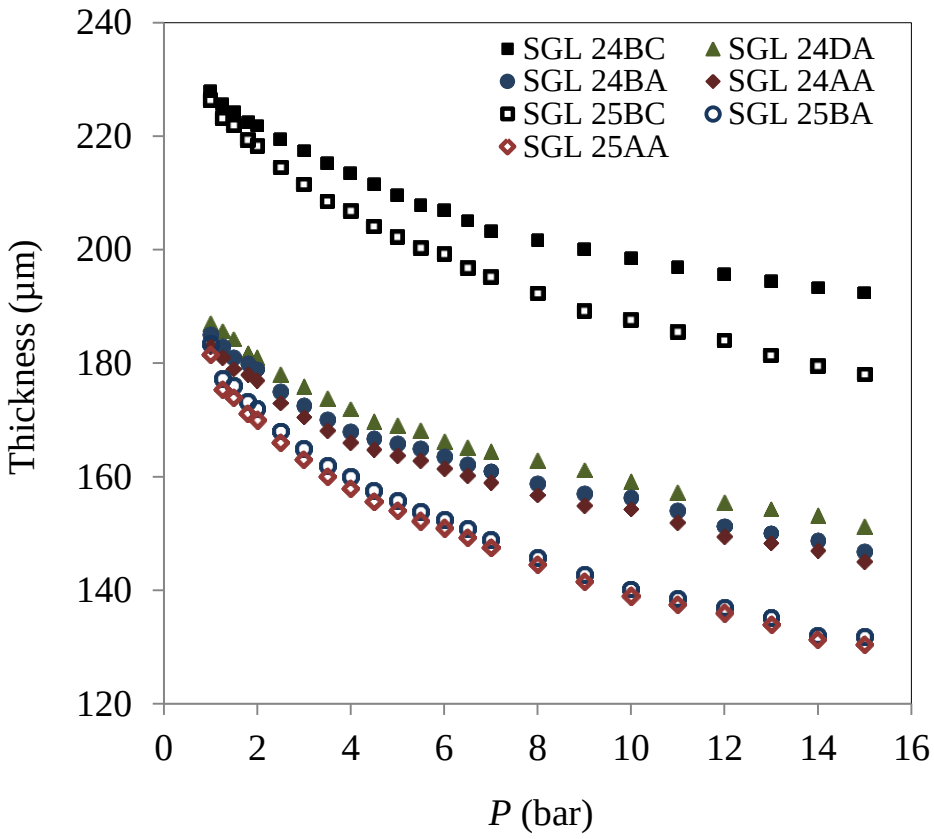

Figure 3.22. Variation of GDL thickness with compression (the thickness measurement uncertainty is ±10 µm)

The curves in Figure 3.22 for each GDL exhibit two parts, a non-linear part extending up to about 7 bar, where the reduction in thickness is steep, and a shallower linear part thereafter for pressure increases from 7 to 15 bar. These trends for the SGL GDLs are consistent with the results in Refs. [90] [113]. Unsworth et al. [119], on the other hand, reported a linear behavior for the entire range of compression for SolviCore GDLs with and without MPL.

The data of MPL thickness with compression, the solid data points shown in Figure 3.23, is based on the assumption that the MPL thickness decreases with compression at a rate equal to the ratio of the virgin MPL thickness to the virgin GDL substrate thickness (e.g., $t_{MPL}(P) = 45 - \frac{45}{235}(235 - t_{SGL\,BC}(P))$ for SGL 24BC). This assumption leads to the thickness-compression curves with trends similar to the MPL-coated GDLs (SGL BC types). Such trends can be considered to be reasonable as they are similar to the trends of GDLs with an MPL (SGL BCs). It should be noted that subtracting the thickness of GDLs SGL BA (GDL substrates) from GDLs SGL BC (MPL-coated GDLs) does not provide any reasonable values of the MPL thickness as shown in Figure 3.23 (hollow data points). As a result, the hollow data points as the variation of the MPL thickness with compression are not acceptable.

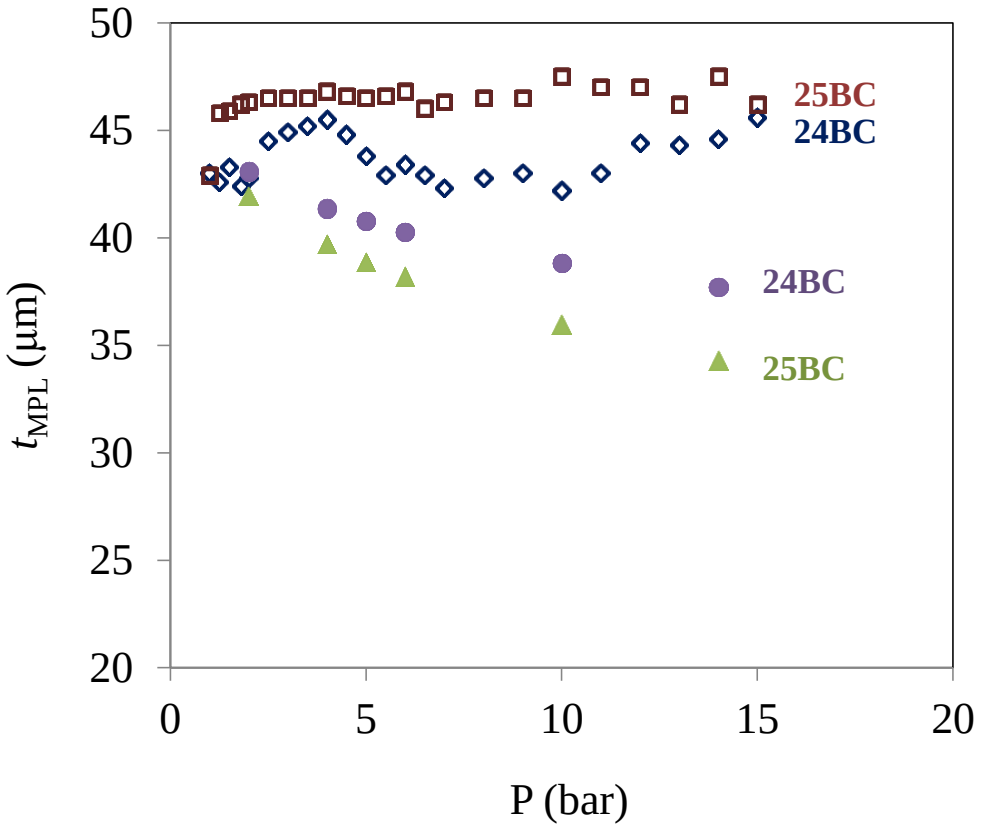

Figure 3.23. Variation of MPL thickness with compression (solid data points)

3.9. Effect of cyclic load on the total thermal resistance of GDLs

Fuel cell components may experience hundreds of thousands of load cycles during their lifetime [177] due to hygrothermal stresses induced by the swelling of the membrane under changing humidity level. The investigation of load cycling effects is important as they induce internal stresses and deformation and exacerbate a variety of chemical and mechanical degradation mechanisms. Figure 3.24 shows the effect of cyclic loading on the total resistance of SGL 34BC at the temperature of 60 ^{o}C and in the pressure range of 0.77-8.2 bar. As seen, the successive cycling loads practically reduce the total resistance, and this reduction continues until 8th loading cycle. However, the highest reduction,

almost 20%, occurs between the first and second loadings. With increasing the compression pressure, the effect of cyclic loading on the total resistance reduces. The more pronounced difference between loading and unloading of one cycle is evidently observed for the first cycle where a difference of as high as 30% can also be seen. From the 1st to the 8th loading, a resistance reduction of 30% can be observed at low pressures.

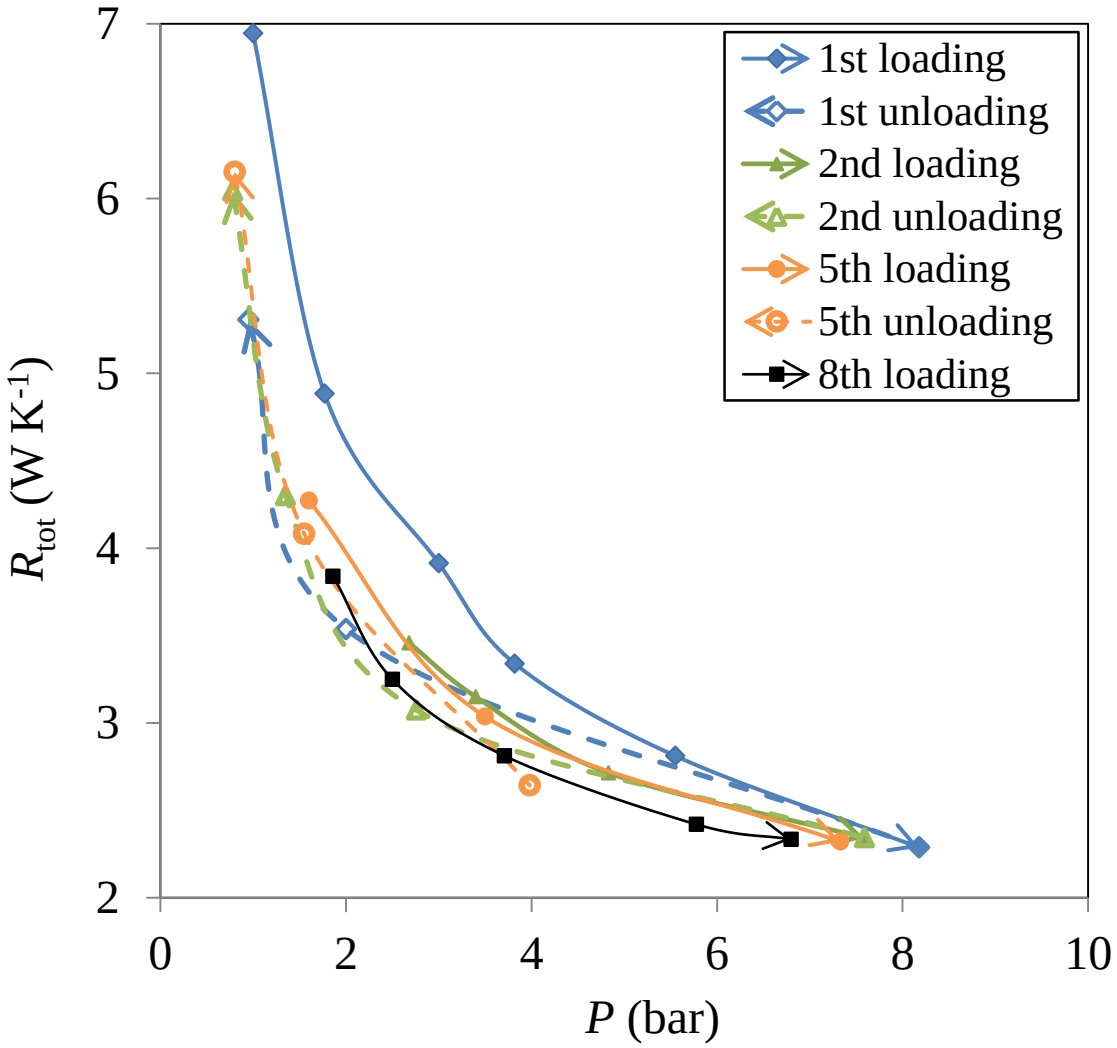

Figure 3.24. Effect of different successive cyclic loads on the total resistance of SGL 34BC at the temperature of 60 °C

3.10. Effect of hysteresis behavior on the total thermal resistance of GDLs

Heat management of PEMFCs is essential over the course of their operational lifetime. The numerous start-up and shut-down cycles of a PEMFC during its lifetime can cause discontinuous compressions and releases, which is different from the cyclic compression effects. In fact, discontinuous successive compressions and releases performed at different periods of time lead to hysteresis behavior of fuel cell components.

Figure 3.25 shows the hysteresis behavior of the already-tested sample of SGL 34BC for subsequent discontinuous cyclic compression tests conducted over four successive days. The data of the first and eighth loadings of sample 34BC, already shown on Figure 3.24, are also added to Figure 3.25 to facilitate comparison of the hysteresis behavior with the successive loading behavior and also with the behavior of a virgin sample. It is worthwhile noting that the sample resistances related to each of the four test days always lay within the resistances of the first and last (8th) compressive loadings already exerted on the sample. In fact, discontinuous compressive tests performed over four separate days on the already-tested sample have never been led to resistances as high as the total resistance of the virgin sample (1^{st} loading). It is evident from Figure 3.25 that there is a big difference between the first loading and the subsequent ones, which shows the noticeable irreversible behavior of compressed GDLs in terms of thermal resistance.

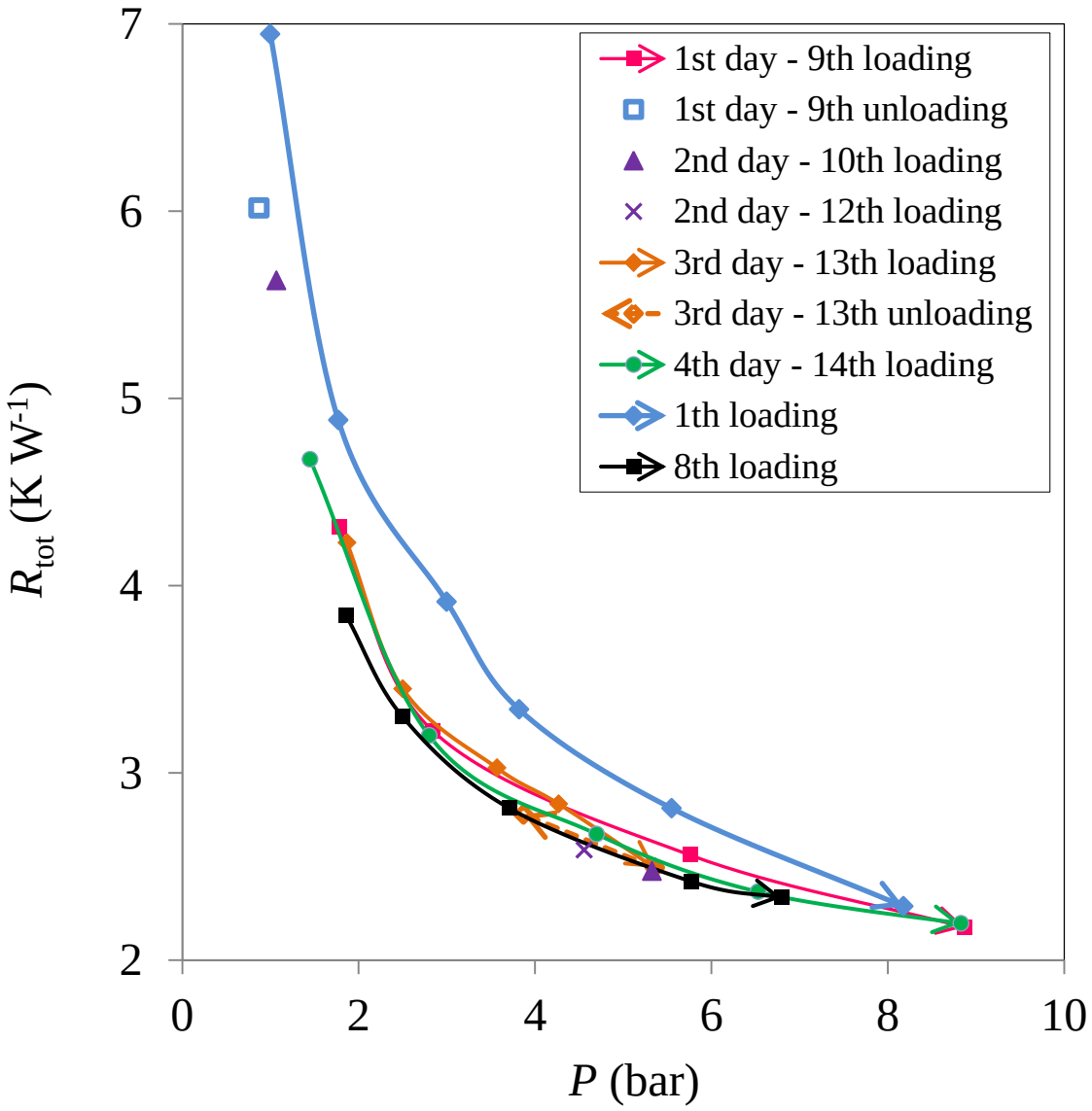

Figure 3.25. **Hysteresis behavior of subsequent discontinuous load cycles on the already-tested sample of SGL 34BC (related to Figure 3.24) over 4 successive days**

3.11. GDL-BPP assembly

3.11.1. Thermal contact resistance between BPP and GDL ($TCR_{GDL\text{-}BPP}$)

To measure the BPP-GDL TCR, the total thermal resistance of a GDL-BPP assembly should be obtained. As a result, in addition to testing the BPP and the GDLs, an assembly of the two has to be tested, as schematically shown in Figure 3.26. To determine the contact resistance between a BPP and a GDL, the thermal conductivity of the BPP needs to be known as well. Each test is repeated at least three times to ensure that the results are repeatable and reproducible.

To measure the thermal contact resistance between BPP and GDL, two GDLs with one BPP in between are sandwiched between the two fluxmeters of the TCR machine, as illustrated in Figure 3.26. The thermal resistance equation for this set of the GDL and BPP assembly is as follows:

$$2TCR_{\mathrm{GDL-BBP}} = R_{\mathrm{tot}} - (R_{\mathrm{BPP}} + 2R_{\mathrm{GDL}} + 2TCR_{\mathrm{GDL-FM}}) \qquad (3\text{-}15)$$

where R_{BPP}, the BPP thermal resistance, R_{GDL} and $TCR_{\mathrm{GDL-FM}}$, the thermal resistance (conductivity) of GDLs and their thermal contact resistances with the two fluxmeters, are all known as measured in this study. Hence, measuring the total resistance (R_{tot}) of the components shown in Figure 3.26, using the TCR machine, the contact resistance between the BPP and each GDL, $TCR_{\mathrm{GDL-BBP}}$, can be determined using Eq. (3-15).

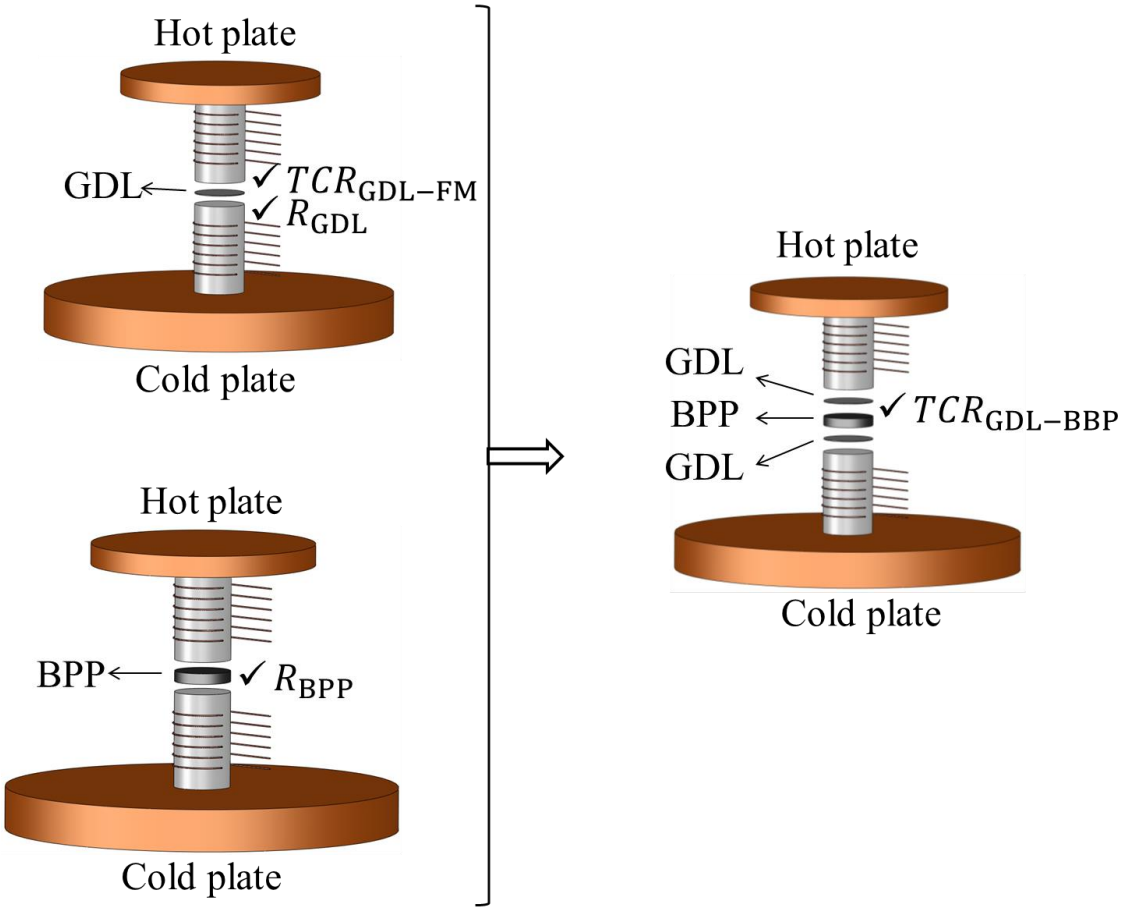

Figure 3.26. In addition to testing GDLs and BPP separately, assemblies of these two materials are to be tested by the TCR machine for measuring the GDL-BPP TCR (the cylindrical fluxmeters and the thermocouples placed inside them were not labeled)

3.11.2. Thermal contact resistance between BPP and MPL

Micro porous layer (MPL) has become an essential component of the MEA [175]. It has been recently asserted [122] that MPL on the BPP side of GDLs can also improve the overall performance of fuel cells. Therefore, measuring the contact resistance between the MPL and BPP can be useful for the purpose of PEMFC heat management.

Gas diffusion layers with an MPL on one side, such as BC type of SGL GDLs, have two different surfaces; the MPL and the substrate. The substrate is a BA-type SGL GDL, which has a carbon-based structure, called plain substrate, treated with 5% PTFE. In fact, SGL GDLs of BC type are fabricated by coating one MPL on the BA types. In order to measure the thermal contact resistance between MPL and BPP, the two GDLs are placed on both sides of the BPP, all sandwiched between the two fluxmeter, so that the MPLs always face up into the upper fluxmeter (the one contacting the hot plate). The resistance equation for such arrangement will thus be:

$$TCR_{\mathrm{MPL-BPP}} = R_{\mathrm{tot}_{\mathrm{SGL\_BC-BPP}}} - (R_{\mathrm{BPP}} + 2R_{\mathrm{SGL\_BC}} + TCR_{\mathrm{MPL-FM}} + TCR_{\mathrm{Sub5\%PTFE-FM}} + TCR_{\mathrm{Sub5\%PTFE-BBP}}) \quad (3\text{-}16)$$

where $TCR_{\mathrm{Sub5\%PTFE-FM}}$ and $TCR_{\mathrm{Sub5\%PTFE-BBP}}$ are the thermal contact resistance of the substrate BA with the (lower) fluxmeter and BPP, respectively. The values of R_{BPP}, $R_{\mathrm{SGL\_BC}}$ and "$TCR_{\mathrm{MPL-FM}}$+ $TCR_{\mathrm{Sub5\%PTFE-FM}}$" have already been measured. Hence, there are only two unknowns, $TCR_{\mathrm{MPL-BPP}}$ and $TCR_{\mathrm{Sub5\%PTFE-BBP}}$, in Eq. (3-16). The unknown $TCR_{\mathrm{Sub5\%PTFE-BBP}}$ can be obtained from the data of similar tests on sample SGL BA, using the following equation:

$$2TCR_{\mathrm{Sub5\%PTFE-BBP}} = R_{\mathrm{tot}_{\mathrm{SGL_{BA}-BPP}}} - (R_{\mathrm{BPP}} + 2R_{\mathrm{SGL_{BA}}} + 2TCR_{\mathrm{Sub5\%PTFE-FM}}) \quad (3\text{-}17)$$

where the thermal resistance of SGL BA (substrate with 5wt% PTFE), i.e., $R_{\mathrm{SGL\_BA}}$, and its contact resistances with fluxmeters, $2TCR_{\mathrm{Sub5\%PTFE-FM}}$, have already been measured. Plugging the value of $TCR_{\mathrm{Sub5\%PTFE-BBP}}$, obtained from Eq. (3-17), into Eq. (3-16) yields the target parameter of the thermal contact resistance between MPL and BPP, i.e., $TCR_{\mathrm{MPL-BBP}}$.

Knowing the thermal conductivity of the BPP and those of GDLs and the thermal contact resistance between GDLs and fluxmeters, the thermal contact resistance between the BPP and GDLs can be determined as explained earlier. The BPP-GDL TCRs presented in Figure 3.27 for different SGLs show that the TCR for all the GDLs decreases with compression. The interesting point to note here is that the reduction rate of $TCR_{\text{GDL-BPP}}$ with compression load decreases with increasing pressure, regardless of the GDL type. In fact, at lower compression, the $TCR_{\text{GDL-BPP}}$ is much more sensitive to compression for all the GDLs, and as the pressure increases, the dependency of $TCR_{\text{GDL-BPP}}$ on the pressure decreases.

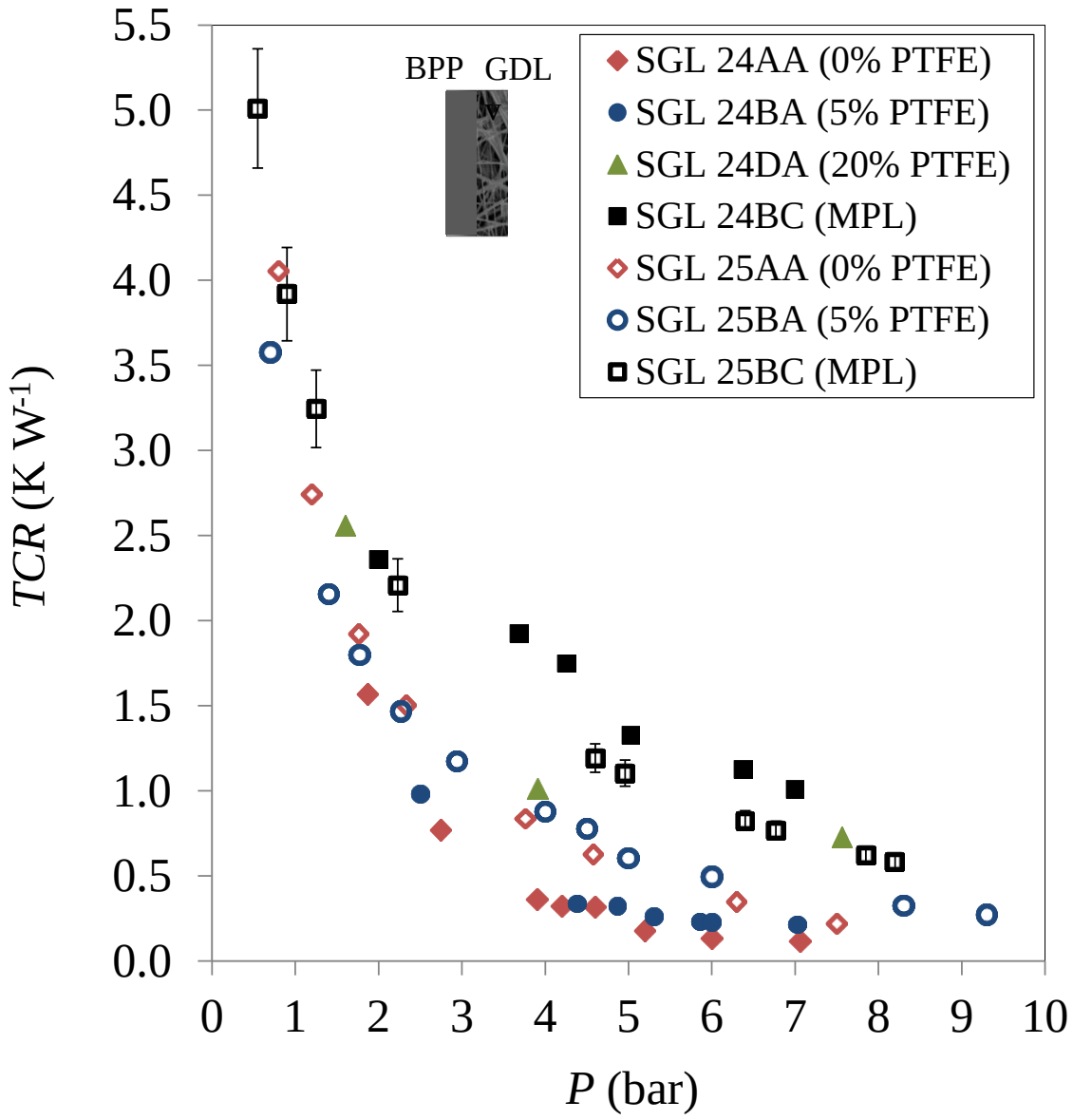

Figure 3.27. Experimental data of TCR between the graphite BPP and 14 different SGL GDLs ($TCR_{GDL\text{-}BPP}$) at an average temperature of 55 °C

3.11.3. Effect of PTFE loading and MPL on $TCR_{GDL\text{-}BPP}$

Figure 3.27 also indicates that for both series of the studied SGLs, i.e., 24 and 34, and 25 & 35, PTFE increases the $TCR_{GDL\text{-}BPP}$, which is similar to the increasing effect of PTFE on the TCR between GDLs and the fluxmeters, as discussed earlier. From Figure 3.27, it is also observed that the effect of 5% PTFE on the $TCR_{GDL\text{-}BPP}$ is minimal, whereas the addition of 20 wt% PTFE to the plain substrate increases the $TCR_{GDL\text{-}BPP}$ dramatically, especially at the higher pressures. For series 24 & 34 of SGLs, the effect of 20 wt% PTFE on the $TCR_{GDL\text{-}BPP}$ is comparable to that of MPL, which has the highest impact on the $TCR_{GDL\text{-}BPP}$ in comparison to the other GDLs of series 24.

It is also interesting to note that the effect of MPL on the BPP-GDL TCR is the same for both series. The MPL markedly increases the TCR, especially in comparison to GDLs treated with low PTFE loadings. In addition, the BBP-MPL TCR for both series of the studied GDLs are very close to each other because the MPLs employed for both series are practically the same [173]. It is also observed that at low compression, there is no appreciable difference between the TCRs of BPP with different GDLs. In other words, the dependency of the TCR on PTFE loadings and MPL increases with compressive load for most of the GDLs.

The contribution of $TCR_{BPP\text{-}GDL}$ to the GDL-BPP total resistance has been shown on Figure 3.28 for different GDLs, to further investigate the importance of $TCR_{BPP\text{-}GDL}$ with regard to the bulk resistances of GDL and BPP. Figure 3.28 shows that the $TCR_{BPP\text{-}GDL}$, a parameter that has been usually overlooked in fuel cell thermal analysis, is indeed a large resistance comparable to the GDL and BPP resistances, especially for the GDLs treated with high PTFE loadings and MPL. For instance, the TCR between BPP and SGL 24DA is approximately 40% of the total resistance at the compression of 4 bar, which makes it the dominant resistance, as the bulk resistance of GDL and BBP contribute, respectively, 35 and 25 % to the total resistance.

Figure 3.28 also indicates that $TCR_{\text{BPP-GDL}}$ for SGL 25 is, to some extent, larger than that for SGL 24. The reason for this is most likely related to the higher porosity and the lower aspect ratio SGL 25 has, as these are the only difference between the two series 24 and 25, see Ref. [52].

It is also worthwhile noting that the contribution of $TCR_{\text{BPP-GDL}}$, which increases dramatically with decreasing the load, reaches approximately 60% and 40% of the total resistance for most of GDLs at the compression of 1 and 5 bar, respectively. The fact that $TCR_{\text{BPP-GDL}}$ is usually the dominant resistance in GDL-BPP thermal resistance network is an important finding that underscores the need to fully count rather than neglect thermal resistance compared to the bulk resistance of BPP and GDL in fuel cell thermal management and modeling.

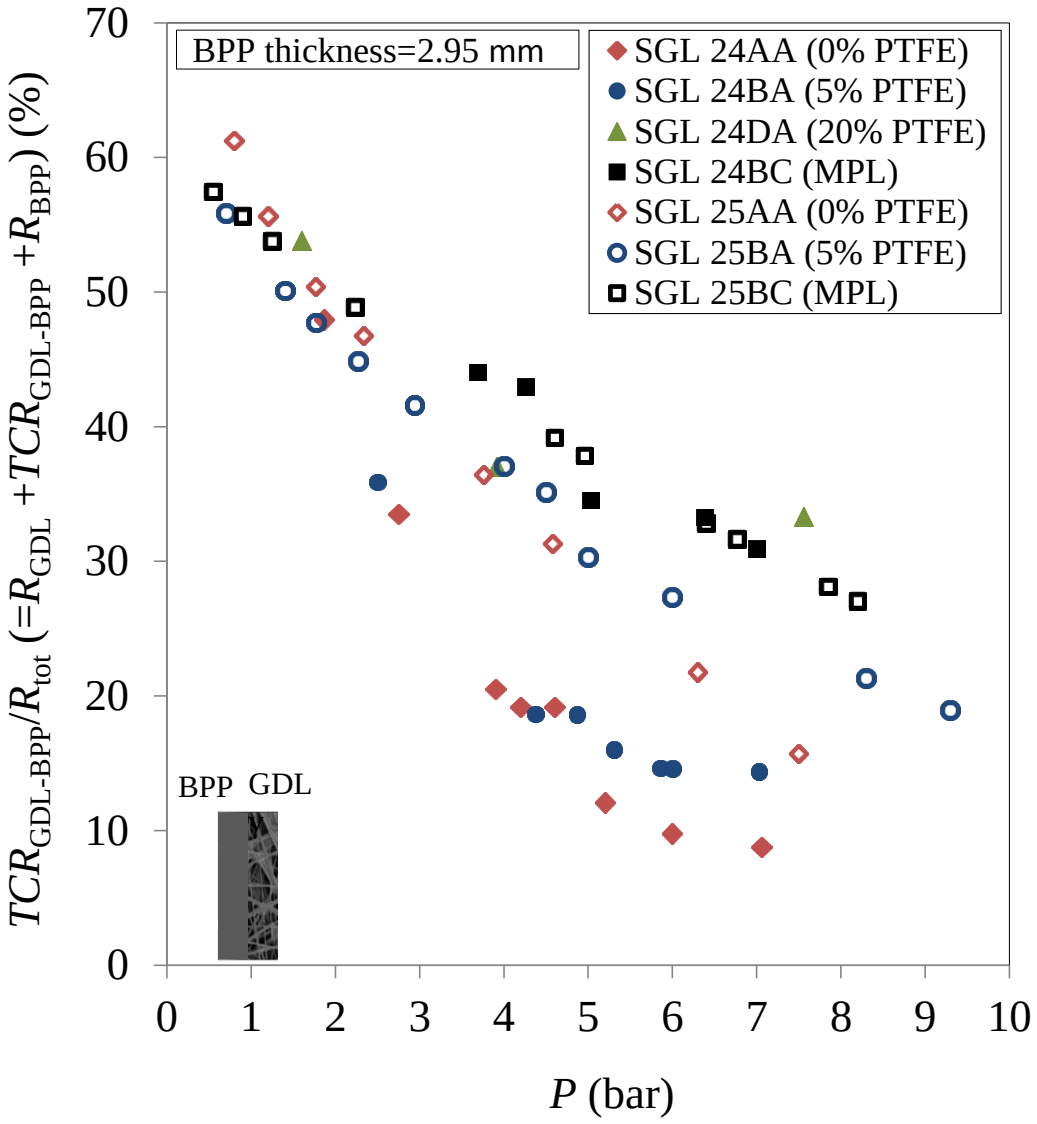

Figure 3.28. Contribution of the TCR between the graphite BPP and different SGL GDLs into the total resistance of the studied BPP-GDL assemblies at an average temperature of 55 °C

3.11.4. Effect of BPP out-of-flatness on $TCR_{GDL\text{-}BPP}$

The remarkable impact of BPP out-of-flatness on the $TCR_{BPP\text{-}GDL}$ can be observed in Figure 3.29 where a comparison between the TCR of different SGLs 24 with two BPP plates with different out-of-flatness can be made. Figure 3.29 shows that the TCR of the GDLs with bumpy BPP 4.94 is much higher than that with more flat BPP 5.84. It should be noted that according to Table 3.4, BPP 4.94 is not excessively wavy and its out-of-flatness would be considered low from the viewpoint of contact mechanics [178] [179]. Nevertheless, even such low out-of-flatness can lead to large $TCR_{BPP\text{-}GDL}$, according to Figure 3.28. Overall, the out-of-flatness of BPP 4.94 increased the $TCR_{BPP\text{-}GDL}$ by a factor of 3, on average.

The results in Figure 3.29 indicate that the BPP out-of-flatness can exacerbate the influence of PTFE and MPL on the TCR, as the gap between the TCR of the untreated SGL 24 (24AA) and the treated ones with BPP 4.94 are larger than the corresponding values for more flat BPP 5.84.

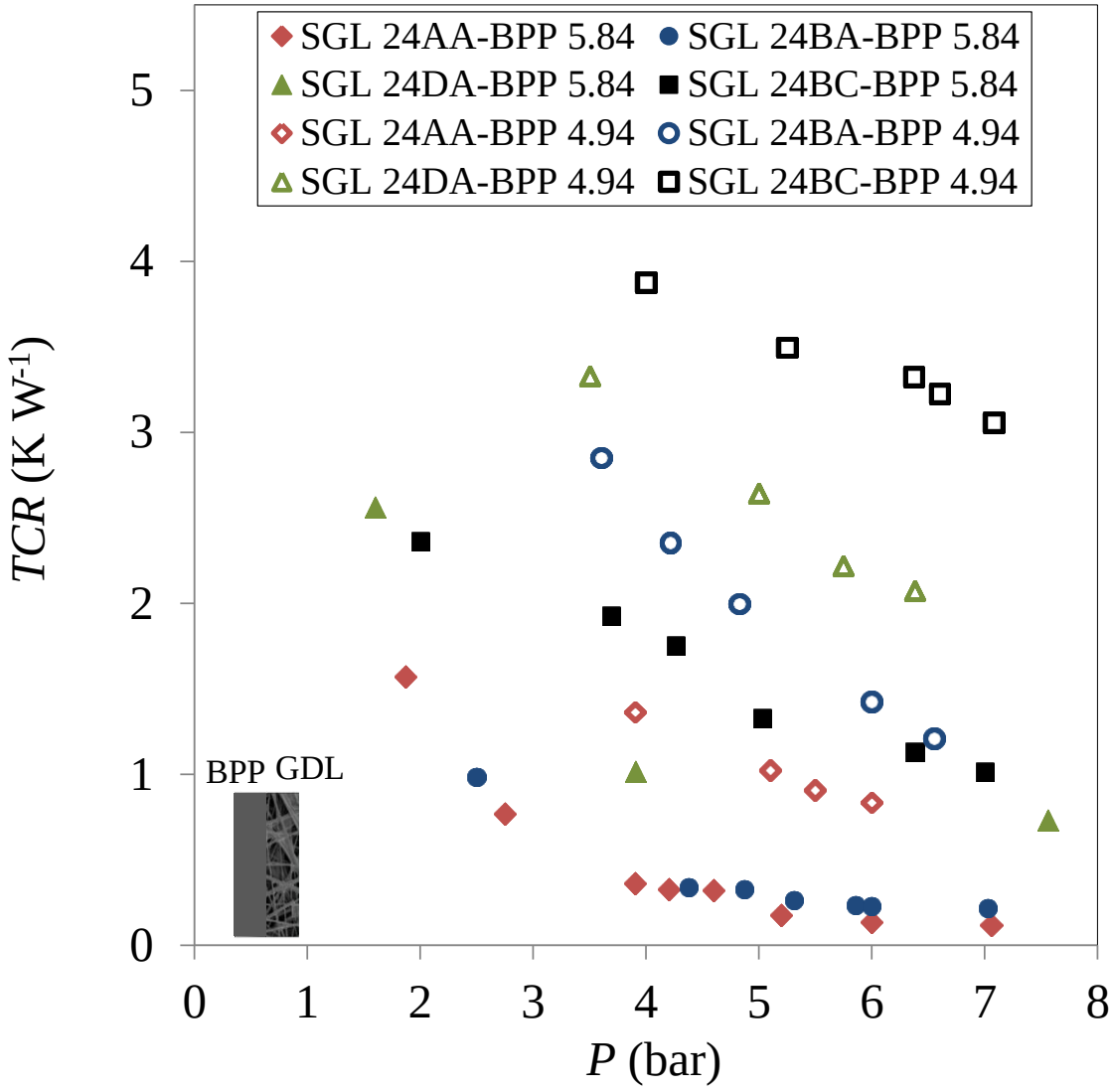

Figure 3.29. **Effect of the BPP out-of-flatness on $TCR_{BPP\text{-}GDL}$ (for comparison, the data of SGL 24 already shown in Figure 3.27 has been duplicated in this figure).**

3.11.5. Effect of cyclic load on BPP-GDL assembly total resistance

The effect of cyclic load on the total resistance of two SGL 24BA, as well as separately on two SGL 24DA, with BPP 5.84 in between, all sandwiched between the two fluxmeters of the TCR machine, are presented in Figure 3.30 and Figure 3.31, respectively. As seen in both Figure 3.30 and Figure 3.31, overall, the load cycles, especially the initial ones, reduce the total resistance. This reduction is more pronounced for SGL 24BA, due to having lower PTFE loading (5%) in comparison to SGL 24DA, which has treated with 20% PTFE.

It is also evident from Figure 3.30 and Figure 3.31 that at high compression, the data of different loadings tend to overlap, which completely conforms with the trend obtained for the cases of one GDL sandwiched between the same two fluxmeters of the TCR machine. No noticeable difference between the 3rd loading and unloading has been observed for SGL 24BA whereas the gap between the successive loadings and unloadings for SGL 24DA is considerable, especially for the initial cycles, as evident in Figure 3.31. Overall, knowledge of the thermal resistance behavior of GDL-BPP assembly under different load cycles, as reported here, can inform the analysis of the temperature field within operating PEMFCs and the design of appropriate heat and water management during their lifetime.

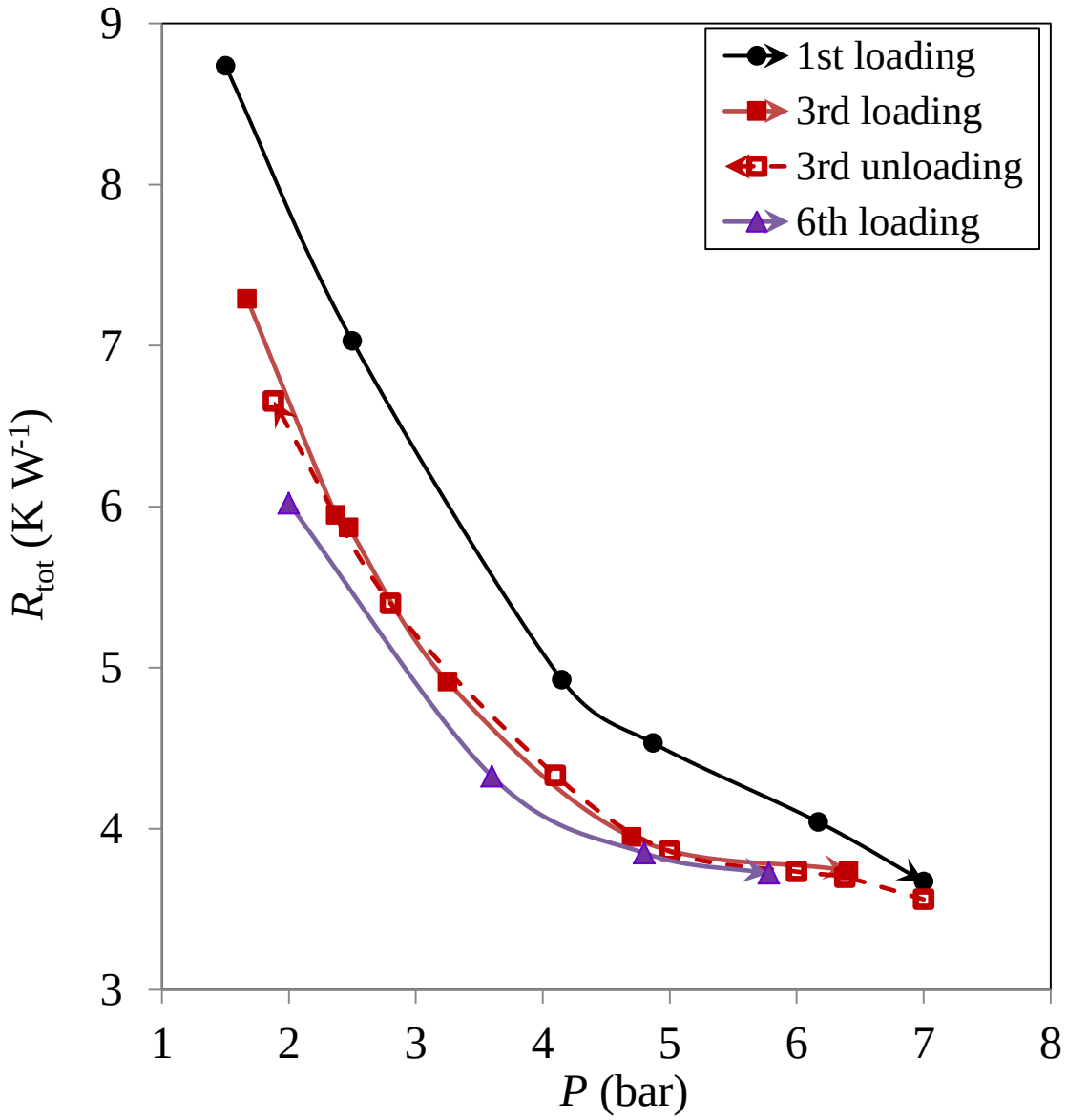

Figure 3.30. Effect of load cycles on the total resistance of SGL 24BA-BPP 5.84 assembly (including the contact resistance of the GDL with the two fluxmeters)

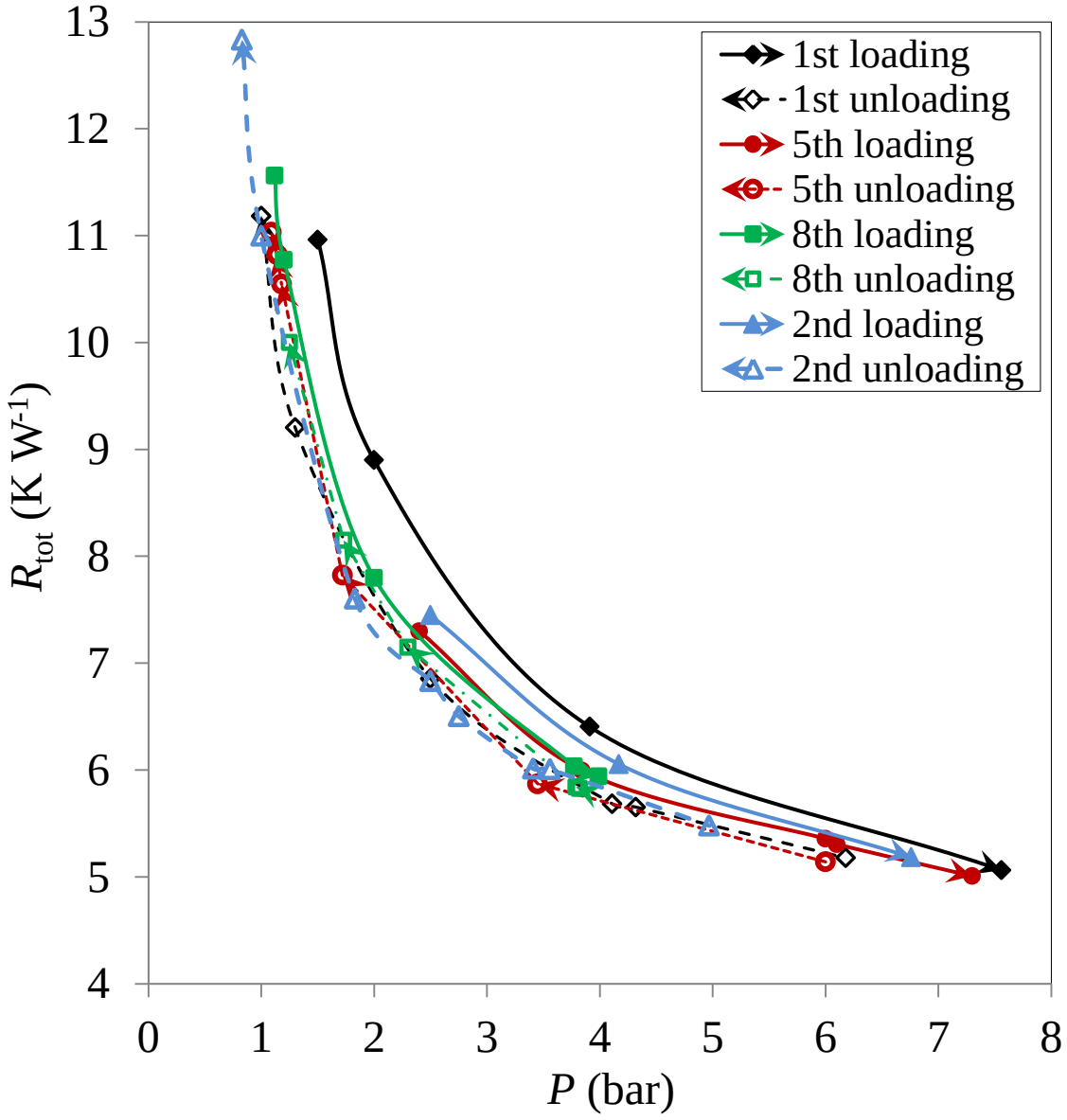

Figure 3.31. Effect of load cycles on the total resistance of SGL 24DA-BPP 5.84 assembly (including the contact resistance of the GDL with the two fluxmeters)

3.12. Concluding remarks

Thermal conductivity of 14 SGL GDLs and its thermal contact resistance with Armco-iron clamping surfaces were measured at the temperature of approximately 60°C at a compression range of 2-14 bar. The carefully conducted measurements, using an equipped device and including accurate deconvolution between bulk and contact resistance, helped resolve some contradictory observation reported in the literature and provided new insights into thermal behavior of GDLs. It is observed that

- Both PTFE and MPL reduce thermal conductivity (even though porosity decreases).
- Both PTFE and MPL increase the contact resistance of GDLs with the iron surfaces.
- MPL increases the contact resistance dramatically compared to untreated GDLs or GDLs with low PTFE content.
- Thermal conductivity of MPL and its contact resistance with iron surface were accurately measured.

In addition to determining the thermal conductivity of GDLs coated with MPL, the experimental procedure presented allowed estimation of the thermal contact resistance between the MPL and the GDL. The results show that this contact resistance is not negligible, and together with the MPL bulk resistance, accounts for roughly half of the GDL total resistance.

Thermal conductivity of a graphite BPP was also measured under different temperatures and pressures, with the following key results:

- Thermal conductivity of the graphite BPP and its thermal contact resistance with the clamping surface (Armco-iron fluxmeters) decrease with increasing temperature.
- The variation of the BPP thermal conductivity as a function of temperature can be conveniently represented in a compact form suitable for thermal analysis and modeling.

The TCR between the BPP and GDLs with different PTFE loadings and/or MPL were also measured in terms of compression. The effect of compression, PTFE, MPL, out-of-flatness, and cyclic loads on the BPP-GDL TCR were investigated thoroughly:

- The TCR between BPP and GDL increases with both MPL and PTFE, irrespective of the PTFE loading.
- High PTFE loading, MPL, and the BPP out-of-flatness increase the GDL-BPP TCR dramatically.
- The BPP-GDL TCR can be the *dominant* resistance in GDL-BPP assembly, as its contribution can increase to almost 60% and 40% at the compression of 1 and 5 bar, respectively.
- Load cycling reduces the total thermal resistance of BPP-GDL assembly considerably.
- The reduction effect of load cycling on the thermal resistance of BPP-GDL assembly is more pronounced for GDLs with lower PTFE loading.

Chapter 4.

Modeling of thermal conductivity of untreated and PTFE-treated gas diffusion layers

4.1. Model assumptions and unit cell approach

The temperature field and heat transfer rates in a fibrous porous media depend on a variety of factors including geometry, type of material, mechanical and thermal properties, and operating conditions. The structure and thermal conductivity of GDLs is anisotropic, and thus representative geometrical modelling will be important. The focus in this chapter is on modeling of the through-plane thermal conductivity, though the presented concept can be adapted for the estimation of other transport properties such as in-plane thermal conductivity and permeability. In general the present model is an extension of the previous work of Bahrami and Djilali (model of Sadeghi et. al. [57]), which relies on a unit cell approach to represent the GDL as a periodic fibrous micro structure, and assumes:

(1) 3-D repeating basic cell

(2) Steady state one-dimensional heat transfer

(3) Negligible natural convection within basic (unit) cell

(4) No radiation heat transfer between neighboring fibres

The additional features introduced here to make the model more general and improve the physical representation of GDL structure are:

(5) Statistical distribution of the angles between fibers in two adjacent layers: i.e. the average value of the angles and their deviations from the average value
(6) Characteristic fibre spacing for various GDL types
(7) Addition of PTFE to the GDL

Our aim is to present a statistical unit cell approach by modifying Sadeghi et al.'s model from the geometrical modelling point of view, which will extend its applicability to a broader range of GDL types, and to use the new model to investigate the effects of geometrical parameters and PTFE on the thermal conductivity. Detailed development of Sadeghi et al.'s model can be found in Ref. [57] and the focus here will be on improvements to that model, more specifically: (i) the determination of the GDL geometrical properties (parameters); (ii) the statistical implementation of these parameters into the unit cell model; and (iii) considering the addition of PTFE to the GDL.

This work builds on the unit cell approach of Bahrami et al. [180] (see also [181] [182] [183] [180] [184] [185]) that was successfully applied to several heat transfer applications, such as packed beds, and of Sadeghi et. al. [57] who presented the first analytical model that takes the main geometrical parameters into account in modelling GDLs. Here we will be introducing new techniques for determining the geometrical parameters of different GDLs and applying the determined parameters to a statistical unit cell approach for the estimation of thermal conductivity. Thermal conductivity of PTFE-treated GDLs will also be modeled by considering the addition of PTFE to the unit cell.

4.1.1. Unit cell for the model

A unit cell is the smallest part of a body that can reproduce the three-dimensional structure of that body. In general, unit cell models are based on one unit (basic) cell repeated through the entire medium. In the case of a fibrous porous material consisting of

layers of fibers, such as most "paper" types of GDL, a simple, still comprehensive, geometrical model like the one shown in Figure 4.1 has the capability to capture the essential features. In this figure, l and w are the distance between fibers in the x and y directions, d the fiber diameter, and θ the angle between fibers in two adjacent layers. The porosity (ε) of the unit cell is a function of all these geometrical parameters, as given in Ref. [57]:

$$\varepsilon = 1 - \frac{\pi d}{8}\left(\frac{l + \frac{w}{\cos(\theta)}}{lw}\right) \tag{4-1}$$

In principle, the unit cell model consists of mechanical and thermal models [57] applied to the defined unit cell. Ultimately, using Fourier's law of heat conduction and the concept of a total thermal resistance network, the effective thermal conductivity can be obtained (k_{eff}) as a function of the geometrical parameters, i.e., $k_{\text{eff}} = f(\varepsilon, \theta, d, l, w)$. The thermal resistance network for the unit cell consisting of the top and bottom blocks is represented in Figure 4.2. The unit-cell thermal model is identical to that of Sadeghi et al [57] and the equations of the model are summarized in Table 4.1.

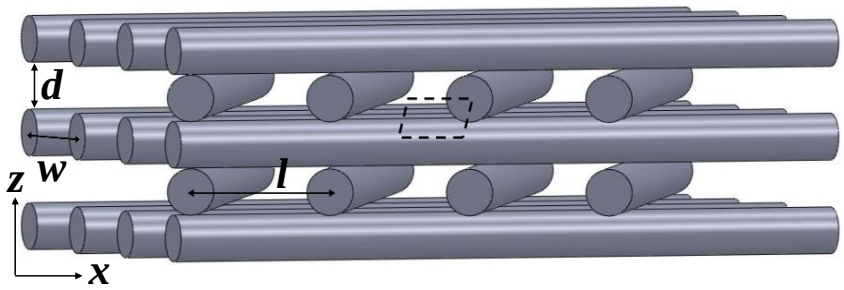

(a)

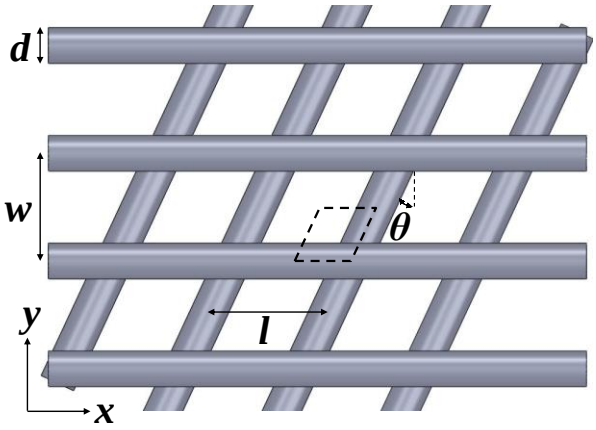

(b)

Figure 4.1. Front isometric view (a) and top view (b) of the geometrical model of GDL (the dashed parallelograms represent the unit cell)

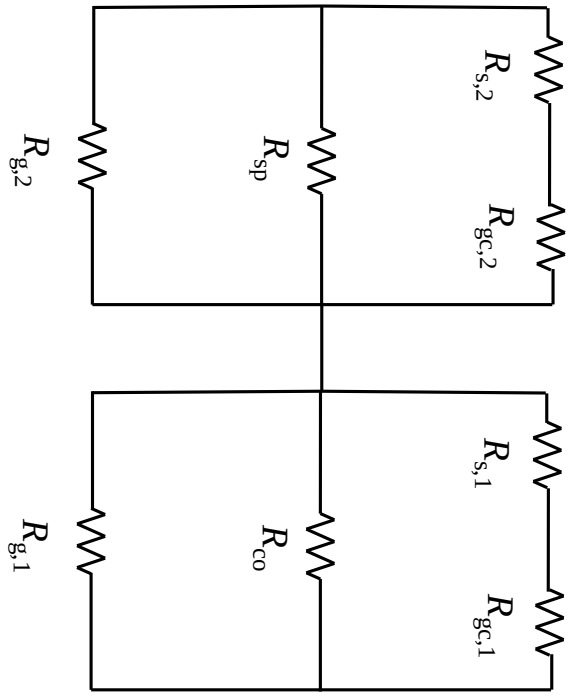

Figure 4.2. Thermal resistance network for the top and bottom blocks of the unit cell shown in Figure 4.1 [57]

Table 4.1. Equations of the unit cell model [57]

Parameter	Equation	Number
Minor relative radius of contact curvature	$\rho'' = \frac{d}{\sqrt{2(1-\cos(2\theta)+2}}$	(4-2)
Major relative radius of contact curvature	$\rho' = \frac{1}{(4/d-1/\rho'')}$	(4-3)
Integral function of $(\rho'\rho''^{-1})$	$F_1 = \frac{19.1\sqrt{\lambda}}{1+16.76\sqrt{\lambda}+1.34\lambda}$, $\lambda = \rho'/\rho''$	(4-4) (4-5)
Maximum force on each contact point	$F_{max} = \frac{P_{GDL} lw}{4}$	(4-6)
Effective elastic modulus	$E' = (\frac{1-\upsilon_1^2}{E_1} + \frac{1-\upsilon_2^2}{E_2})^{-1}$	(4-7)
Major semi axis of elliptical contact	$a = b\,(\frac{\rho'}{\rho''})^{2/3}$	(4-8)
Minor semi axis of elliptical contact	$b = (\frac{\rho''}{\rho'}\frac{3F\sqrt{\rho'\rho''}}{4E'})^{1/3}\,F_1$	(4-9)
Solid thermal accommodation parameter	$\alpha_s = \exp\left[-0.57\left(\frac{T_s-273}{273}\right)\right](\frac{1.4M_g}{6.8+1.4M_g}) + \frac{2.4\left(\frac{M_g}{M_s}\right)}{\left(1+\frac{M_g}{M_s}\right)^2} \times \left\{1 - \exp\left[-0.57\left(\frac{T_s-273}{273}\right)\right]\right\}$	(4-10)
Thermal accommodation parameter	$\alpha = \left(\frac{2-\alpha_s}{\alpha_s}\right) + 1$	(4-11)
Fluid property parameter	$\beta = \frac{2\gamma}{Pr(\gamma+1)}$	(4-12)
Mean free path of gas molecules	$\Lambda = \Lambda_{g,\infty}(\frac{T_g}{T_{g,\infty}})(\frac{P_{g,\infty}}{P_g})$	(4-13)
Gas thermal resistance of bottom block	$\frac{1}{R_{g,1}} = k_g(\frac{l(w-\frac{d}{2})}{2(\frac{d}{2}+\alpha\beta\gamma)})$	(4-14)
Gas filled gap thermal resistance of bottom block	$\frac{1}{R_{gc,1}} = k_g\left(\frac{l}{2}\right)(\frac{2\alpha\beta\gamma}{\sqrt{(\alpha\beta\gamma)^2-1}}\ tan^{-1}(\sqrt{\frac{\alpha\beta\gamma+1}{\alpha\beta\gamma-1}}))$	(4-15)
Gas thermal resistance of top block	$\frac{1}{R_{g,2}} = k_g(\frac{w}{2})\frac{(\frac{l}{2}-\frac{d/2}{\cos(\theta)})}{d/2+\alpha\beta\gamma}$	(4-16)

Gas filled gap thermal resistance of top block	$\frac{1}{R_{gc,2}} = \frac{k_g\left(\frac{w}{2}\right)}{\cos(\theta)}\left(\frac{2\alpha\beta\gamma}{\sqrt{(\alpha\beta\gamma)^2-1}}\ tan^{-1}\left(\sqrt{\frac{\alpha\beta\gamma+1}{\alpha\beta\gamma-1}}\right)\right)$	(4-17)
Spreading/constriction resistance & modulus of elliptic integral	R_{sp} or $R_{co} = \frac{1}{2\pi ka}\int_0^{\frac{\pi}{2}} \frac{dt}{\sqrt{1-\eta^2 sin^2 t}}$, $\eta = \frac{1}{\sqrt{1-(b/a)^2}}$	(4-18) & (4-19)
Total thermal Resistance	$R_{tot} = \left[\frac{1}{R_{g,1}} + \frac{1}{R_{gc,1}} + \frac{1}{R_{co}}\right]^{-1} + \left[\frac{1}{R_{g,2}} + \frac{1}{R_{gc,2}} + \frac{1}{R_{sp}}\right]^{-1}$	(4-20)
Effective thermal conductivity	$k_{\text{eff}} = \frac{4d}{lwR_{tot}}$	(4-21)

4.2. Determination of geometrical parameters

Fibrous porous media such as GDLs can have different structure and geometry in terms of angle distribution, aspect ratio, and fiber diameter. These parameters can generally vary independently of porosity, and it is *a-priori* necessary to take them into account in geometrical modelling targeted at transport property estimation. In order to do so, we need to have a detailed description of the relevant micro structural parameters for each type of GDL. Such data can be measured optically by a microscope or by other methods, as discussed in the following sub-sections.

4.2.1. Fiber angle distribution

In the model of Ref. [57], the angles between fibers are assumed to be equal, typically with a set at the mean value of zero. In turn, a distribution of angles exists, as can be readily seen in GDL images. Individual angles can be measured optically, as shown in Figure 4.3, and a probability distribution can be obtained using statistical methods as described below.

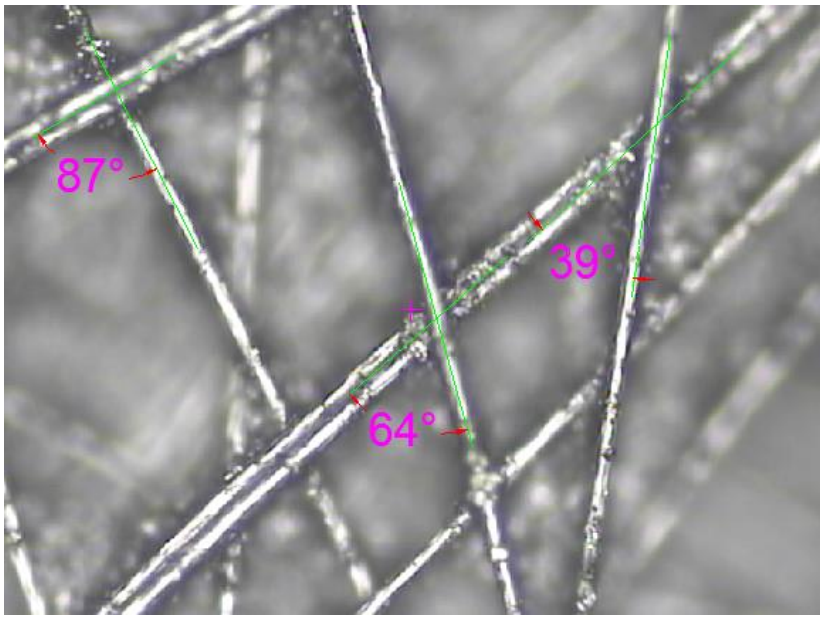

Figure 4.3. Angles between fibers measured optically for Sigracet and Toray GDLs

In this study, the angle distribution for two commonly used GDLs, Toray (TGP-H- 060) and Sigracet (SGL 25AA), have been optically measured and the corresponding distributions are shown in Figure 4.4 and Figure 4.5. The peak probability occurs close to 0° (θ=0; orthogonal arrangement) and the probability of angles larger than θ =70° is low,

especially for the SGL GDL. In fact, in the SGL GDLs, the bell curve is more pronounced with higher probabilities of angles close to the orthogonal arrangement.

The statistical distributions were calculated using the statistical software Easyfit [186], and can be approximated by a Gaussian (Normal) distribution in a –π/2-π/2 scale and/or a Beta distribution in a 0-π/2 scale for the Toray GDL (Figure 4.4). A similar but not identical trend can be seen for the SGL GDL (Figure 4.5). Note that, in general, the angles between two fibers in two neighbouring layers can take any value from 0 to 90°, yet Figure 4.4 and Figure 4.5 is plotted using a –π/2-π/2 scale by considering the supplementary angles, hence resulting in a pseudo Normal distribution. In the thermal model calculations, the Beta distribution (0-π/2 scale) is the appropriate one to use.

Having measured the angles, the main question that remains is how to apply such a large number of data to the model. Based on the work carried out by Bahrami *et. al.* [187] on the pressure drop of rough micro-tubes, an analogous correction factor or deviation from the average angles is introduced. The average value ($\bar{\theta}$) and the statistical distribution of the deviations from the average value ($p=\theta-\bar{\theta}$) can be obtained from the measured distribution. For any quantity of interest, in this case the effective thermal conductivity, a correction factor corresponding to the deviation of that quantity from its average value can be calculated using:

$$M^* = \frac{M_{cor}}{M_{ref}} = \frac{\int_a^b M(\bar{\theta}+p)F(p)dp}{M(\bar{\theta})} \qquad (4\text{-}22)$$

where M is an quantity of interest, M_{ref} and M_{cor} are respectively the reference and corrected (overall) values of M, and $F(p)$ is the statistical distribution of variable p ($a \leq p \leq b$), obtained from the measured angles.

The corrected (overall) values of each quantity (M_{cor}) can also be calculated in a simpler way by

$$M_{cor} = \sum_{i=1}^{N} M(\theta_i)P(\theta_i) \tag{4-23}$$

where $P(\theta_i)$ represents the occurence probability of an angle with the value of θ_i, and N is the number of the measured angles. $P(\theta_i)$ acts as a weighting factor for $M(\theta_i)$, the value of property M corresponding to the angle θ_i.

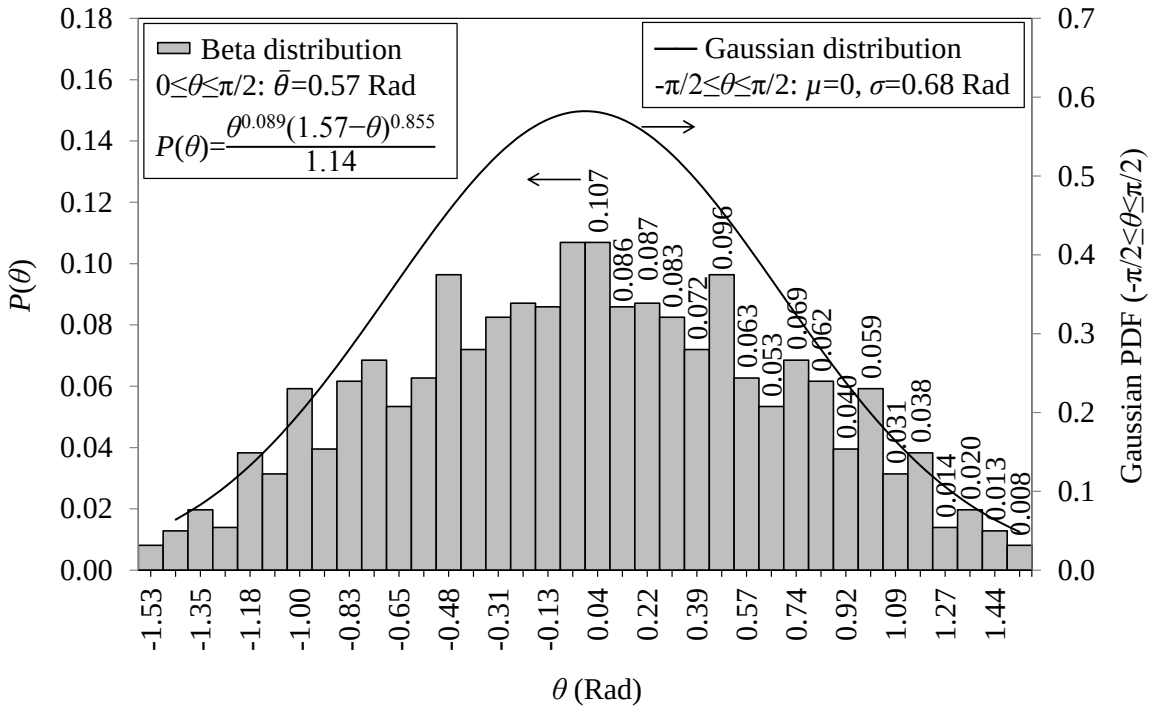

Figure 4.4. Angle distribution of Toray (TGP-060)

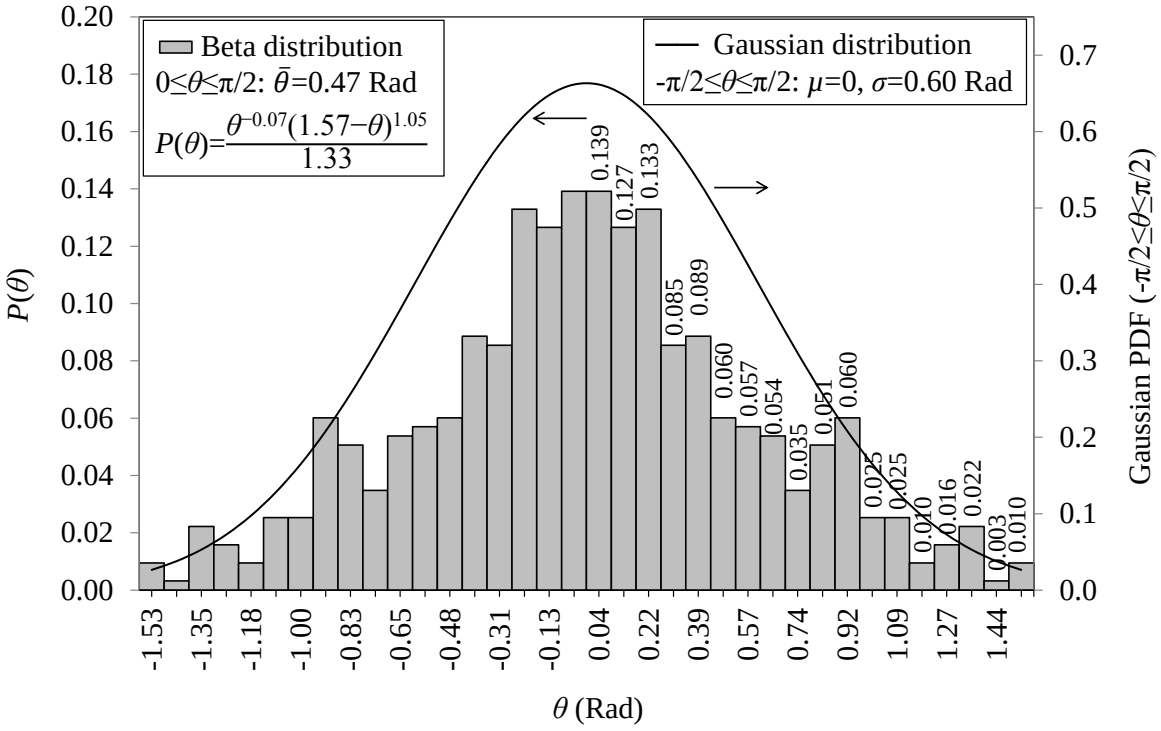

Figure 4.5. Angle distribution of SGL (25AA)

4.2.2. Aspect Ratio (*AR=l/w*)

The distance between fibers, which defines the aspect ratio, affects the heat transfer paths as well as the number of contact points between adjacent layers of fibers in a fibrous medium, and is therefore expected to have a noticeable effect on thermal conductivity. However, to the authors' best knowledge, this important parameter has been overlooked in existing heat transfer analyses on fibrous porous media. All the previous work based on the unit cell approach for the calculation of either thermal conductivity [57] or permeability [188] [189], considered unity aspect ratio (equal distance between fibers in the *x* and *y* directions, see Figure 4.6). Here, for the first time, two techniques are presented for determining the aspect ratio in GDLs. The first is, in principle, similar to the method used for measuring the fiber angles, i.e., optical measurements. The other is

based on the average pore diameter of each GDL obtained by Mercury Intrusion Porosimetry (MIP) measurements. For a given porosity, *l* and *w* are related through the porosity equation (4-1). The common approach in both techniques is to find a second relationship between *l* and *w* and then, solve it simultaneously with Eq. (4-1), to obtain the values of *l* and *w* and, subsequently, their ratio (*AR=l/w*).

- Optical measurement of aspect ratio

A sufficient number of areas enclosed between different fibers in two neighboring layers (see Figure 4.6) can be measured optically, and their average ($A_{ave,m} = \sum_{i=1}^{N_A} A_i \, / N_A$) can be considered equal to the gap area between the fibers in two neighboring layers:

$$A_{ave,m} = (l - d)(w - d) \qquad (4\text{-}24)$$

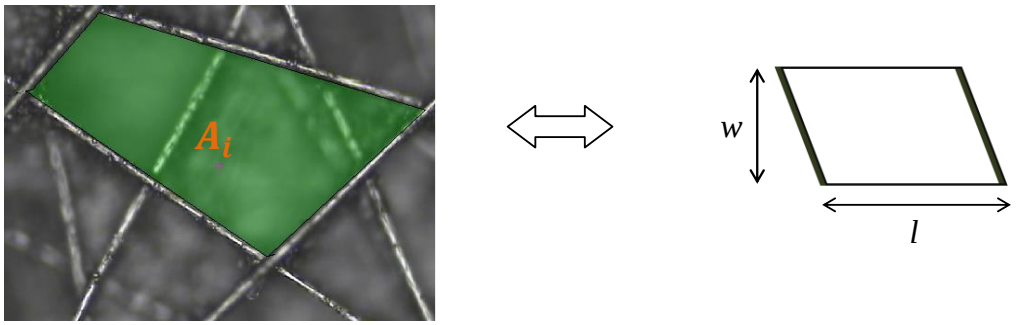

Figure 4.6. Measurement of the gap area between fibers as optical measurement of aspect ratio

From the measured data of A_i, a statistical distribution of aspect ratio and, in turn, of l and w can also be obtained for each GDL. Figure 4.7, Figure 4.8 and Figure 4.9 illustrate the statistical distribution of the aspect ratio for GDLs Toray TGP-060, SGL 24AA, and SGL 25AA, respectively. Similarly to estimating the overall value of quantity M from the angle distribution, i.e., Eq. (4-23), the following equation can be employed for the aspect ratio distribution:

$$M_{cor} = \sum_{k=1}^{N_A} M(AR_i)P(AR_i) \tag{4-25}$$

where $P(AR_i)$ represents the occurrence probability of an aspect ratio with the value of AR_i , and N_A is the number of the measured aspect ratios and, in turn, the number of A_i. In any case, the final value of M_{cor} will generally be an average of the two values of M_{cor} obtained from Eqs. (4-23) and (4-25).

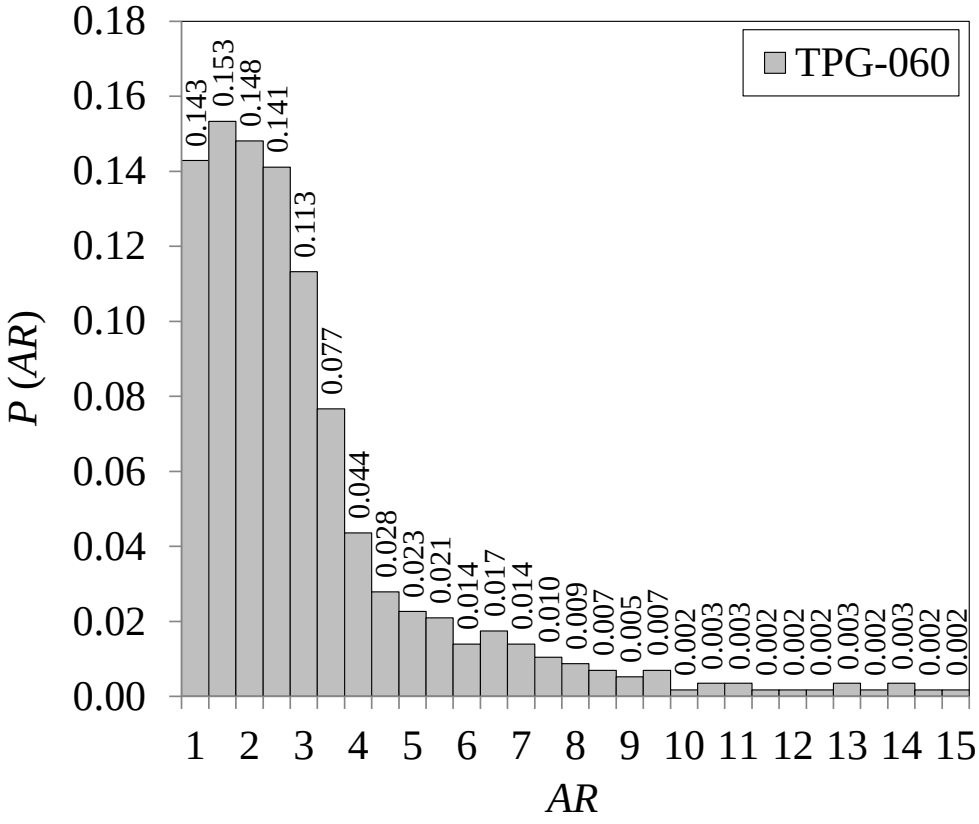

Figure 4.7. Statistical distribution of the aspect ratio for Toray TGP-060

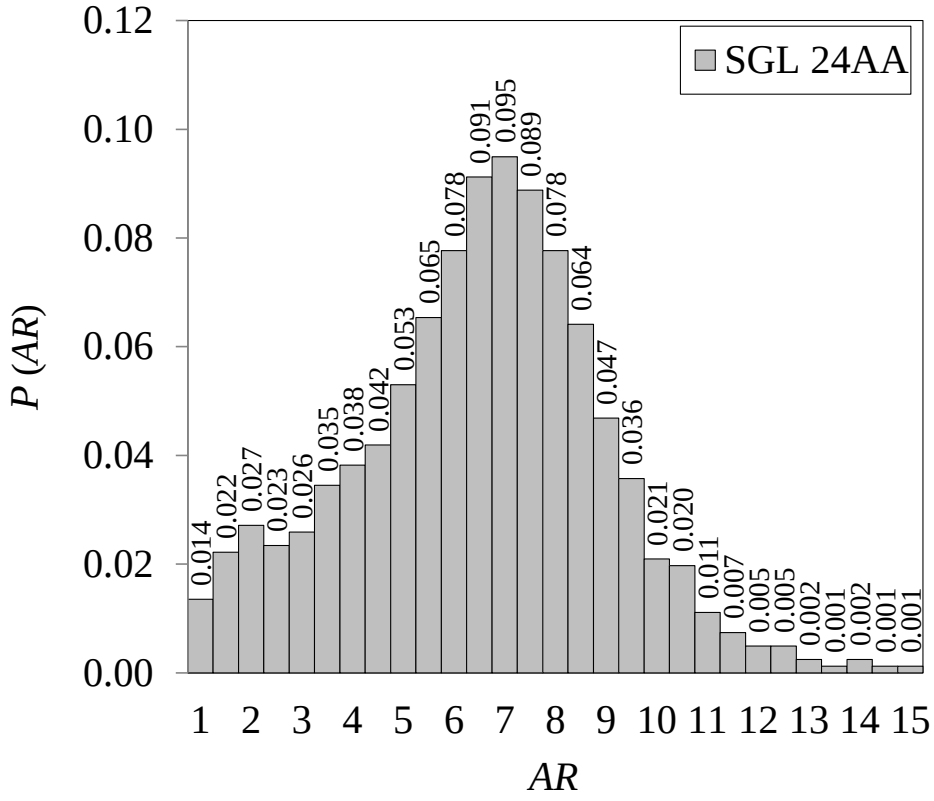

Figure 4.8. Statistical distribution of the aspect ratio for SGL 24AA

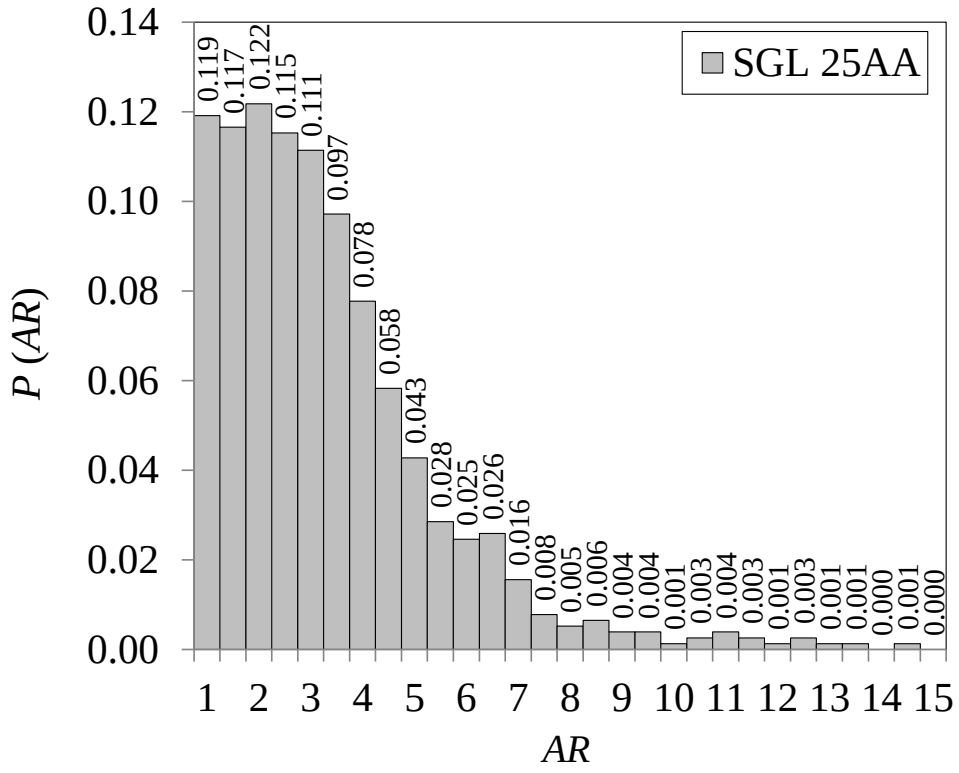

Figure 4.9. Statistical distribution of the aspect ratio for SGL 25AA

- Aspect ratio determination from MIP data

For many of the commonly used GDLs, such as the ones considered in this study, the pore diameter size has been previously reported in the open literature for permeability or other porous media calculations. The pore volume in the unit cell should be the same as the average of the pore volumes inside the GDL of interest, and which can be obtained from MIP measurements. Considering the equivalent diameter of the pore in the MIP method [190] [191], the following relationship between the distance between fibers in the *x* and *y* directions, *l* and *w*, can be written:

$$\frac{\pi d_{p,ave}^2}{4} = (lw\varepsilon) \qquad (4\text{-}26)$$

With a prescribed porosity, solving this equation, or Eq. (4-24), simultaneously with the porosity equation of the unit cell, Eq. (4-1), yields the two unknowns l and w and, therefore, their ratio. Note that the statistical distribution of the aspect ratio in the case of MIP can be obtained from the data of the pore size distribution. The average values of the aspect ratio for some widely-used GDLs obtained from MIP [51] [192] [193] [194] [189] [195] [196] [197] [198] and the optical approach are listed in Table 4.2.

It is worthwhile to mention that either of these two methods, optical or MIP, has advantages and drawbacks. The MIP method gives the pore diameter based on volumetric measurements (pores in all the layers) whereas the optical approach is based on gap area measurements in some upper and lower layers of a GDL. The MIP method uses an equivalent circular cross-section assumption for the gap area, which is not accurate. In addition, for the case of treated GDLs, the contact angle of mercury with carbon fibers is not exactly the same as that with PTFE and/or micro porous layer (MPL). Consequently, the optical approach is more appropriate for thin, treated GDLs, such as most of the Sigracet samples.

Table 4.2. Average aspect ratios and some relevant specifications for the well-known studied GDLs

Quantity	**Porosity (%)**	**Average Pore diameter (μm)**	**Aspect ratio (-)**	
GDL			**MIP**	**Optical**
Toray 060	78	39 [51]	3.9	2.8
Toray 090	78	33 [192] [193]	2.8	-
Toray 120	78	28 [194] [195]	2	-
SGL 24AA	88±0.5	66 [192] [194] [196]	8	6.9
SGL 25AA	92±0.5	60 [192] [197]	2.6	3.4

4.2.3. Fiber diameter

The diameter of fibers can be measured optically as well and a statistical distribution can also be given for this geometrical parameter. However, such measurements are not necessary since considering an average value for fiber diameter is sufficient for the purpose of accurate thermal conductivity modeling, as discussed later. The average fiber diameters measured in this study for the Toray and SGL GDLs are 8.5 and 7.5 μm, respectively.

4.3. PTFE treatment

The GDLs of PEMFCs are usually treated with Teflon (PTFE) in order to make the material hydrophobic and improve water transport. Examination of microscope images of treated GDL samples, such as the ones shown in Figure 4.10, indicates that a considerable portion of PTFE accumulates at the intersection of fibers (Figure 4.10b). For convenience, we refer to the portions corresponding to the upper and lower halves in the through-plane directions as PTFE′ and PTFE″ respectively. In addition, some PTFE (PTFE‴) cover each fiber randomly (Figure 4.10a and c) and a thin layer of PTFE on the first and last layers of fibers in the GDL (PTFE layer) can be seen (Figure 4.10a).

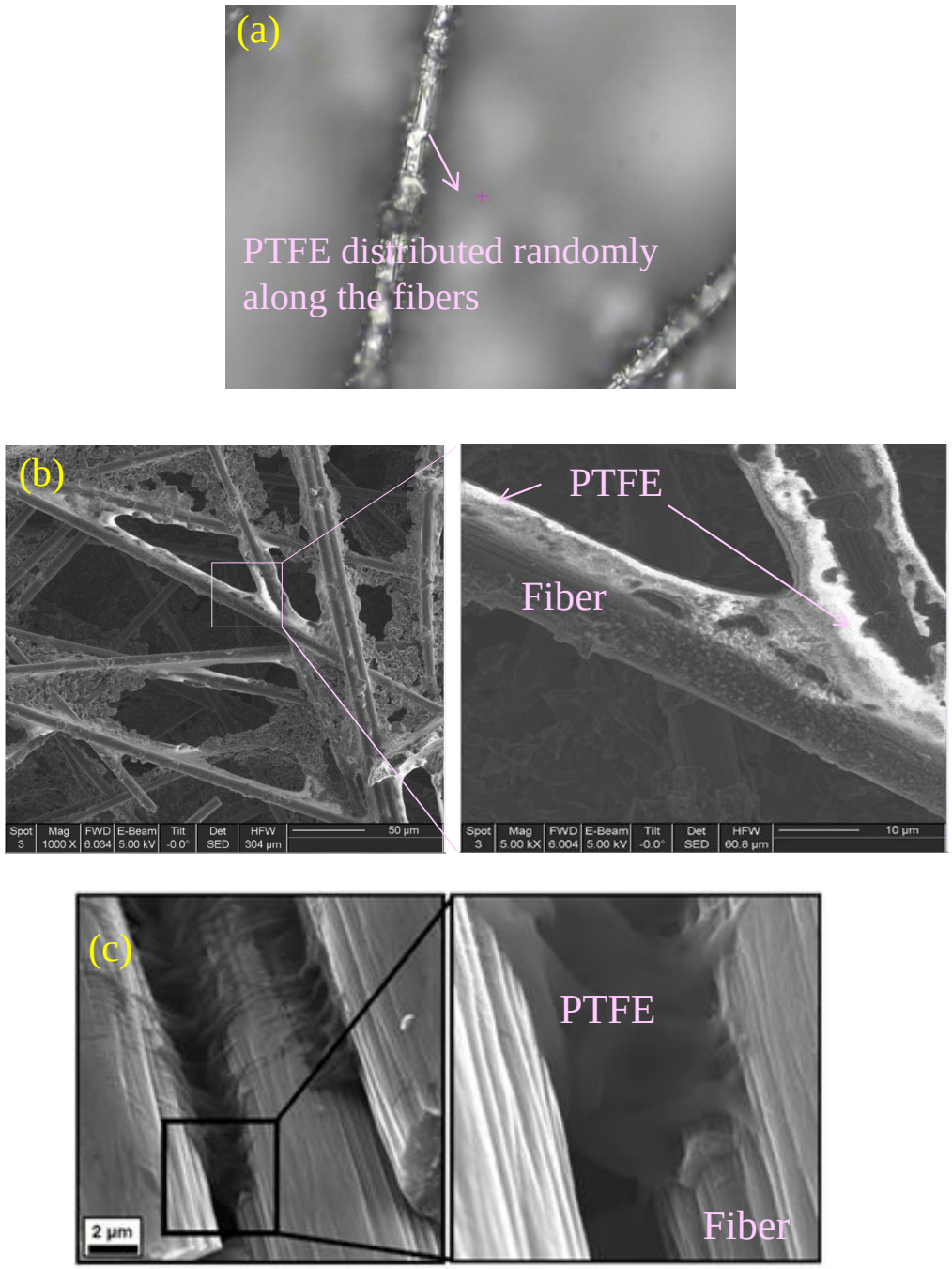

Figure 4.10. PTFE distribution inside different GDLs: (a) and (b) SGL 24BA (present study) and (c) ELAT (with permission from Ref. [189])

A geometric model representation of a PTFE-treated GDL is illustrated in Figure 4.11. The model considers the general case of non-homogeneous penetration, which allows representation of PTFE penetrating into all or only some of the layers at each side. The PTFE treatment procedure commonly used in industry, in which the GDL is dipped in a PTFE solution, is consistent with the latter case with penetration confined to the layers in proximity to the surface. It should also be noted that geometric characteristics such as fiber spacing and angle distribution would not change as a result of PTFE treatment.

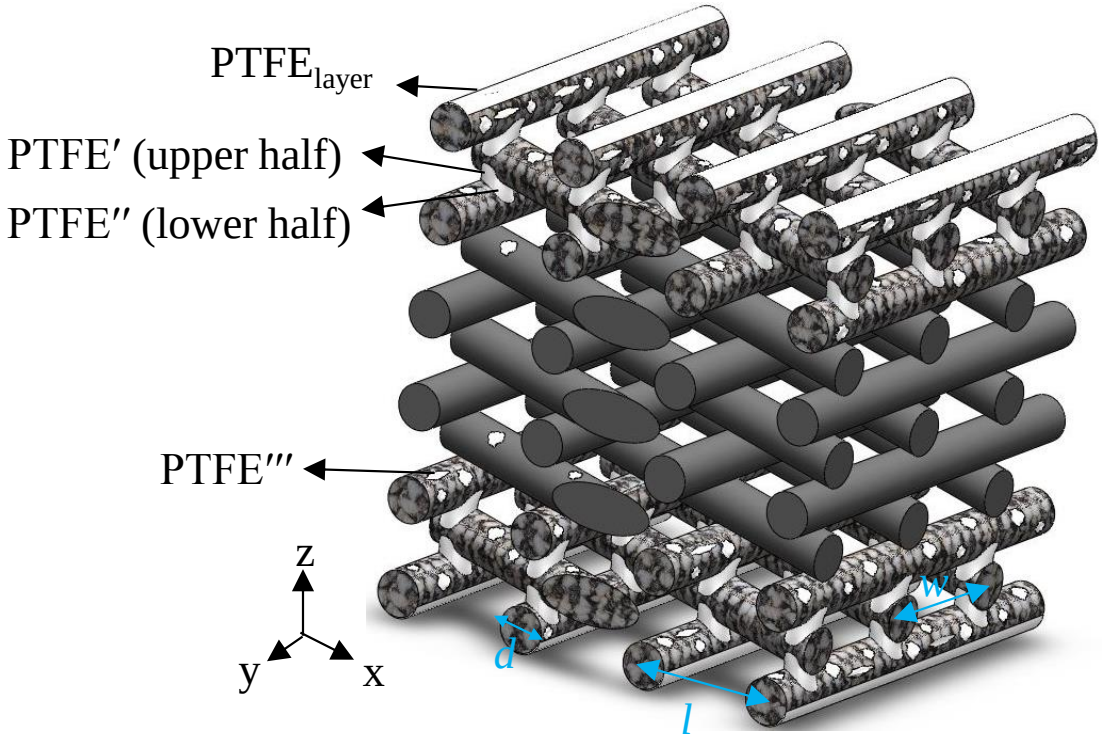

Figure 4.11. Geometric model of GDLs treated with PTFE, see Eq. (4-1)

The present model is based on a unit cell approach that considers a GDL as a periodic fibrous micro structure with a corresponding resistive network through which heat transfer takes place. Extending the unit cell defined for untreated GDLs, a unit cell

consisting of two blocks is taken here to represent the fiber layers containing PTFE and a second unit cell represents the first and last fiber layers with a thin coating of PTFE layers on both surfaces of GDLs, as shown in Figure 4.11 and Figure 4.12.

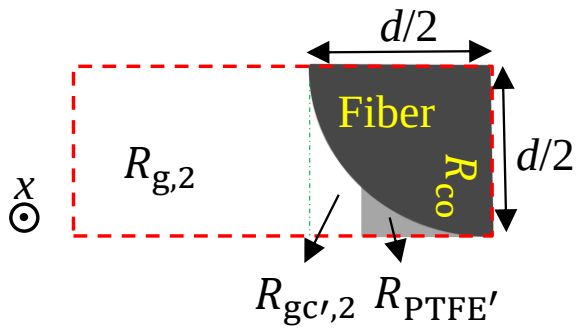

(a) Top block of the unit cell for the PTFE-treated fiber layers inside GDL (also see Figure 4.11)

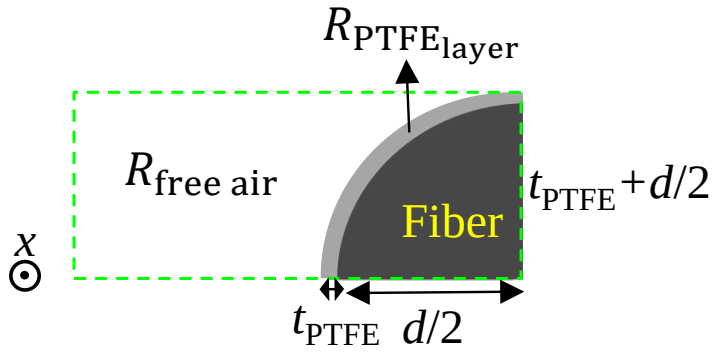

(b) The unit cell for the first and last fiber layers (also see Figure 4.11)

Figure 4.12. Unit cells and top block defined for a PTFE-treated GDL

For a GDL treated with PTFE, the thermal resistance network of the entire GDL, shown in Figure 4.12, will be:

$$
\begin{aligned}
R_{\mathrm{tot}} = 2\left(\frac{1}{R_{\text{free air}}} + \frac{1}{R_{\text{PTFE layer}}}\right)^{-1} \\
+ \frac{\mathrm{n}_{\text{with PTFE}}}{2}\left[\frac{1}{R_{\mathrm{g},1} + R_{\mathrm{PTFE}'''}} + \frac{1}{R_{\mathrm{gc}',1}} + \frac{1}{R_{1,\mathrm{PTFE}''}} + \frac{1}{R_{\mathrm{co}}}\right]^{-1} \\
+ \frac{\mathrm{n}_{\text{with PTFE}}}{2}\left[\frac{1}{R_{\mathrm{g},2}} + \left(\frac{1}{R_{\mathrm{gc}',2}} + \frac{1}{R_{2,\mathrm{PTFE}'}}\right) + \frac{1}{R_{\mathrm{sp}}}\right]^{-1} \\
+ \frac{\mathrm{n}_{\text{without PTFE}}}{2}\left[\frac{1}{R_{\mathrm{g},1}} + \frac{1}{R_{\mathrm{gc},1}} + \frac{1}{R_{\mathrm{co}}}\right]^{-1} \\
+ \frac{\mathrm{n}_{\text{without PTFE}}}{2}\left[\frac{1}{R_{\mathrm{g},2}} + \frac{1}{R_{\mathrm{gc},2}} + \frac{1}{R_{\mathrm{sp}}}\right]^{-1}
\end{aligned}
\tag{4-27}
$$

where all the resistances of $\mathrm{R_{co}}$, $\mathrm{R_{sp}}$, $R_{\mathrm{g},1}, R_{\mathrm{g},2}, R_{\mathrm{gc},1}$, $R_{\mathrm{gc},2}$, $R_{\mathrm{gc}',1}$ and $R_{\mathrm{gc}',2}$ have been defined before, and $\mathrm{R_{PTFElayer}}$ and $\mathrm{R_{freeair}}$ are as follows:

$$
R_{\text{PTFE layer}} = \frac{t_{\mathrm{PTFE}}}{k_{\mathrm{PTFE}} \dfrac{\pi d}{4} \dfrac{(l+\pi)}{4}} \tag{4-28}
$$

$$
R_{\text{free air}} = \frac{\dfrac{d}{2} + t_{\mathrm{PTFE}}}{k_{\mathrm{air}} \dfrac{(l-d)(w-d)}{4}} \tag{4-29}
$$

where k_{PTFE} and k_{air} are thermal conductivities of PTFE and air, respectively, and $\mathrm{t_{PTFE}}$ is the average thickness of the PTFE coating on the fibers of the first and last layers of

GDL, which is given in Table 3.3. The geometrical parameters *l*, *w*, and *d* are shown in Figure 4.11, which have already been given for the studied GDLs.

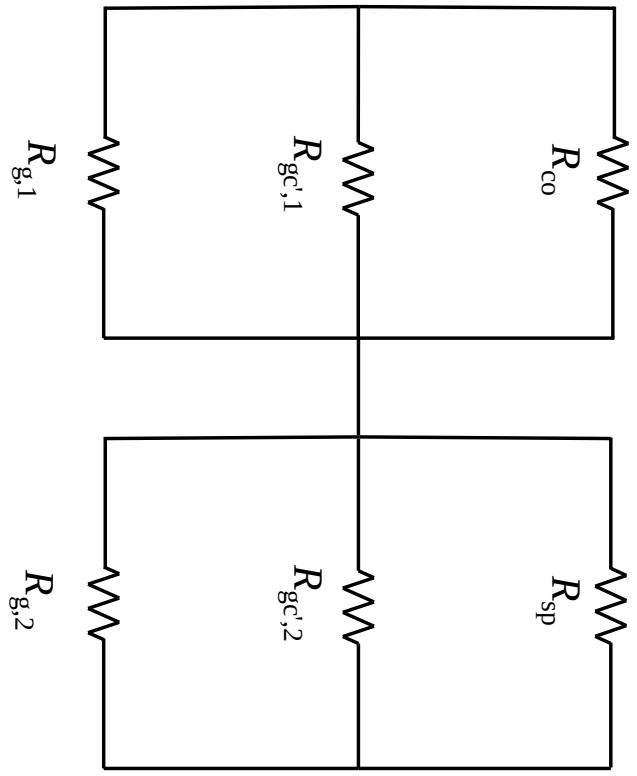

(a) Resistances of layers without PTFE (middle layers) (the negligible bulk resistance of fibers has been omitted)

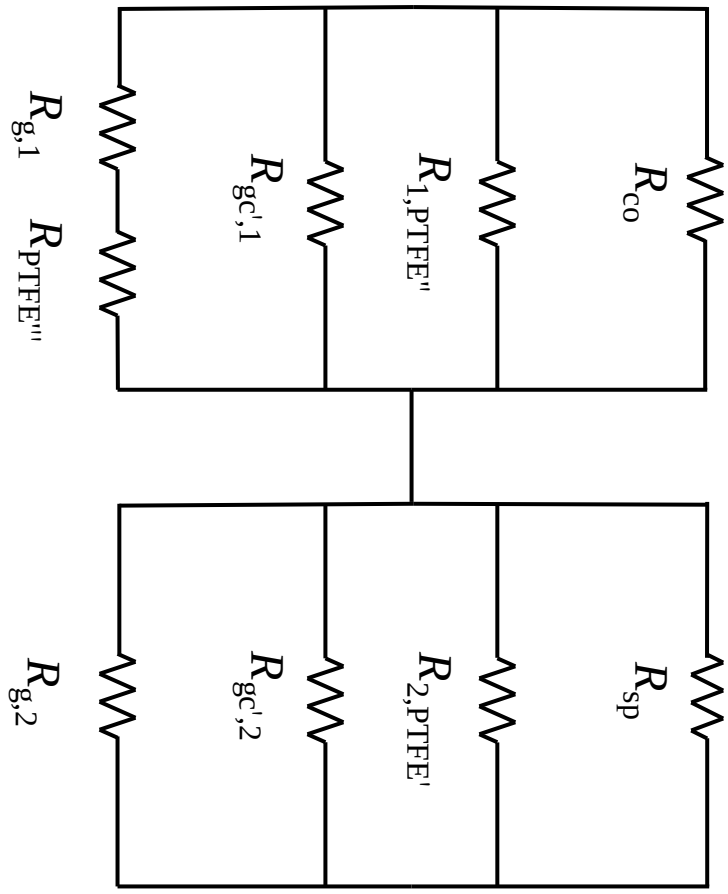

(b) Resistances of layers with PTFE (the negligible bulk resistance of fibers has been omitted)

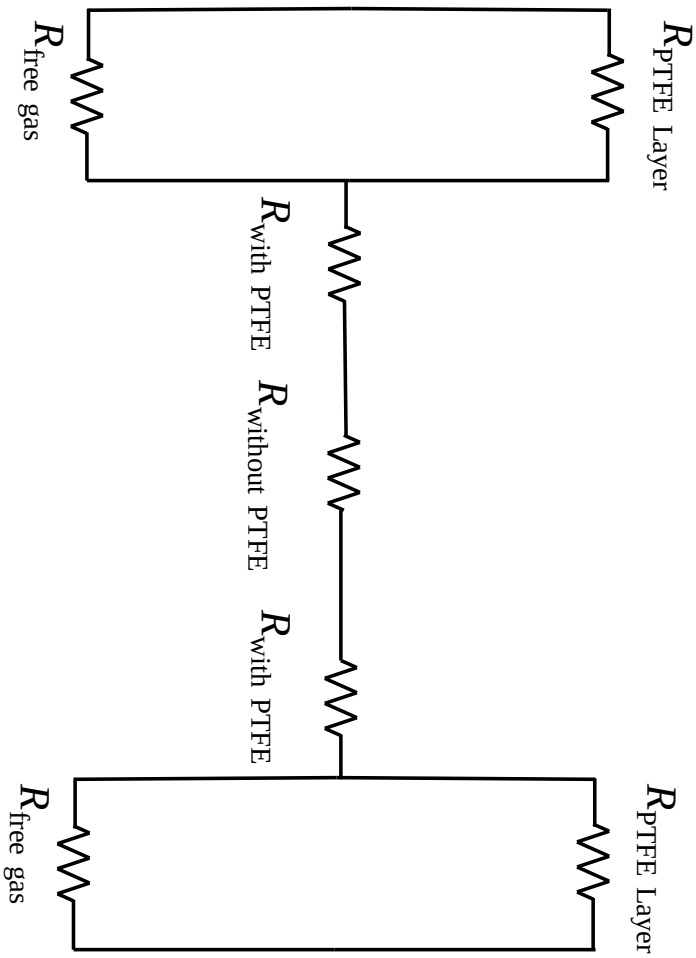

(c) The total thermal resistance network of the GLD treated with PTFE

Figure 4.13. Thermal resistance network for a PTFE-treated GDL

It should be noted that all PTFE resistances inside the GDL, i.e., R_{PTFE} ,$R_{PTFE'}$, $R_{PTFE''}$, and $R_{PTFE'''}$, are in parallel with a much lower resistance, the conduction through fiber-fiber contacts, and therefore, will not have a noticeable impact on the total resistance of the GDL, see Eq. (4-1). Accordingly, these PTFE resistances have secondary effects and need not be considered for estimating the total resistance of the entire GDL. Although the thermal conductivity of PTFE is one order of magnitude higher than that of air

(k_{air}=0.026<k_{PTFE}=0.3 W m^{-1} K^{-1} [36]), it is still some orders of magnitude lower than the thermal conductivity of the fibers. As such, one can conclude that PTFE treatment on GDLs can be modelled as only one "thin layer" on the top/bottom layers of GDLs and will only affect the through plane thermal conductivity and the thermal contact resistance at the interface of GDL-bipolar plate. For this reason, the PTFE distributed inside the GDL does not have a noticeable impact on the through-plane thermal conductivity. Hence, from the viewpoint of through-plane heat transfer, the thermal resistance of a PTFE-treated GDL can be practically approximated in terms of untreated GDL, PTFE, and gas (air) resistances as:

$$R_{\text{tot}}^{\text{PTFE-treated GDL}} \simeq (\text{n}-1)R_{\text{tot}}^{\text{Untreated GDL}} + 2\left(\frac{1}{R_{\text{free air}}} + \frac{1}{R_{\text{PTFE layer}}}\right)^{-1} \qquad (4\text{-}30)$$

where n is the number of fiber layers (=t_{GDL}/d).

The thermal conductivity of GDLs can finally be calculated by:

$$k_{\text{eff}} = \frac{4t_{GDL}}{lwR_{tot}} \qquad (4\text{-}31)$$

It should be noted that resin and other additive materials, which can be randomly distributed inside the "carbon fiber *skeleton*" of the GDL, have not been considered at this stage of our work. However, the modeling framework allows for the treatment of such additives in a similar way to PTFE. The fiber-fiber resistance is always much less than other resistances, including fiber-X-fiber resistance where X can be any phenolic resin or filler. It should be noted that fiber-X-fiber resistance includes the bulk resistance of the lower-conductivity material X as well as two contact resistances of X with the adjacent fibers.

4.4. Parametric study

The code written in the MATLAB environment is used to perform a parametric study and investigate the effects of geometric parameters on thermal conductivity. The present analysis holds for PTFE-treated GDLs as well, even though the model doesn't consider the addition of PTFE to the GDL. As demonstrated earlier, PTFE inside GDL has a negligible effect on the thermal conductivity.

4.4.1. Fiber angle

As noted earlier, each type of GDL has its own micro structure, and thus a different fiber angle distribution. By plugging the angle statistical distribution (0-$\pi/2$ scale) into the correction factor relation, Eq. (4-22), one can calculate the thermal conductivity correction based on the angle distribution. In a simpler way, independent of the type of statistical distribution, the overall thermal conductivity can be estimated by Eq. (4-23).

- Thermal resistance correction factors

From the angle distribution, one can find the average value (see Figure 4.4 and Figure 4.5) and also the correction factors for the deviation of all the possible angles from this average. The values of the correction factors for thermal resistance components of each GDL are given in Table 4.3. Note that the correction factors for gas resistances of the top block are always unity since they are not dependent on fiber angle (see Eqs. (4-14) and (4-15) in Table 4.1); hence they are omitted in Table 4.3. As shown in Table 4.3, the gas thermal resistance correction factor R_{gc2}, contrary to the other gas resistances, is significant and seems to be the most sensitive to the angle distribution. Finally, the most important (controlling) factors are related to the spreading/constriction resistances, which

are close to unity. In fact, these correction factors show the deviation of each angle from the average value for each GDL. It should be noted that the gas resistances are so large (compared to the other resistances) that heat transfer takes place preferentially and almost exclusively through the solid matrix, even though this entails another large resistance (spreading/constriction resistance) which is still much less than the gas resistances themselves. As a result, the gas thermal resistances do not have any noticeable impact on the through-plane thermal conductivity compared to the solid resistances.

Table 4.3. Typical values of correction factors for thermal resistance components of two well-known GDLs

	Thermal resistance correction factors			
GDL	$\boldsymbol{R^*_{sp}}$	$\boldsymbol{R^*_{g,2}}$	$\boldsymbol{R^*_{gc,2}}$	$\boldsymbol{R^*_{tot}}$
Toray 060	1.06	0.94	1.41	1.03
SGL 25AA	1.12	0.95	1.49	1.09

- Thermal resistance and thermal conductivity dependency on angles

The angle between two fibers determines the area of the contact spot, which, indeed, affects the thermal contact resistance, i.e. spreading/constriction resistance. The dependency of the ratio of spreading/constriction to the total resistance is shown in Figure 4.14. The functional dependency is not simple and the contribution of the spreading/constriction resistance is always more than 50%, which indicates the importance of this resistance compared to the other samples. It should be noted that changing the angle (θ) is performed at a constant porosity.

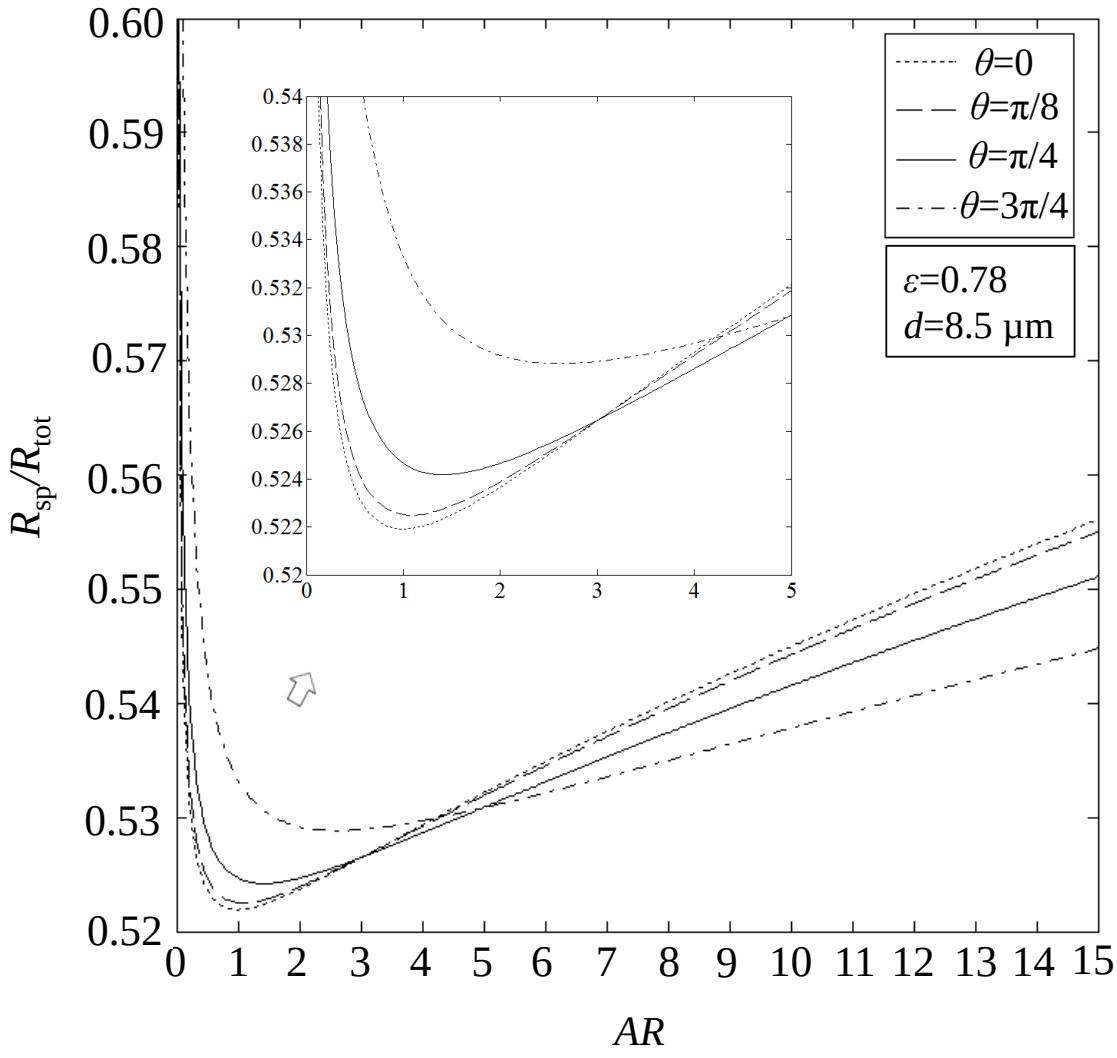

Figure 4.14. Dependence of spreading/constriction resistance on angle for GDLs

Figure 4.15 depicts the variation of the thermal conductivity with aspect ratios for different fiber angles. The general trend of decreasing thermal conductivity with increasing angle at lower aspect ratios, is reversed at higher aspect ratios, and the aspect ratio at which the switch occurs varies from about 3 for small angles (near-orthogonal fibres) to about 6 for the larger angles (near parallel). As noted earlier, the

spreading/constriction resistance is the largest contribution to the total thermal resistance, especially at higher aspect ratios (compared to unity). At aspect ratios close to unity the thermal conductivity curves peak, and the contribution of the spreading/constriction resistance is the lowest. It is worth mentioning that when we change θ at a constant aspect ratio, the porosity has to be kept constant, which changes the number of the contact spots inside the fibrous medium. This makes the analysis of Figure 4.15 very complicated.

Another interesting and important point to note with respect to the manufacturing process is related to the maximum value of thermal conductivity occurring at zero angle (θ=0), which corresponds to the orthogonal arrangement of fibers. If we connect the maximum points, a second-order polynomial can be used to correlate the maximum effective thermal conductivity in terms of the fiber angle (θ) (for each specified porosity and diameter). This indicates that the dependency of the *maximum* thermal conductivity on fiber angles is relatively small, especially for the typical range of fiber angles ($0 \leq \theta \leq \pi/3$). Examination of Figure 4.15 shows that in this range of angles the maximum thermal conductivity is essentially independent of aspect ratio. It would be useful to perform similar studies on the in-plane electrical conductivity, convective heat transfer coefficient [199] [200] [201], permeability [199] and diffusivity, to identify the optimal fiber angle for GDLs.

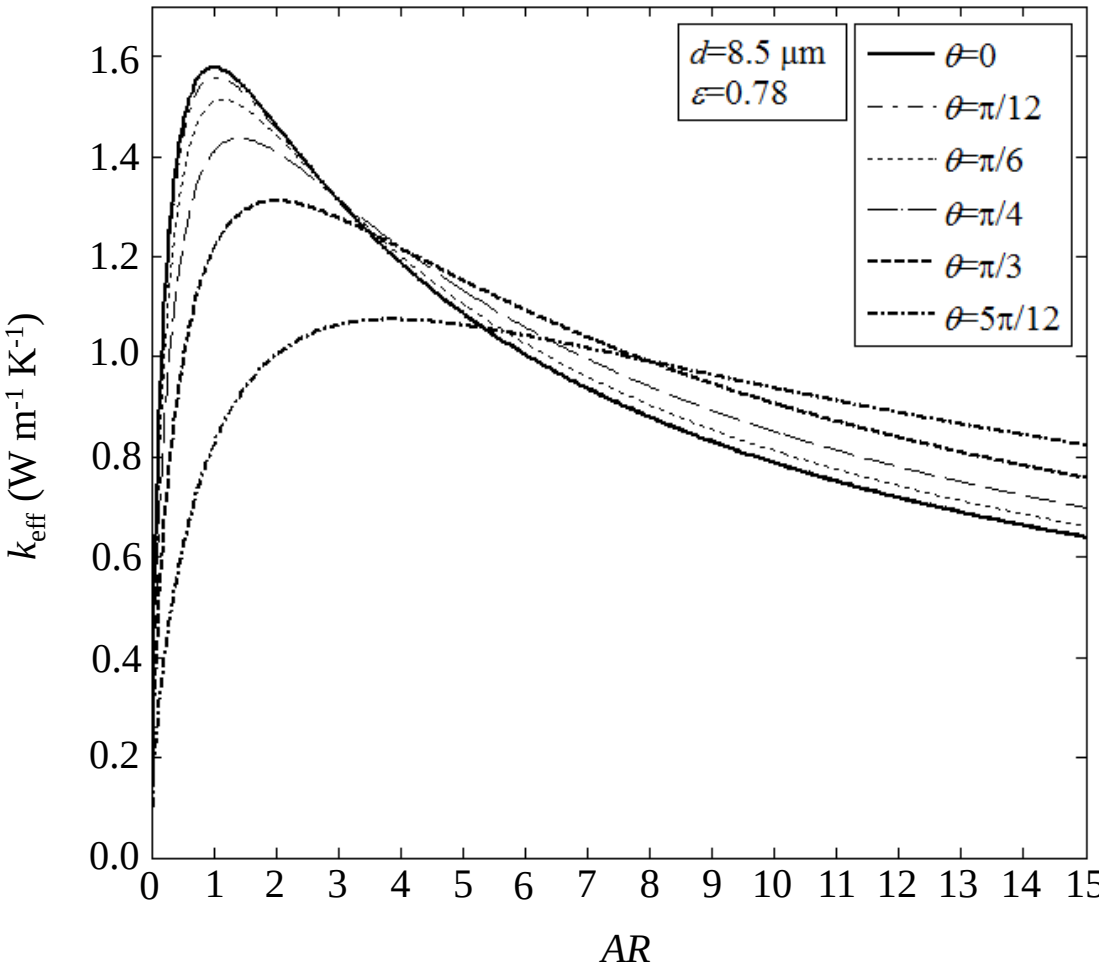

Figure 4.15. Dependence of thermal conductivity on angle for GDLs

4.4.2. Fiber diameter

The change in thermal conductivity for different aspect ratios is shown in Figure 4.16 at different fiber diameters. Both thermal conductivity and its maximum value are virtually independent of the fiber diameter throughout the range of investigated porosities and aspect ratios. This suggests that the fiber diameter can be manipulated for increasing other transport properties such as permeability [199] without incurring any penalty in the

through-plane thermal conductivity. In turn, increasing the fiber diameter does not change the thermal conductivity, but enhances permeability significantly [188] [189]. In practice, the maximum thermal conductivity is not a function of aspect ratio and fiber diameter ($k_{\text{eff max}} \neq \text{f}(d,AR)$).

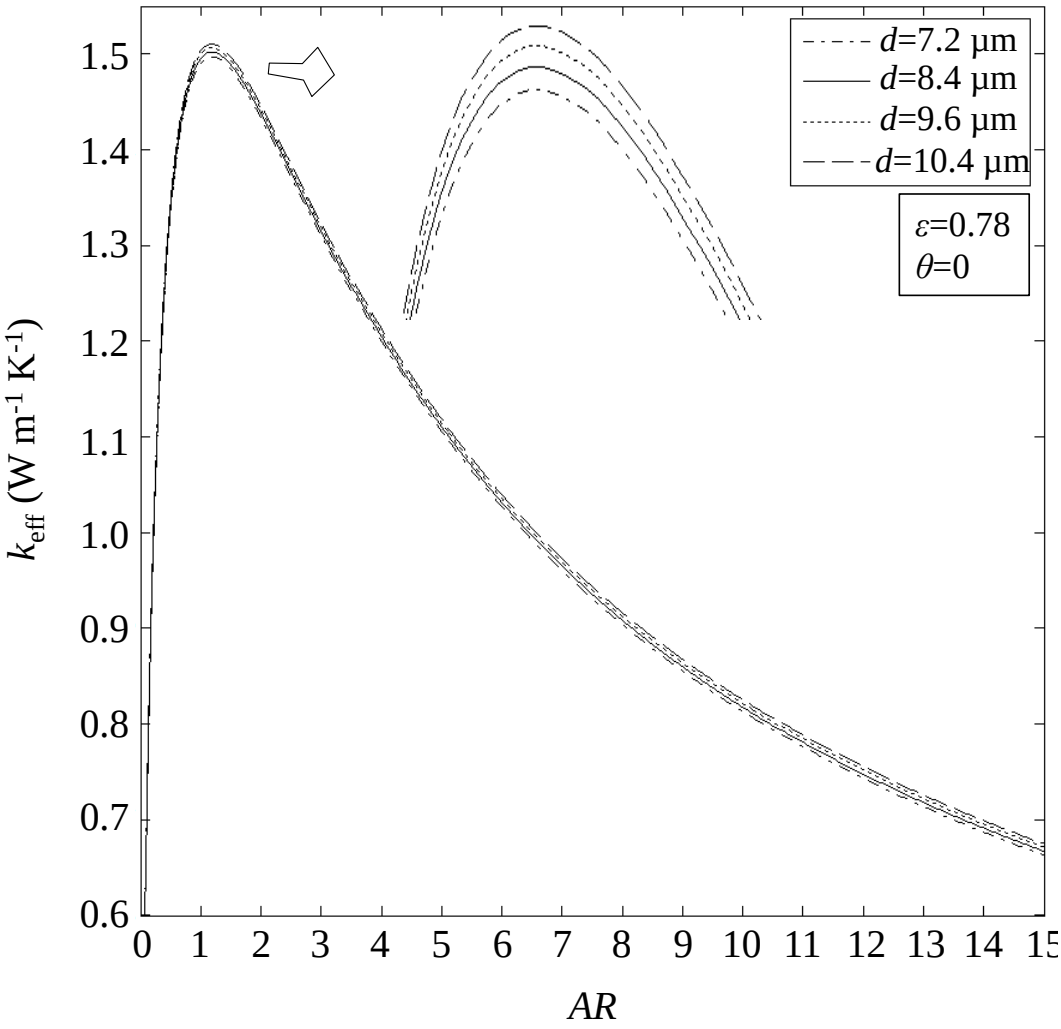

Figure 4.16. Effect of diameter on through-plane thermal conductivity of GDLs

4.4.3. Aspect ratio

One of the most important geometrical parameters of fibrous porous materials is the aspect ratio. The impact of this parameter can be as important to the thermal conductivity as it is to the porosity, as it can be effectively manipulated to achieve the desired transport properties for different purposes. Figure 4.17 represents the thermal conductivity as a function of the two important parameters, aspect ratio and porosity. The dependence of thermal conductivity on porosity is not as complex as the dependence on fiber angle. Figure 4.17, similarly to Figure 4.16, depicts a maximum at an aspect ratio very close, but not at unity, for each value of porosity. At specific values of θ and d (real case), the maximum thermal conductivity, $k_{\text{eff max}}$, is practically independent of the aspect ratio. This can be very important for GDL manufacturing. For a given type of GDL, d and θ are usually fixed, and as a result, it would be sufficient to account for $k_{\text{eff max}}$ [W m^{-1} K^{-1}] as a function of porosity only; i.e., $k_{\text{eff max}} = f(\varepsilon)$. Connecting the maximum points in the cases shown in Figure 4.17, a *linear* relation is obtained in the form of:

$$k_{\text{eff max}} = -8.48\varepsilon + c \qquad (4\text{-}32)$$

where the value of the constant c is depends on θ (and d) (e.g., for θ =0 (d=8.5 μm); then c=8.13). For the typical ranges of the fiber angles in GDLs, that is, $0 \leq \theta \leq \pi/3$ (see Figure 4.4 and Figure 4.5), the maximum thermal conductivity is practically independent of the aspect ratio (Figure 4.15, also see Figure 4.16 and Figure 4.17). As a result, $k_{\text{eff max}}$ can practically be considered as a function of only two geometrical parameters; ε and θ.

It should be noted that an aspect ratio of unity corresponds to the square arrangement, which results in the highest through-plane thermal conductivity. However, other transport properties such as in-plane thermal conductivity, permeability [199] , diffusivity, heat transfer coefficient [199] [200] [201] and electrical conductivity have to be considered as well. A multi-parameter optimization of such properties with respect to the geometrical parameters is ultimately required to determine an optimum structure of a GDL for better

water and heat management of fuel cells. It should also be noted that production of optimally designed arrangements should become possible as precise control of fiber orientations and arrangements during fabrication of fibrous media becomes more practical due to progress in manufacturing technology (see, e.g., [202] [203] [204] [205] [206] [207]).

Figure 4.17 provides a helpful illustration of the importance of the aspect ratio in comparison to the primary parameter characterizing a porous media, i.e., porosity. It is obvious that with increasing porosity (at fixed values of aspect ratio), the thermal conductivity decreases whereas the permeability and diffusivity *increase*. As a result, there is a trade-off between the through-plane thermal conductivity and permeability/diffusivity in terms of porosity. For instance, consider points A, B, C, and D on Figure 4.17. To double the thermal conductivity from 1 to 2 W m^{-1} K^{-1}, the usual approach would be to decrease the porosity (e.g., shown in Figure 4.17, moving from a porosity 0.8 at point C to a porosity of 0.72 at point B), which may markedly reduce other transport properties such as permeability [199] and diffusivity. Based on the insights and results of this study, one can in fact double the thermal conductivity from point A to point B by only manipulating the aspect ratio and keeping the porosity fixed (ε=0.72). This example illustrates the strong dependency of the thermal conductivity on the aspect ratio. As explained, points A and B, which are both on the solid curve, have the same porosities (ε=0.72) but completely different thermal conductivities due to their different aspect ratios.

Conversely, one can keep the through-plane thermal conductivity fixed and increase the porosity or decrease aspect ratio by following any horizontal straight line on Figure 4.17 (e.g., from point A to point C). For instance, points A and C have the same thermal conductivities but different porosities and aspect ratios. In terms of the through-plane heat transfer, there is no difference between points A and C. However, point C is preferred, as it corresponds to a higher porosity, and hence higher permeability and diffusivity, and less solid (fibers), which can reduce the cost of materials in the

manufacturing process. These points might inform GDL manufacturing, as available GDL products usually fall within the regions far from the peak points on Figure 4.17. In general, depending on the specific application and the targeted properties, one can keep one or two of the geometrical parameters fixed and adjust the others to achieve an optimal fibrous medium structure.

Finally, we consider points A and D where point D has a higher thermal conductivity with more porosity. Therefore, a fibrous porous medium with higher porosity does not necessarily have a lower thermal conductivity. This interesting conclusion refutes the traditional notion for heat transfer in porous media on which all the other available models have been implicitly based: the higher the porosity, the less the solid matrix and, therefore, the lower the thermal conductivity.

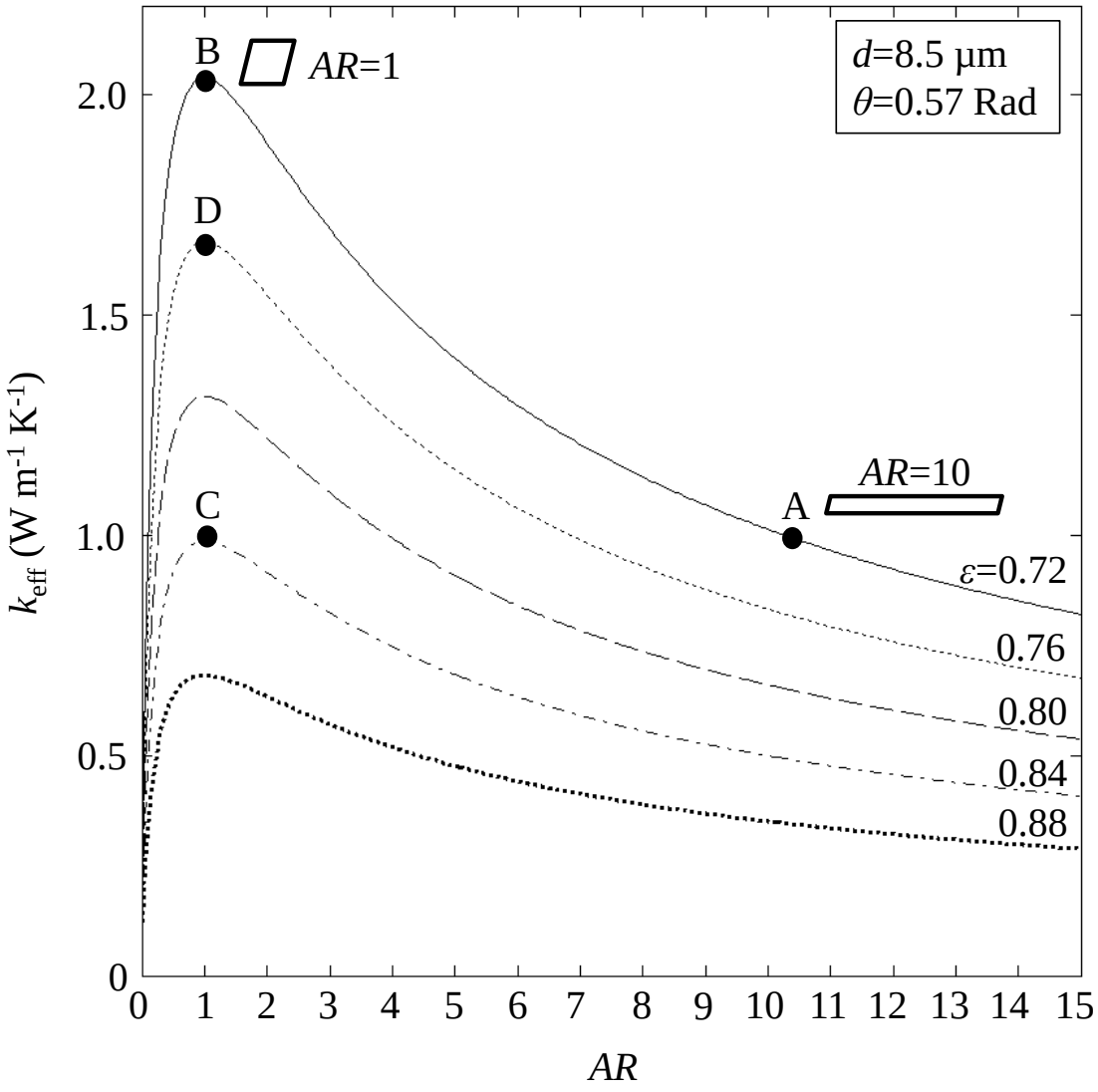

Figure 4.17. Effect of aspect ratio on through-plane thermal conductivity of GDLs with different porosities (the parallelograms shown on the figure represent the *AR* for the unit cell)

It should be noted that for θ=0, the values at a given AR > 1 are equivalent to those for the corresponding 1/AR value on the branch AR < 1, i.e., the curves are symmetric around AR=1 when plotted on a log scale as shown in Figure 4.18. At non-zero θ, the thermal conductivity curves are skewed toward aspect ratios other than unity.

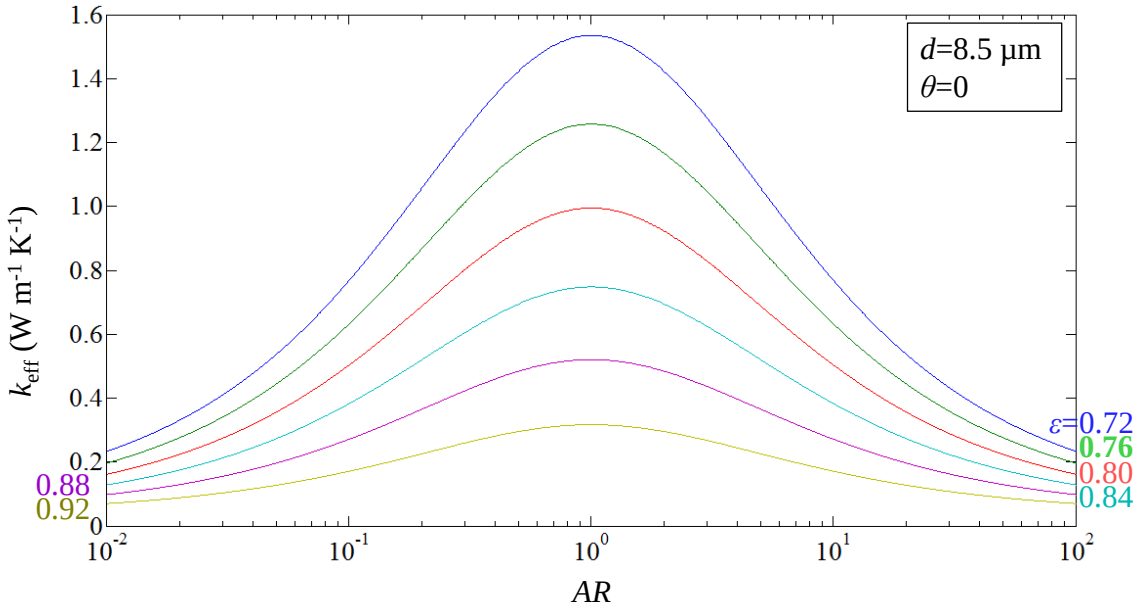

Figure 4.18. Symmetric curves of thermal conductivity-aspect ratio at different GDL porosities (log scale)

4.5. Model validation

Having determined the geometrical parameters of each GDL and a method to apply them to the model, we can proceed to calculate the through-plane thermal conductivity. The thermal conductivities of SGL 24 & 34 AA, BA, DA, and BC and those of series 25 & 35 AA, BA, and BC measured in this study and the Toray data [104] are used for the model validation. Comparison of the experimental thermal conductivities of different treated and untreated SGL GDLs with the model predictions, shown in Figure 4.19, indicate that the model could well capture the experimental data for both untreated and PTFE-treated GDLs. The most significant feature of the presented model is that the model captures the experimental trend, i.e., as PTFE content increases the through-plane thermal conductivity decreases. As mentioned in Chapter 3, the trend observed here is in qualitative agreement with the results of Khandelwal and Mench [91] and Burheim et al. [93] [101], but not with the negligible changes reported in Ref. [43] even for 60 wt% PTFE. The present trends are opposite to the model predictions of Yablecki and Bazylak [115] and Fishman and Bazylak [208] which is representative of the distribution of PTFE in the bulk of the GDL but overlooks the thin coating of PTFE that forms on the surface of the first and last fiber layers. PTFE distributed inside the GDL does not have any noticeable impact on through-plane thermal conductivity. It is worth noting that although PTFE displaces air “pores” that have lower thermal conductivity and reduces the GDL porosity, it does not enhance the overall thermal conductivity of GDLs as discussed.

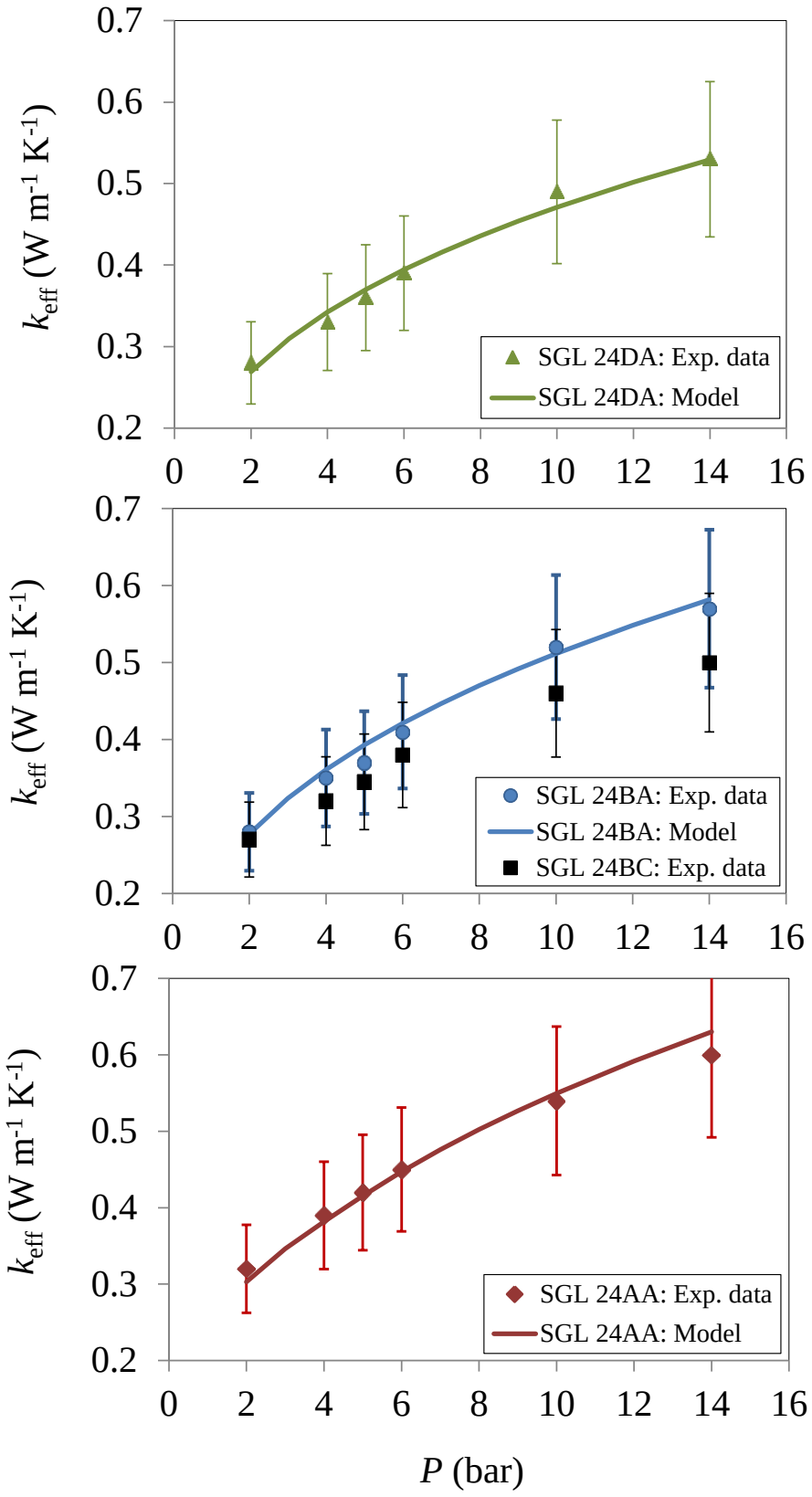
0.7
0.6
0.5
0.4
0.3
0.2
k_{eff} (W m^{-1} K^{-1})
SGL 24DA: Exp. data
SGL 24DA: Model
SGL 24BA: Exp. data
SGL 24BA: Model
SGL 24BC: Exp. data
SGL 24AA: Exp. data
SGL 24AA: Model
0
2
4
6
8
10
12
14
16
P (bar)

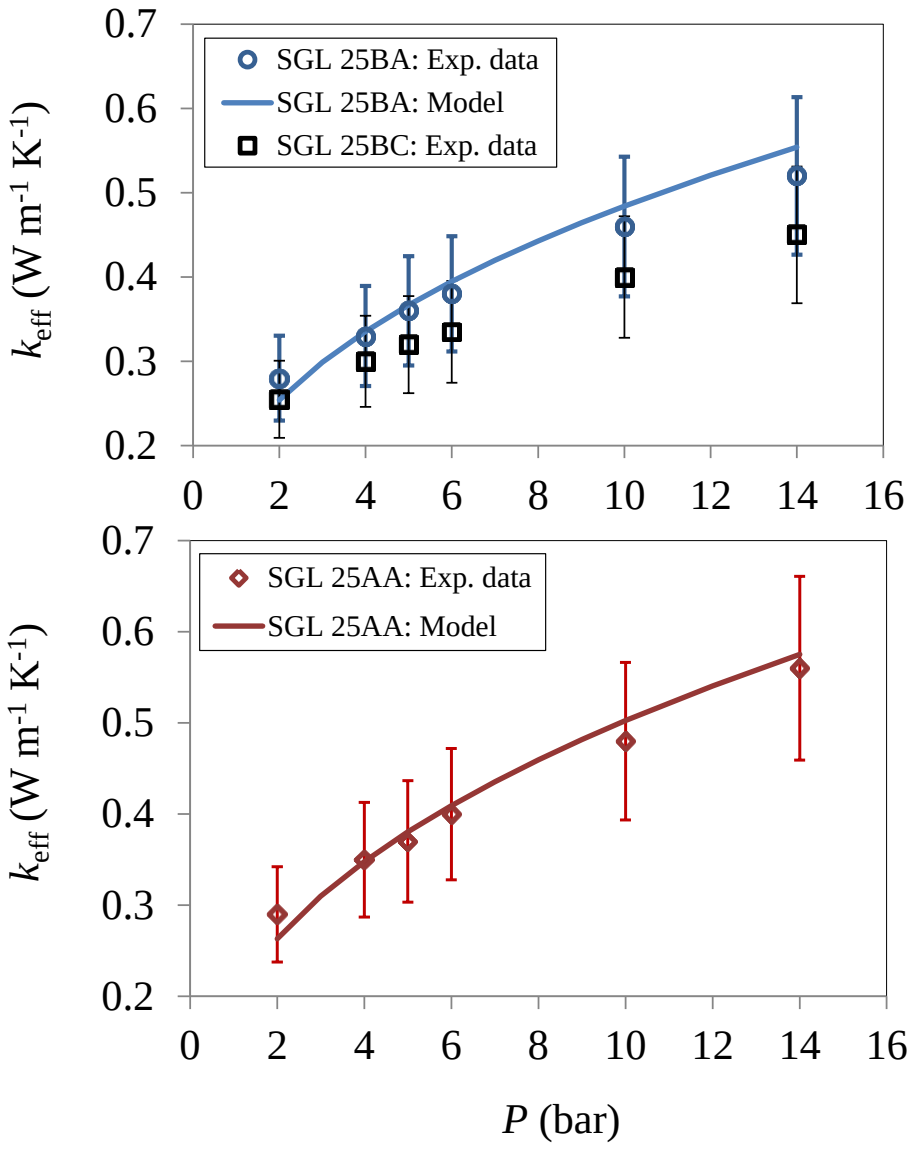

Figure 4.19. Variation of thermal conductivity with pressure: Comparison of model predictions with experiments for GDLs with different PTFE loadings

4.5.1. Model improvement

Different types of commonly used GDLs with documented through-plane thermal conductivity (Toray TGP-H-060 to 120 and also SGL 24AA and 25AA) have been selected, and their thermal conductivities were calculated using both the model presented here and the model of Sadeghi et al. [57], with the results shown in Figure 4.20.

As shown in Figure 4.20, both models yield reasonable predictions of the thermal conductivity of the untreated Toray GDLs (TGP H-060 and TGP H-090), with overall better agreement for the present model, especially with respect to SGL 24AA, a GDL with a high aspect ratio. It should be noted that in Ref. [91], the thermal conductivity measurements were not performed under vacuum conditions (even though some insulation was used), which resulted in a small over-estimate of the thermal conductivity, as pointed out by the authors. Another point to note here is that the thermal conductivities measured in Ref. [91] have been obtained from the so-called two-thickness method for TGP-H-060 and TGP-H-090. As shown in Table 4.2, the porosities of these two GDLs are the same and their aspect ratios are close to each other. As a result, the only value of the thermal conductivity obtained for both GDLs TGP-H-060 and -090 by using the two-thickness method can be considered as the average value of their actual thermal conductivities.

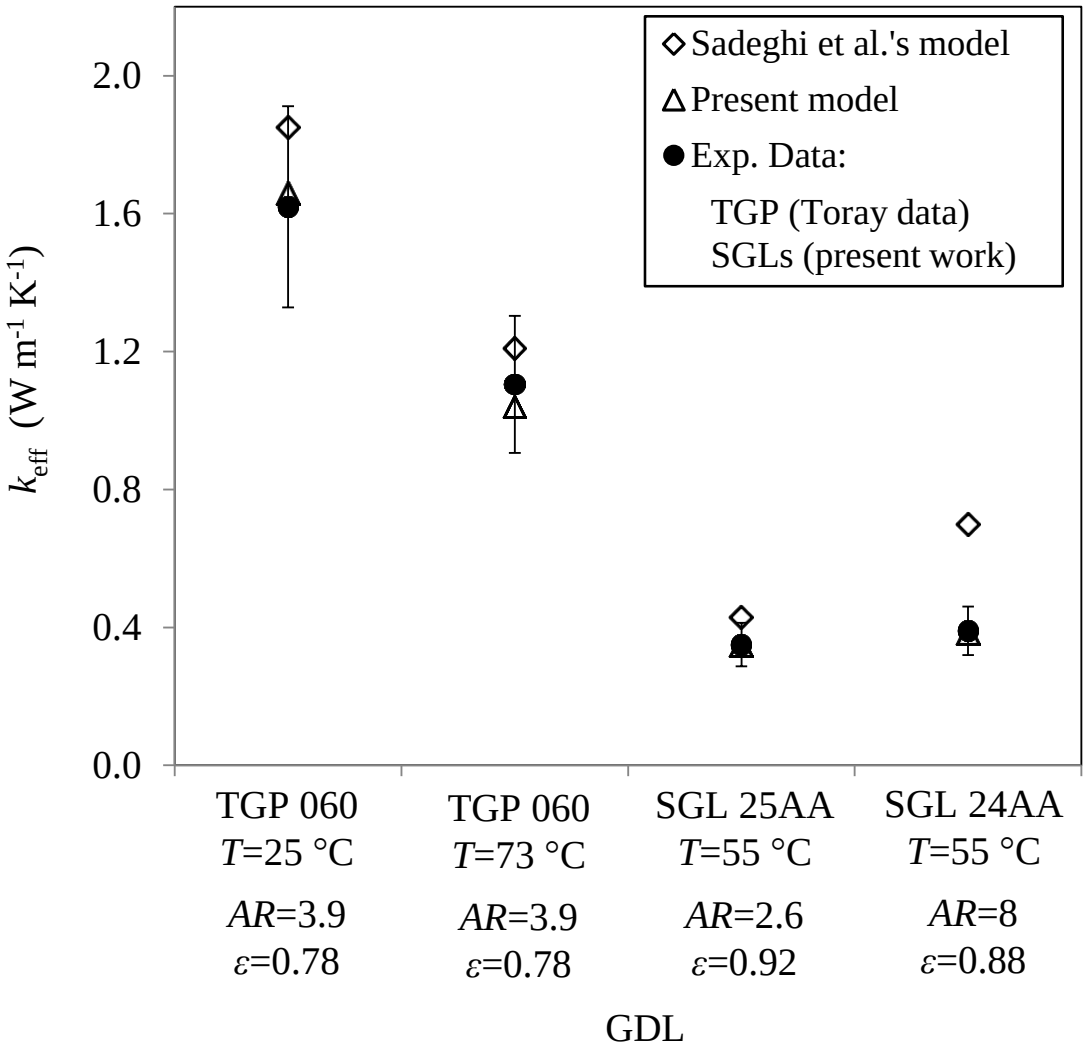

Figure 4.20. Comparison of the thermal conductivities calculated by the models with experimental data

We also implemented both models for another temperature, 73 °C, for which experimental data is also available. The comparisons indicate that both models account well for the effect of temperature on effective thermal conductivity.

Some thermal conductivity data measured under different conditions have been reported in Ref. [101] for each of the treated Torays: TGP-H-060, 090, and 120 (5% PTFE) and is

presented separately in Table 4.4. The authors of Ref. [101] assumed a negligible thermal contact resistance between two samples based on the observation that increasing compression led to small changes in the sample-sample contact resistance. However, the relative independence of sample-sample contact resistance with respect to changes in compression pressure does not necessarily indicate that the contact resistance is negligible. Nevertheless, the data of Ref. [101] can still be used for the purpose of qualitative comparisons between the considered Toray GDLs. The measured data in Table 4.4 show a reduction in the thermal conductivity from TGP-H-120 to TGP-H-060 at all compressive loads. This interesting reduction trend can now be explained by the effect of the aspect ratio parameter; with increasing aspect ratio from TGP-H-120 to TGP-H-060 (see Table 4.2), the effective thermal conductivity decreases. This trend cannot be explained or justified by other models. Finally, we consider SGL 24AA and 25AA to further investigate the effect of the geometrical parameters on the thermal conductivity. As shown in Figure 4.20, the models have markedly different estimates for SGL 24AA. The present (statistical) model improves the prediction significantly compared to the previous model [57], which is based on a unity aspect ratio and a homogeneous GDL with zero value of angle (orthogonal arrangement of fibers).

The experimental data also indicates that the thermal conductivities of SGLs 24AA and 25AA are almost the same even though they have different porosities, a result that can be explained by the present study. The porosity of SGL 24AA is 0.88, while that of SGL 25AA is 0.92. This might erroneously lead to the expectation that SGL 24AA would have a higher thermal conductivity because of its lower porosity. However, the increase in conductivity arising from the lower porosity of SGL 24AA is offset by the higher aspect ratio compared to SGL 25AA. This can be considered as experimental evidence of the physical realism of the present model, as points A and C on Figure 4.17 qualitatively correspond to the real cases of SGL 24AA and 25AA, respectively.

Table 4.4. Experimental data of Ref. [101] for evaluation of the aspect ratio effect on thermal conductivity for different Torays

	$k_{eff}(W\,m^{-1}K^{-1})$		
	Compression pressure (bar)		
Type of Toray	**4.6**	**9.3**	**13.9**
TGP-H-060	0.41	0.53	0.66
TGP-H-090	0.50	0.65	0.73
TGP-H-120	0.62	0.81	0.89

4.6. Concluding remarks

A statistical unit cell model was proposed for estimating the through-plane thermal conductivity of GDLs. This model considers not only porosity, but also other geometrical properties such as angle distribution and aspect ratio. The geometrical parameters of a GDL structure, their effects on through-plane thermal conductivity, and how to measure or determine them for different types of GDL were discussed in detail. These parameters were determined for several types of commonly used GDLs. The aspect ratio was found to be as important as porosity in determining conduction heat transfer. The results also shed a new perspective on the notion that a fibrous porous medium with higher porosity yields a lower thermal conductivity, and show that it is possible for two fibrous media with the same porosity to have completely different thermal conductivity and vice versa, due to the contributions of other geometrical parameters, especially the aspect ratio. The important insight on the role of aspect ratio in changing thermal conductivity provides a rational explanation of some experimental trends and results that were considered contradictory. The results of the model also yield the structure of a GDL providing the

maximum through-plane thermal conductivity. It was found that, the maximum thermal conductivity is not a function of fiber diameter and aspect ratio ($k_{\text{eff max}} \neq f(d,AR)$) and depends primarily on porosity and fiber angle ($k_{\text{eff max}} = f(\varepsilon,\theta)$).

In general, the concepts and approaches presented in this study can be extended to the determination of geometrical properties of any fibrous porous media, and can be adapted to estimate other GDL transport properties such as permeability and diffusivity. The insights gained through this work can open alternative avenues for tailoring and optimizing the geometrical parameters of fibrous porous media from the viewpoint of manufacturing process and transport properties.

Chapter 5.

Modeling of GDL-graphite BPP thermal contact resistance

5.1. Model development

A mechanistic analytic model is developed for predicting the thermal contact resistance between a GDL, a fibrous porous material, and a flat surface, e.g. a graphite or metallic BPP. The present model is built using: (i) GDL and BPP salient geometric parameters, such as waviness, diameter, distribution and orientation of fibers, and GDL porosity; (ii) applied load, mechanical deformation, and Hertzian theory; (iii) thermophysical properties of both contacting bodies, i.e. thermal conductivity and effective Young's modulus; and (iv) heat conduction in GDL fibres (spreading/constriction resistances). The true area between the two contacting bodies is the key parameter in determining both electrical and thermal contact resistance. The contact area can be determined using geometrical and mechanical modeling. The TCR at the interface can then be obtained using an appropriate thermal model that includes heat transfer in both contacting bodies through the contacting areas.

5.1.1. Geometrical modeling

Based on images of different GDLs, the fibers are assumed to have a circular cross-section. In almost all previous GDL geometric models, the fibers are assumed to be straight cylinders, see Figure 5.1. For modeling interfacial phenomena, which are highly dependent on surface topography and morphology, more realistic assumptions are required. The analysis of the GDL images reveals that fibers are in fact wavy, as can be seen in Figure 5.2. Consequently, in this study, fibers are considered as wavy cylinders, with a sinusoidal profile in this study, see Figure 5.3. The waviness of the fibers is measured optically using a Nanovea M1 hardness tester (NANOVEA). This instrument allows micro-scale imaging/filming while scanning the sample in different directions. The statistical data for fiber waviness and amplitude are presented in Figure 5.4 for Sigracet (SGL) GDLs. The wavelength (λ) and amplitude (Δ) data fall in the ranges 50-1900 μm and 2-5d_f for the Sigracet samples. For most engineering applications, however, using the average values of fiber amplitude and wavelength may lead to sufficient accuracy.

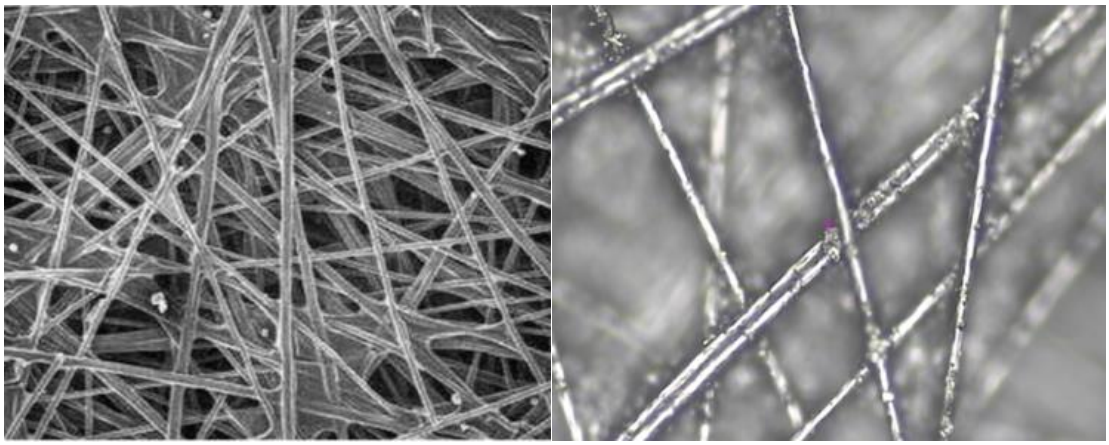

(a)

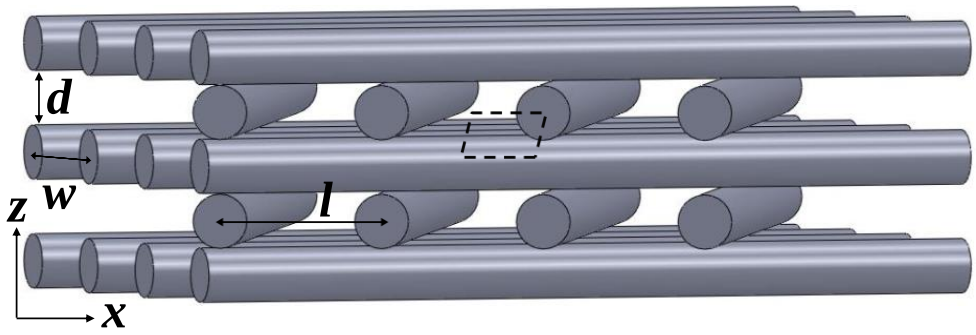

(b)

Figure 5.1. (a) GDL surface images (Sigracet GDLs) and (b) Proposed geometrical model for GDLs

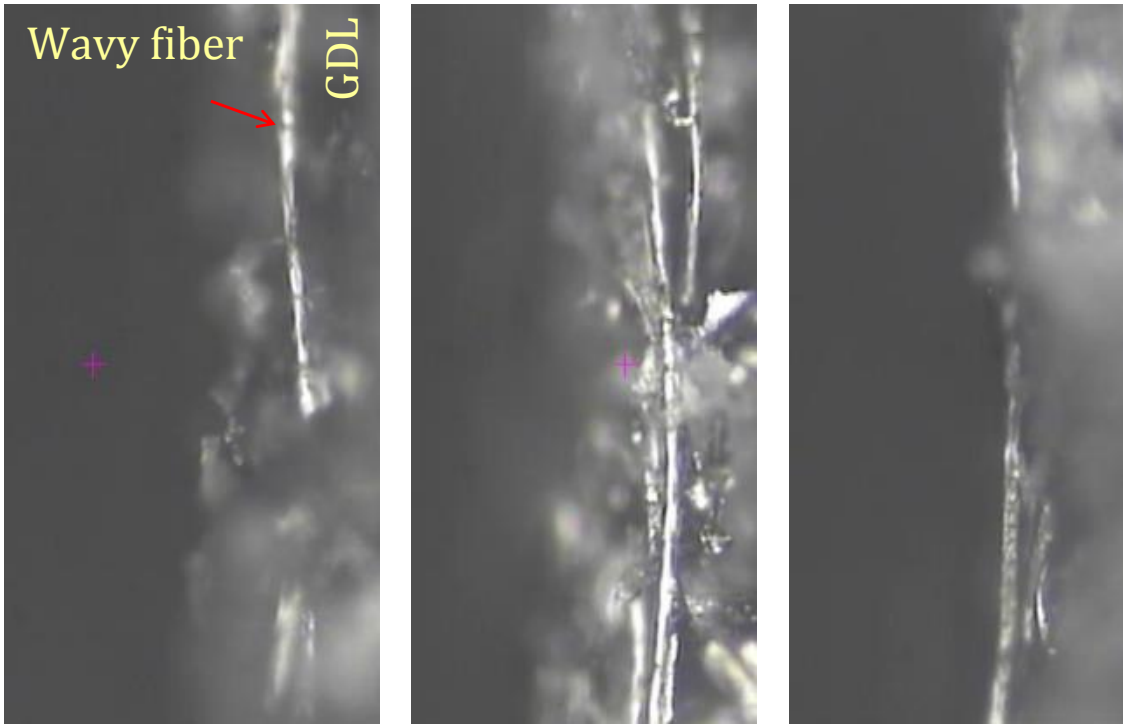

Figure 5.2. GDL images showing waviness of the fibers

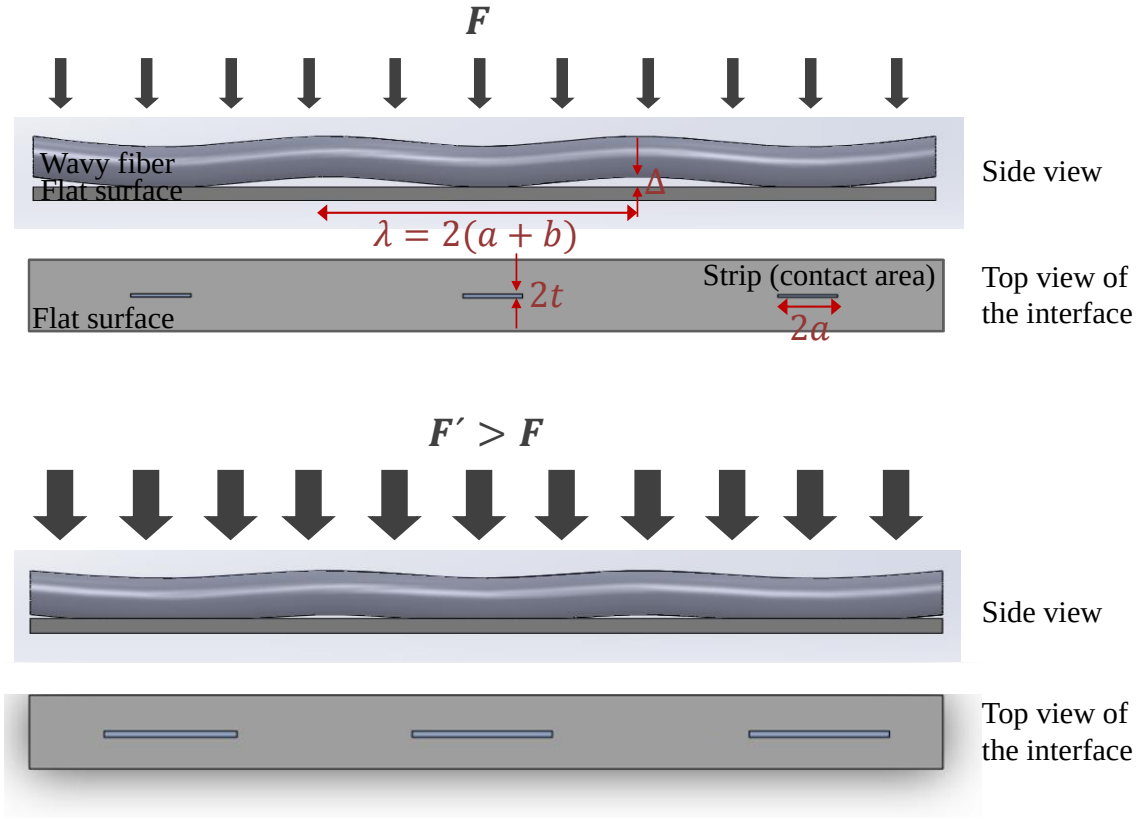

Figure 5.3. A wavy fiber under compression: increasing contact areas between a wavy fiber and a flat surface with increasing compression

The proposed model is developed based on the following assumptions: 1) steady state heat transfer; 2) constant thermophysical properties; 3) wavy GDL fibers; 4) smooth flat surface, i.e., the surface roughness of the plate is neglected; 5) no out-of-flatness on the plate; 6) static mechanical contact, i.e., no vibration effects; 7) negligible radiation effects due to low typical operating temperature range of PEMFC < 100 ^{o}C [89] [209] [210]; 8) first loading cycle only, i.e. no hysteresis effect is considered; but the proposed methodology is also applicable to deformed (cycled) GDLs if the deformed samples geometric parameters are available; and 9) contact occurs in a vacuum environment. It should be noted that heat transfer due to interstitial gases can be added to the present model using the model of Ref. [181].

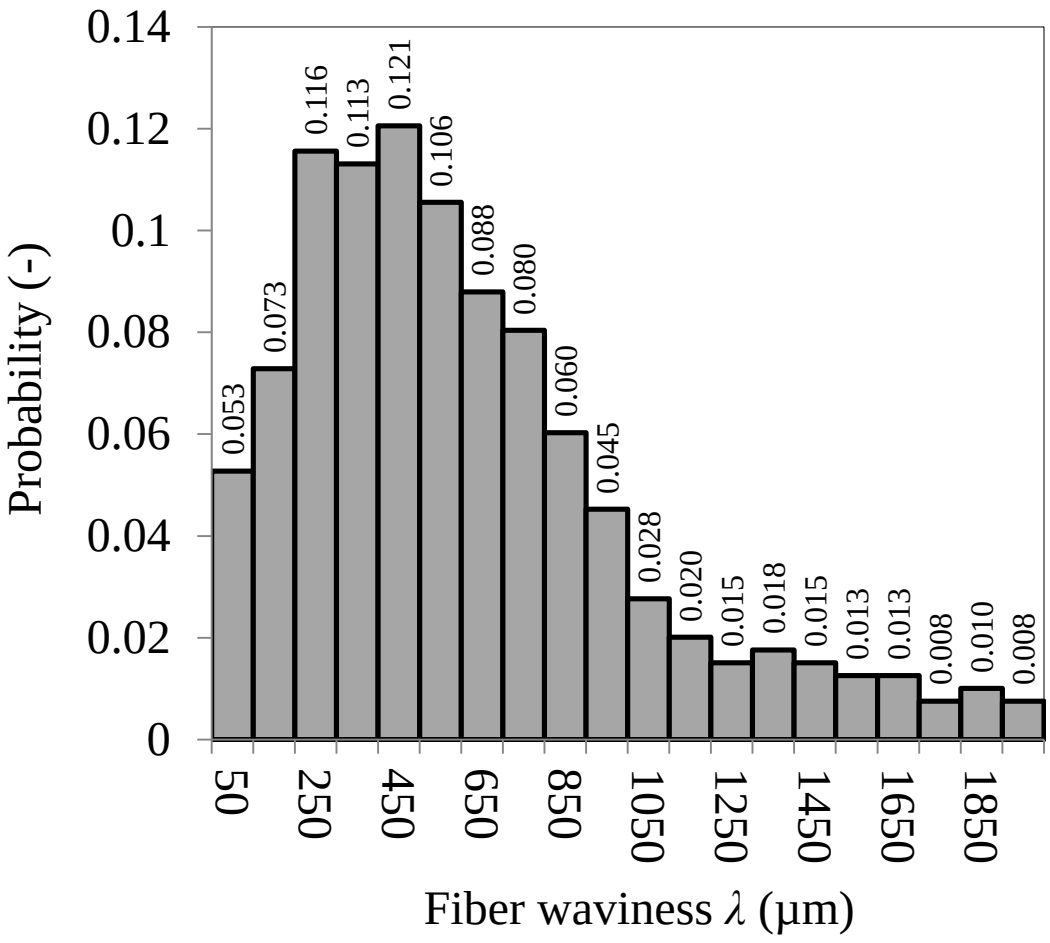

(a) Distribution of fiber waviness

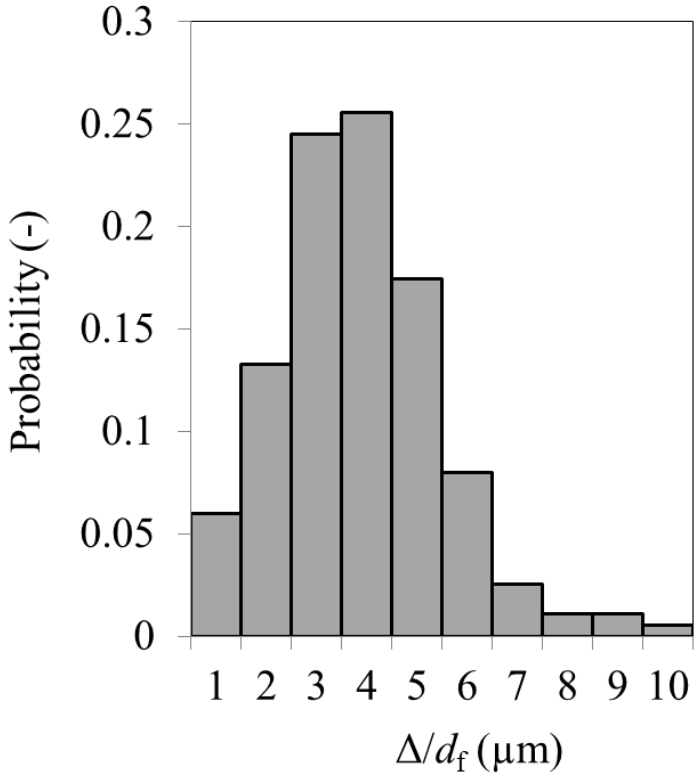

(b) Distribution of fiber amplitude

Figure 5.4. Statistical data of (a) fiber waviness and (b) fiber amplitude for Sigracet (SGL) GDLs

The apparent lengths of the GDL fibers were optically measured and their lengths were obtained by calculating the length of the sinusoidal arc. Nevertheless, because of the small waviness, the real length can be simply calculated mathematically:

$$l_f = 2(N_s - 1)\sqrt{\Delta^2 + \lambda^2/4} \approx l_{fap} \qquad (5\text{-}1)$$

The total number of fibers in one layer of GDL, N_{ft}, and the number of contact strips that each fiber can form on the flat surface, N_s, can also be obtained from the geometrical data of the GDL:

$$N_{ft} = \frac{4A(1-\varepsilon)}{\pi d_f l_f} \tag{5-2}$$

$$N_s = \frac{L_{fap}}{\lambda} + 1 \tag{5-3}$$

The geometrical equations and GDL's parameters required in the model have already been presented in detail (also see Refs. [52] [89] [110]) and are simply summarized in Table 5.1.

Figure 5.3 shows the 'contact strips' in the contact plane, where the contact area between the flat surface and the wavy fibrous porous medium occurs. The GDL fibers have a relatively small amplitude Δ and a wavelength λ. The dimensions of these contact strips, a and t, grow with increasing compression as illustrated in Figure 5.3. The contact strips dimensions can be calculated using the Hertzian contact theory and by applying a force balance. Here we first focus on the contact between one fiber and a flat surface and, then, extend the model to all contacting fibers.

Table 5.1. Summary of geometrical and mechanical parameters of the studied GDLs and mechanical variables used in the present model

Symbol	Parameter	Units	Value/equation	Basis	Eq./Fig.
E	Young modulus of fiber & plate	GPa	210 & 210 [89] [57]	Meas.	-
υ	Poisson ratio of fiber & plate	-	0.3 & 0.3 [89] [57]	Meas.	-
k	Thermal conductivity of fiber & plate	W m^{-1} K^{-1}	115 [89] [57] & 70 [110]	Meas.	-
l_{fap}	Apparent fiber length	µm	3,000	Meas.	-
d_f	Fiber diameter	µm	7.5	Meas.	-
λ	Wavelength	µm	50-1,900	Meas.	Figure 5.4a
Δ	Amplitude	µm	$4d_f$	Meas.	Figure 5.4b
A	GDL cross-sectional area (apparent surface area)	m^2	0.000507	Meas.	-
ε	Nominal porosities of SGL 24AA & 25AA	-	0.88 & 0.92 [52]	Meas.	-
σ	Roughness of GDLs SGL 24AA & 25AA	µm	17.0 ±3.5 & 31.0 ±4.5 [159]	Meas.	-
m	Asperities slope for GDL	-	$0.076\sigma^{0.52}$ [182] [185] [181] [211]	Calc.	-
H_{el}	Effective elastic modulus	Pa	$\frac{E^* m}{\sqrt{2}}$ [212] [213] [214]	Calc.	-

5.1.2. Mechanical modeling

Thermal energy transfers from one fiber to the flat surface through the contact strips at the interface. The resistance to heat conduction depends on the contact area. The pressure distribution can be calculated for an elastic flat surface in contact with an elastic wavy cylinder, as shown in Figure 5.3, from Ref. [215]:

$$p(x) = \frac{2\bar{\mathrm{p}}\cos\left(\frac{\pi x}{\lambda}\right)}{\sin^2\left(\frac{\pi a}{\lambda}\right)}\left(\sin^2\left(\frac{\pi a}{\lambda}\right) - \sin^2\left(\frac{\pi x}{\lambda}\right)\right)^{\frac{1}{2}} \tag{5-4}$$

where x is a space variable defined along the cylinder axis and $\bar{p}$ is the mean pressure, which is related to the length of each contact strip using Hertzian theory as:

$$\bar{p} = \left(\frac{\pi E^* \Delta}{\lambda}\right)\sin^2\left(\frac{\pi a}{\lambda}\right) \tag{5-5a}$$

This can be written in an explicit form in terms of contact strip length as [215]:

$$2a = \frac{2\lambda}{\pi}\arcsin\left(\frac{\lambda\bar{p}}{\pi E^* \Delta}\right) \tag{5-5b}$$

Using both Hertzian theory and force balances on fibers contacting the flat surface, the width of each contact strip, $2t$, can be obtained as a function of the apparent load F (the load applied on the entire GDL, see Figure 5.3 and Figure 5.5):

$$2t = \left(\frac{4F d_f}{N_f(N_s - 1)aE^*\pi}\right)^{\frac{1}{2}} \tag{5-6}$$

(a):

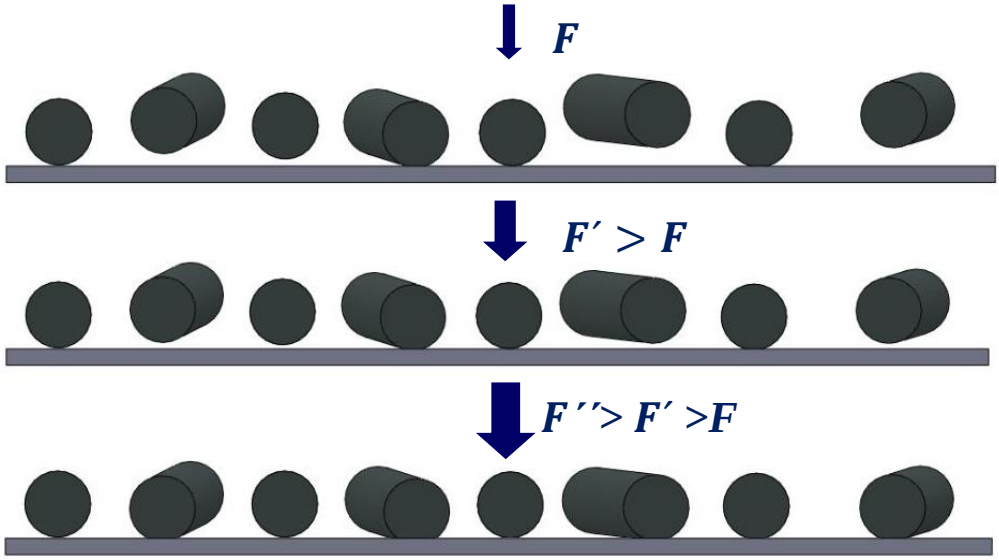

(b):

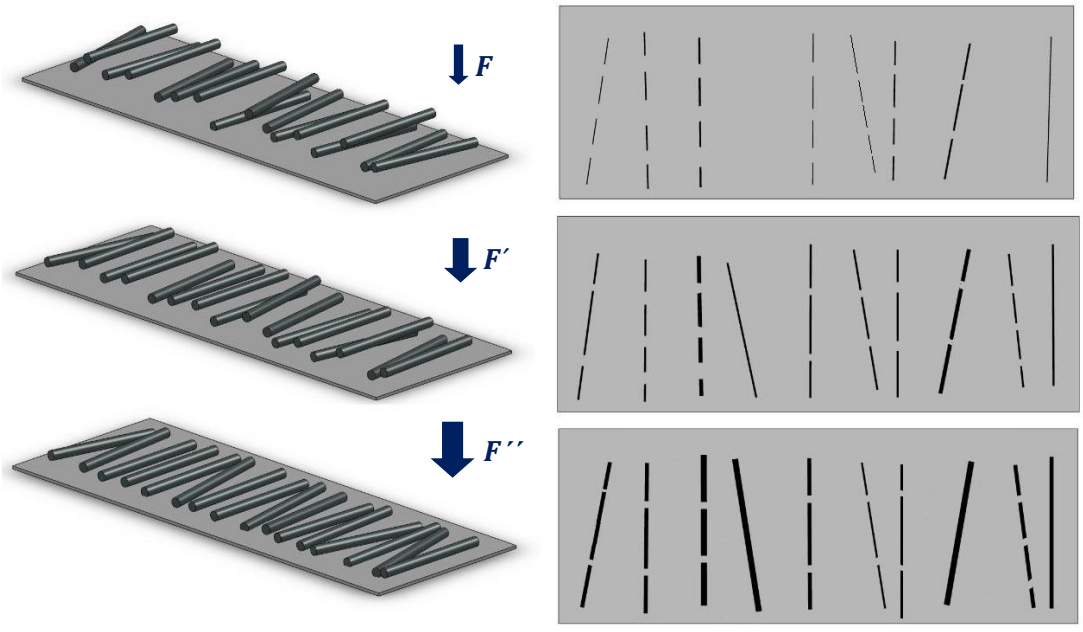

Figure 5.5. **(a) Gaussian distribution of the distance of fibers at the GDL *surface* from the flat plate; (b) the variations in the number and size of contact areas with respect to compression (*F′′> F′>F*)**

It is evident from the above equations that the geometrical parameters of the contact strips are highly nonlinear and coupled, and hence no explicit functionality can be derived for the contact area dimensions. However, for most applications, the value of a/λ is small, and the term $\sin(\pi a/\lambda)$ reduces to $\pi a/\lambda$, which makes the analysis simpler. Hence, for most applications including GDLs, one can obtain the length of each contact strip ($2a$) in terms of accessible/measurable parameters (especially *F*), directly from the following equation:

$$2a = \frac{1}{8\pi^4}\left(\frac{\lambda^2}{\pi\Delta}\right)^{\frac{2}{3}}\left(\frac{2F}{N_f(N_s-1)E^* d_f}\right)^{\frac{1}{3}} \tag{5-7}$$

Having calculated the contact strip length ($2a$), the value of the strip width ($2t$) can be directly obtained from Eq. (5-6).

GDL surfaces are not flat and show a random distribution of the surface asperities. Following Mikic [214] and Bahrami [213], we here assume a Gaussian distribution for the distance between fibers and the flat surface, which is a function of compression as shown schematically in Figure 5.5. Mikic [214] reported a relationship for the number of Gaussian asperities of an elastic body contacting a flat surface, as a function of compression, as:

$$n_s = \frac{1}{16}\left(\frac{m}{\sigma}\right)^2 \frac{\exp(-2\gamma^2)}{\operatorname{erfc}(\gamma)} A \tag{5-8a}$$

$$\gamma = \operatorname{erfc}^{-1}\left(\frac{4P}{H_{\text{el}}}\right) \tag{5-8b}$$

where m, σ, γ, A, H_{el}, P are asperity slope, GDL effective surface roughness, dimensionless mean plane separation, apparent (total) area, elastic micro-hardness, and pressure, respectively. It is worth mentioning that m is a weak function of σ (see Table 6.1) and, for most applications, a value of m=0.1 can be used [214]. The number of fibers

contacting the surface (N_f) at any compression of P can be obtained by the same proportionality as Eq. (5-8) proposes:

$$\frac{N_f}{N_{ft}} = \frac{n_s}{n_{st}} \tag{5-9}$$

where N_{ft} is the total number of fibers as given in Table 6.1. According to Eq. (5-9), the present model uses only the proportionality of Eq. (5-8), as it obtains N_{ft} from the GDL porosity. Therefore, the TCR results are not sensitive to overall GDL roughness in the range of 1-3d_f reported in the literature [104] [159] [216]. n_s is calculated at the compression applied on the sample (e.g., P=4-20 bar) and n_{st} at a compression where no further fiber slippage occurs [56] and also the main gaps between consecutive fibers [217] [218] disappear as a result of compression. This compressive pressure (P_{st}) corresponds to the compression after which no practical change can be observed in the population density of the contact spots on a pressure indicating film [219] compressed against the sample. Figure 5.6 illustrates this behavior and shows how the contact spots population increases with compression up to a value of approximately 50 bar. It can be observed from Figure 5.6a that the change in the number of contact spots from the image related to P=10 bar to that of P=45 bar (the first row) is significant (with a change in the contact area percentage from 3.5 to 42.4%) but no considerable change can be seen between the two images related to the pressures of 45 and 55 bar (contact area percentages of 42.4 % and 47.2%) compared to the transition from 10 to 45 bar. A similar discussion can be made for the images in the second row mapping the contact spots pressures ranging from 100 to 500 bars. It should be noted that the model sensitivity on P_{st} is low. Therefore, an approximate value of P_{st} also leads to sufficiently accurate TCR results. For this reason, the P_{st} obtained for a virgin sample can also be used for any compressed samples for cyclic loading of the samples.

It is also worth mentioning here that the model uses GDL surface image, or the stress-strain data, to only estimate the compression at which *all* fibers come into contact with

the plate surface (P_{st}), which is completely different from the fuel cell stack clamp pressure (P) as a variable in the model. In turn, P_{st} is only one constant parameter in the model, similar to the other properties used.

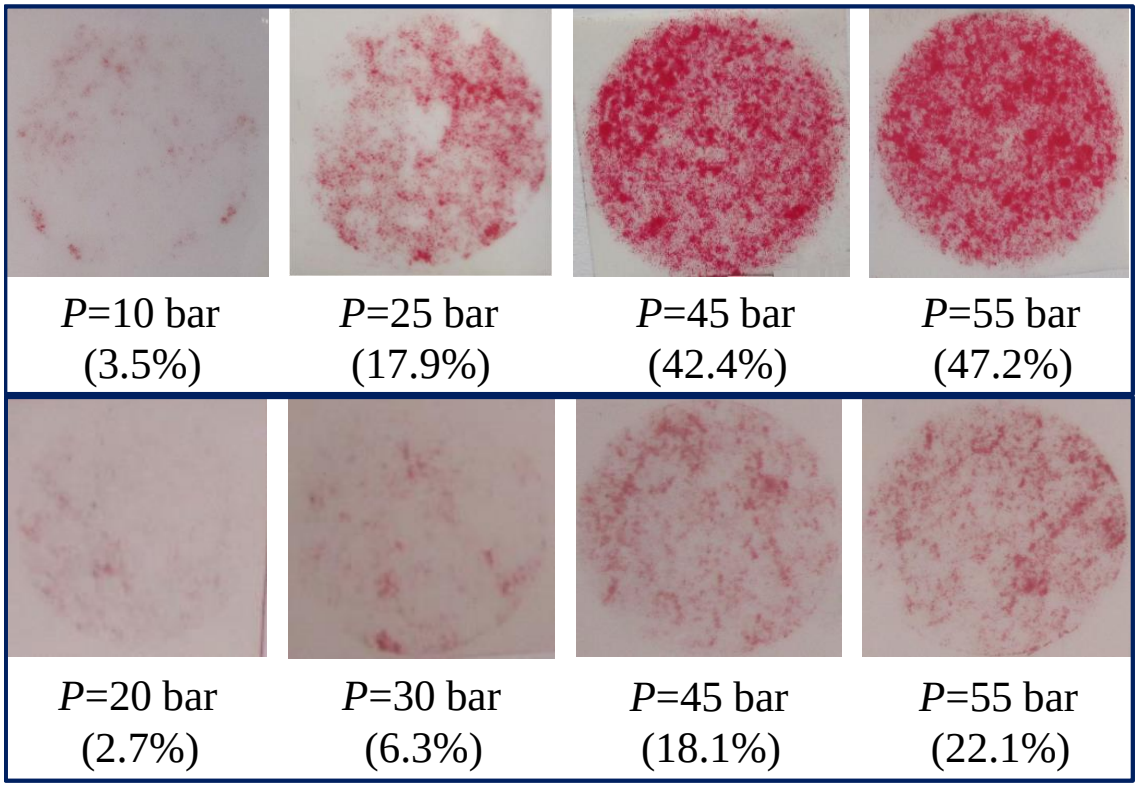

(a)

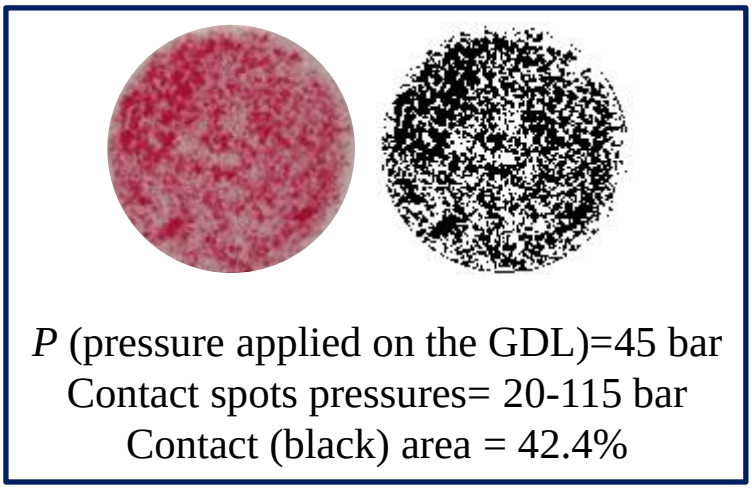

(b)

Figure 5.6. **(a) Image of a GDL (24BA) on a pressure indicating films (Fujifilm) [219], with contact spots pressures in the range of 20-115 and 100-500 bars (light red-dark red) shown in the first and second rows, respectively. These images show how the population of the contact spots increases with compression up to a value of approximately P_{st}=50 bar. Using the "ImageJ" software [220], percentage of the contact area for each image has been calculated and reported in parentheses, and is shown for one of the images in Fig. 10b; (b) In the black-and-white image produced by the "ImageJ" software, the black color represents the contact area and the while color shows the non-contact area**

5.1.3. Thermal modeling

Due to the very small area of the contact strips, the heat transferred from one fiber to the flat surface encounters a large resistance, mostly referred to as spreading/constriction resistance. The spreading/constriction resistance that occurs on the cylinder (fiber) side can be obtained by [221]:

$$R_c = \frac{1}{2a\pi k_c}\ln\left(\frac{2d_f}{t}\right) - \frac{1}{4ak_c} \tag{5-10}$$

And that on the flat surface is given as [221]:

$$\begin{aligned} R_F &= \\ &= \frac{1}{a^2 u\lambda k_F}\sum_{n=1}^{\infty}\frac{\sin^2\left(\frac{2n\pi a}{\lambda}\right)}{\left(\frac{2n\pi}{\lambda}\right)^3} + \frac{1}{t^2 u\lambda k_F}\sum_{n=1}^{\infty}\frac{\sin^2\left(\frac{n\pi t}{u}\right)}{\left(\frac{n\pi}{u}\right)^3} \\ &+ \frac{2}{a^2 t^2 u\lambda k_F}\sum_{n=1}^{\infty}\sum_{n=1}^{\infty}\frac{\sin^2\left(\frac{2n\pi a}{\lambda}\right)\sin^2\left(\frac{n\pi t}{u}\right)}{\left(\frac{2n\pi}{\lambda}\right)^2\left(\frac{n\pi}{u}\right)^2\sqrt{\left(\frac{2n\pi}{\lambda}\right)^2+\left(\frac{n\pi}{u}\right)^2}} \end{aligned} \tag{5-11}$$

where u is the half width of the rectangular heat channels on which the isoflux (rectangular) contact strips are located centrally and can be obtained by:

$$2u = \frac{A}{\lambda N_f(N_s - 1)} \tag{5-12}$$

It is worth mentioning that the summation of all the heat channels on the flat surface is equal to the GDL cross-sectional area. A detailed explanations on the heat channel concept for contact resistance estimation can be found elsewhere [213] [221].

The TCR for each contact strip is the sum of the two resistances given by Eqs. (5-10) and (5-11). Ultimately, the TCR between the GDL and the flat surface can be obtained using a parallel summation of all the contact strip resistances:

$$TCR = \frac{R_C + R_F}{N_f(N_s - 1)} \tag{5-13}$$

The TCR averaged over the entire range of the fiber waviness can be obtained by the summation of the TCRs for different waviness based on their occurrence probability for the GDL of interest:

$$TCR_{ave\,\lambda} = \sum_{j=1}^{n_j} p_{\lambda j} TCR_{\lambda j} \tag{5-14}$$

where $p_{\lambda j}$ is the probability of having the waviness of λj, which is given in Figure 5.4a, and $TCR_{\lambda j}$ is the value of TCR obtained from Eq. (5-13) for fiber waviness of λj. It should be noted that since the majority of the fiber amplitudes usually lies within a narrow range, using an average value of the amplitude is appropriate for the TCR calculations.

5.2. Model validation

Once the geometrical parameters of a GDL are determined, one can calculate the associated TCR as a function of compression. A computer code is developed in MATLAB to facilitate the TCR=f(P, λ, Δ, ε, d_f, d_{fsc}, l_f) calculations for the parametric study. It should be noted that fiber specifications (λ, Δ, d_f, d_{fsc}, l_f) and porosity (ε) of the virgin GDLs are geometric parameters required as input for the model and are thus used in the parametric study. The effect of these parameters on TCR is accounted for in conjunction with compression. For instance, with increasing compression, the number of fibers contacting the plate and the contact area dimensions (a and t) increase, as explained in Section "5.1.2 Mechanical modeling" and shown schematically in Figure 5.3 and Figure 5.5. The wavelength however does not change. It should be noted that all the *TCR* calculations in this study are based on one-inch circular GDLs (A=0.000507 m^2). The TCR per unit area of a GDL (TCR_A) can be obtained as TCR_A=TCR×A.

Figure 5.7 compares the results of the present model with the experimental data of this work for two GDLs, SGL 24AA and SGL 25AA. The results, shown by solid lines, are in good agreement with the experimental data and the model captures the experimental TCRs over a wide range of compression. Figure 5.7 shows that the TCR decreases with increasing compression, but the slope becomes progressively shallower and eventually, at high compression, the impact of compression on TCR becomes negligible, as expected. For SGL GDLs having an average amplitude of Δ/d_f=4 (Figure 5.4b), the model is in good agreement with experiments, except for very low pressures (2 bar) where the model provided less accurate estimations of the TCR at the complex interface of the GDL and the plate.

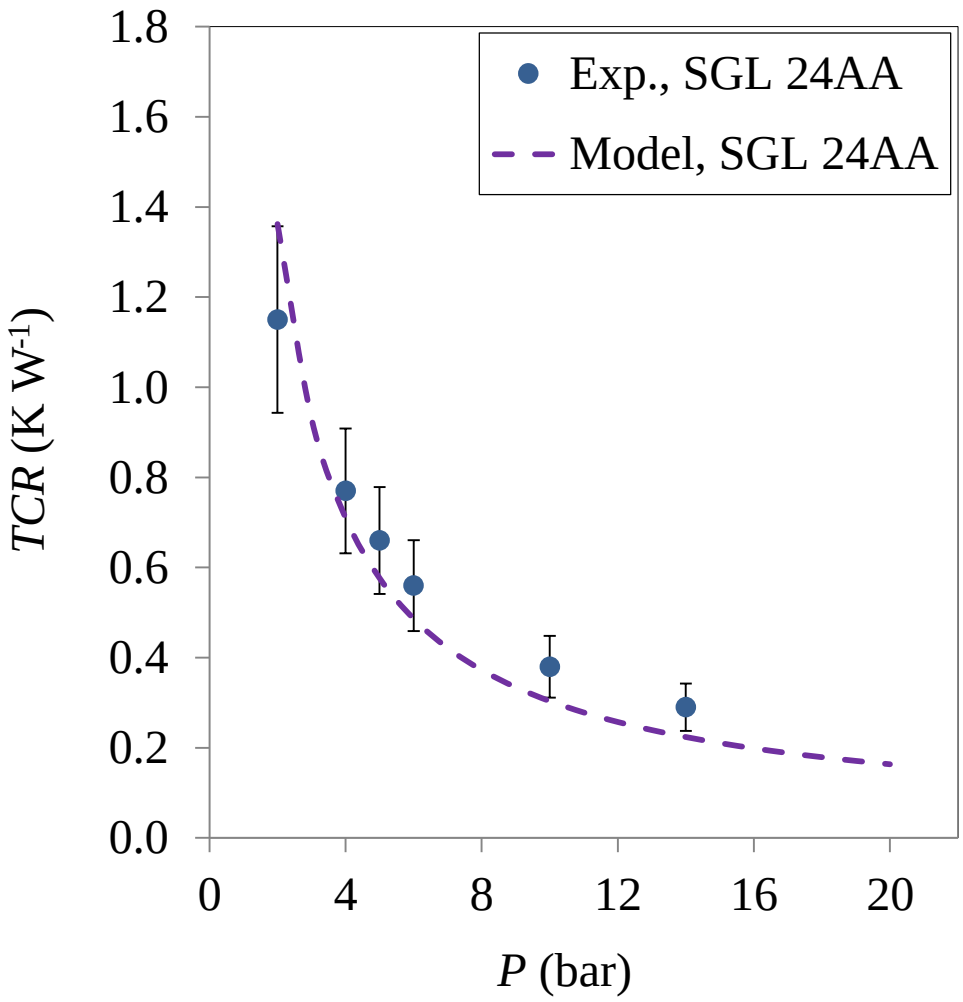

(a) GDL SGL 24AA

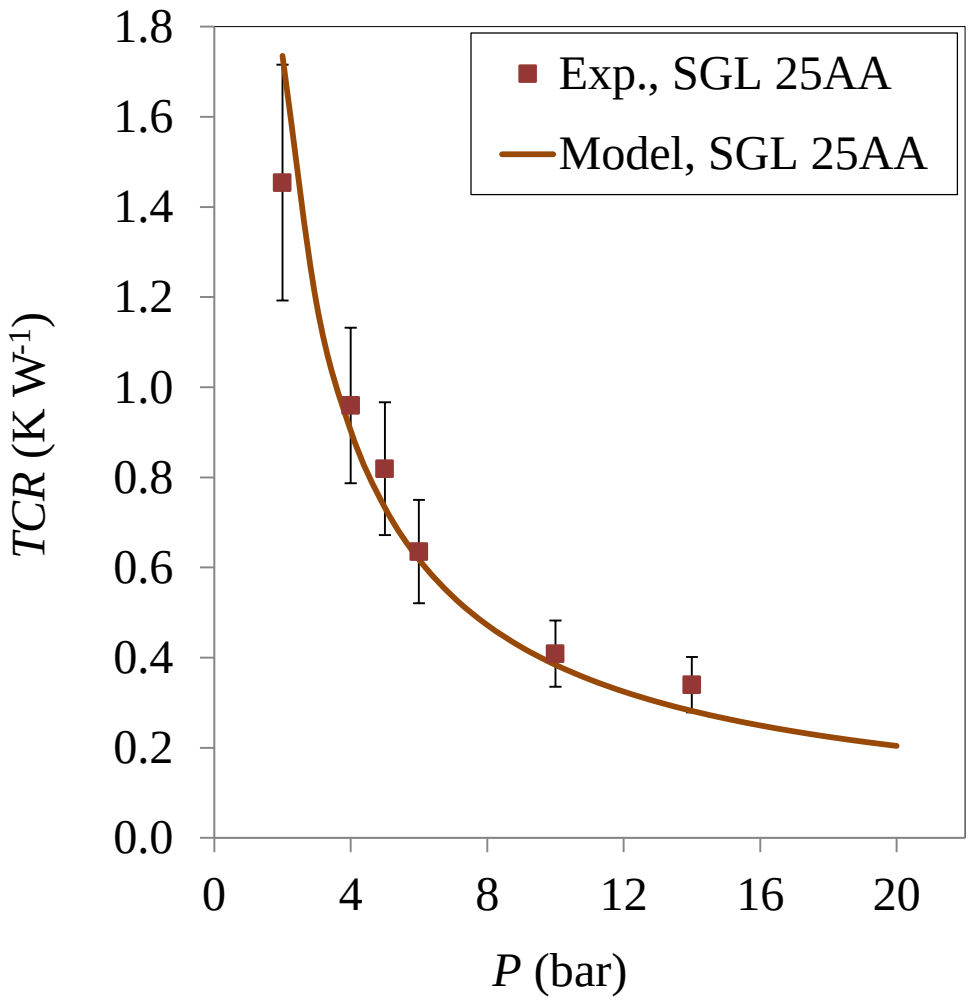

(b) GDL SGL 25AA

Figure 5.7. Comparison of model results (solid lines) and experimental data for SGL 24AA and 25AA (the GDL specifications are d_f=7.5 µm, l_f=3000 µm, Δ/d_f =4, A=0.000507 m^2, ε=88.3 & 92.1 % for the GDLs SGL 24AA & 25AA, respectively, as seen in Figure 5.4 and Table 6.1)

5.3. Parametric study

In order to investigate the effects of key parameters on the GDL-BPP TCR, a parametric study is performed in this section. For each case study, when a parameter is changed, the other parameters are kept constant unless otherwise mentioned.

5.3.1. GDL porosity (ε)

The most important and experimentally accessible parameter of a porous medium is porosity, whose effect on all the transport properties is usually significant. The effect of porosity on the TCR is shown in Figure 5.8 for three compressions of 4, 10 and 20 bar. The curves show similar trends for all three compressions and with increasing porosity, the TCR increases as well. One important point is that for each curve, especially at lower compressions, there is a specific value of the porosity at which a noticeable increase can be observed at the *rate* of the TCR variations. This specific porosity, determined here at the average slope of each *TCR-ε* curve on Figure 5.8, is approximately 89% at all three compressions. This point should be accounted for in GDL manufacturing and fuel cell design.

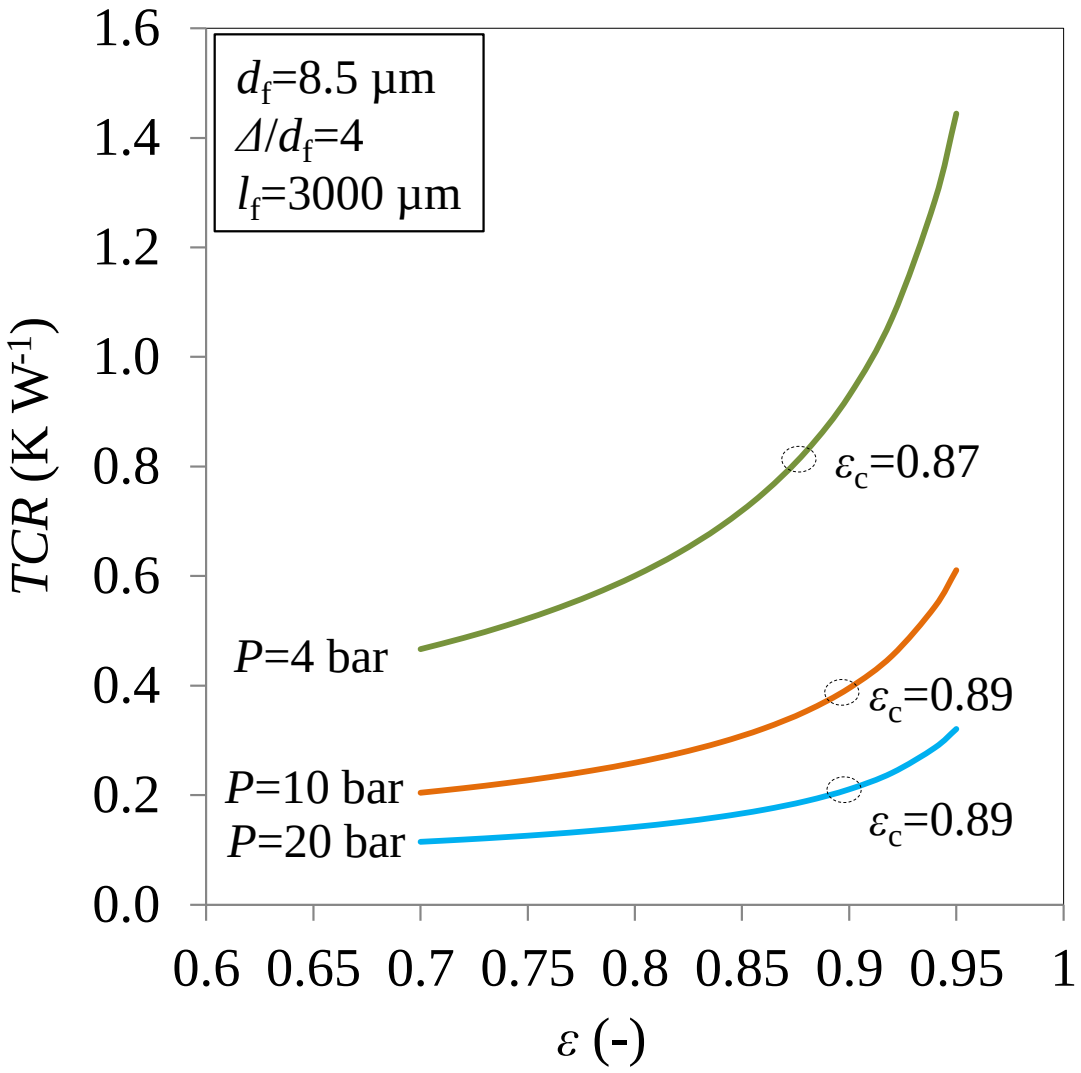

Figure 5.8. Impact of porosity on the TCR at different compressions

5.3.2. Fiber length (l_f)

Figure 5.9 shows that the fiber length does not have any effect on the TCR at different constant porosities. This is due to a trade-off between the number of fibers (N_f) and the number of contact strips each fiber can form on the surface (N_s) at a constant porosity. Increasing fiber lengths at constant porosity is equivalent to decreasing the number of

fibers; however, the number of contact strips increases as well, so that the total number of strips remains constant throughout the interface. As a result, the contact area does not change with changing average fiber length at a constant porosity, as observed in Figure 5.9.

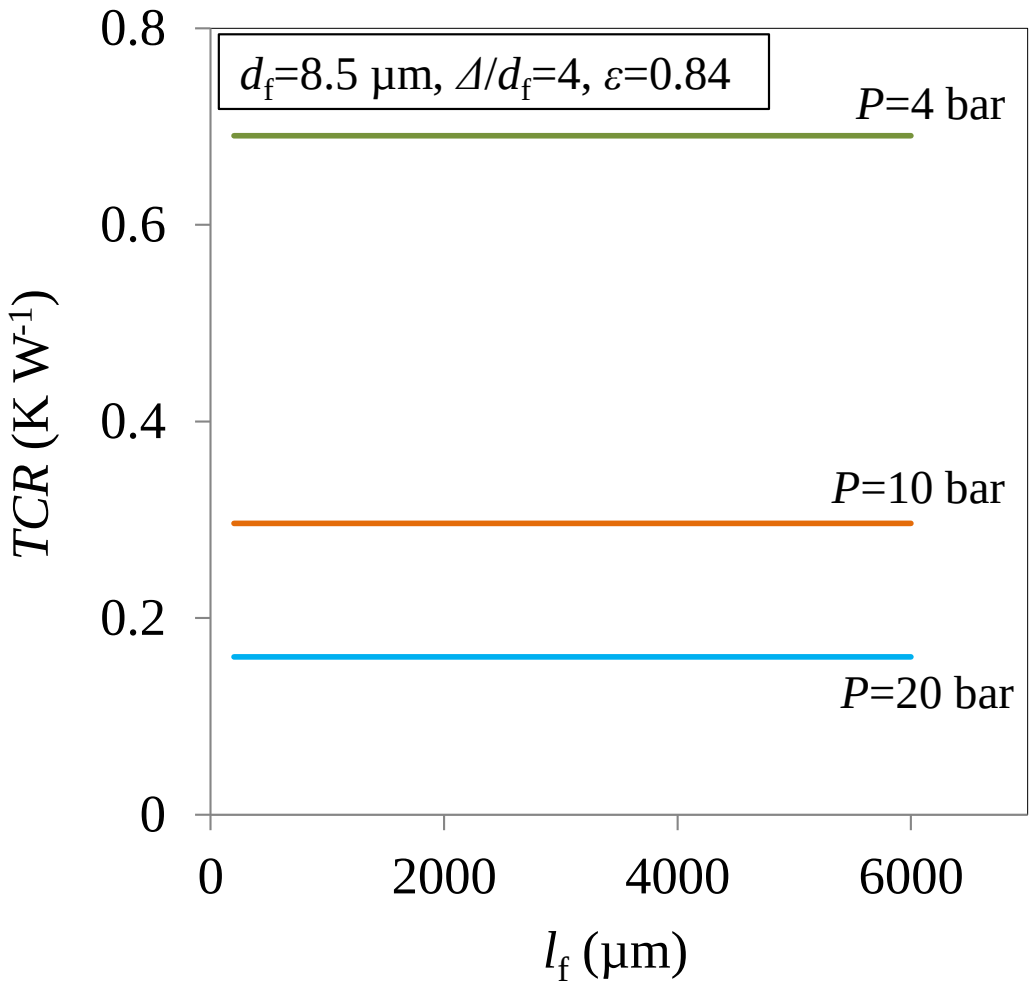

Figure 5.9. Effect of fiber length on the TCR at three compressions of 4, 10 and 20 bar

5.3.3. Fiber wavelength (λ)

One of the two key parameters in determining the GDL-BPP TCR is the fiber wavelength and amplitude, which determines the degree of waviness that the GDL fibers have. The impact of fiber wavelength is presented in Figure 5.10 for high and low porosity. TCR decreases noticeably with increasing fiber wavelength with a slope that is much more pronounced for lower compression (P=4 bar) and shorter wavelengths. The rate at which the TCR decreases become markedly lower where λ reaches a specific wavelength, determined at the average slope of any of the TCR curves in Figure 5.10, and corresponds approximately to 600 and 700 μm for the low and high porosity cases, respectively. This point can be an important consideration from the viewpoint of GDL manufacturing.

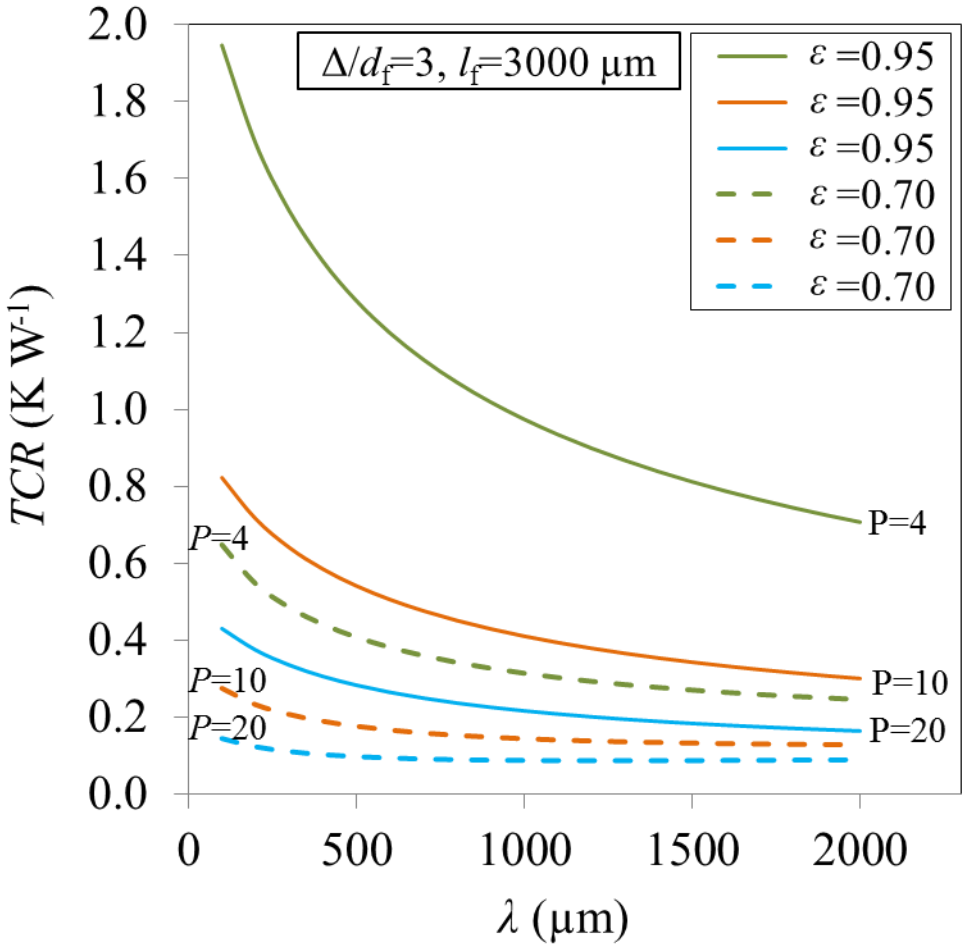

Figure 5.10. Impact of fiber wavelength on the TCR for low and high porosities at three different compressions

5.3.4. Fiber amplitude (Δ)

Figure 5.11 shows that the fiber amplitude can have a strong effect on TCR. However, for typical fiber amplitudes, i.e., 3-4d_f, the effect on TCR is not significant. At larger amplitudes, especially higher than 3d_f, this effect becomes negligible at medium to high compression. A similar trend was already seen in Figure 5.10 regarding the effect of the fiber wavelength on TCR.

Comparing the results of zero amplitude (Δ=0 µm), which corresponds to straight fibers, with those of other amplitudes clearly shows that the fibers waviness can increase the TCR drastically, even though its effect on the TCR drops noticeably beyond a specific value of approximately 1.5d_f. This point should be taken into account in design of both GDLs and fuel cell stacks in terms of heat management. For instance, GDLs consisting of very wavy fibers are expected to have a large contact resistance with the neighboring BPP and, hence, may be less effective in PEMFCs in terms of heat (and electrical) management.

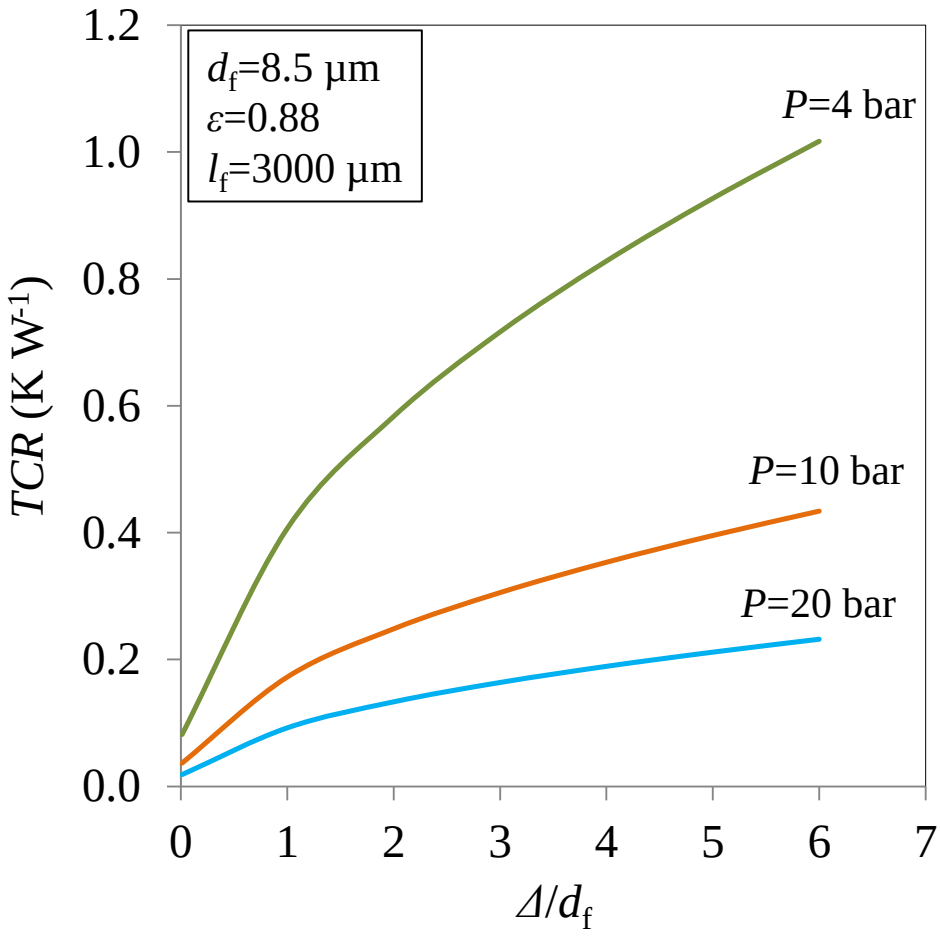

Figure 5.11. Effect of amplitude on the TCR for three different compressions

5.3.5. Fiber diameter (d_f)

Figure 5.12 shows that fiber diameter can significantly change the GDL-BPP TCR at low contact pressures and with increasing compression, its effect decreases. At high compressions, for a typical range of GDL fiber diameter, i.e., 7-10 µm [52] [89], the effect of fiber diameter on TCR becomes insignificant.

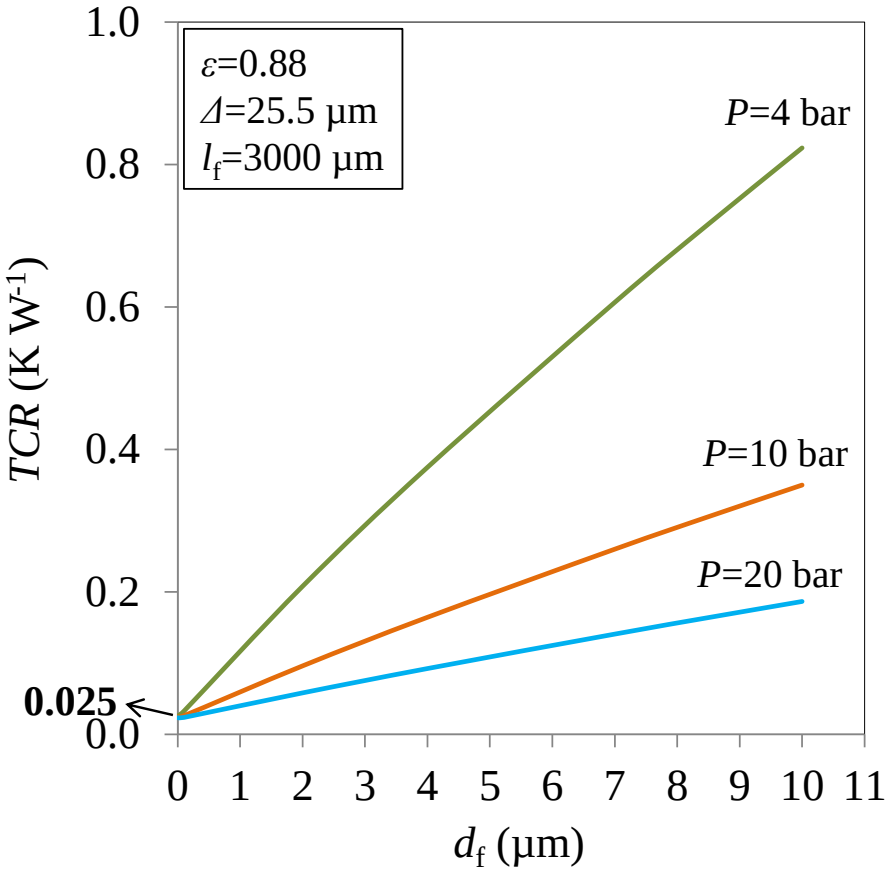

Figure 5.12. Effect of fiber diameter on TCR at three compressions of 4, 10, and 20 bar: Due to almost linear functionality of TCR with fiber diameter, no critical value for fiber diameter can be determined. However, the TCR reduces to 0.025 K W^{-1} as fiber diameter decreases

It is worth noting that the functionality of the TCR with fiber diameter is practically linear and, hence, no critical value for fiber diameter can be determined with respect to the TCR. However, as Figure 5.12 shows, with smaller fiber diameters, the TCR decreases and, eventually, converges to a very low value of 0.025 K W^{-1}, independent of the compression. This strongly suggests that GDL manufacturers explore production of GDLs with thinner fibers as long as other factors such as manufacturing capabilities or GDL mechanical strength allow.

5.3.6. Fiber surface curvature at the contact interface (d_{fsc})

Some types of fibers are not completely cylindrical; e.g., they may be ellipsoidal, while having the *same volume* as a cylindrical fiber. The deviation from a perfectly cylindrical shape can be accounted for by considering the effect of fiber surface curvature at the contact interface. The effect on TCR of fiber curvature (which in the limit of a cylinder is the fiber diameter) can be analyzed without changing any parameters to keep the GDL porosity constant (e.g., without changing the number of fibers). Figure 5.13 shows that, whereas TCR varies linearly with fiber diameter, its dependence on fiber surface curvature is highly non-linear and is particularly significant at very small curvatures. Comparing Figure 5.12 and Figure 5.13 also shows that, for typical values of fiber diameter and fiber curvature, the TCR is not as sensitive to the fiber surface curvature as to the fiber diameter (which determines both fiber surface curvature and fiber volume). Overall, the points presented in this study can also be taken into account in determining the TCR or ECR of GDLs with catalyst coated membranes (CCMs) [222] and micro porous layers (MPLs) [223].

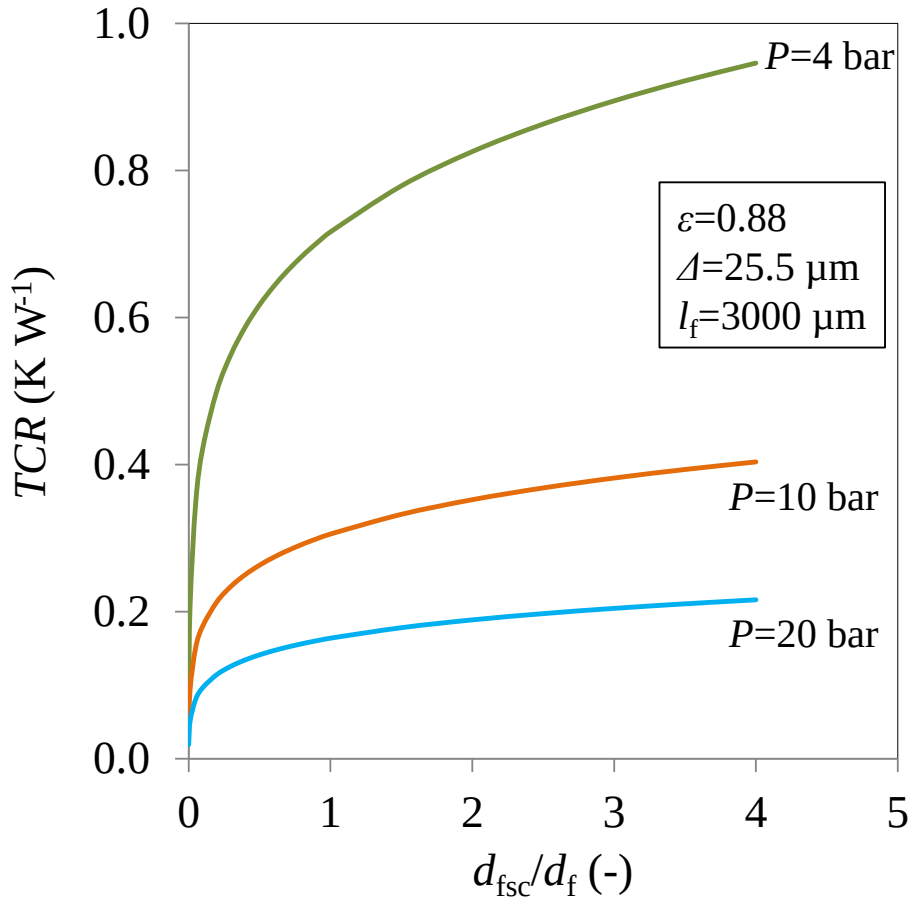

Figure 5.13. Effect of fiber surface curvature at the contact interface on the TCR: $d_f = d_{fsc}$ in all the equations except for Eq. (5-2) which relates the GDL porosity with the number and volume of the fibers

5.4. Concluding remarks

A new and robust mechanistic model was developed for predicting the thermal contact resistance between a general fibrous medium and a flat surface, and was used to analyze the contact between PEMFC gas diffusion layers and bipolar plates. The model accounts for the salient geometrical parameters, mechanical deformation and thermophysical properties, and captured accurately experimentally observed behavior over a wide range

of compression, except for very low compression (less than ~ 2 bar) where the model provided rough predictions of the TCR.

The model allows systematic investigation of the impact of the main GDL micro structural properties on TCR without having to rely entirely on more difficult experimental measurements. The simple and general model developed in this study can be readily implemented in fuel cell models and may also be used for modeling the behavior of any other fibrous porous materials such as fibrous insulations.

Chapter 6.

Modeling of MPL-GDL thermal contact resistance

Among the interfacial resistances in PEMFCs, the contact resistance between the gas diffusion layer substrate and neighboring micro porous layer (MPL) is important because of the potential impact of this interface on water transport. The contact resistance is challenging to study because of the different scales, porous structures and surface morphologies of GDLs (Figure 3.6) and MPLs (Figure 6.1) [224] [225] [226]. The MPL carbon particle clusters and their contact to one fiber are schematically illustrated in Figure 6.2 and Figure 6.3. The thermal contact resistances (TCR) of several Sigracet GDLs substrates with an MPL were measured in this work and reported in Chapter 3. The results showed that the contact resistance is not negligible. To the authors' knowledge, there has been no attempt to date to model the GDL-MPL contact resistance, from both thermal and electrical points of view.

The objective of the present modeling is to develop a robust analytic model to predict the TCR at the interface between a GDL and an MPL as a function of their salient morphological properties. The present model allows systematic investigation of the effect of various GDL and MPL specifications and provides insights and guidance for the development of new and improved materials for PEMFCs.

The present model is built using: (i) GDL and MPL geometric parameters, such as fiber/particle diameter, distribution and orientation of fibers, and GDL porosity; (ii) applied load, mechanical deformation, and Hertzian theory [215]; (iii) thermophysical

and mechanical properties of both contacting bodies, i.e., fibrous porous medium and MPL, properties such as thermal conductivities, and effective Young's modulus; and (iv) heat conduction through GDL fibers to MPL carbon particles (spreading/constriction resistances) considering rarefaction effects.

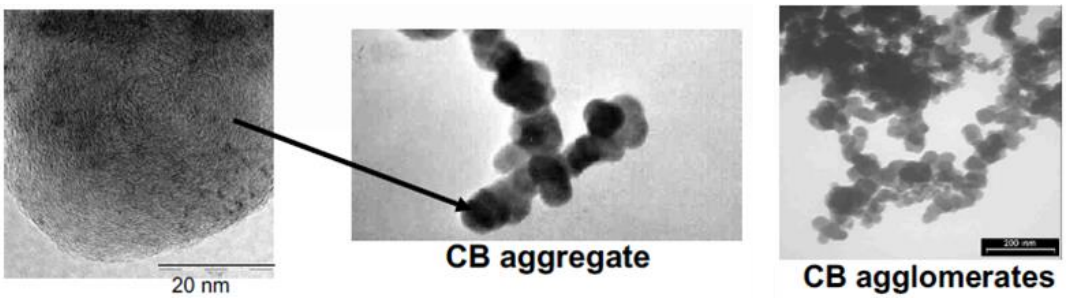

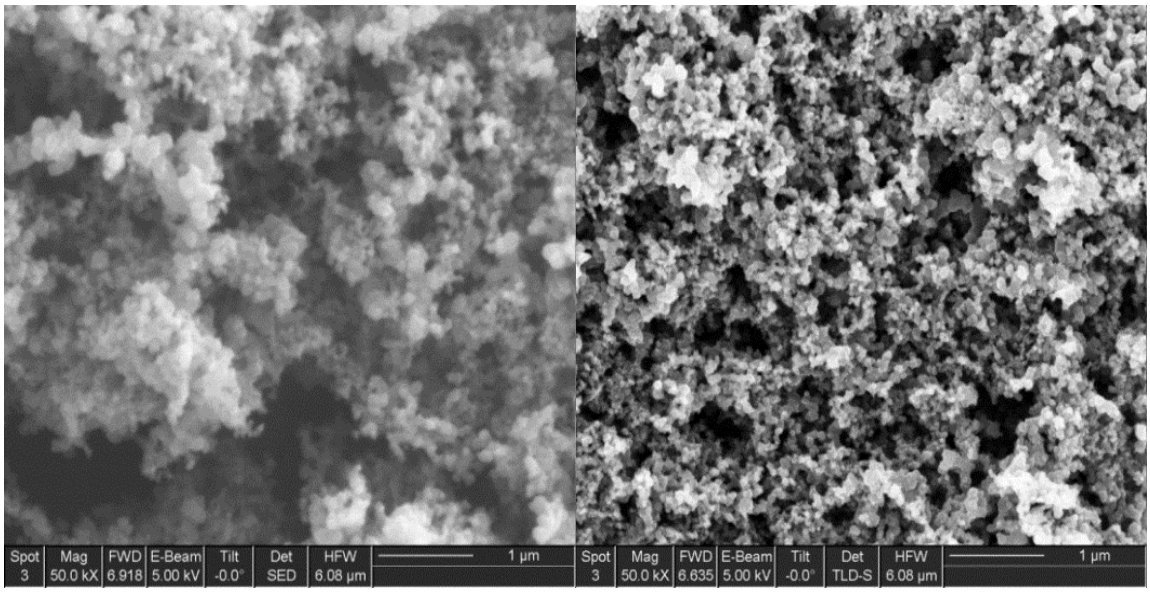

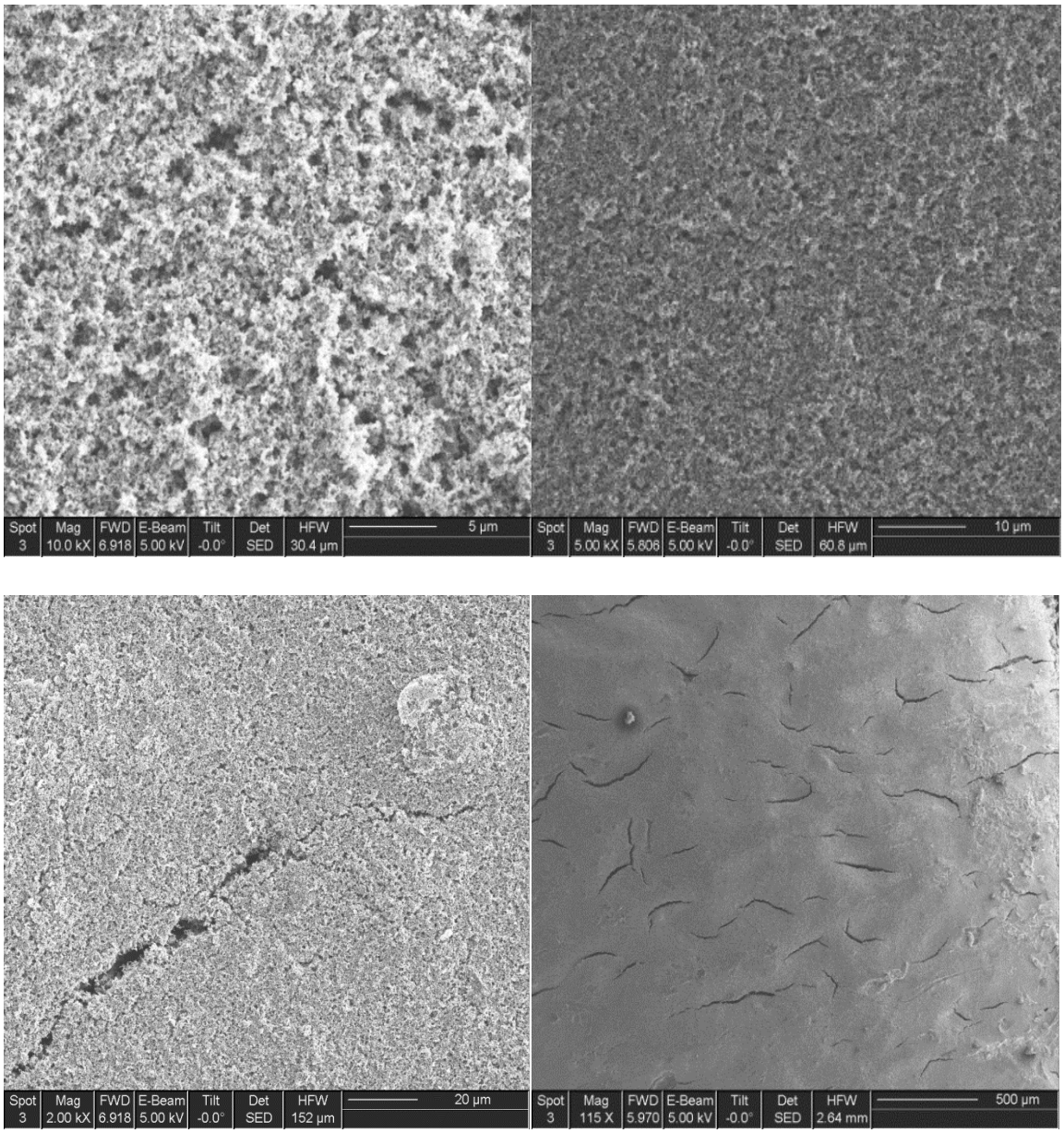

Figure 6.1. Images of an SGL MPL (present study) and carbon black (CB) agglomerates, clusters and particles [227]

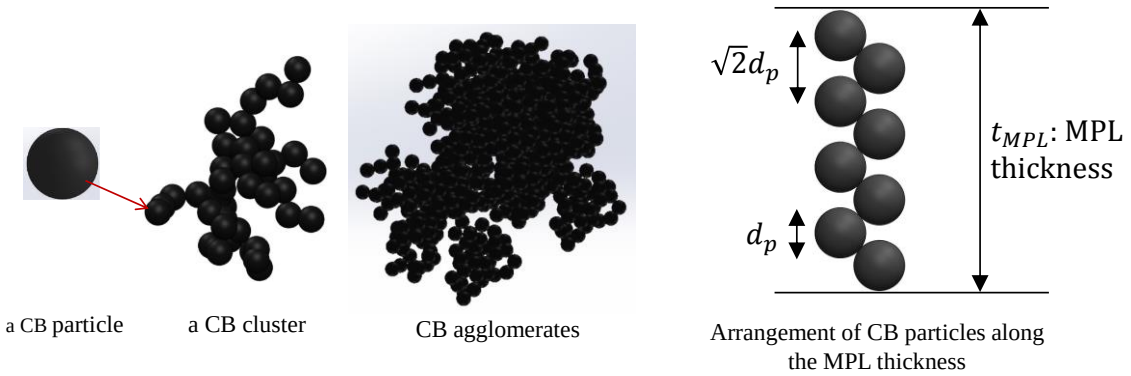

Figure 6.2. Geometrical modeling of the arrangement of spherical carbon particles arrangement inside an MPL: The number of MPL carbon particle layers can be obtained as $\sqrt{2}\ t_{MPL}/d_p$

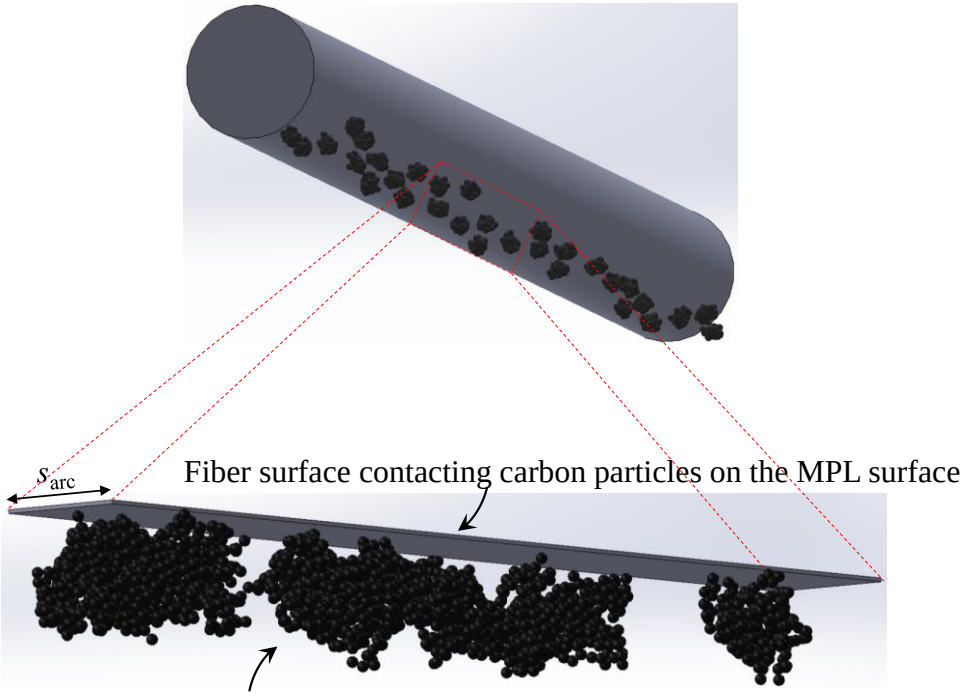

Figure 6.3. MPL carbon particles clusters and agglomerates, as the unit components of an MPL, contacting fibers (not to scale for the purpose of illustration); only carbon particles on the MPL surface touch the GDL fibers

The interfacial contact area of two contacting bodies is the key parameter in determining both electrical and thermal contact resistance, as well as in predicting other interfacial transport properties such as water and species transport. This area can be determined using geometrical and mechanical modeling. The TCR between the two mating bodies can then be obtained through the thermal modeling of the interface.

6.1. Geometrical modeling

6.1.1. MPL geometrical modeling

Scanning electron microscopic (SEM) and TEM images of MPL, as shown in Figure 6.1 (also see Ref. [227]), shows its structure as numerous clusters of randomly distributed spherical carbon particles. In terms of modeling, an MPL can be assumed as spheres clustered in different groups. Therefore, the MPL surface can be considered as a layer of spheres randomly located at different spots, with a Gaussian distribution of distances from the GDL fiber surface (Figure 6.4).

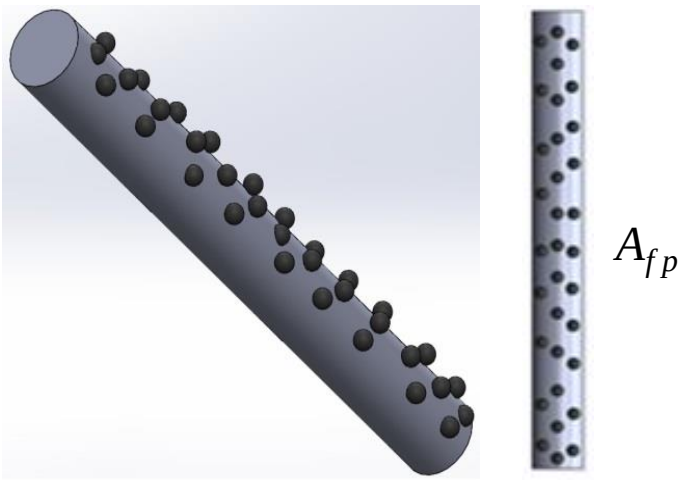

Figure 6.4. MPL spherical carbon particles contacting one GDL fiber: Left: isometric view and right: top view, showing the area of contact zone or macroscopic contact area (Not to scale: the size of particles has been exaggerated for clarity)

A thorough measurement was performed to determine the distribution of MPL carbon particle diameters. The statistical distribution of the MPL particle diameters shown in Figure 6.5 indicates that the majority of the particle diameters lie within the range of 40-70 nm (see also Ref. [228]), showing that the MPL carbon particles are small compared with the GDL fibers with diameters on the order of 10^4 nm. As a result, each of the fibers can be considered as a flat surface that the MPL carbon particles are in contact with.

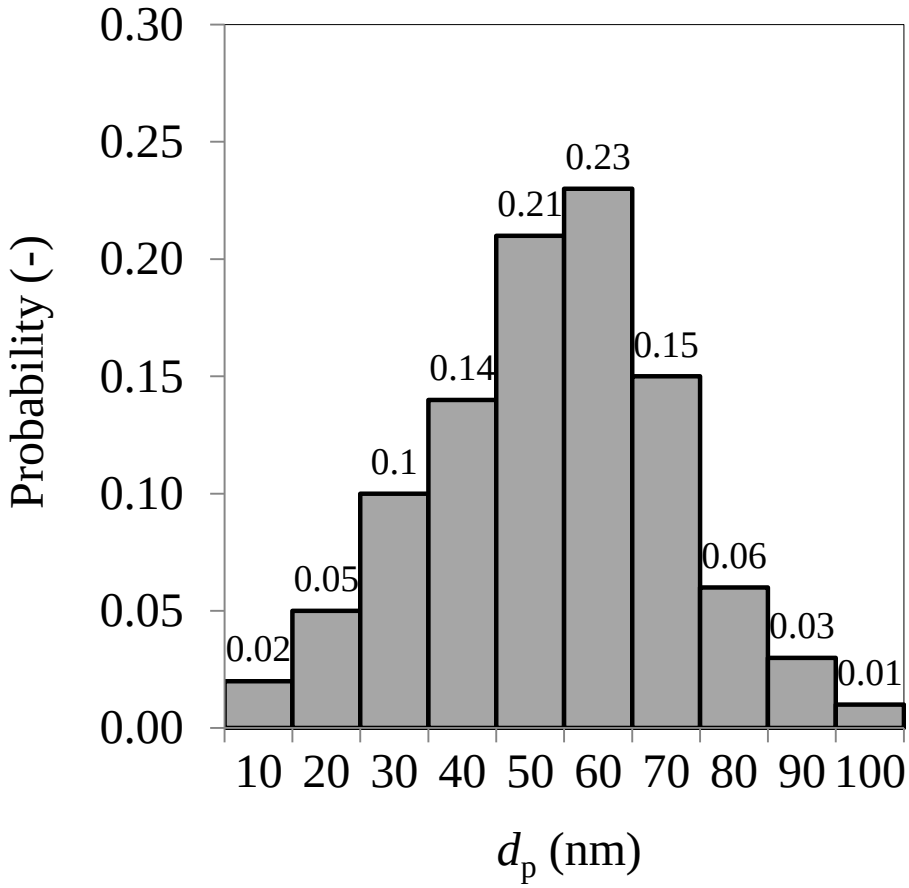

Figure 6.5. Statistical distribution of MPL carbon particles diameters: Probability of occurring each particle diameter in an MPL (p_{dp}) versus particle diameter (d_p)

MPL is made from carbon black and PTFE particles. The MPL coated on Sigracet GDLs has 23% PTFE [173], most of which accumulates inside the MPL. Energy dispersive X-ray (EDX) analyses of MPL surfaces show that the percentage of total PTFE area on the MPL surface is approximately 5% ($p_{\mathrm{MPL_S}}^{\mathrm{PTFE}}$=0.05) [224], also see Figure 6.6. The PTFE gives rise to large resistances in parallel to the lower resistances of the MPL carbon particles coated on the carbon fibers and, therefore, its effect on the TCR is negligible. For this reason, the small contact of MPL's PTFE with GDL is neglected in the thermal modeling but taken into account in calculating the active area of the coated MPL

contacting the GDL (Eq. (6-7)). A similar discussion can be made on GDL substrates with low PTFE loading, such as SGL GDLs 24BA and 25BA with 5% PTFE studied in this work, which are the substrates of SGL GDLs 24BC and 25BC, respectively. EDX analyses of SGL GDLs 24BA and 25BA show that the total area of the PTFE spots randomly scattered on the GDL surface is approximately 5% ($p_{\mathrm{GDL_S}}^{\mathrm{PTFE}}$=0.05) of the fiber surfaces (see Figure 6.7). The large thermal resistance of the PTFE on the fiber coming in parallel to the low resistance of the fiber carbon surface guarantees that the PTFE cannot directly affect the TCR and, hence, need not to be considered in the thermal modeling. However, this PTFE is accounted for in estimating the active area of the GDL contacting the coated MPL, see Eq. (6-6).

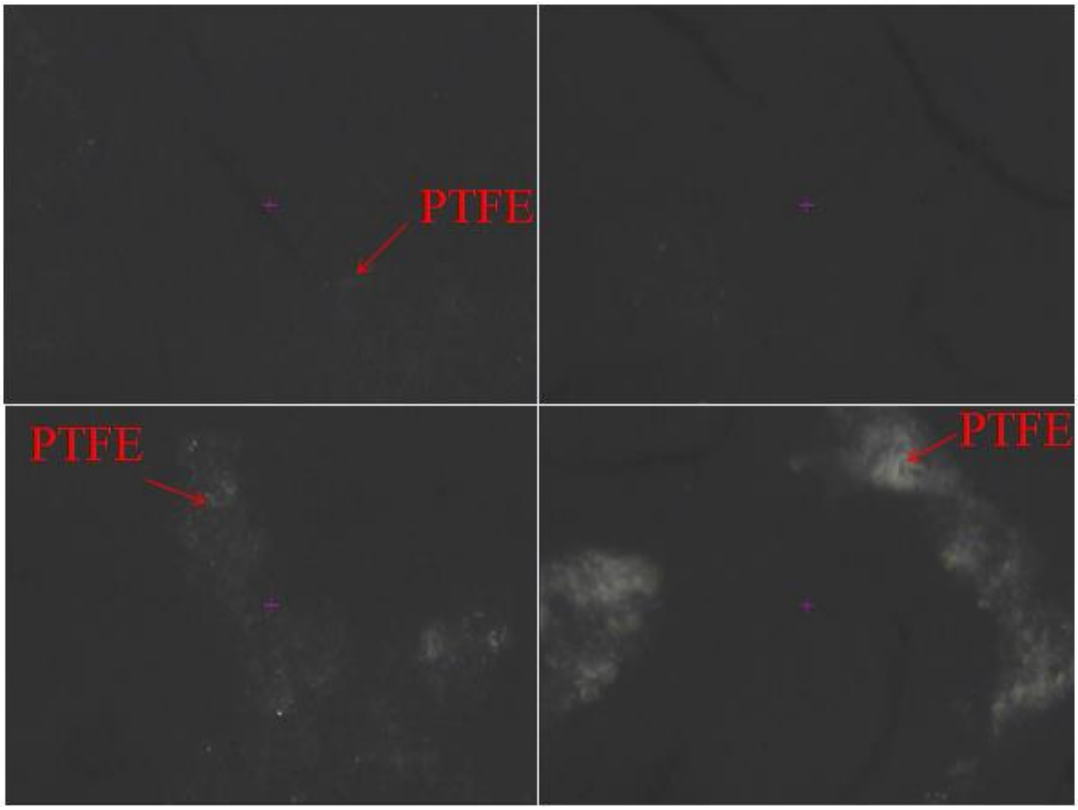

Figure 6.6. Optical images of an MPL showing PTFE on its surface (GDL SGL 25BC): This figure shows images of four different spots of an SGL MPL with randomly-scattered PTFE on it. Distribution of the 23% wt. PTFE across the MPL is not uniform and in some areas, more PTFE accumulations are observed. However, the PTFE detected on the most part of the MPL surface is low, with a surface coverage of approximately 5%, on average

a: GDL SGL 25BA (5% PTFE)

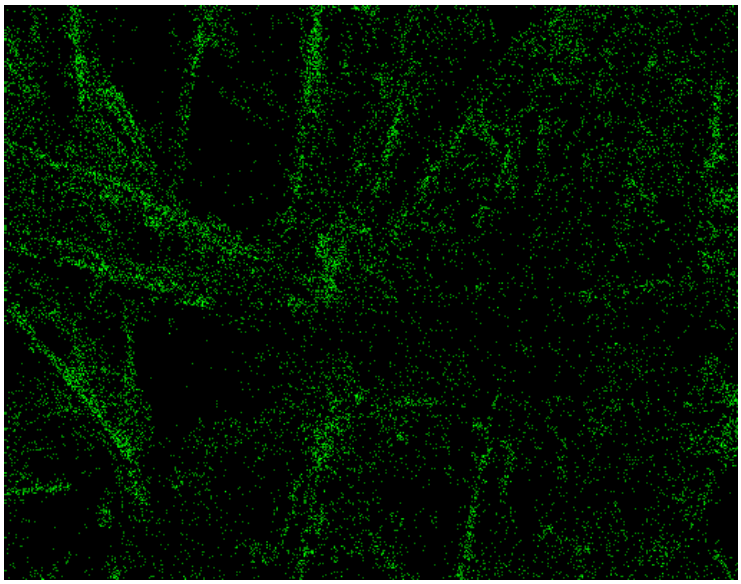

b: Green dots show fluorine in PTFE on each fiber of GDL SGL 25BA

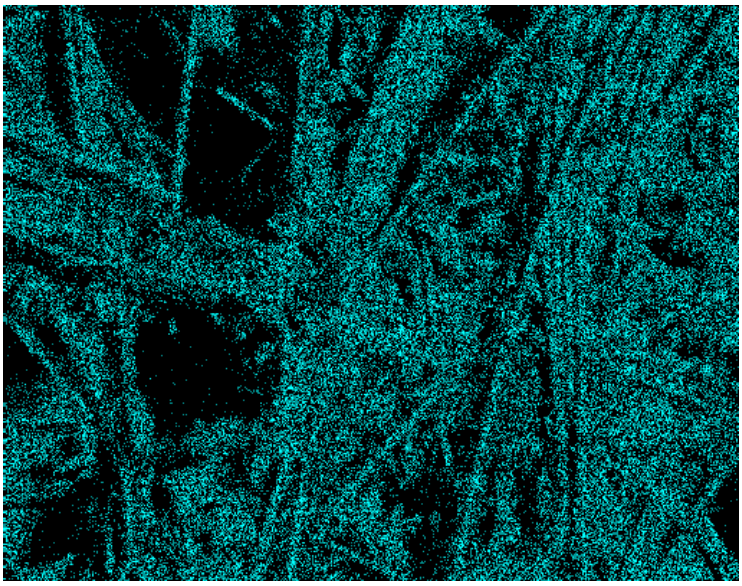

c: Blue dots represent the Carbon element on the GDL surfaces (GDL SGL 25BA)

Figure 6.7. GDL SGL 25BA and its EDX images for Fluorine (PTFE) and Carbon detection. It is observed that the PTFE amount scattered on the fibers surfaces is low (5%, on average) for this 5% PTFE-treated GDL

6.1.2. GDL geometric modeling

Based on microscopic GDL images, the fibers can be modeled as long cylinders with a Gaussian distribution of distances from the MPL surface, as schematically shown in Figure 6.8. Indeed, in terms of macroscopic modeling, the MPL can be considered to act as a flat surface with asperities of carbon particles in contact with the GDL fibers.

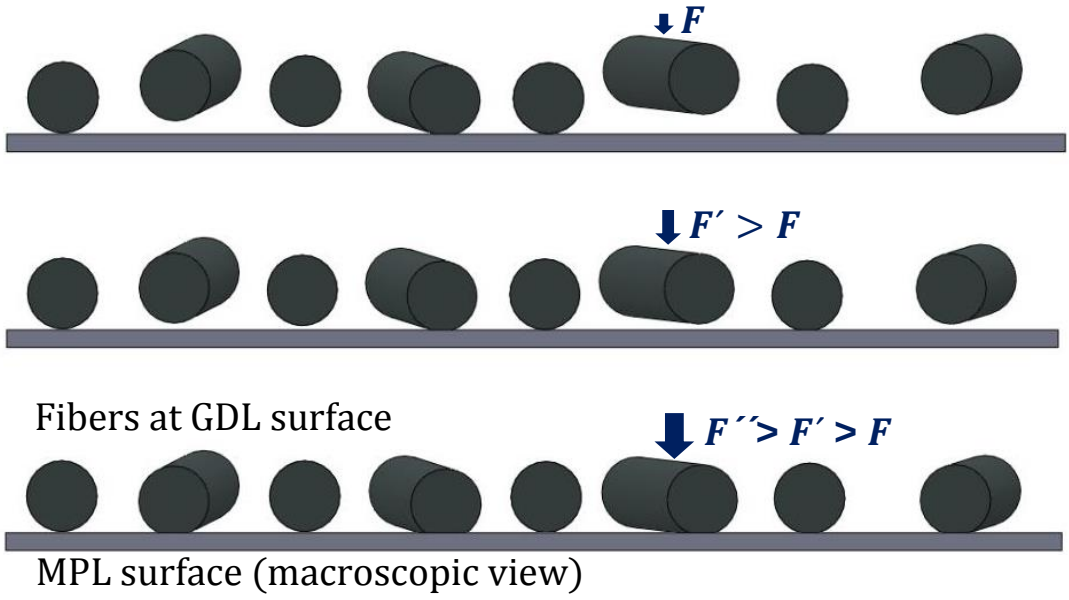

Figure 6.8. Gaussian distribution of the fibers at the GDL interface with an MPL: Increasing the compression brings more fibers into contact with the MPL

The assumptions of the proposed model include: 1) steady state heat transfer; 2) constant thermophysical properties; 3) cylindrical GDL fibers; 4) spherical MPL carbon particles; 5) elastic deformation; 6) static mechanical contact, i.e., no vibration effects; 7) small or negligible radiation effects (considering typical operating temperature range of PEMFC < 100 ^{o}C); 8) first loading cycle only, i.e. no hysteresis effects are considered (it should be noted that the proposed methodology is applicable to deformed (cycled) GDLs, given the deformed samples' geometric parameters can be measured); 9) short-range surface forces are negligible (Hertz/Surface forces $\approx 10^2$ for carbon particle-fiber contacts) [229] [230] [231] [215]; and 10) contact occurs in vacuum environment. It is worth mentioning that the effects of heat transfer on interstitial gases can be added to the model using the model of Ref. [232]. However, for convenience, the contact is studied in a vacuum. The geometrical equations and parameters of the GDLs and MPLs required in the present model are summarized in Table 6.1.

6.1.3. GDL-MPL interface

A schematic of the contact between spherical carbon particles of an MPL and cylindrical carbon fibers of a GDL is shown in Figure 6.9. The random distance between the fibers of the GDL surface and the carbon particles of the MPL surface are exaggerated in Figure 6.9. It is important to mention that although the MPL and GDL substrate interpenetrate each other rather than form a sharp and well-defined interface, there is nonetheless a contact resistance between the two media. The model focuses on the solid contact area and considers the total number of fibers and carbon particles at the interface. As a result, the model counts all of the contact spots (fibers-particles) even though they do not occur at the same plane or level.

Figure 6.9 also shows some ellipses as the contact area between one fiber and several carbon particles. The major and minor radii of these ellipses (a and b), which grow with increasing the load as illustrated in Figure 6.9, can be calculated using the Hertzian theory and force balances. Here we first focus on the contact between one (cylindrical) fiber and one (spherical) particle, and then extend the modeling to all the carbon particles contacting one fiber and, eventually, to all the fibers on the GDL surface.

Table 6.1. Geometrical specification and mechanical properties of the GDLs fibers

Symbol	Parameter	Units	Value or equation	Basis	Eq./Fig.
E	Young modulus of fiber & MPL carbon particles	GPa	210 & 210	Meas.	-
v	Poisson ratio of fiber & MPL carbon particles	-	0.3 & 0.3	Meas.	-
k	Thermal conductivity of fiber & MPL carbon particles	W m^{-1} K^{-1}	115 & 1.5 [110] [233]–[239]	Meas.	-
l_{fap}	Apparent fiber length	µm	3000	Meas.	-
d_f	GDL fiber diameter	µm	7.5, 8.5	Meas.	-
d_p	MPL carbon particle diameter	nm	10-100	Meas.	Figure 6.5
Δ	Fiber amplitude	µm	$4d_f$	Meas.	-
λ	Fiber wavelength	µm	50-1900	Meas.	-
N_s	Number of troughs of each fiber	-	$N_s = \frac{L_{fap}}{\lambda} + 1$	Derv.	(6-1)
l_f	Fiber length	m	$2(N_s - 1)\sqrt{\Delta^2 + \lambda^2/4}$ $\approx l_{fap}$	Derv.	(6-2)
s_{arc}	Arc length of fiber circumference in contact with MPL particles	m	$d_f \tan^{-1}\left(2\frac{d_p}{d_f}\sqrt{1+\frac{d_f}{d_p}}\right)$	Derv.	(6-3)
t_{MPL}	MPL thickness	µm	45 [173]	Meas.	-
ε_{MPL}	MPL porosity	-	0.42 (MPL mass=0.029 gram)	Meas.	-
ε_{GDL}	Nominal substrate porosities of GDLs SGL 24BA and 25BA	-	0.88 and 0.92 [173]	Meas.	-

N_{ft}	Total number of fibers at the GDL surface	-	$\frac{4A(1-\varepsilon_{GDL})}{\pi d_f l_f}$	Derv.	(6-4)
N_{pt}	Total number of carbon particles at the MPL surface	-	$\frac{\sqrt{2}d_p A(1-\varepsilon_{MPL})}{\frac{8}{3}\pi(\frac{d_p}{2})^3}$	Derv.	(6-5)
A	GDL and MPL cross-sectional area (apparent surface area)	m^2	0.000507	Meas.	-
ψ_{acGDL}	Active area percentage of a GDL surface at compression of *P*	m^2/m^2	$(N_f l_f s_{arc})(1-p_{GDLs}^{PTFE})/A$	Derv.	(6-6)
ψ_{acMPL}	Active area percentage of an MPL surface at compression of *P*	m^2/m^2	$(N_P \frac{\pi d_p^2}{4})(1-p_{MPLs}^{PTFE})/A$	Derv.	(6-7)
$p_{\psi\psi}$	GDL-MPL solid-phase contact probability	-	$\psi_{acMPL} \times \psi_{acGDL}$	Calc.	(6-8)
N_{p-1f}	Total number of carbon particles that come into contact with one fiber	-	$p_{\psi\psi} N_p / N_f$	Derv.	(6-9)
σ_{GDL}	Roughness of GDLs SGL 24BA & SGL 25BA	µm	17, 31 [159]	Meas.	-
m_{GDL}	Asperities slope (GDL)	-	$0.076\sigma_{GDL}^{0.52}$ [213]	Calc.	(6-10)
$H_{\text{el GDL}}$	Effective elastic modulus	Pa	$\frac{E^* m_{GDL}}{\sqrt{2}}$ [213]	Calc.	(6-11)
σ_{MPL}	MPL roughness of GDLs SGL 24BA & SGL 25BA	µm	2.5, 1.3 [159]	Meas.	-
m_{MPL}	Asperities slope (MPL)	-	$0.076\sigma_{MPL}^{0.52}$ [213]	Calc.	(6-12)

$H_{\text{el MPL}}$	Effective elastic modulus	Pa	$\frac{E^* m_{MPL}}{\sqrt{2}}$ [213]	Calc.	(6-13)

6.2. Mechanical modeling

Heat conduction from one GDL fiber to the MPL carbon particles it is in contact with occurs through the contact spots at the interface and the resistance to heat conduction depends on the contact area dimensions. The dimensions of the contact spots that appear in the case of the sphere-cylinder contact and the related Hertzian parameters and equations are summarized in Table 6.2.

Due to the low ratio of $d_p/d_f \approx 10^{-3}$, the sphere-cylinder contact can be considered as sphere-flat contact, which makes the modeling simpler. As a result, one can obtain the major and minor radii of the Hertzian contact area, i.e., a and b, from the sphere-flat contact relation listed in Table 6.2.

Table 6.2. Hertzian equations of a sphere-cylinder and sphere-plane contact [229]

Contact	Contact radius	Eq.
Sphere-cylinder contact	$1+\frac{d_p}{d_f}=\frac{(1/k^2)E(k')-K(k')}{K(k')-E(k')}$	(6-14a)
	$k'=\sqrt{1-k^2}$	(6-14b)
	$b=\sqrt[3]{\frac{3FkE(k')}{4\pi E^*}\left(\frac{1}{d_p}+\frac{1}{d_f}\right)^{-1}}=ka$	(6-14c)
Sphere-plane contact	$a=b=\sqrt[3]{\frac{3Fd_p}{8E^*}}$	(6-15)

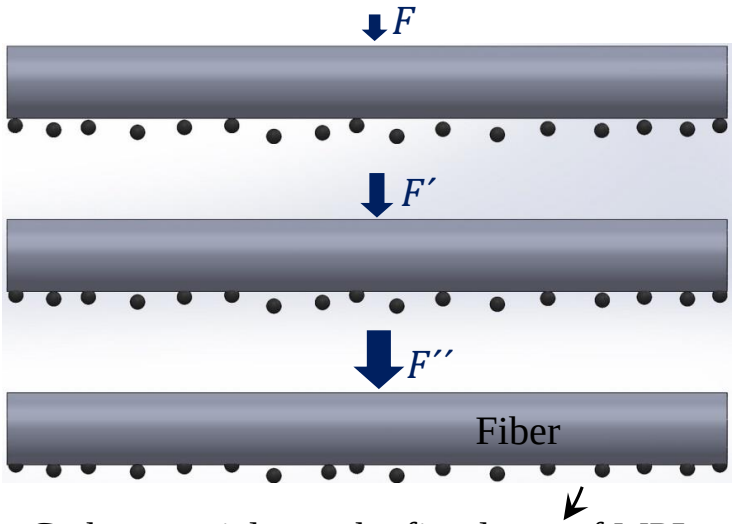

Carbon particles at the first layer of MPL contacting the fibers at the GDL surface

Figure 6.9. MPL carbon particles in contact with a GDL fiber: Increasing compression (*F*<*F′*<*F″*) increases the number and contact area of Hertzian contact ellipses (the size of particles and contact areas have been exaggerated for clarity)

GDL surfaces have a random distribution of surface asperities. Following Mikic [214] and Bahrami *et al.* [181] [182] [213], we assume a Gaussian distribution of spacings between fibers and the MPL surface (Figure 6.4 and Figure 6.9), which will be a function of compression:

$$n_{sGDL} = \frac{1}{16}\left(\frac{m_{GDL}}{\sigma_{GDL}}\right)^2 \frac{exp(-2\gamma_{GDL}^2)}{erfc(\gamma_{GDL})} A \tag{6-16a}$$

$$\gamma_{GDL} = \text{erfc}^{-1}\left(\frac{4P}{H_{elGDL}}\right) \tag{6-16a}$$

where m_{GDL}, σ_{GDL}, γ_{GDL}, A, H_{elGDL} and P are, respectively, asperity slope, GDL surface roughness, dimensionless mean plane separation, apparent (total) area, elastic micro-hardness, and compression (see Table 6.1). It is worth mentioning that m, the asperity slope, is a weak function of σ (RMS surface roughness) and, for most applications, a value of m=0.15 can be used [213] [221]. Considering this point and also the fact that the present model uses only the proportionality of Eq. (6-16), the TCR results are not sensitive to m and σ. The number of fibers contacting the surface (N_f) at a given compression of P can be obtained by the same proportionality as Eq. (6-16) proposes:

$$\frac{N_f}{N_{ft}} = \frac{n_{sGDL}}{n_{stGDL}} \tag{6-17}$$

where N_{ft} is the total number of fibers as given in Table 6.1. n_{sGDL} is obtained at the compression applied on the sample (e.g., P=4-20 bar) and n_{stGDL} at a compression where no further fiber slippage occurs [56] and the main gaps between consecutive fibers [217][218] disappear as a result of compression. This pressure (P_{st}) corresponds to the compression at which no practical change can be observed in the population density of the contact spots on a pressure indicating film [219] compressed against the sample. Figure 5.6a illustrates this behavior and shows how the contact spots population increases with compression up to a value of approximately 50 bar. Comparing the thickness-compression curves for GDLs with and without the MPL shows that the elastic behavior of the GDL substrate does not change much with the MPL coated on it. The population of MPL carbon black particles on the pressure indicating film shown in Figure 6.10 proves that at the pressure of approximately 50 bar, all carbon particles come in contact with the flat surface. It should be noted that the model sensitivity on P_{st} is low, as shown later in Figure 6.11. Therefore, an approximate value of P_{st} also leads to sufficiently accurate TCR results. For this reason, the P_{st} obtained for a virgin sample (assumption #8 of the model) can also be used for any compressed samples and for cyclic loading of the samples.

Similarly to GDLs, a Gaussian distribution of Eq. (6-16) can account for the distance of MPL carbon particles from a fiber surface, which is considered flat relative to the small MPL particles:

$$n_{sMPL} = \frac{1}{16}\left(\frac{m_{MPL}}{\sigma_{MPL}}\right)^2 \frac{\exp(-2\gamma_{MPL}^2)}{\text{erfc}(\gamma_{MPL})} A_{fP} \tag{6-18a}$$

$$\gamma_{MPL} = \text{erfc}^{-1}\left(\frac{4P}{H_{elMPL}}\right) \tag{6-18b}$$

where A_{fP} is the area of each fiber surface that MPL carbon particles can come in contact with, as shown in Figure 6.4 (also see Figure 6.2):

$$A_{fP} \approx l_f d_f \tan^{-1}\left(2\frac{d_p}{d_f}\sqrt{1+\frac{d_f}{d_p}}\right) = l_f s_{arc} \tag{6-19}$$

The number of MPL carbon particles in contact with all the fibers at a compression of *P*, N_p, can be found using the following equation:

$$\frac{N_p}{N_{pt}} = \frac{n_{sMPL}}{n_{stMPL}} \tag{6-20}$$

The number of MPL carbon particles contacting one GDL fiber will be:

$$N_p^{1f} = \frac{N_p}{N_f} \tag{6-21}$$

However, the number of MPL carbon particles that may contact one fiber (N_{p-1f}) should be obtained from Eq. (6-9) accounting for the GDL-MPL solid-phase contact probability.

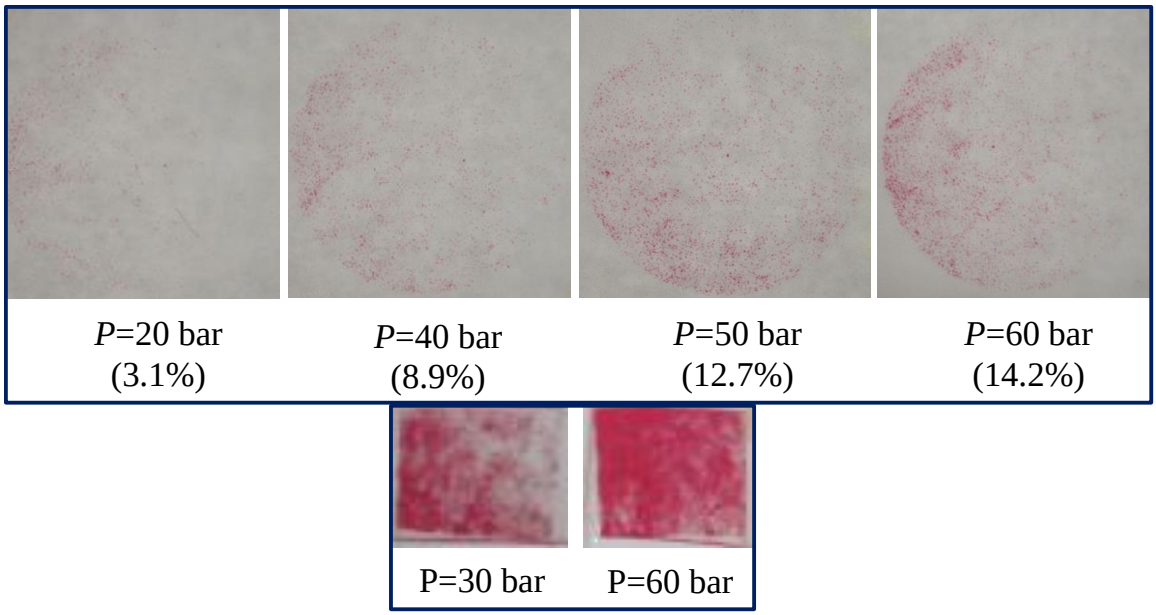

Figure 6.10. Image of a SGL MPL on a pressure indicating films (Fujifilm) [219], with contact spots pressures in the range of 100-500 and 20-115 bars (light red-dark red) shown in the first and second rows, respectively. These images show how the population of the contact spots increases with compression up to a value of approximately P_{st}=50 bar. Using the "ImageJ" software [220], percentage of the contact areas has been calculated and reported in parentheses.

6.3. Thermal modeling

Due to the very small area of the contact (10^{-17}-10^{-15} m^2), the heat transferring from one GDL fiber to the MPL carbon particles encounters a large resistance, known as spreading/constriction resistance. According to Bahrami *et al.* [182] [213] [232] [240], the total thermal contact resistance of non-conforming surfaces, here for one fiber, is a summation of the macrocontact and all the microcontact resistances:

$$R_{tot}^{f-MPL} = R_{mac}^{f-MPL} + R_{mic}^{f-MPL} \quad (6\text{-}22)$$

The spreading/constriction macrocontact resistance that occurs on each cylindrical fiber surface contacting the carbon particles of MPL can be obtained by [6]:

$$R_{mac}^{f-MPL} = \frac{1}{\pi l_f k_f} \ln\left(\frac{4d_f}{s_{arc}}\right) - \frac{1}{2l_f k_f} \tag{6-23}$$

where k_f is the thermal conductivity of fibers (=115 W/m K [110]). It should be noted that due to the large number of carbon particles contacting each GDL fiber and the small pores on the MPL surface, a continuous contact area with a width of s_{arc} is assumed on the fiber surface for calculating the 'macro' contact area.

Each particle contact spot provides a parallel path for heat transfer. Therefore, the microcontact resistance for each fiber is an inverse of the parallel summation of all the microcontact resistances created on its surface:

$$R_{mic}^{f-MPL} = \left(\sum_{i=1}^{N_p^{f-MPL}} \frac{1}{R_{mic_i}^{f-p}}\right)^{-1} \tag{6-24}$$

where $R_{mic_i}^{f-p}$ is the spreading/constriction resistance between one fiber and one arbitrary carbon particle contacting that fiber:

$$R_{mic_i}^{f-p} = R_{mic_i}^{f} + R_{mic_i}^{p} \tag{6-25}$$

Since a and b are much smaller than the fiber diameter ($a/d_f \sim 10^{-3}$), the concept of heat transfer on a half space is used for the fiber side of any fiber-particle contact [57]:

$$R_{mic_i}^{f} = \frac{1}{2\pi k_f a} \int_0^{\frac{\pi}{2}} \frac{dt}{\sqrt{1-\eta^2 sin^2 t}} \tag{6-26}$$

$$\eta = \frac{1}{\sqrt{1-(b/a)^2}} \tag{6-27}$$

And for the particle side, since $a \approx b$ (circular contact spots) and the fibers can be considered as flat surface against the small particles of MPL, the equation of smooth sphere-flat contact can be employed [180] [213] [221] [241]:

$$R^{p}_{mic_i} = \frac{\left(1-\frac{2a}{d_p}\right)^{1.5}}{2\left(\frac{2k_f k_p}{k_f + k_p}\right)a} \tag{6-28}$$

where k_p is the thermal conductivity of carbon particles that are made of amorphous carbon black (see Table 6.1). The thermal contact resistance between the GDL and MPL for one carbon particle diameter can be obtained using the parallel summation of all the fiber-MPL resistances:

$$TCR_{d_{pj}} = \frac{R^{f-MPL}_{tot}}{N_f} \tag{6-29}$$

Ultimately, the TCR between the GDL and MPL is the TCRs of different carbon particle diameters (Eq. (6-29)) averaged based on their occurrence probability in an MPL:

$$TCR = \sum_{j=1}^{n_{ptotal}} p_{d_{pj}} TCR_{d_{pj}} \tag{6-30}$$

where $p_{d_{pj}}$ the probability of occurrence of each particle diameter (d_p) has already been provided in Figure 6.5.

6.4. Model validation

After determining the geometrical parameters of each GDL and MPL, we can calculate the thermal contact resistance. Mathematical code was written in MATLAB to facilitate the calculations and a parametric study of TCR=$f(P, \varepsilon_{GDL}, \varepsilon_{MPL}, d_p, d_f, l_f)$ was performed.

As mentioned in Chapter 3, the through-plane thermal resistances of several 5%-PTFE treated SGL GDL substrates with different thicknesses (SGL GDL 24 & 34 and SGL GDLs 25 & 35) were measured using the two thickness method. The thermal resistances of the MPL-coated type of these GDL substrates (SGL GDLs 24BC and 25BC) were also measured, which allowed deconvoluting the undesirable clamping plate-GDL and clamping plate-MPL contact resistances from the GDL and MPL bulk resistances. Subsequently, the thermal contact resistances of the coated MPL with the GDL substrates 24BA and 25BA (see Table 6.1) were obtained using the two-thickness method. The details of the experimental apparatus and the measurement method have already been explained in Chapter 3 and the values of the MPL-GDL TCR are reported here.

Figure 6.11 compares the present model with the experimental GDL-MPL contact resistances for two GDLs, SGL 24BC (24BA-MPL) and SGL 25BC (25BA-MPL). The model results are in good agreement with experimental data and the model captures the experimental trend over a wide range of compression with a very small difference in slopes that might indicate a slight departure from the purely elastic deformation assumed in the model. Figure 6.11 also shows that, as mentioned earlier, the model result is not sensitive to P_{st}.

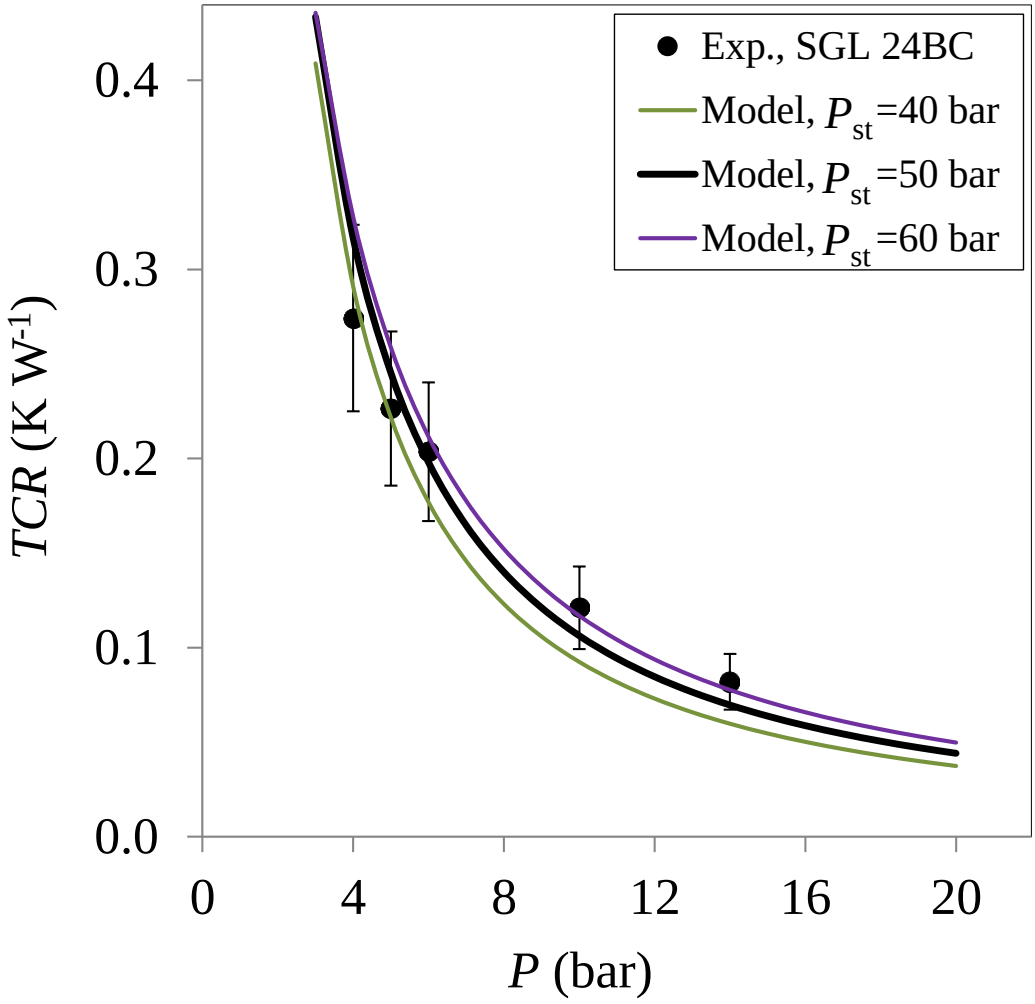
Exp., SGL 24BC
Model, P_{st}=40 bar
Model, P_{st}=50 bar
Model, P_{st}=60 bar
0.4
0.3
0.2
0.1
0.0
TCR (K W^{-1})
0
4
8
12
16
20
P (bar)

(a)

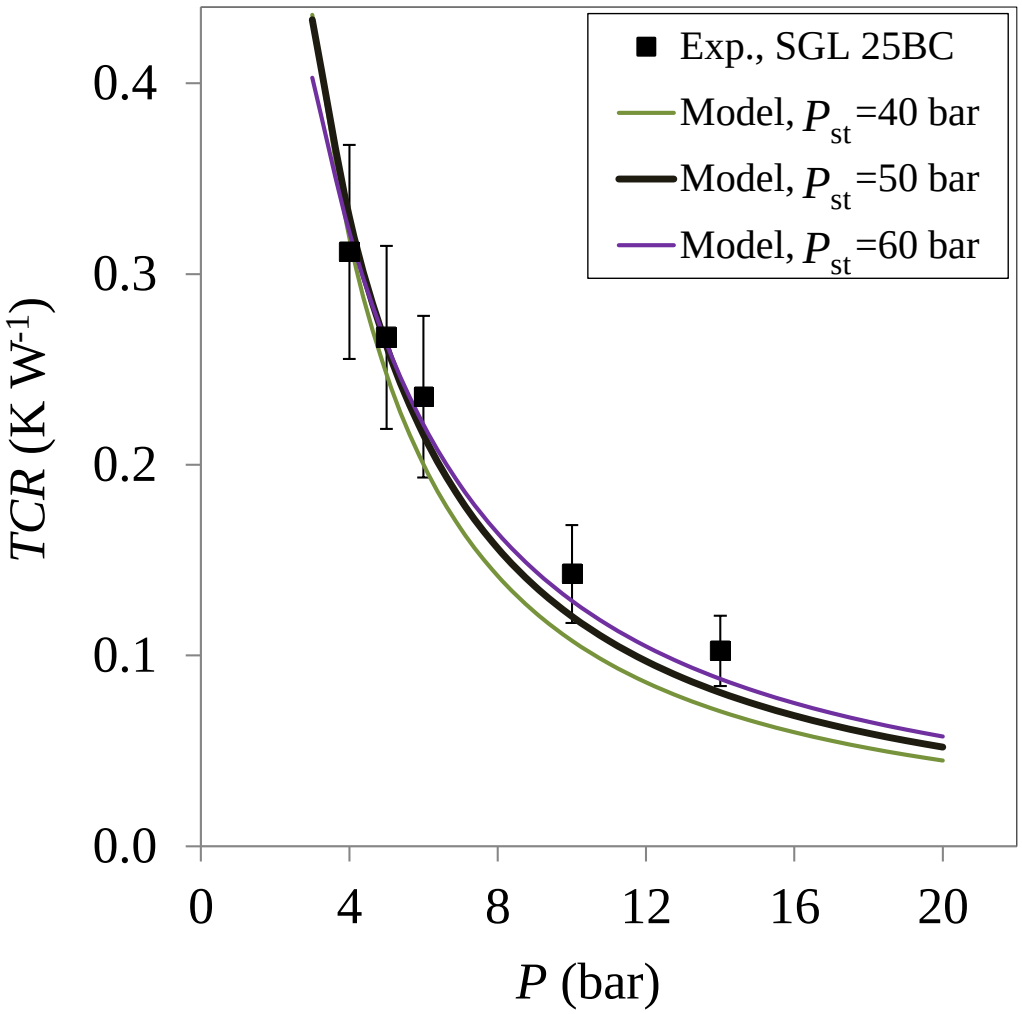

(b)

Figure 6.11. Comparison of the present model with experimental data for (a) SGL 24BC and (b) 25BC. P_{st}, the compression at which all fibers can come into contact to the MPL surface, is a constant parameter to which the model is not sensitive, but the model is sensitive to varying compression P (fuel cell stack clamp pressure)

6.5. Parametric study

In order to determine the key parameters affecting TCR and their impacts, a parametric study is performed. For each case, only one parameter is varied, while other parameters are kept constant unless otherwise mentioned. The most important parameter of a porous medium is its porosity, whose effect on the transport properties of the medium is expected to be noticeable. Therefore, the effect of both GDL and MPL porosity on the TCR of GDL-MPL is studied here.

6.5.1. GDL porosity (ε_{GDL})

The influence of GDL porosity on the TCR as plotted in Figure 6.12 reveals that TCR is more sensitive to porosity at lower compression and higher porosities. It is visible from Figure 6.12 that increasing the compression reduces its impact on the TCR, irrespective of the GDL porosity.

One important point to notice here is that TCR counter-intuitively decreases beyond a porosity of approximately 84% at the low pressure of 2 bar. Overall, at lower compression, there can be a critical porosity beyond which the TCR decreases. This can be justified as the following: according to Eq. (6-29) and Figure 6.13, the size of each contact spot (Figure 6.13a) and the number of contact points (Figure 6.13b) are both important in determining the TCR. Any porous medium with very high porosity, which results in low number of contact spots, can lead to a lower TCR if accompanied with low compression. This can be attributed to the rate of the growth of the contact spot area with the GDL porosity (Figure 6.13a) or that the rate of reduction in the TCR between each fiber and the carbon particles it is in contact with is higher than the rate of decrease in the number of contacts (Figure 6.13b), also see Eq. (6-29). This is an important trend that can be used for GDL manufacturing and fuel cell design. In other words, GDLs with very high porosities, which can lead to high diffusivities of components and low mass transfer

limitations, can be used for applications in fuel cells as long as other issues, such as any possible reduction in bulk conductivity and/or mechanical strength, are not critical.

It is well known that the size (Figure 6.13a) and the number of contact spots (Fig. 13b) determine the TCR. For a fixed compression, the radius or size of contact spots decreases with their population (Figure 6.13a) since the force is divided between more spots and thus the force per spot is lower. This effect is more pronounced at lower number of contact spots, i.e., higher porosities and lower compression as shown in Figure 6.13a, e.g., compare a change from 1 to 2 spots with a change from 1 million to one million and one (or even one million and a few thousands) spots. In other words, for typical GDLs porosities, the number of fibers is so high that any reduction in it (as a result of porosity increase) can lead to little increase in the size of the contact spots and, as a result, TCR increases with porosity. However, as the GDL porosity approaches very high values close to unity, the number of contact spots (Figure 6.13b) becomes so low that the effect of the spots size growth on the TCR becomes competitive with, and beyond specific (critical) values of porosity (see Figure 6.12), dominant over, the effect of the increased population of spots. This effect becomes more critical at lower compression where the number of contact spots is (much) lower (Figure 6.13b). For this reason, as shown in Figure 6.12, with increasing compression, higher critical porosities are observed and at very high compression, the critical porosity (peaks) may disappear.

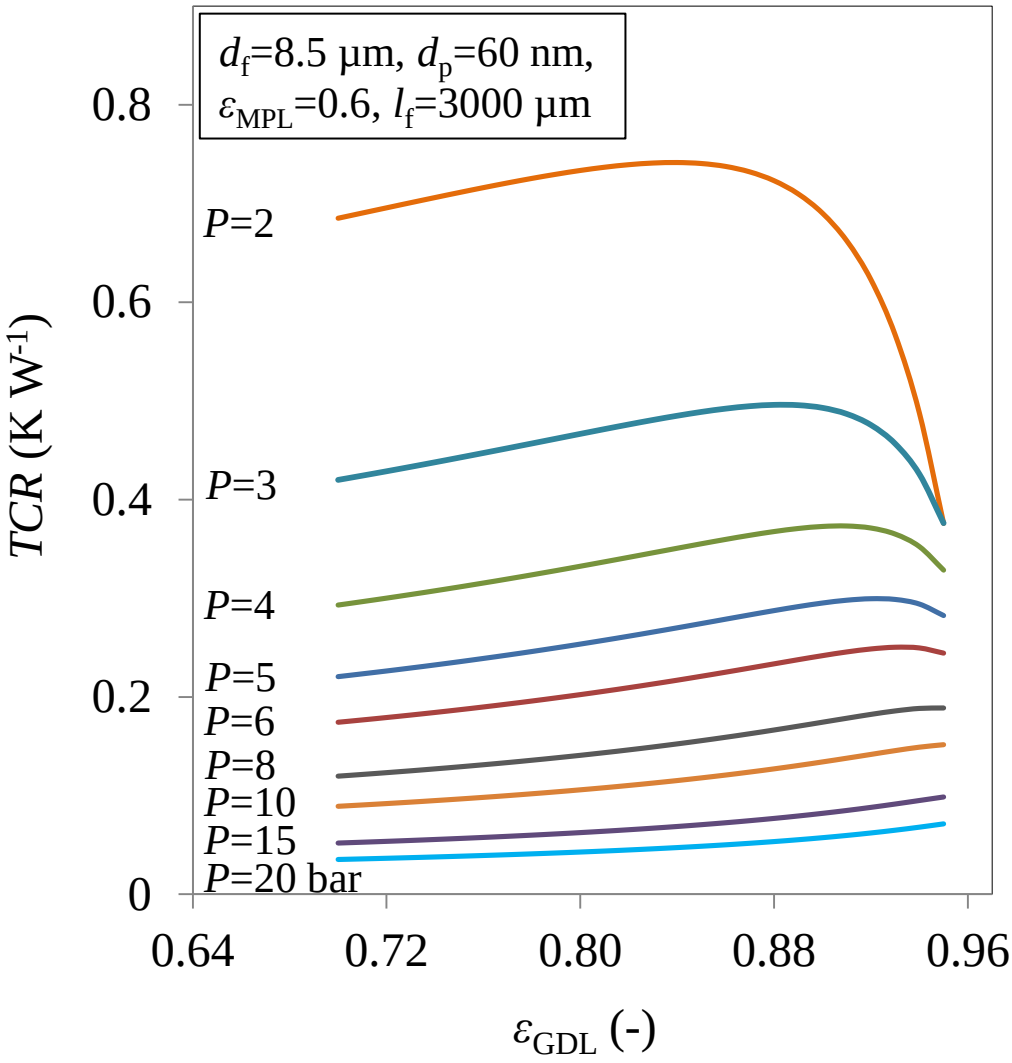

Figure 6.12. Effect of GDL porosity on the TCR at different compressions: With increasing compression, the critical porosity increases and at high compression, it disappears

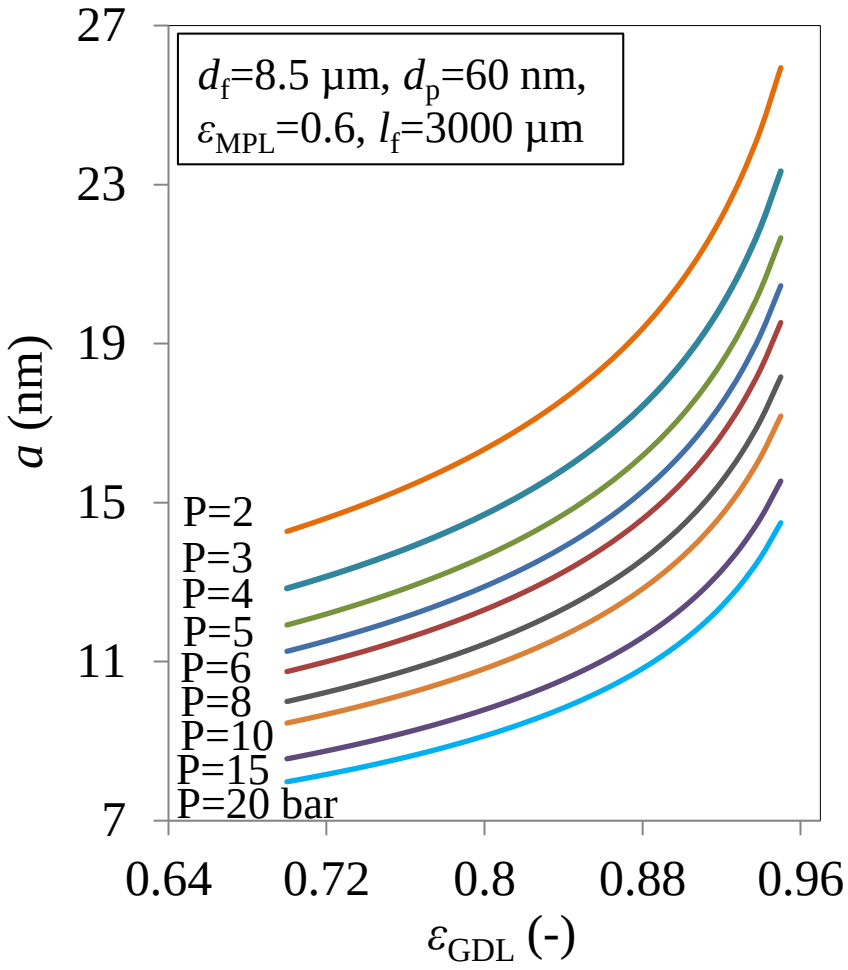
d_f=8.5 µm, d_p=60 nm,
ε_{MPL}=0.6, l_f=3000 µm
P=2
P=3
P=4
P=5
P=6
P=8
P=10
P=15
P=20 bar
a (nm)
27
23
19
15
11
7
0.64
0.72
0.8
0.88
0.96
ε_{GDL} (-)

(a)

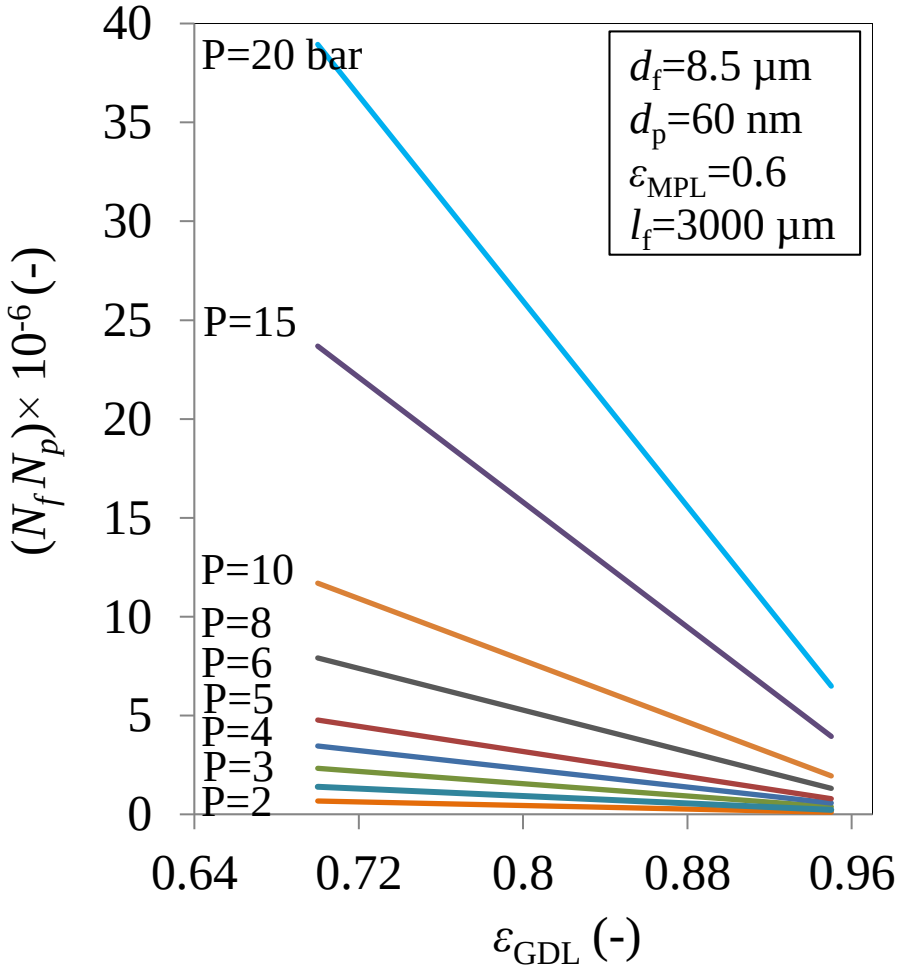

(b)

Figure 6.13. Variations of the radius of each contact spot (a) and the number of contact spots (b) with the GDL porosity

6.5.2. MPL porosity (ε_{MPL})

Figure 6.14 shows that the trends of the TCR variations with MPL porosity are similar to the ones observed for the case of GDL porosity, i.e., Figure 6.12. At lower compressions, the effect of porosity on the TCR is more pronounced and with increasing compression, the effect decreases and an almost linear trend is observed at high compression of 20 bar.

At the compression of 2 bar, a reduction in TCR is observed with increasing MPL porosity to values higher than 0.58. A similar trend was observed in Figure 6.12 for the same compression. It is worth emphasizing that with increasing the MPL porosity beyond specific (critical) values, under the same compression, it is possible to observe a reduction in the TCR. In other words, with increasing MPL porosity, the contact spot radius *a* increases (Figure 6.15a) and the number of contact points decreases (Figure 6.15b), which lead to the appearance of a maximum value for the TCR for a range of compression (Figure 6.14). This is because with increasing MPL porosity beyond certain values, the rate of the growth of each contact area (Figure 6.15a), or the rate of decreasing of the TCR at each contact spot, becomes higher than the rate of reduction in the number of contacts (Figure 6.15b). This important finding can be beneficial for the design and manufacturing of fuel cells, GDL, MPLs, and in general, any other porous media.

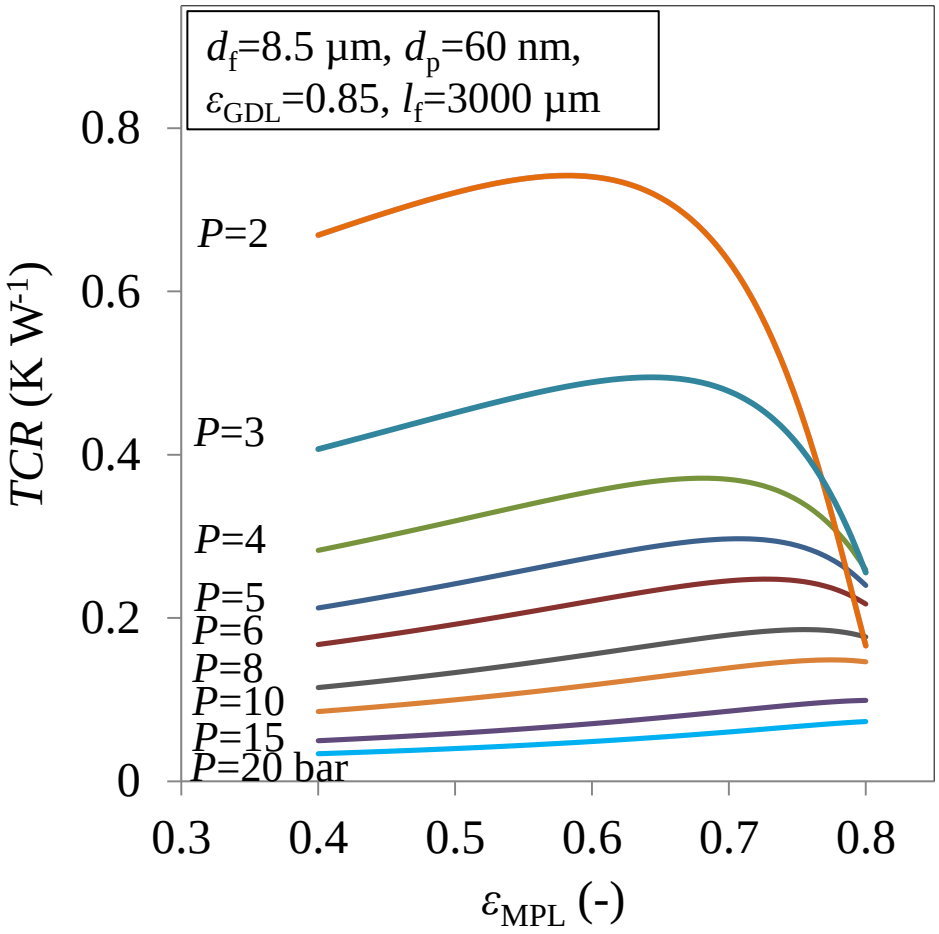

Figure 6.14. Effect of MPL porosity on the TCR at different compressions: With increasing compression, the critical porosity increases and at high compression, it disappears

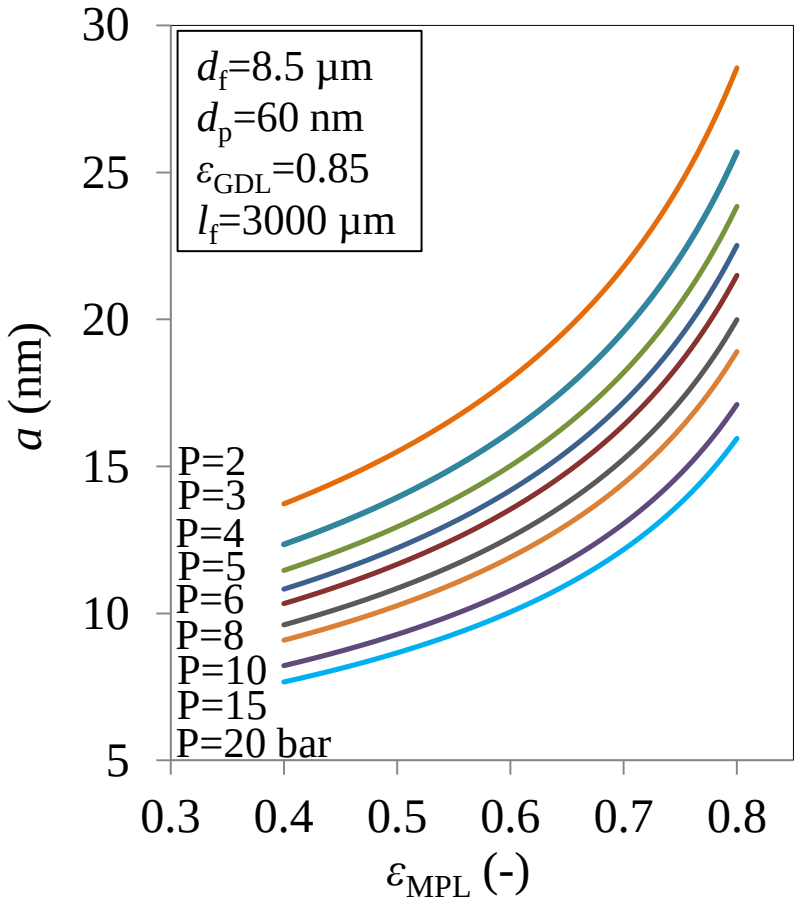
30
25
20
15
10
5
a (nm)
d_f=8.5 µm
d_p=60 nm
ε_{GDL}=0.85
l_f=3000 µm
P=2
P=3
P=4
P=5
P=6
P=8
P=10
P=15
P=20 bar
0.3
0.4
0.5
0.6
0.7
0.8
ε_{MPL} (-)

(a)

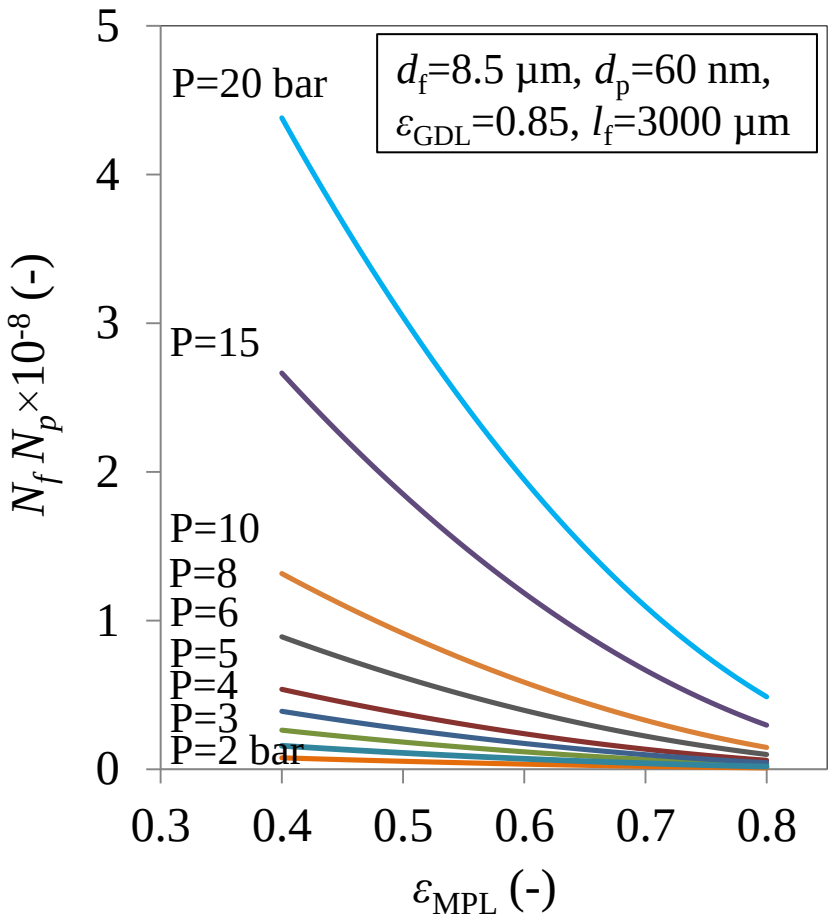

(b)

Figure 6.15. Variations of the radius of each contact spot (a) and the number of contact spots (b) with the MPL porosity

6.5.3. Fiber length (l_f)

Figure 6.16 shows that the fiber length does not affect the TCR when the *GDL porosity is kept constant*. Increasing fiber length at constant porosity is equivalent to decreasing the number of fibers; however, the number of contact spots increases as well so that their total number remains constant across the interface. As a result, it may be concluded that the contact area does not change with changing fiber length at a constant porosity.

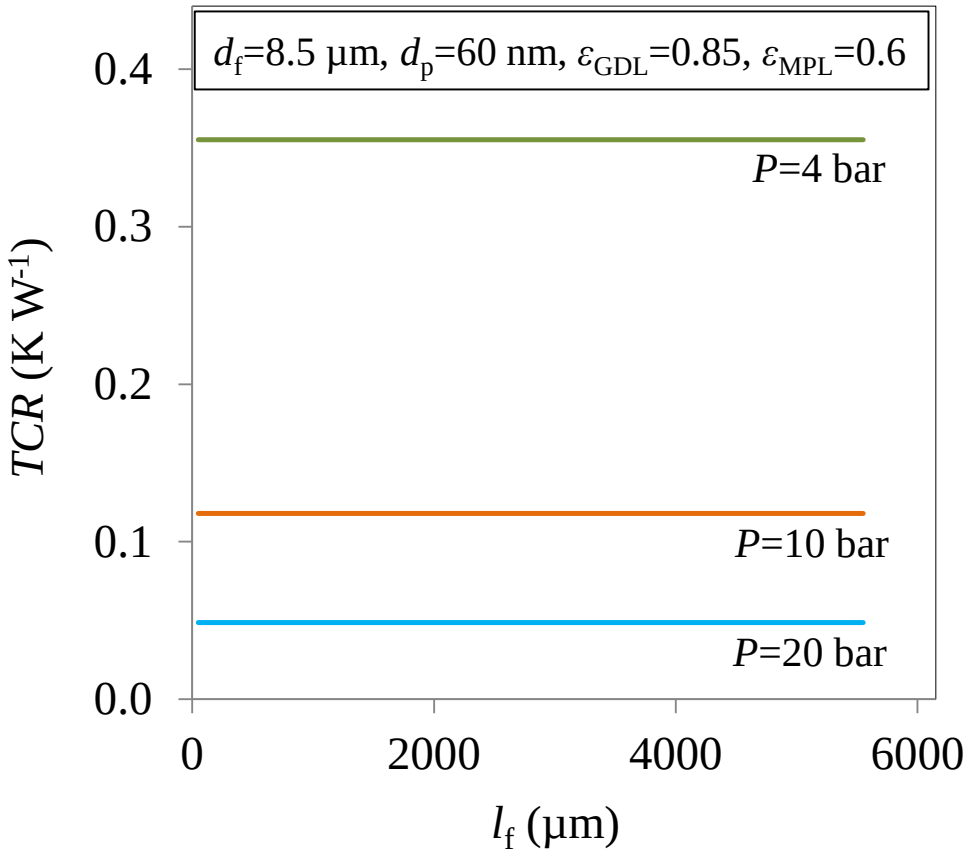

Figure 6.16. Effect of fiber length on TCR

6.5.4. Fiber diameter (d_f)

Figure 6.17 shows that the effect of fiber diameter on the GDL-MPL TCR is negligible, contrary to its effect on GDL-plate TCR where it is significant as shown in Figure 5.12. This is due to the large ratio of the fiber to particle diameter (~10^3), which causes small carbon particles to feel the fibers as flat surfaces, as explained.

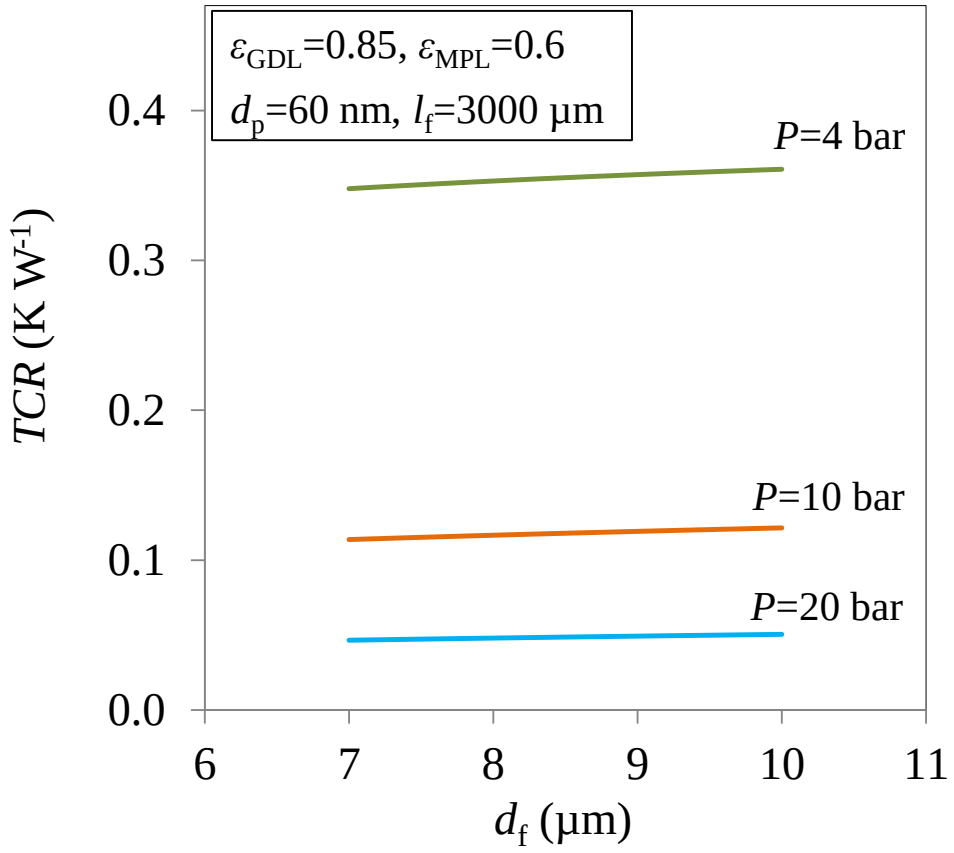

Figure 6.17. Effect of fiber diameter on TCR

6.5.5. Carbon particles diameter (d_p)

Carbon particles diameters can change the TCR dramatically at low compression, as shown in Figure 6.18. However, for the typical range of MPL particles, i.e., 40-80 nm, the effect is not significant at high compressions. With increasing compression, the effect of MPL particles diameters on the TCR decreases, as the slopes of the curves reduce.

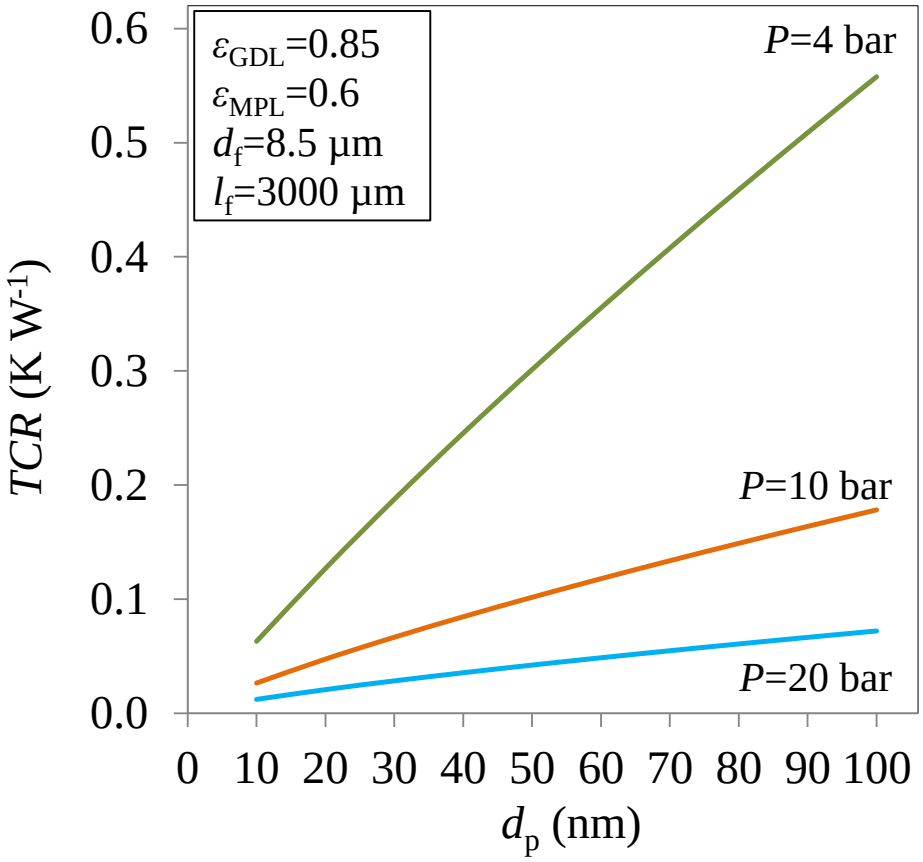

Figure 6.18. TCR changes with MPL carbon particles diameter

As the particles become smaller, the TCR reduces significantly and become less dependent on the compression. In other words, increasing particle diameter (at constant porosity) increases the TCR. As a result, it is recommended that fuel cell manufacturers use MPLs with smaller carbon particles (with the same porosity) as long as other issues such as MPL manufacturing restrictions and/or any reduction in MPL mechanical strength are not compromised.

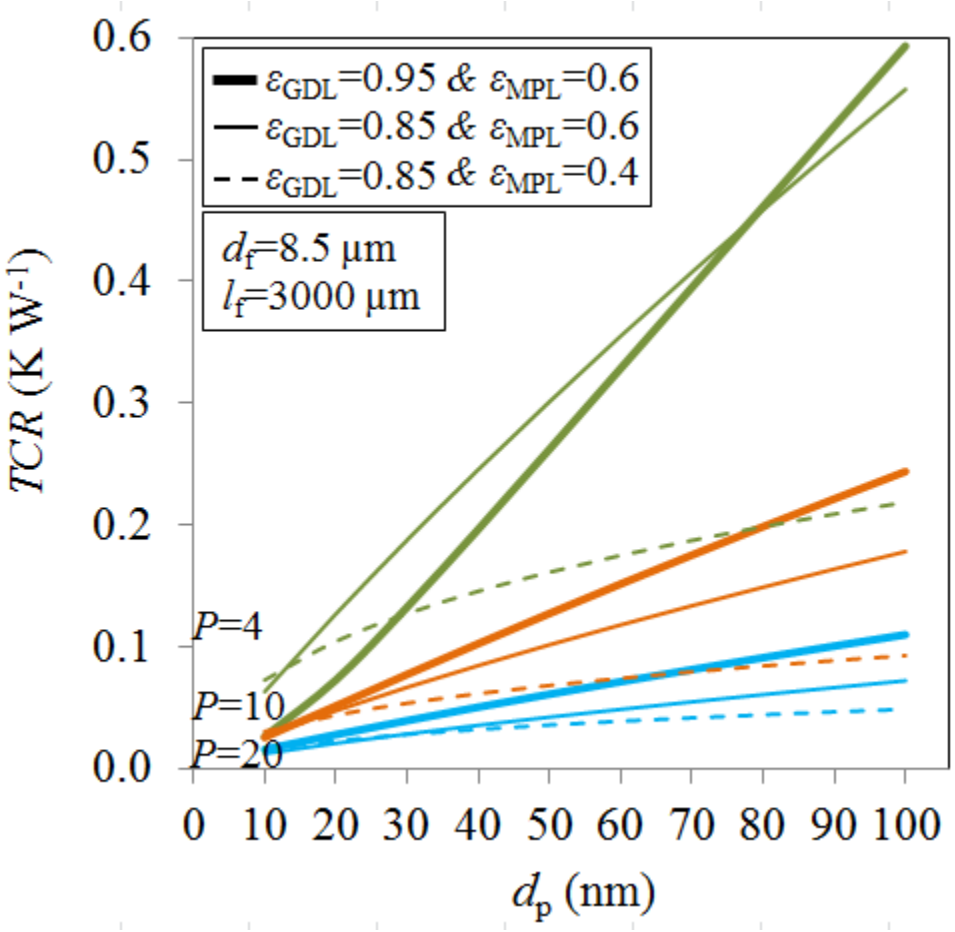

Figure 6.19. Impact of GDL and MPL porosities on TCR over a range of MPL carbon particles diameter under three different compressions of *P*=4, 10 and 20 bar

Comparing the TCR for different GDL and MPL porosities, as shown in Figure 6.19, reveals that the overall impact of GDL porosity on the TCR is more than that of the MPL. Figure 6.19 also shows that a GDL with a porosity of 95% (thick green solid curve) has lower TCR than the one with a lower porosity of 85% (thin green solid curve) for particle diameters smaller than 80 μm, considering the same MPL porosity of 60% and the same compression of 4 bar. This can be attributed to a trade-off between the number of contact spots and the TCR that each *individual* contact spot has, as explained in the discussion of Figure 6.14.

6.6. Concluding remarks

An analytic mechanistic model was developed for predicting the contact resistance between GDL and MPL that takes into account salient geometric parameters and contact pressure. The model is in close agreement with the reported experimental data, especially for medium to high compression.

A comprehensive parametric study was performed to analyze the trends, and the effects of MPL and GDL morphological features and of compression on TCR. The model also reveals that the traditional notion that TCR increases with porosity does not always hold; under certain circumstances, a critical porosity value is reached when the trend is reversed making it possible for the contact resistance between two mating porous materials to drop with lower solid phase fraction (higher porosity). The key factors affecting this phenomenon are porosity, compression and carbon particle diameters, but not the length and diameter of the GDL fibers. The critical values of the dominant parameters are determined by the model and are useful reference values for GDL manufacturing [202] [203] [204] [205] [206] [207] [242] and fuel cell design in order to improve the heat/electrical management of PEMFCs.

Chapter 7.

Management, support and sources

7.1. Work plan and schedule

The challenges encountered in this research have been mainly related to the experimental setup and tests: (i) calibration of the TCR machine; (ii) deconvolution of bulk from the contact resistance; (iii) measuring the properties of materials coated on a substrate (MPL coated on GDL substrate); (iv) working with brittle and delicate fuel cell materials; (v) material handling. Table 7.1 summarizes the work plan and schedule followed in this research, the encountered problems and solutions and the status of the related projects.

Table 7.1. Review on the work plan and schedule, as well as the encountered problems and solutions

Task/work plan	Procedure and/or solution	Support & sources	Year	Remarks & status
TCR machine calibration	Calibrating the machine with Pyrex calibration samples; Using new thermocouples and proper installation	LAEC	2011	Completed
TCR machine modifications	Adding pressure hydraulic device; installation laser displacement device; Adding tubes and pipes for wet porous material tests	LAEC	2011-2012	Completed
Electrical testbed & Micro Junior 2 micro-ohmmeter	Gold-plating copper probes; Purchasing a micro-ohm-meter device suitable for low electrical resistance materials	LAEC	2013	Completed
SEM/FIB images	Helpful for geometrical modeling and analyzing the data	4D Labs	2013	Completed
GDLs with two thicknesses	Sigracet (SGL Group) GDLs	SGL	2012-2014	Completed
Deconvolution of bulk from thermal contact resistance	Using GDLs with two thicknesses provided by Sigracet (SGL Group)	SGL	2011-2014	Completed
Deconvolution of bulk from electrical contact resistance	Using GDLs with two thicknesses provided by Sigracet (SGL Group)	SGL	2014-2015	Ongoing
In-plane electrical conductivity of MEA components	Using CCM, MPLs, MEAs and GDLs from different manufacturers	SGL MBFC AFCC	2014-2015	Ongoing
Thermal conductivity of 14 SGL GDLs	Measuring thermal conductivity using two thickness method; Modeling and experiments: Effect of compression, PTFE, MPL, cyclic loading and hysteresis behaviour	SGL	2011-2012	Completed

Designing and building a proper sealed chamber	Development and preliminary testing of controlled relative humidity flow chamber for thermal conductivity testing was supported by multiple co-op students and lab engineers	LAEC	2011-2013	Preliminary results obtained
Ballard graphite BPP: thermal resistance measurements	Measuring thermal conductivity of Ballard's graphite BPPs as a function of temperature	Ballard	2012	Completed
Thermal contact resistance of 14 SGL GDLs with Ballard BPP	Modeling and experiments: Effect of compression, PTFE, MPL, cyclic loading and hysteresis behavior	SGL & Ballard	2012-2013	Completed
NSERC Engage project with MBFC	Effect of manufacturing processes on MEA, GDL and CCM properties; In-plane and through plane resistances of the samples	MBFC, AFCC	2013	Completed
AFCC project	Measuring electrical and thermal resistance of GDLs and CCM; GDL thermal conductivity & TCR modeling	AFCC	Start: 2013	Ongoing
PhD program & thesis defense	-	SFU, UVic (NSERC)	April 2015	Completed

7.2. Support and sources

(1) **SGL Carbon Group** provided a great number of SGL GDLs with different PTFE loading and MPL.

(2) Several graphite plates with different thicknesses were prepared by **Ballard Power Systems** [54] [243].

(3) **Mercedes Benz Canada Fuel Cell Division (MBFC)** provided CCM, GDL and MEA samples, which allows investigating the effect of manufacturing processes on MEA and studying the effect of thermal and electrical resistances of CCM and GDL before and after assembly. In addition, the in-plane electrical conductivities of CCM and MEA were also measured [244] (data not reported in this thesis).

(4) **Automotive Fuel Cell Cooperation Corp. (AFCC)** supplied some Toray GDLs [244] (data not reported in this thesis).

Chapter 8.

Conclusion and future work

A comprehensive study was conducted to determine, and also guide the improvement of, the bulk and interfacial thermal properties of micron/nano-sized fibrous and porous materials, with an application to PEMFCs. Table 8.1 summarizes all the major work included in this thesis. The results of the conducted studies show that:

- Contact resistance, usually overlooked in the literature, can be as important as bulk resistance.
- The BPP-GDL TCR can be the *dominant* resistance in GDL-BPP assembly.
- GDL micro-structure can affect its thermal properties significantly.
- Fiber spacing, angle and diameter can be optically measured and determined.
- GDL and MPL micro-structures can be optimized at constant porosity to enhance their thermal (and possibly electrical) resistances noticeably.
- PTFE and MPL adversely affect the thermal management, even though they may improve water management.
- PTFE decreases GDL thermal conductivity in spite of decreasing the porosity.
- MPL increases the contact resistance dramatically compared to untreated GDLs or GDLs with low PTFE content.
- Thermal conductivity of a fibrous material may increase with porosity.
- Contact resistance may decrease with porosity under specific circumstances.
- Load cycling reduces the thermal resistance of GDLs and MPLs considerably.
- Fiber waviness significantly increases the contact resistance of GDLs with BPP.

The present thesis provides a framework and a data base of deconvoluted interfacial (contact) resistance from bulk resistance for three main components of PEMFCs: BPPs, GDLs (PTFE-treated) and MPLs. This data base, along with the comprehensive experimental explanations supported by the modeling results, can shed light on the thermal behavior of these components and give insights into their effects on the thermal management of PEMFCs. The analytic models developed in this work can also be readily implemented in the simulation and modeling of PEMFCs, and can be extended with minor modifications to other fibrous porous media such as fibrous catalysts, insulating media and sintered metals. These models can also be used, with some modifications, for predicting the bulk and interfacial electrical properties of GDLs. Figure 8.1 and Figure 8.2 show graphical summaries of the projects included in this thesis.

Table 8.1. Experimental (Exp.) and modeling work included in this thesis

Study of	Exp.	Modeling
Thermal conductivity of 14 untreated & PTFE-treated (5 and 20%) Sigracet GDLs as a function of compression	✓	✓
Thermal conductivity of a coated MPL	✓	-
Thermal conductivity of a graphite BPP as a function of temperature (Ballard project)	✓	-
Effect of compression, PTFE and MPL on GDL thermal conductivity	✓	✓
$TCR_{GDL\text{-}BPP}$ & $TCR_{GDL\text{-}FM}$	✓	✓
$TCR_{MPL\text{-}BPP}$ & $TCR_{MPL\text{-}FM}$	✓	-
$TCR_{GDL\text{-}MPL}$	✓	✓

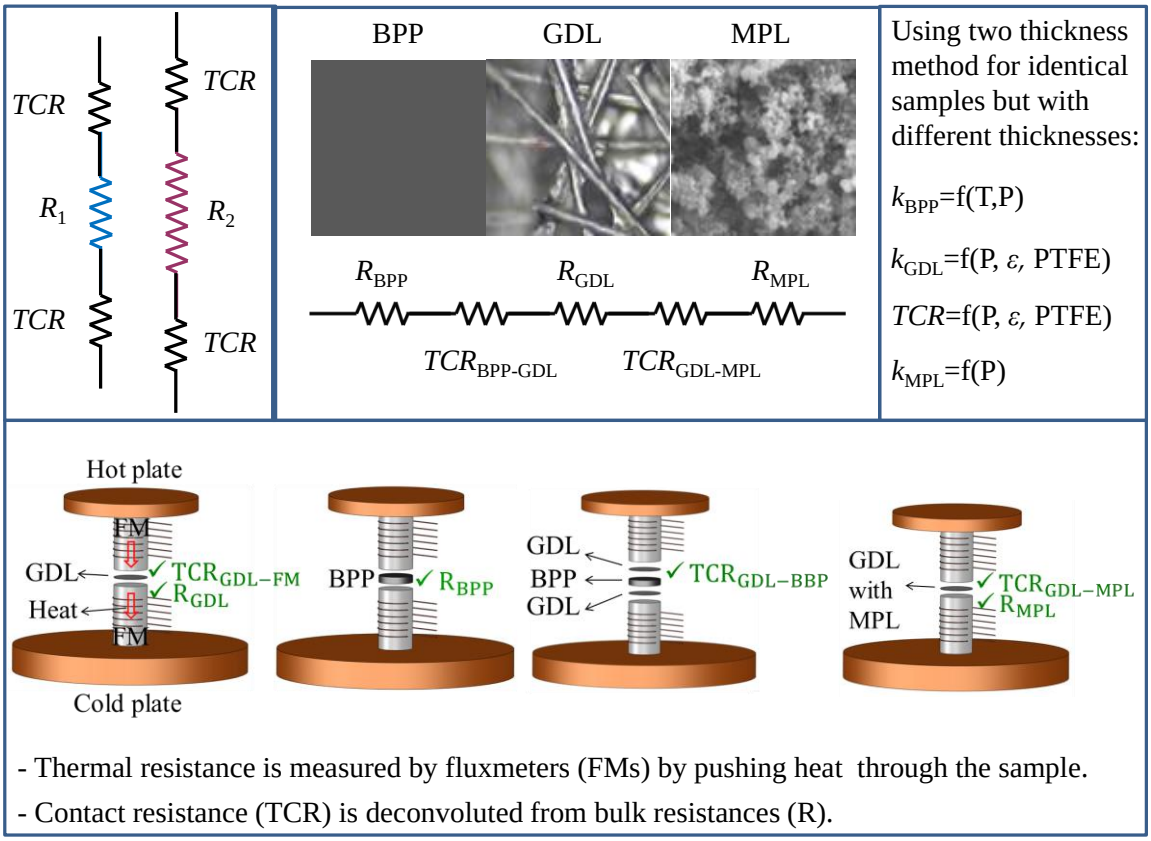

Figure 8.1. Graphical summary of the experimental part of this thesis

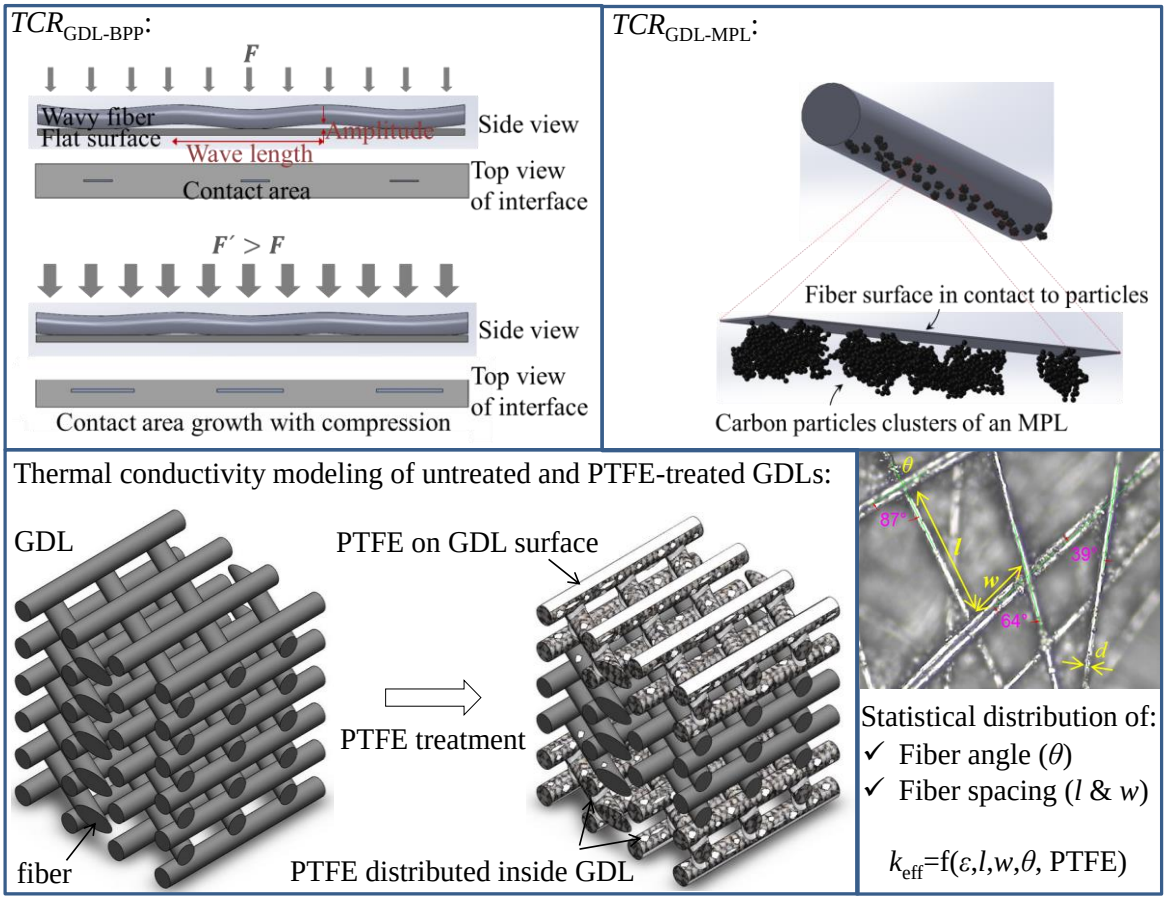

Figure 8.2. Graphical summary of the modeling part of this thesis

8.1. Non-reported work

Due to the confidentiality of some of the data regarding our industrial collaborators (MBFC and AFCC) and/or the later possibility of the publication of non-published data, only half of the work conducted during this four-year PhD program has been incorporated into this thesis. The topics of those projects that conducted during this PhD program but not included in this thesis, are listed below:

(a) Role of MPL in thermal and electrical resistance of GDLs (NSERC Engage project with MBFC and AFCC) [223]

(b) Effect of manufacturing process on thermal and electrical resistances of MEAs, CCMs (thermal) and anode and cathode GDLs (NSERC Engage project with MBFC) [244]

(c) Effect of gas flow passing through a GDL on its thermal resistance [199]

(d) Electrical conductivity of CL coated on a CCM and effect of humidity [222]

(e) Comparison of in-plane electrical conductivities of GDLs, CCMs and MEAs [222]

(f) Effect of PTFE, MPL and humidity on in-plane electrical conductivity of GDLs [222] [223]

(g) A closed-form compact easy-to-use Nusselt formula for laminar longitudinal flow between rectangular arrays of parallel cylinders with unequal row temperatures [201]

(h) A closed-form compact Nusselt formula for fibrous porous materials including PEMFC GDLs [200]

8.2. Future work

The GDLs micro-structure can be optimized to reach their best transport properties (thermal conductivity, electrical conductivity, diffusivity, convective heat transfer and permeability) that enhance the PEMFC performance noticeably. Some preliminary results have been obtained to enhance the convective heat transfer [199] [200] [201] and permeability [199] of GDLs, yet further research is required. The thermal (and possibly electrical) conductivities and interfacial resistances of GDLs were optimized in this thesis. A GDL structure optimization on diffusivity still lacks in the literature and the optimized GDL micro-structure can be useful to fuel cell manufacturers for the development of new GDLs.

The thermal properties of BPP-GDL-MPL assembly were thoroughly studied in this thesis. The following bulk and interfacial resistances were not reported and can be considered as future work:

- CL and PEM thermal conductivity
- CL-GDL/MPL & CL-membrane contact resistance

A study similar to the one conducted in this program can be performed to determine the above-mentioned thermal resistances. In parallel, analytic and numerical models can be developed to facilitate optimizing the micro-structure of CLs to improve PEMFCs heat and the coupled water management.

A similar study is being performed on the electrical resistance of fuel cell components, which can provide a data-base useful to the electrical management of PEMFCs. All the concepts and approaches used for the thermal part can be extended, with some changes, to the electrical part for modeling and studying the electrical resistance and conductivity of fuel cell materials (except membrane).

References

[1] N. Djilali, "Computational modelling of polymer electrolyte membrane (PEM) fuel cells: Challenges and opportunities," *Energy*, vol. 32, pp. 269–280, 2007.

[2] Y. Wang, K. S. Chen, J. Mishler, S. C. Cho, and X. C. Adroher, "A review of polymer electrolyte membrane fuel cells: Technology, applications, and needs on fundamental research," *Appl. Energy*, vol. 88, no. 4, pp. 981–1007, 2011.

[3] V. Mehta and J. S. Cooper, "Review and analysis of PEM fuel cell design and manufacturing," *Journal of Power Sources*, vol. 114. pp. 32–53, 2003.

[4] L. Hedstrom, "Fuel Cells and Biogas," PhD Thesis, KTH – Royal Institute of Technology Stockholm, Sweden, 2010.

[5] J. Wu, X. Z. Yuan, J. J. Martin, H. Wang, J. Zhang, J. Shen, S. Wu, and W. Merida, "A review of PEM fuel cell durability: Degradation mechanisms and mitigation strategies," *J. Power Sources*, vol. 184, pp. 104–119, 2008.

[6] S. Zhang, X. Yuan, H. Wang, W. Mérida, H. Zhu, J. Shen, S. Wu, and J. Zhang, "A review of accelerated stress tests of MEA durability in PEM fuel cells," *Int. J. Hydrogen Energy*, vol. 34, pp. 388–404, 2009.

[7] J. Marcinkoski and S. Jacob, "Fuel Cell System Cost," DOE Hydrogen and Fuel Cells Program Record # 14012, 2014. http://www.hydrogen.energy.gov/pdfs/14012_fuel_cell_system_cost_2013.pdf

[8] J. Spendelow, D. Papageorgopoulos, and J. Garbak, "Fuel Cell Stack Durability," DOE Hydrogen and Fuel Cells Program Record # 11003, 2012. http://www.hydrogen.energy.gov/pdfs/11003_fuel_cell_stack_durability.pdf

[9] N. Bessette, "Development of a Low Cost 3-10 kW Tubular SOFC Power System," in *FY 2011 Progress report for the DOE Hydrogen and Fuel Cell Program*, 2011, p. 890. http://www.hydrogen.energy.gov/pdfs/progress12/v_j_2_bessette_2012.pdf

[10] J. Morgan, D. Connors, and M. Hickner, “Reduction in Fabrication Costs of Gas Diffusion Layers,” Ballard Material Products, USA, FG36-08GO18051, 2012.

[11] J. Ito, M. Takaya, T. Miyamura, and T. Yamauchi, “Fibrous catalyst,” US20080132409 A1 (EP1927400A1), US Patent, 2008.

[12] M. Maity and U. Maitra, “An easily prepared palladium-hydrogel nanocomposite catalyst for C–C coupling reactions,” *J. Mater. Chem. A*, vol. 2, pp. 18952–18958, 2014.

[13] J. T. McCann, M. Marquez, and Y. Xia, “Highly porous fibers by electrospinning into a cryogenic liquid,” *J. Am. Chem. Soc.*, vol. 128, pp. 1436–1437, 2006.

[14] B. M. Baker, A. O. Gee, R. B. Metter, A. S. Nathan, R. A. Marklein, J. A. Burdick, and R. L. Mauck, “The potential to improve cell infiltration in composite fiber-aligned electrospun scaffolds by the selective removal of sacrificial fibers,” *Biomaterials*, vol. 29, pp. 2348–2358, 2008.

[15] A. Tamayol, K. W. Wong, and M. Bahrami, “Effects of microstructure on flow properties of fibrous porous media at moderate Reynolds number,” *Phys. Rev. E*, vol. 85, pp. 1–7, 2012.

[16] K. K. Aligizaki, *Pore structure of cement-based materials: Testing, interpretationa and requirements*. New York, USA: Taylor & Francis, 2006.

[17] S. G. Kandlikar and Z. Lu, “Thermal management issues in a PEMFC stack - A brief review of current status,” *Appl. Therm. Eng.*, vol. 29, no. 7, pp. 1276–1280, 2009.

[18] A. Faghri and Z. Guo, “Challenges and opportunities of thermal management issues related to fuel cell technology and modeling,” *Int. J. Heat Mass Transf.*, vol. 48, pp. 3891–3920, 2005.

[19] R. Cozzolino, S. P. Cicconardi, E. Galloni, M. Minutillo, and A. Perna, “Theoretical and experimental investigations on thermal management of a PEMFC stack,” *Int. J. Hydrogen Energy*, vol. 36, no. 13, pp. 8030–8037, 2011.

[20] E. Harikishan Reddy and S. Jayanti, “Thermal management strategies for a 1 kWe stack of a high temperature proton exchange membrane fuel cell,” *Appl. Therm. Eng.*, vol. 48, pp. 465–475, 2012.

[21] S. G. Kandlikar and Z. Lu, “Fundamental Research Needs in Combined Water and Thermal Management Within a Proton Exchange Membrane Fuel Cell Stack Under Normal and Cold-Start Conditions,” *Journal of Fuel Cell Science and Technology*, vol. 6, no. 4. p. 044001, 2009.

[22] M. J. Lampinen, “Analysis of Free Energy and Entropy Changes for Half-Cell Reactions,” *Journal of The Electrochemical Society*, vol. 140, no. 12. p. 3537, 1993.

[23] F. Chen, W.-M. Yan, H.-S. Chu, H.-Y. Wu, and C.-Y. Soong, “Analysis of thermal and water management with temperature-dependent diffusion effects in membrane of proton exchange membrane fuel cells,” *J. Power Sources*, vol. 129, no. 2, pp. 127–137, 2004.

[24] H. Ju, C.-Y. Wang, S. Cleghorn, and U. Beuscher, “Nonisothermal Modeling of Polymer Electrolyte Fuel Cells: I. Experimental Validation,” *J. Electrochem. Soc.*, vol. 152, no. 8, pp. A1645–A1653, 2005.

[25] H. Ju, C. Wang, S. Cleghorn, and U. Beuscher, “Nonisothermal Modeling of Polymer Electrolyte Fuel Cells II. Parametric Study of Low-Humidity Operation,” *J. Electrochem. Soc.*, vol. 153, no. 2, pp. A249–A254, 2006.

[26] C. Y. Wang, “Fundamental models for fuel cell engineering,” *Chem. Rev.*, vol. 104, no. 10, pp. 4727–4765, 2004.

[27] S. G. Goebel, “Evaporative cooled fuel cell,” US Patent 6,960,404, 2005.

[28] S. Tsushima, K. Teranishi, and S. Hirai, “Magnetic resonance imaging of the water distribution within a polymer electrolyte membrane in fuel cells,” *Electrochem. Solid State Lett.*, vol. 7, no. 9, pp. A269–A272, 2004.

[29] J. B. Heywood, *Internal combustion enginee fundamentals*. New York: McGraw-Hill, 1988.

[30] W. Sun, B. A. Peppley, and K. Karan, “An improved two-dimensional agglomerate cathode model to study the influence of catalyst layer structural parameters,” *Electrochim. Acta*, vol. 50, no. 16–17, pp. 3359–3374, 2005.

[31] J. G. Pharoah and O. S. Burheim, “On the temperature distribution in polymer electrolyte fuel cells,” *Journal of Power Sources*, vol. 195. pp. 5235–5245, 2010.

[32] H. Lin, T.-F. Cao, L. Chen, Y.-L. He, and W.-Q. Tao, “In situ measurement of temperature distribution within a single polymer electrolyte membrane fuel cell,” *International Journal of Hydrogen Energy*, vol. 37, no. 16. pp. 11871–11886, 2012.

[33] H. Y. Wang, W. J. Yang, and Y. B. Kim, “Analyzing in-plane temperature distribution via a micro-temperature sensor in a unit polymer electrolyte membrane fuel cell,” *Appl. Energy*, vol. 124, pp. 148–155, 2014.

[34] S. L. J.-P. Maes, “Methods for fuel cell coolant systems,” U.S. Patent 7,201,982, 2007.

[35] J. G. Pharoah, K. Karan, and W. Sun, “On effective transport coefficients in PEM fuel cell electrodes: Anisotropy of the porous transport layers,” *J. Power Sources*, vol. 161, pp. 214–224, 2006.

[36] N. Djilali and D. Lu, “Influence of heat transfer on gas and water transport in fuel cells,” *Int. J. Therm. Sci.*, vol. 41, pp. 29–40, 2002.

[37] Y. Shan and S.-Y. Choe, “A high dynamic PEM fuel cell model with temperature effects,” *Journal of Power Sources*, vol. 145, no. 1. pp. 30–39, 2005.

[38] M. Hara, J. Inukai, K. Miyatake, H. Uchida, and M. Watanabe, “Temperature dependence of the water distribution inside a Nafion membrane in an operating polymer electrolyte fuel cell. A micro-Raman study,” *Electrochim. Acta*, vol. 58, no. 1, pp. 449–455, 2011.

[39] C. J. Bapat and S. T. Thynell, “Effect of anisotropic thermal conductivity of the GDL and current collector rib width on two-phase transport in a PEM fuel cell,” *J. Power Sources*, vol. 179, pp. 240–251, 2008.

[40] M. Eikerling, “Water Management in Cathode Catalyst Layers of PEM Fuel Cells,” *Journal of The Electrochemical Society*, vol. 153, no. 3. p. E58, 2006.

[41] A. Radhakrishnan, “Thermal Conductivity Measurement of Gas Diffusion Layer Used in PEMFC,” PhD Thesis, Rochester Institute of Technology, New York, USA, 2009.

[42] G. Xu, J. M. Lamanna, J. T. Clement, and M. M. Mench, “Direct measurement of through-plane thermal conductivity of partially saturated fuel cell diffusion media,” *J. Power Sources*, vol. 256, pp. 212–219, 2014.

[43] J. Ramousse, S. Didierjean, O. Lottin, and D. Maillet, “Estimation of the effective thermal conductivity of carbon felts used as PEMFC Gas Diffusion Layers,” *Int. J. Therm. Sci.*, vol. 47, no. 1, pp. 1–6, Jan. 2008.

[44] M. Wang, J. He, J. Yu, and N. Pan, “Lattice Boltzmann modeling of the effective thermal conductivity for fibrous materials,” *Int. J. Therm. Sci.*, vol. 46, no. 9, pp. 848–855, 2007.

[45] A. Pfrang, D. Veyret, F. Sieker, and G. Tsotridis, “X-ray computed tomography of gas diffusion layers of PEM fuel cells: Calculation of thermal conductivity,” *Int. J. Hydrogen Energy*, vol. 35, no. 8, pp. 3751–3757, 2010.

[46] B. Markicevic, A. Bazylak, and N. Djilali, “Determination of transport parameters for multiphase flow in porous gas diffusion electrodes using a capillary network model,” *J. Power Sources*, vol. 171, pp. 706–717, 2007.

[47] Joshua David Sole, “investigation of novel gas diffusion media for application in PEM fuel cell ribbon assemblies,” PhD Thesis, Virginia Polytechnic Institute and State University, Blacksburg, USA, 2005.

[48] N. Zamel, X. Li, J. Becker, and A. Wiegmann, “Effect of liquid water on transport properties of the gas diffusion layer of polymer electrolyte membrane fuel cells,” *Int. J. Hydrogen Energy*, vol. 36, pp. 5466–5478, 2011.

[49] N. Zamel, E. Litovsky, X. Li, and J. Kleiman, “Measurement of the through-plane thermal conductivity of carbon paper diffusion media for the temperature range from -50 to +120 ^{o}C,” *Int. J. Hydrogen Energy*, vol. 36, no. 19, pp. 12618–12625, 2011.

[50] H. Ju, H. Meng, and C. Y. Wang, “A single-phase, non-isothermal model for PEM fuel cells,” *Int. J. Heat Mass Transf.*, vol. 48, pp. 1303–1315, 2005.

[51] M. F. Mathias, J. Roth, J. Fleming, and W. Lehnert, “Diffusion media materials and characterisation,” in *Handbook of Fuel Cells*, 2010, pp. 517–537.

[52] H. Sadeghifar, M. Bahrami, and N. Djilali, “A statistically-based thermal conductivity model for fuel cell Gas Diffusion Layers,” *J. Power Sources*, vol. 233, pp. 369–379, Jul. 2013.

[53] H. Sadeghifar, N. Djilali, and M. Bahrami, “A new model for thermal contact resistance between fuel cell gas diffusion layers and bipolar plates,” *J. Power Sources*, vol. 266, pp. 51–59, 2014.

[54] H. Sadeghifar, N. Djilali, and M. Bahrami, “Thermal conductivity of a graphite bipolar plate (BPP) and its thermal contact resistance with fuel cell gas diffusion layers: Effect of compression, PTFE, micro porous layer (MPL), BPP out-of-flatness and cyclic load,” *J. Power Sources*, vol. 273, pp. 96–104, 2015.

[55] H. Sadeghifar, N. Djilali, and M. Bahrami, “Thermal contact resistance between gas diffusion layer substrates and micro porous layers of fuel cells: Counter-intuitive reduction of contact resistance with porosity.” Under review, 2015.

[56] E. Sadeghi, N. Djilali, and M. Bahrami, “Effective thermal conductivity and thermal contact resistance of gas diffusion layers in proton exchange membrane fuel cells. Part 1: Effect of compressive load,” *J. Power Sources*, vol. 196, no. 1, pp. 246–254, Jan. 2011.

[57] E. Sadeghi, M. Bahrami, and N. Djilali, “Analytic determination of the effective thermal conductivity of PEM fuel cell gas diffusion layers,” *J. Power Sources*, vol. 179, no. 1, pp. 200–208, Apr. 2008.

[58] E. Sadeghi, N. Djilali, and M. Bahrami, “A novel approach to determine the in-plane thermal conductivity of gas diffusion layers in proton exchange membrane fuel cells,” *J. Power Sources*, vol. 196, no. 7, pp. 3565–3571, Apr. 2011.

[59] A. Arvay, E. Yli-Rantala, C.-H. Liu, X.-H. Peng, P. Koski, L. Cindrella, P. Kauranen, P. M. Wilde, and A. M. Kannan, “Characterization techniques for gas diffusion layers for proton exchange membrane fuel cells – A review,” *Journal of Power Sources*, vol. 213. pp. 317–337, 2012.

[60] W. R. Chang, J. J. Hwang, F. B. Weng, and S. H. Chan, “Effect of clamping pressure on the performance of a PEM fuel cell,” *J. Power Sources*, vol. 166, pp. 149–154, 2007.

[61] S. Miachon and P. Aldebert, “Internal hydration H_2/O_2 100 cm^2 polymer electrolyte membrane fuel cell,” *J. Power Sources*, vol. 56, no. 1, pp. 31–36, 1995.

[62] H. A. Gasteiger and M. F. Mathias, “Materials for High Temperature PEM Fuel Cells.” Workshop at Energy Institute, The Pennsylvania State University, 2013. http://www.woocovers.co/reading/workshop-materials-for-high-temperature-pem-fuel-cells-Gvcd.html

[63] J. J. Hwang and H. S. Hwang, “Parametric studies of a double-cell stack of PEMFC using Grafoil^{TM} flow-field plates,” *J. Power Sources*, vol. 104, pp. 24–32, 2002.

[64] J. Ge, A. Higier, and H. Liu, “Effect of gas diffusion layer compression on PEM fuel cell performance,” *J. Power Sources*, vol. 159, pp. 922–927, 2006.

[65] Y. Yin, X. Lin, X. Yang, S. Yu, and Q. Du, “Effect of compressing pressure on performance of a DMFC,” in *Proc. Int. Conf. on Remote Sensing, Environment and Transp. Eng. (RSETE)*, Nanjing, 2011, pp. 1139–1142.

[66] P. A. García-Salaberri and M. Vera, “On the effects of assembly compression on the performance of liquid-feed DMFCs under methanol-limiting conditions: A 2D numerical study,” *Journal of Power Sources*, vol. 285. pp. 543–558, 2015.

[67] W. K. Lee, C. H. Ho, J. W. Van Zee, and M. Murthy, “Effects of compression and gas diffusion layers on the performance of a PEM fuel cell,” *J. Power Sources*, vol. 84, pp. 45–51, 1999.

[68] L. Zhang, Y. Liu, H. Song, S. Wang, Y. Zhou, and S. J. Hu, “Estimation of contact resistance in proton exchange membrane fuel cells,” *J. Power Sources*, vol. 162, pp. 1165–1171, 2006.

[69] T. Berning and N. Djilali, “Three-dimensional computational analysis of transport phenomena in a PEM fuel cell—a parametric study,” *Journal of Power Sources*, vol. 124. pp. 440–452, 2003.

[70] S. D. Yim, B. J. Kim, Y. J. Sohn, Y. G. Yoon, G. G. Park, W. Y. Lee, C. S. Kim, and Y. C. Kim, “The influence of stack clamping pressure on the performance of PEM fuel cell stack,” *Curr. Appl. Phys.*, vol. 10, no. 2, pp. S59–S61, 2010.

[71] S. Karvonen, T. Hottinen, J. Ihonen, and H. Uusalo, “Modeling of Polymer Electrolyte Membrane Fuel Cell Stack End Plates,” *Journal of Fuel Cell Science and Technology*, vol. 5. p. 041009, 2008.

[72] Y. Zhou, G. Lin, A. J. Shih, and S. J. Hu, “Multiphysics Modeling of Assembly Pressure Effects on Proton Exchange Membrane Fuel Cell Performance,” *Journal of Fuel Cell Science and Technology*, vol. 6. p. 041005, 2009.

[73] C. Carral and P. Mélé, “A numerical analysis of PEMFC stack assembly through a 3D finite element model,” *Int. J. Hydrogen Energy*, vol. 39, pp. 4516–4530, 2014.

[74] I. Gatto, F. Urbani, G. Giacoppo, O. Barbera, and E. Passalacqua, “Influence of the bolt torque on PEFC performance with different gasket materials,” *Int. J. Hydrogen Energy*, vol. 36, pp. 13043–13050, 2011.

[75] H. S. Chu, C. Yeh, and F. Chen, “Effects of porosity change of gas diffuser on performance of proton exchange membrane fuel cell,” *J. Power Sources*, vol. 123, pp. 1–9, 2003.

[76] V. Mishra, F. Yang, and R. Pitchumani, “Measurement and Prediction of Electrical Contact Resistance Between Gas Diffusion Layers and Bipolar Plate for Applications to PEM Fuel Cells,” *Journal of Fuel Cell Science and Technology*, vol. 1. p. 2, 2004.

[77] B. Avasarala and P. Haldar, “Effect of surface roughness of composite bipolar plates on the contact resistance of a proton exchange membrane fuel cell,” *J. Power Sources*, vol. 188, pp. 225–229, 2009.

[78] X. Q. Xing, K. W. Lum, H. J. Poh, and Y. L. Wu, “Optimization of assembly clamping pressure on performance of proton-exchange membrane fuel cells,” *J. Power Sources*, vol. 195, pp. 62–68, 2010.

[79] Inc. EG&G Technical Services, *Fuel Cell Handbook*, 7th ed. 2004.

[80] M. M. Mench, C. Wang, and S. T. Thynell, “An Introduction to Fuel Cells and Related Transport Phenomena,” *Int. J. Transp. Phenom.*, vol. 3, pp. 1–58, 2001.

[81] M. M. Mench, *Fuel Cell Engines*. New Jersey: Wiley, 2008.

[82] K. J. Lange, P.-C. Sui, and N. Djilali, “Determination of effective transport properties in a PEMFC catalyst layer using different reconstruction algorithms,” *J. Power Sources*, vol. 208, pp. 354–365, Jun. 2012.

[83] F. N. Büchi, M. Inaba, and T. J. Schmidt, *Polymer Electrolyte Fuel Cell Durability*, 1st ed., vol. 1. New York: Springer-Verlag, 2009.

[84] N. David, K. Von Schilling, P. M. Wild, and N. Djilali, “ScienceDirect In situ measurement of relative humidity in a PEM fuel cell using fibre Bragg grating sensors,” *Int. J. Hydrogen Energy*, vol. 39, no. 31, pp. 17638–17644, 2014.

[85] B. Markicevic and N. Djilali, “Analysis of liquid water transport in fuel cell gas diffusion media using two-mobile phase pore network simulations,” *J. Power Sources*, vol. 196, no. 5, pp. 2725–2734, 2011.

[86] N. Zamel, E. Litovsky, S. Shakhshir, X. Li, and J. Kleiman, “Measurement of in-plane thermal conductivity of carbon paper diffusion media in the temperature range of −20°C to +120°C,” *Appl. Energy*, vol. 88, no. 9, pp. 3042–3050, Sep. 2011.

[87] N. Zamel, J. Becker, and A. Wiegmann, “Estimating the thermal conductivity and diffusion coefficient of the microporous layer of polymer electrolyte membrane fuel cells,” *J. Power Sources*, vol. 207, pp. 70–80, Jun. 2012.

[88] H. M. Chang, C. W. Lin, M. H. Chang, H. R. Shiu, W. C. Chang, and F. H. Tsau, “Optimization of polytetrafluoroethylene content in cathode gas diffusion layer by the evaluation of compression effect on the performance of a proton exchange membrane fuel cell,” *J. Power Sources*, vol. 196, pp. 3773–3780, 2011.

[89] H. Sadeghifar, N. Djilali, and M. Bahrami, “Effect of Polytetrafluoroethylene (PTFE) and micro porous layer (MPL) on thermal conductivity of fuel cell gas diffusion layers: Modeling and experiments,” *J. Power Sources*, vol. 248, pp. 632–641, Feb. 2014.

[90] G. Karimi, X. Li, and P. Teertstra, “Measurement of through-plane effective thermal conductivity and contact resistance in PEM fuel cell diffusion media,” *Electrochim. Acta*, vol. 55, no. 5, pp. 1619–1625, Feb. 2010.

[91] M. Khandelwal and M. M. Mench, “Direct measurement of through-plane thermal conductivity and contact resistance in fuel cell materials,” *J. Power Sources*, vol. 161, no. 2, pp. 1106–1115, Oct. 2006.

[92] E. Sadeghi, N. Djilali, and M. Bahrami, “Effective thermal conductivity and thermal contact resistance of gas diffusion layers in proton exchange membrane fuel cells. Part 2: Hysteresis effect under cyclic compressive load,” *J. Power Sources*, vol. 195, no. 24, pp. 8104–8109, Dec. 2010.

[93] O. Burheim, P. J. S. Vie, J. G. Pharoah, and S. Kjelstrup, “Ex situ measurements of through-plane thermal conductivities in a polymer electrolyte fuel cell,” *J. Power Sources*, vol. 195, no. 1, pp. 249–256, Jan. 2010.

[94] N. Alhazmi, D. B. Ingham, M. S. Ismail, K. Hughes, L. Ma, and M. Pourkashanian, “The through-plane thermal conductivity and the contact resistance of the components of the membrane electrode assembly and gas diffusion layer in proton exchange membrane fuel cells,” *J. Power Sources*, vol. 270, pp. 59–67, 2014.

[95] D. J. Burford and M. M. Mench, “Heat transport and temperature distribution in PEFCS,” in *ASME 2004 International Mechanical Engineering Congress and Exposition*, 2004, vol. 2, pp. 317–339.

[96] P. J. S. Vie and S. Kjelstrup, “Thermal conductivities from temperature profiles in the polymer electrolyte fuel cell,” *Electrochimica Acta*, vol. 49. pp. 1069–1077, 2004.

[97] M. Kawase, T. Inagaki, S. Kawashima, and K. Miura, “Effective Thermal Conductivity of Gas Diffusion Layer in Through-Plane Direction,” *ECS Trans.*, vol. 25, pp. 1529–1537, 2009.

[98] S. E. Gustafsson, E. Karawacki, and M. N. Khan, “Transient hot-strip method for simultaneously measuring thermal conductivity and thermal diffusivity of solids and fluids,” *Journal of Physics D: Applied Physics*, vol. 12. pp. 1411–1421, 2001.

[99] S. E. Gustafsson, E. Karawacki, and M. A. Chohan, “Thermal transport studies of electrically conducting materials using the transient hot-strip technique,” *J. Phys. D. Appl. Phys.*, vol. 19, p. 727, 1986.

[100] J. Ihonen, M. Mikkola, and G. Lindbergh, “Flooding of Gas Diffusion Backing in PEFCs,” *Journal of The Electrochemical Society*, vol. 151. p. A1152, 2004.

[101] O. S. Burheim, J. G. Pharoah, H. Lampert, P. J. S. Vie, and S. Kjelstrup, “Through-Plane Thermal Conductivity of PEMFC Porous Transport Layers,” *J. Fuel Cell Sci. Technol.*, vol. 8, no. April 2011, p. 021013, 2011.

[102] P. Teertstra, G. Karimi, and X. Li, “Measurement of in-plane effective thermal conductivity in PEM fuel cell diffusion media,” *Electrochim. Acta*, vol. 56, no. 3, pp. 1670–1675, Jan. 2011.

[103] O. S. Burheim, G. Ellila, J. D. Fairweather, a. Labouriau, S. Kjelstrup, and J. G. Pharoah, “Ageing and thermal conductivity of Porous Transport Layers used for PEM fuel cells,” *J. Power Sources*, vol. 221, pp. 356–365, 2013.

[104] “Toray carbon paper-Manufacturer data sheet,” *http://www.torayca.com/index2.html*. .

[105] A. Pfrang, D. Veyret, and G. Tsotridis, “Computation of Thermal Conductivity of Gas Diffusion Layers of PEM Fuel Cells,” in *Convection and Conduction Heat Transfer*, A. Ahsan, InTech, 2011.

[106] J. K. Carson, S. J. Lovatt, D. J. Tanner, and A. C. Cleland, “Thermal conductivity bounds for isotropic, porous materials,” *Int. J. Heat Mass Transf.*, vol. 48, pp. 2150–2158, 2005.

[107] J. Wang, J. K. Carson, M. F. North, and D. J. Cleland, "A new structural model of effective thermal conductivity for heterogeneous materials with co-continuous phases," *Int. J. Heat Mass Transf.*, vol. 51, pp. 2389–2397, 2008.

[108] A. Eucken, "Gesetzmässigkeiten für das Wärmeleitvermögen verschiedener Stoffarten und Aggregatzustände," *Forsch. auf dem Gebiete des Ingenieurwesens*, vol. 11, no. 1, pp. 6–20, 1940.

[109] P. K. Das, X. Li, and Z. S. Liu, "Effective transport coefficients in PEM fuel cell catalyst and gas diffusion layers: Beyond Bruggeman approximation," *Appl. Energy*, vol. 87, pp. 2785–2796, 2010.

[110] N. Zamel, X. Li, J. Shen, J. Becker, and A. Wiegmann, "Estimating effective thermal conductivity in carbon paper diffusion media," *Chem. Eng. Sci.*, vol. 65, pp. 3994–4006, 2010.

[111] X.-M. Zhang and X.-X. Zhang, "Impact of Compression on Effective Thermal Conductivity and Diffusion Coefficient of Woven Gas Diffusion Layers in Polymer Electrolyte Fuel Cells," *Fuel Cells*, vol. 14, no. 2, pp. 303–311, 2014.

[112] J. Becker, R. Flückiger, M. Reum, F. N. Büchi, F. Marone, and M. Stampanoni, "Determination of Material Properties of Gas Diffusion Layers: Experiments and Simulations Using Phase Contrast Tomographic Microscopy," *Journal of The Electrochemical Society*, vol. 156. p. B1175, 2009.

[113] I. Nitta, O. Himanen, and M. Mikkola, "Thermal conductivity and contact resistance of compressed gas diffusion layer of PEM fuel cell," *Fuel Cells*, vol. 8, pp. 111–119, 2008.

[114] D. Veyret and G. Tsotridis, "Numerical determination of the effective thermal conductivity of fibrous materials. Application to proton exchange membrane fuel cell gas diffusion layers," *J. Power Sources*, vol. 195, pp. 1302–1307, 2010.

[115] J. Yablecki and A. Bazylak, "Determining the effective thermal conductivity of compressed PEMFC GDLs through thermal resistance modelling," *J. Power Sources*, vol. 217, pp. 470–478, 2012.

[116] B. P. Jiang, F. L. Chen, P. Yan, and F. Song, "Prediction of effective stagnant thermal conductivities of porous materials at high temperature by the generalized self-consistent method," *Philos. Mag.*, vol. 92, no. 2032–2047, 2012.

[117] C. Huang and Y. Zhang, “Calculation of high-temperature insulation parameters and heat transfer behaviors of multilayer insulation by inverse problems method,” *Chinese Journal of Aeronautics*, 2014.

[118] S. Y. Zhao, B. M. Zhang, and S. Y. Du, “An inverse analysis to determine conductive and radiative properties of a fibrous medium,” *J. Quant. Spectrosc. Radiat. Transf.*, vol. 110, pp. 1111–1123, 2009.

[119] G. Unsworth, N. Zamel, and X. Li, “Through-plane thermal conductivity of the microporous layer in a polymer electrolyte membrane fuel cell,” *Int. J. Hydrogen Energy*, vol. 37, no. 6, pp. 5161–5169, 2012.

[120] G. Unsworth, “Measurement and Characterization of Heat and Mass Diffusion in PEMFC Porous Media,” M.Sc. Thesis, University of Waterloo, Waterloo, Canada, 2012.

[121] S. F. Burlatsky, V. V. Atrazhev, M. Gummalla, D. A. Condit, and F. Liu, “The impact of thermal conductivity and diffusion rates on water vapor transport through gas diffusion layers,” *J. Power Sources*, vol. 190, pp. 485–492, 2009.

[122] X. Wang, H. Zhang, J. Zhang, H. Xu, X. Zhu, J. Chen, and B. Yi, “A bi-functional micro-porous layer with composite carbon black for PEM fuel cells,” *J. Power Sources*, vol. 162, pp. 474–479, 2006.

[123] A. Z. Weber and J. Newman, “Effects of Microporous Layers in Polymer Electrolyte Fuel Cells,” *J. Electrochem. Soc.*, vol. 152, p. A677, 2005.

[124] O. S. Burheim, H. Su, S. Pasupathi, J. G. Pharoah, and B. G. Pollet, “Thermal conductivity and temperature profiles of the micro porous layers used for the polymer electrolyte membrane fuel cell,” *Int. J. Hydrogen Energy*, vol. 38, no. 20, pp. 8437–8447, 2013.

[125] F. Barbir, *PEM fuel cells: theory and practice*. Elsevier, 2005.

[126] W.-J. Chen, M.-C. Yip, S. C. Chen, C. C. M. Ma, and Y. Li, “Preparation sheet and Characterization of Carbon Nano Tube /Phenolic resin Nanocomposite for Fuel Cell Bipolar Plate,” in *16th International Conference on Composite Materials*, Kyoto International Conference Center (ICC Kyoto), 2007, pp. 1–10.

[127] Colleen Spiegel, *Designing and Building Fuel Cells*, 1st ed., Mc Graw Hill, 2007.

[128] S. Shimpalee, M. Ohashi, J. W. Van Zee, C. Ziegler, C. Stoeckmann, C. Sadeler, and C. Hebling, "Experimental and numerical studies of portable PEMFC stack," *Electrochim. Acta*, vol. 54, pp. 2899–2911, 2009.

[129] M.-C. Hsiao, S.-H. Liao, M.-Y. Yen, C.-C. Teng, S.-H. Lee, N.-W. Pu, C.-A. Wang, Y. Sung, M.-D. Ger, C.-C. M. Ma, and M.-H. Hsiao, "Preparation and properties of a graphene reinforced nanocomposite conducting plate," *Journal of Materials Chemistry*, vol. 20. p. 8496, 2010.

[130] D. Zhu, X. Li, N. Wang, X. Wang, J. Gao, and H. Li, "Dispersion behavior and thermal conductivity characteristics of Al2O3-H2O nanofluids," *Curr. Appl. Phys.*, vol. 9, pp. 131–139, 2009.

[131] X. Zheng, D. Yang, K. Tao, H. Zhang, and M. Jianxin, "Design of Forced Air-cooling Structure for Elevated Temperature PEMFC," *World Electr. Veh. J.*, vol. 4, pp. 000464–000469, 2010.

[132] Y. Wang and K. S. Chen, "Elucidating two-phase transport in a polymer electrolyte fuel cell, Part 1: Characterizing flow regimes with a dimensionless group," *Chem. Eng. Sci.*, vol. 66, pp. 3557–3567, 2011.

[133] R. Taherian, A. N. Golikand, and M. J. Hadianfard, "Preparation and Properties of a Novel Phenolic/Graphite Nanocomposite Bipolar Plate for Proton Exchange Membrane Fuel Cell," *J. Solid State Sci. Technol.*, vol. 1, pp. M39–M46, 2012.

[134] R. Taherian, "A review of composite and metallic bipolar plates in proton exchange membrane fuel cell: Materials, fabrication, and material selection," *J. Power Sources*, vol. 265, pp. 370–390, 2014.

[135] F. Gao, B. Blunier, and A. Miraoui, *Proton Exchange Membrane Fuel Cells Modeling*. London, UK: Wiley-ISTE, 2012.

[136] S. Shahsavari, A. Desouza, M. Bahrami, and E. Kjeang, "Thermal analysis of air-cooled PEM fuel cells," *Int. J. Hydrogen Energy*, vol. 37, no. 23, pp. 18261–18271, 2012.

[137] A. Ghosh, P. Goswami, P. Mahanta, and A. Verma, "Effect of carbon fiber length and graphene on carbon-polymer composite bipolar plate for PEMFC," *J. Solid State Electrochem.*, vol. 18, no. 12, pp. 3427–3436, 2014.

[138] U. Pasaogullari, C.-Y. Wang, and K. S. Chen, "Two-Phase Transport in Polymer Electrolyte Fuel Cells with Bilayer Cathode Gas Diffusion Media," *J. Electrochem. Soc.*, vol. 152, p. A1574, 2005.

[139] Z. Fishman and A. Bazylak, “Heterogeneous Through-Plane Porosity Distributions for Treated PEMFC GDLs. II. Effect of MPL Cracks,” *J. Electrochem. Soc.*, vol. 158, no. 8, p. B846, 2011.

[140] R. C. Makkus, A. H. H. Janssen, F. A. De Bruijn, and R. K. A. M. Mallant, “Use of stainless steel for cost competitive bipolar plates in the SPFC,” *J. Power Sources*, vol. 86, pp. 274–282, 2000.

[141] J. Ihonen, F. Jaouen, G. Lindbergh, and G. Sundholm, “A novel polymer electrolyte fuel cell for laboratory investigations and in-situ contact resistance measurements,” *Electrochim. Acta*, vol. 46, pp. 2899–2911, 2001.

[142] F. Barbir, J. Braun, and J. Neutzler, “Properties of Molded Graphite Bi-Polar Plates for PEM Fuel Cell Stacks,” *J. New Mater. Electrochem. Syst.*, vol. 2, pp. 197–200, 1999.

[143] H. Wang, “Stainless steel as bipolar plate material for polymer electrolyte membrane fuel cells,” *Journal of Power Sources*, vol. 115. pp. 243–251, 2003.

[144] D. P. Davies, P. L. Adcock, M. Turpin, and S. J. Rowen, “Bipolar plate materials for solid polymer fuel cells,” *J. Appl. Electrochem.*, vol. 30, pp. 101–105, 1999.

[145] E. A. Cho, U. S. Jeon, H. Y. Ha, S. A. Hong, and I. H. Oh, “Characteristics of composite bipolar plates for polymer electrolyte membrane fuel cells,” *J. Power Sources*, vol. 125, pp. 178–182, 2004.

[146] T. Matsuura, M. Kato, and M. Hori, “Study on metallic bipolar plate for proton exchange membrane fuel cell,” *J. Power Sources*, vol. 161, pp. 74–78, 2006.

[147] P. Zhou, C. W. Wu, and G. J. Ma, “Contact resistance prediction and structure optimization of bipolar plates,” *J. Power Sources*, vol. 159, pp. 1115–1122, 2006.

[148] X. Yan, M. Hou, H. Zhang, F. Jing, P. Ming, and B. Yi, “Performance of PEMFC stack using expanded graphite bipolar plates,” *J. Power Sources*, vol. 160, pp. 252–257, 2006.

[149] Y. Zhou, G. Lin, A. J. Shih, and S. J. Hu, “A micro-scale model for predicting contact resistance between bipolar plate and gas diffusion layer in PEM fuel cells,” *J. Power Sources*, vol. 163, no. 2, pp. 777–783, 2007.

[150] W. X. Yin, Z. P. Li, J. K. Zhu, and H. Y. Qin, “Effects of NaOH addition on performance of the direct hydrazine fuel cell,” *J. Power Sources*, vol. 182, pp. 520–523, 2008.

[151] R. Holm, “Electric Contacts,” *Springer-Verlag New York*, pp. 1–55,367–397, 1967.

[152] A. Kraytsberg, M. Auinat, and Y. Ein-Eli, “Reduced contact resistance of PEM fuel cell’s bipolar plates via surface texturing,” *J. Power Sources*, vol. 164, pp. 697–703, 2007.

[153] Z. Wu, S. Wang, L. Zhang, and S. J. Hu, “An analytical model and parametric study of electrical contact resistance in proton exchange membrane fuel cells,” *J. Power Sources*, vol. 189, pp. 1066–1073, 2009.

[154] J. A. Greenwood and J. H. Tripp, “The contact of two nominally flat rough surfaces,” *ARCHIVE: Proceedings of the Institution of Mechanical Engineers 1847-1982 (vols 1-196)*, vol. 185. pp. 625–634, 2006.

[155] X. Lai, D. Liu, L. Peng, and J. Ni, “A mechanical-electrical finite element method model for predicting contact resistance between bipolar plate and gas diffusion layer in PEM fuel cells,” *J. Power Sources*, vol. 182, pp. 153–159, 2008.

[156] J. André, L. Antoni, J. P. Petit, E. De Vito, and A. Montani, “Electrical contact resistance between stainless steel bipolar plate and carbon felt in PEFC: A comprehensive study,” *Int. J. Hydrogen Energy*, vol. 34, pp. 3125–3133, 2009.

[157] P. Zhou, P. Lin, C. W. Wu, and Z. Li, “Effect of nonuniformity of the contact pressure distribution on the electrical contact resistance in proton exchange membrane fuel cells,” *International Journal of Hydrogen Energy*, vol. 36. pp. 6039–6044, 2011.

[158] T. J. Mason, J. Millichamp, T. P. Neville, A. El-Kharouf, B. G. Pollet, and D. J. L. Brett, “Effect of clamping pressure on ohmic resistance and compression of gas diffusion layers for polymer electrolyte fuel cells,” *J. Power Sources*, vol. 219, pp. 52–59, 2012.

[159] A. El-Kharouf, T. J. Mason, D. J. L. Brett, and B. G. Pollet, “Ex-situ characterisation of gas diffusion layers for proton exchange membrane fuel cells,” *Journal of Power Sources*, vol. 218. pp. 393–404, 2012.

[160] M. S. Ismail, D. B. Ingham, L. Ma, and M. Pourkashanian, “The contact resistance between gas diffusion layers and bipolar plates as they are assembled in proton exchange membrane fuel cells,” *Renew. Energy*, vol. 52, pp. 40–45, 2013.

[161] C. J. Netwall, B. D. Gould, J. A. Rodgers, N. J. Nasello, and K. E. Swider-Lyons, "Decreasing contact resistance in proton-exchange membrane fuel cells with metal bipolar plates," *J. Power Sources*, vol. 227, pp. 137–144, 2013.

[162] D. Singdeo, T. Dey, and P. C. Ghosh, "Contact resistance between bipolar plate and gas diffusion layer in high temperature polymer electrolyte fuel cells," *Int. J. Hydrogen Energy*, vol. 39, no. 2, pp. 987–995, 2014.

[163] P. R. Nayak, "Random process model of rough surfaces in plastic contact," *Wear*, vol. 26. pp. 305–333, 1973.

[164] R. Taherian, M. J. Hadianfard, and A. N. Golikand, "A new equation for predicting electrical conductivity of carbon-filled polymer composites used for bipolar plates of fuel cells," *J. Appl. Polym. Sci.*, vol. 128, pp. 1497–1509, 2013.

[165] G. Li, J. Tan, and J. Gong, "Effect of Compressive Pressure on the Contact Behavior Between Bipolar Plate and Gas Diffusion Layer in a Proton Exchange Membrane Fuel Cell," *J. Fuel Cell Sci. Technol.*, vol. 11, no. 4, pp. 041009–041009–6, 2014.

[166] P. K. Sow, S. Prass, P. Kalisvaart, and W. Mérida, "Deconvolution of electrical contact and bulk resistance of gas diffusion layers for fuel cell applications," *Int. J. Hydrogen Energy*, vol. 40, pp. 2850–2861, 2015.

[167] "ASTM E1225-13, Standard Test Method for Thermal Conductivity of Solids Using the Guarded-Comparative-Longitudinal Heat Flow Technique, ASTM International," West Conshohocken, USA, 2013. *www.astm.org/Standards/E1225.htm*.

[168] R.W. Powell, "Thermal Conductivity of Selected Materials, National Standard Reference Data Series– 8, 25." National Bureau of Standards, 1966.

[169] E. Sadeghi, N. Djilali, and M. Bahrami, "Effective thermal conductivity and thermal contact resistance of gas diffusion layers in proton exchange membrane fuel cells. Part 1: Effect of compressive load," *J. Power Sources*, vol. 196, pp. 246–254, 2011.

[170] P. R. Bevington, *Data reduction and error analysis for the physical sciences*, 3rd ed. McGraw-Hill Science/Engineering, 1969.

[171] H. W. Coleman, J. Steele, and W. Glenn, *Experimentation and Uncertainty Analysis for Engineers*. New York, USA: Wiley, 1999.

[172] E. R. Cohen, *An Introduction to Error Analysis: The Study of Uncertainties in Physical Measurements*, 2nd ed., University Science Books, 2009.

[173] "SGL Group – The Carbon company. SIGRACET diffusion media, manufacture data sheet. Web: http://www.sglgroup.com/cms/international/home."

[174] D. Bi, H. Chen, and T. Ye, "Influences of temperature and contact pressure on thermal contact resistance at interfaces at cryogenic temperatures," *Cryogenics (Guildf).*, vol. 52, pp. 403–409, 2012.

[175] R. P. Ramasamy, E. C. Kumbur, M. M. Mench, W. Liu, D. Moore, and M. Murthy, "Investigation of macro- and micro-porous layer interaction in polymer electrolyte fuel cells," *Int. J. Hydrogen Energy*, vol. 33, pp. 3351–3367, 2008.

[176] K. Kang and H. Ju, "Numerical modeling and analysis of micro-porous layer effects in polymer electrolyte fuel cells," *J. Power Sources*, vol. 194, pp. 763–773, 2009.

[177] M. K. Debe, "Electrocatalyst approaches and challenges for automotive fuel cells," *Nature*, vol. 486. pp. 43–51, 2012.

[178] W. Yovanovich, M, Rohsenow, "Influence of surface roughness and waviness upon thermal contact resistance," Cambridge, Mass. : M.I.T. Dept. of Mechanical Engineering, USA, 14135679, 1967.

[179] K. Kumar, S. Sunil, Ramamurthi, "Influence of Flatness and Waviness of Rough Surfaces on Surface Contact Conductance," *ASME J. Heat Transf.*, vol. 125, pp. 394–402, 2003.

[180] M. Bahrami, M. M. Yovanovich, and J. R. Culham, "Effective thermal conductivity of rough spherical packed beds," *Int. J. Heat Mass Transf.*, vol. 49, no. 19–20, pp. 3691–3701, Sep. 2006.

[181] M. Bahrami, M. M. Yovanovich, and J. R. Culham, "Thermal Joint Resistances of Nonconforming Rough Surfaces with Gas-Filled Gaps," *J. Thermophys. Heat Transf.*, vol. 18, no. 3, pp. 326–332, 2004.

[182] M. Bahrami, J. R. Culham, M. M. Yovanovich, and G. E. Schneider, "Thermal Contact Resistance of Nonconforming Rough Surfaces, Part 2: Thermal Model," *J. Thermophys. Heat Transf.*, vol. 18, no. 2, pp. 218–227, 2004.

[183] M. Bahrami, M. M. Yovanovich, and R. J. Culham, "Assessment of Relevant Physical Phenomena Controlling Thermal Performance of Nanofluids," *J. Thermophys. Heat Transf.*, vol. 21, no. 4, pp. 673–680, 2007.

[184] M. Bahrami, M. Yovanovich, and J. Culham, "Thermal contact resistance at low contact pressure: Effect of elastic deformation," *Int. J. Heat Mass Transf.*, vol. 48, no. 16, pp. 3284–3293, Jul. 2005.

[185] M. Bahrami, M. M. Yovanovich, and J. R. Culham, "Thermal Contact Resistance : Effect of Elastic Deformation," in *Semiconductor Thermal Measurement and Management IEEE Twenty First Annual IEEE Symposium, 2005.*, 2005, pp. 44 – 52.

[186] "Easyfit software, MathWave Technology, http://www.mathwave.com/help/easyfit/index.html."

[187] M. Bahrami, M. Yovanovich, and R. Culham, "Pressure Drop of Fully Developed, Laminar Flow in Rough Microtubes," *ASME J. Fluid Eng.*, vol. 128, pp. 632–637, 2006.

[188] A. Tamayol and M. Bahrami, "Analytical determination of viscous permeability of fibrous porous media," *Int. J. Heat Mass Transf.*, vol. 52, no. 9–10, pp. 2407–2414, 2009.

[189] J. T. Gostick, M. W. Fowler, M. D. Pritzker, M. a. Ioannidis, and L. M. Behra, "In-plane and through-plane gas permeability of carbon fiber electrode backing layers," *J. Power Sources*, vol. 162, pp. 228–238, 2006.

[190] P. Webb, "An introduction to the physical characterization of materials by mercury intrusion porosimetry with emphasis on reduction and presentation of experimental data," Norcross, USA, 2001.

[191] L. Ritter, HL; Drake, "Pore-size distribution in porous materials. Pressure porosimeter and determination of complete macropore-size distribution," *Ind. Eng. Chem. Anal.*, vol. 17, pp. 782–786, 1945.

[192] A. El-kharouf, B. G. Polleta, and D. Brettb, "Effect of commercial gas diffusion layer (gdl) properties on pemfc performance – from ex-situ testing to modelling," http://www.megs.ac.uk/megs/images-multimedia/documents/megs09-12/postertemplatehfcmexico2011.pdf, 2009.

[193] P. Cheung, J. D. Fairweather, and D. T. Schwartz, “Characterization of internal wetting in polymer electrolyte membrane gas diffusion layers,” *J. Power Sources*, vol. 187, pp. 487–492, 2009.

[194] V. Radhakrishnan and P. Haridoss, “Effect of cyclic compression on structure and properties of a Gas Diffusion Layer used in PEM fuel cells,” *Int. J. Hydrogen Energy*, vol. 35, no. 20, pp. 11107–11118, 2010.

[195] J. T. Gostick, M. A. Ioannidis, M. D. Pritzker, and M. W. Fowler, “Impact of Liquid Water on Reactant Mass Transfer in PEM Fuel Cell Electrodes,” *Journal of The Electrochemical Society*, vol. 157. p. B563, 2010.

[196] P. Fluckiger, “Transport Phenomena on the Channel-Rib Scale of Polymer Electrolyte Fuel Cells,” PhD Thesis, Fluckiger, Zurich, Switzerland, 2009.

[197] J. Scholta, M. Schulze, S. Donath, J. Pauchet, S. Fell, G. Tsotridis, and T. Damjanovic, “Gas Diffusion Layer (GDL) Degradation in Polymer Electrolyte Fuel Cells,” in *2nd CARISMA International Conference on Progress in MEA Materials for Medium and High Temperature Polymer Electrolyte Fuel Cells*, La Grande Motte, France, 2010.

[198] A. Bazylak, D. Sinton, Z. S. Liu, and N. Djilali, “Effect of compression on liquid water transport and microstructure of PEMFC gas diffusion layers,” *J. Power Sources*, vol. 163, pp. 784–792, 2007.

[199] H. Sadeghifar, M. Bahrami, and N. Djilali, “Interfacial and Bulk Transport Properties of Gas Diffusion Layers,” *4th Canada-China Clean Energy Conference*. Victoria, BC, Canada, 2014.

[200] H. Sadeghifar, N. Djilali, and M. Bahrami, “A cloased-form compact formula for Nusselt number inside fibrous materials.” (In preparation), 2015.

[201] H. Sadeghifar, N. Djilali, and M. Bahrami, “A compact closed-form Nusselt formula for laminar longitudinal flow between rectangular/square arrays of parallel cylinders with unequal row temperatures.” Under review, 2015.

[202] D. Li, Y. Wang, and Y. Xia, “Electrospinning of polymeric and ceramic nanofibers as uniaxially aligned arrays,” *Nano Lett.*, vol. 3, pp. 1167–1171, 2003.

[203] D. Li and Y. Xia, “Electrospinning of nanofibers: Reinventing the wheel?,” *Advanced Materials*, vol. 16. pp. 1151–1170, 2004.

[204] J. Xie and Y. Xia, "Electrospinning: An Enabling Technique for Nanostructured Materials," *Mater. Matters*, vol. 3, no. 1, p. 19, 2008.

[205] S. Jana, A. Cooper, F. Ohuchi, and M. Zhang, "Uniaxially aligned nanofibrous cylinders by electrospinning," *ACS Appl. Mater. Interfaces*, vol. 4, pp. 4817–4824, 2012.

[206] Q. P. Pham, U. Sharma, and A. G. Mikos, "Electrospinning of polymeric nanofibers for tissue engineering applications: a review.," *Tissue Eng.*, vol. 12, pp. 1197–1211, 2006.

[207] I. S. Chronakis, "Novel nanocomposites and nanoceramics based on polymer nanofibers using electrospinning process - A review," *Journal of Materials Processing Technology*, vol. 167. pp. 283–293, 2005.

[208] Z. Fishman, J. Hinebaugh, and A. Bazylak, "Microscale Tomography Investigations of Heterogeneous Porosity Distributions of PEMFC GDLs," *J. Electrochem. Soc.*, vol. 157, p. B1643, 2010.

[209] L. Jia, Z. Tan, M. Kang, and Z. Zhang, "Experimental investigation on dynamic characteristics of proton exchange membrane fuel cells at subzero temperatures," *Int. J. Hydrogen Energy*, vol. 39, no. 21, pp. 11120–11127, 2014.

[210] J. J. Hwang, C. H. Chao, C. L. Chang, W. Y. Ho, and D. Y. Wang, "Modeling of two-phase temperatures in a two-layer porous cathode of polymer electrolyte fuel cells," *Int. J. Hydrogen Energy*, vol. 32, pp. 405–414, 2007.

[211] M. Bahrami, J. R. Culham, and M. M. Yovanovich, "Modeling Thermal Contact Resistance: A Scale Analysis Approach," *J. Heat Transfer*, vol. 126, no. December, p. 896, 2004.

[212] M. Bahrami, J. R. Culham, M. M. Yananovich, and G. E. Schneider, "Review of Thermal Joint Resistance Models for Nonconforming Rough Surfaces," *Applied Mechanics Reviews*, vol. 59. p. 1, 2006.

[213] M. Bahrami, "Modeling of thermal joint resistance for rough sphere-flat contact in a vacuum," PhD Thesis, University of Waterloo, Waterloo, Canada, 2004.

[214] B. B. Mikic, "Analytic Studies of Contact of Nominally Flat Surfaces; Effect of ... Theoretical Considerations," *Int. J. Heat Mass Transf.*, vol. 17, pp. 205–214, 1974.

[215] K. Johnson, *Contact mechanics*, 1st ed., Cambridge University Press, 1987.

[216] C. Leising, “fuel cell gas diffusion layer inspection with 3D profilometry, Today’s standard for tomorrow's materials,” http://www.nanovea.com/Application%20Notes/FuelCell3DMetrology.pdf, Irvine, USA, 2010.

[217] V. Norouzifard and M. Bahrami, “Deformation of PEM fuel cell gas diffusion layers under compressive loading: An analytical approach,” *J. Power Sources*, vol. 264, pp. 92–99, 2014.

[218] H. Sadeghifar, V. Norouzifard, and M. Bahrami, “Bulk and interfacial transport properties of porous fuel cell materials, AFCC-NSERC CRD Grant Proposal, Laboratory for Alternative Energy Conversion, Simon Fraser University,” Vancouver, BC, Canada, 2014.

[219] “Sensor Expert.” Madison, USA, 2014. http://www.sensorexpert.com/aboutus.php.

[220] “Image Processing and Analysis in Java. http://imagej.nih.gov/ij/.” .

[221] M. Yovanovich and E. Marotta, “Thermal spreading and contact resistance,” in *Heat Transfer Handbook*, A. Bejan and A. D. Kraus, Eds. New York: Wiley, 2003.

[222] H. Sadeghifar, N. Djilali, M. Eikerling, and M. Bahrami, “A novel approach to measuring in-plane electrical conductivity of a catalyst coated membrane (CCM) and its electrical contact resistance with fuel cell gas diffusion layers (GDLs) and micro porous layers (MPLs): Effect of compression, PTFE and humidity,” *97th Canadian Chemistry Conference and Exhibition*. Vancouver, BC, Canada, 2014.

[223] H. Sadeghifar, N. Djilali, and M. Bahrami, “Role of micro porous layer (MPL) in electrical and thermal resistances of fuel cell gas diffusion layers (GDLs),” *97th Canadian Chemistry Conference and Exhibition*. Vancouver, BC, Canada, 2014.

[224] H. Schulenburg, C. Roth, and F. Scheiba, “Advanced microscopy techniques for the characterization of polymer electrolyte membrane fuel cell components,” in *In Situ Characterization Techniques for Low Temperature Fuel Cells*, Elsevier, 2012, pp. 26–64.

[225] C. Hartnig, L. Jörissen, J. Scholta, and W. Lehnert, “Gas diffusion media, flowfields and system aspects in low temperature fuel cells,” in *Polymer Electrolyte Membrane and Direct Methanol Fuel Cell Technology: Fundamentals and Performance of Low Temperature Fuel Cells*, Elsevier, 2012, pp. 81–116.

[226] H. Sadeghifar, M. Bahrami, and N. Djilali, "Thermal conductivity of Sigracet gas diffusion layers and MPL: Part I. Effect of compression, PTFE, MPL, cyclic load and hysteresis behavior," *Hydrogen & Fuel Cell conference*. Vancouver, BC, Canada, 2013.

[227] Ch. Van Bellingen, N. Probst, E. Grivei, and C. Ciallella, "Additives for Electrical and Thermal Conductivity," *BPRI meeting on additives*. Gent, 2008.

[228] S. J. Botelho and A. Bazylak, "Impact of polymer electrolyte membrane fuel cell microporous layer nano-scale features on thermal conductance," *J. Power Sources*, vol. 280, pp. 173–181, 2015.

[229] I. Palaci, "Atomic Force Microscopy Studies of Nanotribology and Nanomechanics," PhD Thesis, École Polytechnique Fédérale De Lausanne, Switzerland, 2007.

[230] R. Brunner, G. W. Tyndall, R. J. Waltman, and F. E. Talke, "Adhesion Between Surfaces Separated by Molecularly Thin Perfluoropolyether Films," *Triboilogy Lett.*, vol. 40, pp. 41–48, 2010.

[231] E. Charrault, C. Gauthier, P. Marie, and R. Schirrer, "Experimental and Theoretical Analysis of a Dynamic JKR Contact," *Langmuir*, vol. 25, no. 10, pp. 5847–5854, 2009.

[232] M. Bahrami, M. M. Yovanovich, and J. R. Culham, "Thermal joint resistance of conforming rough surfaces with gas-filled gaps," *AIAA J. Thermophys. Heat Transf.*, vol. 18, pp. 318–325, 2004.

[233] A. J. Bullen, K. E. O'Hara, D. G. Cahill, O. Monteiro, and A. von Keudell, "Thermal conductivity of amorphous carbon thin films," *J. Appl. Phys.*, vol. 88, pp. 6317–6320, 2000.

[234] S. R. P. Silva, "Properties of Amorphous Carbon," *EMIS data Rev. Ser.*, no. 29, pp. 154–160, 2003.

[235] A. A. Balandin, M. Shamsa, W. L. Liu, C. Casiraghi, and A. C. Ferrari, "Thermal conductivity of ultrathin tetrahedral amorphous carbon films," *Appl. Phys. Lett.*, vol. 93, p. 043115, 2008.

[236] A. Nanjundappa, A. S. Alavijeh, M. El Hannach, D. Harvey, and E. Kjeang, "A customized framework for 3-D morphological characterization of microporous layers," *Electrochim. Acta*, vol. 110, pp. 349–357, 2013.

[237] I. N. Remediakis, M. G. Fyta, C. Mathioudakis, G. Kopidakis, and P. C. Kelires, "Structure, elastic properties and strength of amorphous and nanocomposite carbon," *Diam. Relat. Mater.*, vol. 16, pp. 1835–1840, 2007.

[238] G. M. Pharr, D. L. Callahan, S. D. McAdams, T. Y. Tsui, S. Anders, A. Anders, J. W. A. III, I. G. Brown, C. S. Bhatia, S. Silva, and J. Robertson, "Hardness, elastic modulus, and structure of very hard carbon films produced by cathodic- arc deposition with substrate pulse biasing," *Appl. Phys. Lett.*, vol. 68, no. 6, pp. 779–781, 1996.

[239] A. C. Ferrari, B. Racine, N. A. Morrison, I. Hutchings, W. I. Milne, and J. Robertson, "Amorphous carbon silicon alloys prepared by a high plasma density source," in *Materials Research Society Symposium Proceedings 593*, 2000, pp. 523–528.

[240] M. Bahrami, J. R. Culham, M. M. Yovanovich, and G. E. Schneider, ""Thermal contact resistance of non-conforming rough surfaces part 1: contact mechanics model," *AIAA J. Thermophys. Heat Transf.*, vol. 18, no. 2, pp. 209–217, 2004.

[241] M. Bahrami, M. M. Yovanovich, and J. R. Culham, "A compact model for contact of rough spheres," *ASME J. Tribol.*, vol. 127, pp. 884–889, 2005.

[242] Y. Liu, X. Zhang, Y. Xia, and H. Yang, "Magnetic-field-assisted electrospinning of aligned straight and wavy polymeric nanofibers," *Adv. Mater.*, vol. 22, pp. 2454–2457, 2010.

[243] H. Sadeghifar and M. Bahrami, "Thermal conductivity of Ballard's Bipolar Plates, Ballard technical report; No. BPP-0926-12/1, Laboratory for Alternative Energy Conversion, Simon Fraser University," Vancouver, BC, Canada, Sep. 2012.

[244] H. Sadeghifar and M. Bahrami, "Thermal and Electrical Resistances of Mercedes Benz Fuel Cell Samples: Effects of Compression, Temperature, Load Cycling, and Assembly, Mercedes Benz Fuel Cell (MBFC) technical report; No. MEAGDLCCM-1030-13/1, Laboratory for Alternative Energy Conversion," Vancouver, BC, Canada, Oct. 2013.

[245] S. J. Kline and F. A. McClintock, "Describing the uncertainties in single sample experiments," *Mech. Eng.*, vol. 75, no. 1, pp. 3–8, 1953.

Appendix A.

Thermal conductivity of Pyrex 7740 as a function of temperature

Table A1 Thermal conductivity of Pyrex 7740 calibration samples in terms of temperatures

T (°C)	k (W m^{-1} K^{-1})
0	1.058
20	1.087
40	1.116
60	1.145
80	1.175
100	1.203

Appendix B.

Uncertainty analysis

When measured values are used to calculate another value, the uncertainties propagate to the calculated value [170]. There are various approaches to evaluating the propagation of uncertainties based on the application of a statistical theorem using approximations. Here we follow the method proposed by Kline and McClintock [245]. Suppose quantity z is a function of two measured quantities x and y with uncertainties δx and δy. The uncertainty in the quantity z, δz, can be obtained using the rules below.

B1. Addition and Subtraction rule

The relative (fractional) uncertainty in $z = x + y$ or $z = x - y$ is calculated from Addition and Subtraction rule:

$$\frac{\delta z}{z} = \frac{\sqrt{(\delta x)^2 + (\delta y)^2}}{z} \qquad \text{(B-1)}$$

B2. Multiplication and Division rule

If $z = xy$ or $z = x/y$, then the fractional uncertainty in the quantity z is obtained using Multiplication and Division rule:

$$\frac{\delta z}{z} = \sqrt{(\frac{\delta x}{x})^2 + (\frac{\delta y}{y})^2} \qquad \text{(B-2)}$$

Appendix C.

Experimental data reported in this research

Table C1 Related to Figure 1.6 Effect of GDL compression ratio on the performance of a PEMFC. The compression ratio of the GDL is defined as the ratio of the change in operating thickness to the GDL original thickness (reprinted with permission from Ref. [64])

Compression ratio=15%		**Compression ratio=32.5%**	
***I* (*A* cm^{-2})**	**Voltage (*V*)**	***I* (*A* cm^{-2})**	**Voltage (*V*)**
0.0035	0.9647	0.0019	0.9647
0.0035	0.9336	0.0035	0.9356
0.0035	0.8921	0.0020	0.8941
0.0220	0.8423	0.0251	0.8423
0.0789	0.7885	0.0835	0.7906
0.1558	0.7430	0.1543	0.7389
0.2495	0.6913	0.2449	0.6913
0.3510	0.6418	0.3356	0.6417
0.4386	0.5921	0.4156	0.5900
0.5247	0.5529	0.4770	0.5549
0.6015	0.4991	0.5309	0.4928
0.6907	0.4454	0.5862	0.4452
0.7537	0.3936	0.6155	0.3933
0.8060	0.3439	0.6447	0.3436
0.8583	0.2943	0.6709	0.2918
0.9075	0.2425	0.6894	0.2441
0.9506	0.1928	0.7094	0.1964
0.9798	0.1451	0.7172	0.1467
0.9952	0.0912	0.7326	0.0928

Table C2 Related to Figure 3.11 Thermal conductivity of the graphite BPP (k_{BPP}) at different temperatures and compression (obtained from repeated tests): $R_{BPP}=t_{BPP}/(k_{BPP}A)$

T=10 °C	*P* (bar)	3.2	4.0	5.5	4.4		
	k (W m^{-1} K^{-1})	22.4	22.0	22.8	22.6		
25 °C	*P* (bar)	4.0	5.2	5.4	5.0		
	k (W m^{-1} K^{-1})	18.1	18.5	17.9	17.8		
45 °C	*P* (bar)	5.5	5.4	5.1	5.0	3.8	3
	k (W m^{-1} K^{-1})	11.7	11.7	12.0	12.1	11.6	11.7
55 °C	*P* (bar)	5.0	4.8	4.3	3.6	3.7	3.6
	k (W m^{-1} K^{-1})	9.8	10.1	10.1	10.1	10.1	10.1
70 °C	*P* (bar)	3.5	5.6	3.9	4.8		
	k (W m^{-1} K^{-1})	8.3	8.6	7.86	8.4		

Table C3 Related to Figure 3.13 TCR between the graphite BPP and the Armco-iron fluxmeters at different temperatures and compression (obtained from repeated tests)

T=10 °C	*P* (bar)	3.2	4.0	5.5	4.4		
	TCR (K W^{-1})	0.700	0.690	0.653	0.671		
25 °C	*P* (bar)	4.0	5.2	5.4	5.0		
	TCR (K W^{-1})	0.599	0.568	0.563	0.562		
45 °C	*P* (bar)	3.0	5.5	3.8	5.0	5.1	5.4
	TCR (K W^{-1})	0.441	0.378	0.423	0.395	0.393	0.378
55 °C	*P* (bar)	3.7	4.3	5.0	3.6	3.7	4.8
	TCR (K W^{-1})	0.344	0.333	0.324	0.367	0.365	0.357
70 °C	*P* (bar)	3.5	5.6	3.9	4.8		
	TCR (K W^{-1})	0.310	0.252	0.282	0.270		

Table C4 Related to Figure 3.12 Thermal conductivity of the graphite BPP (k_{BPP}) as a function of temperature

***T* (°C)**	10	25	45	55	70
***k* (W m^{-1} K^{-1})**	22.4	18.1	11.8	10.0	8.3

Table C5 Related to Figure 3.15 Thermal conductivity of Sigracet untreated and treated GDLs (k_{GDL}) as a function of compression: $R_{GDL}=t_{GDL}/(k_{GDL}A)$

***P* (bar)**	**2**	**4**	**5**	**6**	**10**	**14**
24AA	0.32	0.39	0.42	0.45	0.54	0.60
25AA	0.29	0.35	0.37	0.40	0.48	0.56
24BA	0.28	0.35	0.37	0.41	0.52	0.57
25BA	0.28	0.33	0.36	0.38	0.46	0.52
24DA	0.28	0.33	0.36	0.39	0.49	0.53
24BC	0.27	0.32	0.35	0.38	0.46	0.50
25BC	0.26	0.30	0.32	0.34	0.40	0.45

Table C6 Related to Figure 3.17 In-plane thermal conductivity of Toray carbon paper TGP-H-120 over a range of PTFE contents [58]

***P* (bar)**	***k* (W m^{-1} K^{-1})**
4.90	17.37
9.88	17.38
19.84	17.64
29.80	17.86

Table C7 Related to Figure 3.18 Thermal contact resistances of Sigracet untreated and treated GDLs with the Armco-iron fluxmeters (FM) as a function of compression: $TCR_{\text{GDL-FM}}$ & $TCR_{\text{MPL-FM}}$

***P* (bar)**	**2**	**4**	**5**	**6**	**10**	**14**
24AA	1.15	0.77	0.68	0.59	0.40	0.31
25AA	1.45	0.96	0.82	0.64	0.41	0.35
24BA	1.23	0.86	0.80	0.70	0.53	0.40
25BA	1.55	1.12	0.98	0.82	0.58	0.47
24DA	1.28	0.95	0.86	0.78	0.62	0.50
24BC	1.50	1.12	1.01	0.93	0.77	0.66
25BC	1.60	1.28	1.15	1.02	0.80	0.67

Table C8 Related to Figure 3.20 Thermal conductivity of SGL MPLs as a function of compression

***P* (bar)**	**2**	**4**	**5**	**6**	**10**	**14**
24BC	0.37	0.45	0.50	0.55	0.55	0.41
25BC	0.41	0.51	0.64	0.70	0.71	0.58

Table C9 Related to Figure 3.22 Variation of GDL thickness (μm) with compression

***P* (bar)**	**24BC**	**25BC**	**24DA**	**24BA**	**24AA**	**25BA**	**25AA**
1.0	228.0	226.5	187.0	185.0	183.0	183.5	181.5
1.3	225.5	223.0	186.0	183.0	181.0	177.5	175.5
1.5	224.5	222.0	184.5	181.0	179.0	176.0	174.0
1.8	222.5	219.5	182.0	180.0	178.0	173.0	171.0
2.0	222.0	218.5	181.0	179.0	177.0	172.0	170.0
2.5	219.5	214.5	178.0	175.0	173.0	168.0	166.0
3.0	217.5	211.5	176.0	172.5	170.5	165.0	163.0
3.5	215.5	208.5	174.0	170.0	168.0	162.0	160.0
4.0	213.5	207.0	172.0	168.0	166.0	160.0	158.0
4.5	211.5	204.0	170.0	167.0	165.0	157.5	155.5
5.0	209.5	202.5	169.0	166.0	164.0	156.0	154.0
5.5	208.0	200.5	168.0	165.0	163.0	154.0	152.0
6.0	207.0	199.5	166.0	163.5	161.5	152.5	151.0
6.5	205.0	197.0	165.0	162.0	160.0	151.0	149.5
7.0	203.5	195.0	164.5	161.0	159.0	149.0	147.5
8.0	201.5	192.5	163.0	159.0	157.0	146.0	144.5
9.0	200.0	189.0	161.0	157.0	155.0	143.0	141.5
10.0	198.5	188.0	159.0	156.5	154.5	140.0	139.0
11.0	197.0	185.5	157.0	154.0	152.0	138.5	137.5
12.0	195.5	184.0	155.5	151.5	149.5	137.0	136.0
13.0	194.5	181.5	154.5	150.0	148.5	135.0	134.0
14.0	193.5	179.5	153.0	149.0	147.0	132.0	131.5
15.0	192.5	178.0	151.0	147.0	145.0	132.0	130.5

Table C10 Related to Figure 3.24 Effect of different successive cyclic loads on the total resistance of SGL 34BC at the temperature of 60 ^{o}C

1st loading	*P* (bar)	1.00	1.77	3.00	3.82	5.55	8.18
	R (K W^{-1})	6.946	4.884	3.914	3.340	2.812	2.288
1st unloading	*P* (bar)	0.78	1.35	2.76	7.59		
	R (K W^{-1})	6.043	4.300	3.074	2.343		
2nd loading	*P* (bar)	2.68	3.40	4.83	7.59		
	R (K W^{-1})	3.459	3.150	2.715	2.343		
2nd unloading	*P* (bar)	0.78	1.35	2.76	7.59		
	R (K W^{-1})	6.043	4.300	3.074	2.343		
5th loading	*P* (bar)	1.60	3.50	7.33			
	R (K W^{-1})	4.273	3.037	2.322			
5th unloading	*P* (bar)	0.80	1.55	3.98			
	R (K W^{-1})	6.153	4.082	2.643			
8th loading	*P* (bar)	1.86	2.50	3.71	5.78	6.80	
	R (K W^{-1})	3.840	3.250	2.812	2.420	2.335	

Table C11 Related to Figure 3.25 Hysteresis behavior of subsequent discontinuous load cycles on the already-tested sample of SGL 34BC (related to Figure 3.24) over 4 successive days

1st loading	*P* (bar)	1.00	1.77	3.00	3.82	5.55	8.18
	R (K W^{-1})	6.946	4.884	3.914	3.340	2.812	2.288
1st day – 9th loading	*P* (bar)	0.87					
	R (K W^{-1})	6.017					
2nd day – 10th loading	*P* (bar)	1.07	5.327				
	R (K W^{-1})	5.630	2.477				
2nd day – 12th unloading	*P* (bar)	4.56					
	R (K W^{-1})	2.590					
3rd day – 13th loading	*P* (bar)	1.87	2.50	3.57	4.27	5.36	
	R (K W^{-1})	4.230	3.450	3.027	2.835	2.494	
3rd day – 13th unloading	*P* (bar)	3.87	5.36				
	R (K W^{-1})	2.779	2.494				
4th day – 14th loading	*P* (bar)	1.45	2.80	4.70	6.53	8.83	
	R (K W^{-1})	4.676	3.200	2.674	2.366	2.197	
8th loading	*P* (bar)	1.86	2.50	3.71	5.78	6.80	
	R (K W^{-1})	3.840	3.300	2.812	2.420	2.335	

Table C12 Related to Figure 3.27 Experimental data of TCR between the graphite BPP and 14 different SGL GDLs ($TCR_{GDL\text{-}BPP}$) at an average temperature of 55 ^{o}C

25BC	*P* (bar)	0.55	0.90	1.25	2.23	4.60	4.96	6.40	6.77	7.85	8.20	
	TCR (K W^{-1})	5.01	3.92	3.25	2.21	1.19	1.10	0.83	0.77	0.62	0.58	
24BC	*P* (bar)	2.00	3.69	4.26	5.03	6.38	7.00					
	TCR (K W^{-1})	2.36	1.93	1.75	1.33	1.13	1.01					
24DA	*P* (bar)	1.60	3.91	7.56								
	TCR (K W^{-1})	2.56	1.01	0.73								
24BA	*P* (bar)	2.50	4.38	4.87	5.31	5.86	6.00	7.03				
	TCR (K W^{-1})	0.98	0.34	0.33	0.26	0.23	0.23	0.22				
25BA	*P* (bar)	0.70	1.40	1.77	2.27	2.94	4.00	4.50	5.00	6.00	8.30	9.30
	TCR (K W^{-1})	3.58	2.16	1.80	1.47	1.17	0.88	0.78	0.61	0.50	0.33	0.27
24AA	*P* (bar)	1.87	2.75	3.90	4.20	4.60	5.20	6.00	7.06			
	TCR (K W^{-1})	1.57	0.77	0.36	0.33	0.32	0.18	0.14	0.12			
25AA	*P* (bar)	0.80	1.20	1.76	2.33	3.76	4.58	6.30	7.50			
	TCR (K W^{-1})	4.06	2.74	1.93	1.50	0.84	0.63	0.35	0.22			

Table C13 Related to Figure 3.29 Effect of the BPP out-of-flatness on $TCR_{BPP\text{-}GDL}$ (for comparison, the data of SGL 24 already shown in Figure 3.27 has been duplicated in this figure)

24BC	*P* (bar)	4.00	5.25	6.37	6.60	7.08
	TCR (K W^{-1})	3.88	3.50	3.33	3.23	3.06
24DA	*P* (bar)	3.50	5.00	5.75	6.38	
	TCR (K W^{-1})	3.33	2.64	2.22	2.07	
24BA	*P* (bar)	3.60	4.22	4.83	6.00	6.55
	TCR (K W^{-1})	2.85	2.36	2.00	1.42	1.21
24AA	*P* (bar)	3.90	5.10	5.50	6.00	
	TCR (K W^{-1})	1.36	1.02	0.91	0.83	

Table C14 Related to Figure 3.30 Effect of load cycles on the total resistance of SGL 24BA-BPP 5.84 assembly (including the contact resistance of the GDL with the two fluxmeters)

1st loading	*P* (bar)	1.50	2.50	4.15	4.87	6.17	7.00
	R (K W^{-1})	8.738	7.030	4.926	4.533	4.043	3.672
3rd loading	*P* (bar)	1.67	2.37	2.47	3.25	4.70	6.41
	R (K W^{-1})	7.291	5.949	5.871	4.914	3.950	3.741
3rd unloading	*P* (bar)	1.90	2.80	4.10	5.00	6.00	6.38
	R (K W^{-1})	6.656	5.400	4.333	3.860	3.735	3.700
6th loading	*P* (bar)	2.00	3.60	4.80	5.78		
	R (K W^{-1})	6.021	4.326	3.850	3.724		

Table C15 Related to Figure 3.31 Effect of load cycles on the total resistance of SGL 24DA-BPP 5.84 assembly (including the contact resistance of the GDL with the two fluxmeters)

1st loading	*P* (bar)	1.50	2.00	3.91	7.56				
	R (K W^{-1})	10.963	8.900	6.406	5.064				
1st unloading	*P* (bar)	1.00	1.30	2.50	4.11	4.32	6.18		
	R (K W^{-1})	11.184	9.204	6.856	5.685	5.654	5.179		
2nd loading	*P* (bar)	2.50	4.17	6.76					
	R (K W^{-1})	7.450	6.056	5.185					
2nd unloading	*P* (bar)	0.83	1.00	1.83	2.50	2.75	3.41	3.56	4.97
	R (K W^{-1})	12.833	11.000	7.604	6.833	6.504	6.014	6.006	5.481
5th loading	*P* (bar)	2.40	3.84	6.00	6.10	7.30			
	R (K W^{-1})	7.300	5.997	5.358	5.307	5.009			
5th unloading	*P* (bar)	1.09	1.14	1.18	1.72	3.45	6.00		
	R (K W^{-1})	11.033	10.823	10.547	7.824	5.872	5.142		
8th loading	*P* (bar)	1.12	1.20	2.00	3.77	3.99			
	R (K W^{-1})	11.563	10.776	7.800	6.036	5.943			
8th unloading	*P* (bar)	1.25	1.73	2.30	3.79	3.82			
	R (K W^{-1})	10.000	8.150	7.150	5.843	5.830			

Appendix D.

Article Usage Dashboard

Since the first article published from this thesis, i.e., Ref. [52], was published prior to May 2013, no report of "Article Usage Dashboard" was presented. For each article published after May 2013, an "Article Usage Dashboard" was sent to the corresponding author if the article was downloaded more than 25 times per month.

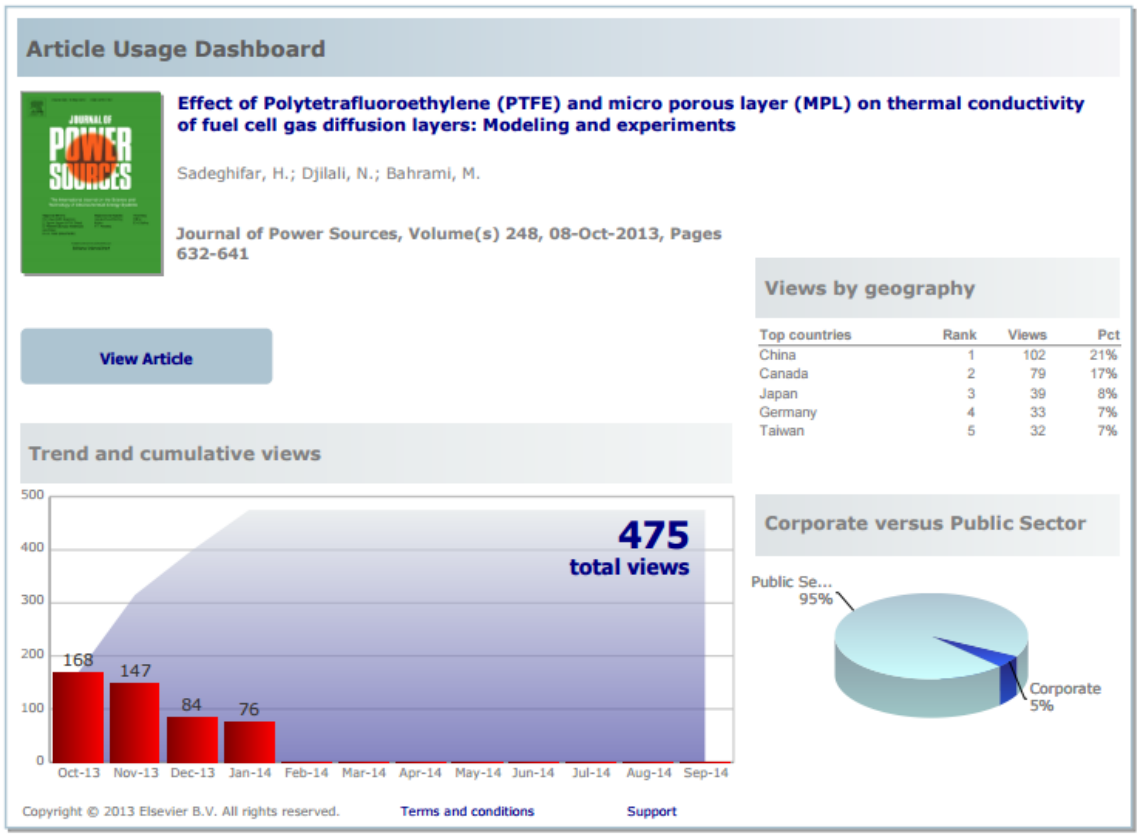

Article Usage Dashboard

A new model for thermal contact resistance between fuel cell gas diffusion layers and bipolar plates

Sadeghifar, H.; Djilali, N.; Bahrami, M.

Journal of Power Sources, Volume(s) 266, 15-May-2014, Pages 51-59

Share your article

Tips and Tricks to let the world know about your research

Download this dashboard

View Article

Trend and cumulative views

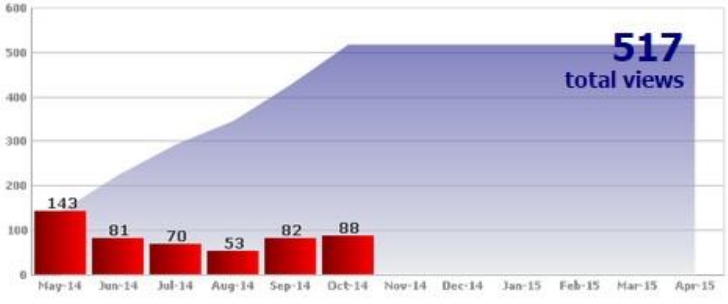

Views by geography

Top countries	Rank	Views	Pct
China	1	113	22%
Canada	2	105	20%
United States	3	37	7%
France	4	35	7%
Japan	5	32	6%

Corporate versus Public Sector

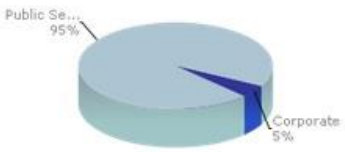

 Terms and conditions Support

Article Usage Dashboard

Thermal conductivity of a graphite bipolar plate (BPP) and its thermal contact resistance with fuel cell gas diffusion layers: Effect of compression, PTFE, micro porous layer (MPL), BPP out-of-flatness and cyclic load

Sadeghifar, H.; Djilali, N.; Bahrami, M.

Journal of Power Sources, Volume(s) 273, 18-Sep-2014, Pages 96-104

Share your article

Tips and Tricks to let the world know about your research

Download this dashboard

View Article

Trend and cumulative views

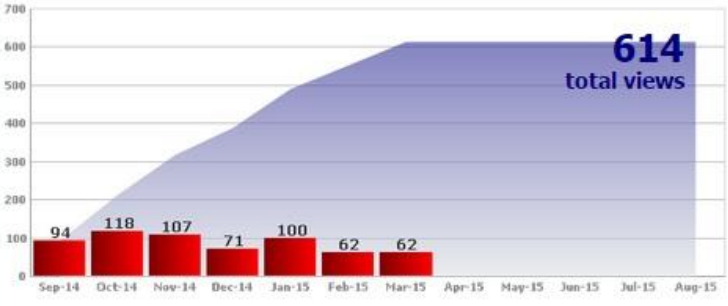

Views by geography

Top countries	Rank	Views	Pct
China	1	185	30%
Canada	2	160	26%
United States	3	55	9%
Germany	4	25	4%
India	5	23	4%

Corporate versus Public Sector